Analysis of X-Ray Observations of the Binary Hercules X-1

Dissertation
der Mathematisch-Naturwissenschaftlichen Fakultät
der Eberhard Karls Universität Tübingen
zur Erlangung des Grades eines
Doktors der Naturwissenschaften
(Dr. rer. nat.)

vorgelegt von

Davide Vasco

aus Mailand, Italien

Tübingen
2012

Tag der mündlichen Qualifikation:	20.04.2012
Dekan:	Prof. Dr. Wolfgang Rosenstiel
1. Berichterstatter:	Prof. i.R. Dr. Rüdiger Staubert
2. Berichterstatter:	Prof. Dr. Andrea Santangelo

E quindi uscimmo a riveder le stelle.
Dante Alighieri, Inferno, XXXIV Canto

Abstract

Her X-1 is one of the most observed and well-studied sources among accreting X-ray pulsars, but despite the detailed insights it provides, a large number of open questions are still to be answered.

The light curve of this source shows a strong modulation of the X-ray flux with a super-orbital period of about 35 days. This modulation is well known since the first observation made by *Uhuru* and consists of two *on-states* (high X-ray flux) and two *off-states* (low X-ray flux), with a *Main-On* ($\sim$ 7 orbital cycles) and a *Short-On* ($\sim$ 5 orbital cycles), separated by two *off*-states ($\sim 4 \div 5$ orbital cycles each). The maximum X-ray flux of the Main-On is higher than the maximum X-ray flux of the Short-On by a factor of three to four. This is a clear evidence for a tilted, warped and counter-orbitally precessing accretion disk which covers temporarily the X-ray emission regions.

The onset of the flux, the *turn-on* (often identified with 35 day phase 0.0), is believed to occur when the outer rim of the disk opens up the view to the X-ray emitting regions near the polar caps on the surface of the neutron star, while the flux decrease towards the end of the on-states is associated with the inner parts of the disk covering these regions from the observer.

This source was also the first accreting X-ray pulsar where a cyclotron line was discovered. This feature, which is present in several X-ray binaries, transient and persistent sources, correlates in a positive way with the bolometric luminosity of the source. This is in contrast with other super-Eddington transient pulsars for which a negative correlation is observed. Other interesting observational properties are the systematic energy- and time-evolution of the pulse profiles as function of the 35 day phase and the particular evolution of the spectral parameters as function of the pulse phase.

The dissertation presents the analysis and interpretation of X-ray observations of Her X-1 using data of the X-ray observatories *RXTE* and *INTEGRAL*. Using archival data of these two satellites several analyses have been performed. The collection of the data allowed to construct the X-ray light curves and to monitor systematic variations with the phase of the 35 day flux modulation. In parallel to this analysis, several pulse profiles in the energy range $9-13$ keV have been produced to allow a model-independent investigation of the periodic pulse profile variations. This permitted to extrapolate the so called "phase-zero" which corresponds to the transitions between the off-state and the Main-On, namely the turn-ons. These were compared with the turn-ons observed from the flux modulation. Within statistical uncertainties the two turn-on histories track each other perfectly. On the basis of this analysis, the free precession model which was proposed to explain the variation of the pulse profile is discussed.

Further, a deep spectral investigation of the source has been performed. The positive correlation between the centroid of the cyclotron line energy and the bolometric luminosity of the source was confirmed and all the spectral parameters were studied as function of the 35 day phase. The latter, allowed to understand whether within the 35 day super-orbital period, some spectral parameters show variations. This is the case for the absorption N_H, the photon-index Γ and the intensity of the iron line emission. On the other hand, both the folding energy E_{fold}

and the cutoff energy E_{cut} remain relatively constant.

Finally, the pulse phase resolved spectroscopy of *RXTE* data to monitor the variation of spectral parameters as function of the pulse phase was performed. This improved the picture already known from previous analyses and provided new insights. The variation of the iron line intensity as function of the pulse phase permitted to suggest a possible geometry for the accretion column.

Zusammenfassung

Her X-1 ist eine der am meisten beobachteten und besten untersuchten akkretierenden Röntgenpulsare. Jedoch gibt es trotz genauer Untersuchungen immer noch eine Vielzahl von offenen Fragen.

Im Röntgenbereich zeigt die Quelle eine starke Schwankung der Intensität mit einer "Super-Periode" von ungefähr 35 Tagen auf. Diese Schwankung ist seit den ersten Beobachtungen von Uhuru bekannt und besteht aus zwei On-Zuständen (hoher Röntgenfluss) und zwei Off-Zuständen (niedriger Röntgenfluss). Diese Zustände werden als "Main-On" (~ 7 orbitale Umläufe) und "Short-On" (~ 5 orbitale Umläufe) bezeichnet. Sie sind durch zwei Off-Zustände ($\sim$ 4-5 orbitale Umläufe) voneinander getrennt. Der maximale Röntgenfluss des "Main-Ons" ist drei- bis viermal so hoch wie der des "Short-Ons". Dies ist ein eindeutiger Hinweis für eine geneigte, verbogene und gegenläufig-präzedierende Akkretionsscheibe, welche zeitweise die Röntgenquelle verdeckt.

Es wird vermutet, dass der Flussanstieg, der Turn-On, der oft mit der Phase 0.0 des 35-Tage Zykluses gleichgesetzt wird, dann auftritt, wenn der äußere Rand der Scheibe den Blick auf die Bereiche freigibt, die Röntgenstrahlung emittieren. Diese befinden sich nahe der Polkappen auf der Oberfläche des Neutronensterns. Dagegen wird die Flussminderung am Ende des On-Zustandes mit der Abdeckung dieser Bereiche durch die innere Scheibe erklärt.

Her X-1 war ebenfalls der erste akkretierende Röntgenpulsar in dem eine Zyklotronlinie nachgewiesen wurde. In zahlreichen Röntgendoppelsternen, sowohl in "transients" als auch in "persistent" Quellen, wurde diese spektrale Besonderheit entdeckt. Bei Her X-1 wurde eine positive Abhängigkeit der Zyklotronlinie mit der bolometrischen Helligkeit beobachtet. Dies steht im Gegensatz zu anderen super-Eddington "transient" Pulsaren, die eine negative Abhängigkeit aufweisen. Die systematische Energie- und Zeitentwicklung des Pulsprofils in Abhängigkeit des 35-Tage Zykluses sowie die Entwicklung der spektralen Größen in Abhängigkeit der Puls Phase sind weitere interessante beobachtbare Eigenschaften.

In dieser Dissertation wird eine Analyse und Interpretation der Röntgenbeobachtungen von Her X-1 präsentiert. Die Beobachtungen wurden mit den Röntgenobservatorien RXTE und Integral durchgeführt. Archivdaten boten die Möglichkeit mehrere Analysen anzufertigen.

Mit Hilfe dieser Datensammlung konnte eine Röntgenlichtkurve erstellt werden und systematische Änderungen mit der Phase der 35 – Tage Flussänderung verfolgt werden. Zusätzlich zu dieser Analyse wurden Pulsprofile im Energiebereich von 9 – 13 keV angefertigt um eine Modell-unabhängige Untersuchung der periodischen Pulsprofil-Änderungen zu ermöglichen. Desweiteren erlaubt dies die Extrapolation des sogenannten "Phase-zero", welches den Übergang von dem "Off-Zustand" und dem "Main-On", den "Turn-On", beschreibt. Die Ergebnisse wurden mit den "Turn-Ons", die durch die Flussmodulation bestimmt wurden, verglichen. Innerhalb statistischer Unsicherheiten deckt sich der Verlauf der "Turn-ons" perfekt.

Anhand dieser Analysen wird das Modell der freien Präzession diskutiert, das entwickelt wurde um die Variation des "Pulsprofils" zu erklären. Ebenfalls wurde eine detaillierte spektrale Untersuchung der Quelle durchgeführt.

Die positive Abhängigkeit der Energie der Zyklotronlinie mit der bolometrischen Helligkeit wurde bestätigt und spektrale Parameter als Funktion der 35 – Tage Phase untersucht. Das Letztere bietet die Möglichkeit zu verstehen, ob innerhalb der 35 – Tage "Super-Periode" einige spektrale Größen Veränderungen aufweisen. Dies ist der Fall für die Absorption N_H, für den Photonen Index Γ und für die Intensität der Eisenlinie. Andererseits bleiben die Faltungsenergie E_{fold} und die "cut off" Energie E_{cut} relativ konstant.

Schließlich wurde eine Puls Phasen aufgelöste Spektroskopie der RXTE Daten durchgeführt.

Hiermit wurde das Bild, das vorherige Analysen geliefert hatten verbessert und neue Einblicke waren möglich. Durch die Variation der Eisenlinien Intensität als Funktion der Puls Phase wird eine bestimmte Geometrie der Akkretionssäule nahe gelegt.

Contents

1 Outline of the Thesis

X-ray Astronomy can be considered a relatively young science. Despite this fact, it plays a key role in understanding physical processes which describe the behavior of many astronomical objects. From the first extrasolar detection of X-rays by Giacconi et al. (1962) with an Aerobee rocket to the current modern observatories, X-ray Astronomy has considerably improved our knowledge about X-ray emitting sources.

A particular field of X-ray astronomy is the one of compact objects. These are black holes, neutron stars and white dwarfs and represent the endpoint of stellar evolution. The study of compact objects is related to the physics of highly condensed matter. In particular, pulsars with their properties such as a temperature T of $\sim 10^8$ K, a density comparable to the nuclear density and magnetic fields of the order of 10^{12} G are an ideal laboratory for probing physics under extreme conditions.

X-ray pulsars are one of the most interesting and complex objects. Their history started when, during *Uhuru* observations, pulsations from Cen X-3 were discovered and the source was later identified as an X-ray pulsar by Giacconi et al. (1971). These objects are highly magnetized, rotating neutron stars which are observed from Earth as pulsating sources. This is because their emission, depending on the spin period of the star, intersects regularly the line of sight of the observer, much like the flashing emission of a light house. A special sub-class of pulsars are the so-called accreting X-ray pulsars. Cyclic variations of the pulse period have revealed that these objects are part of a close binary system (Pringle & Rees 1972, Davidson & Ostriker 1973, Lamb et al. 1973). From this suggestion, all of the physics about X-ray pulsars powered by accretion mechanisms started.

X-ray pulsars show several phenomena on different timescales which are not always clear. Free precession of neutron stars has been assumed as the mechanism behind some long-period variations in the fluxes of X-ray binaries or other observational properties like the pulse profiles variation.

Neutron stars in binary systems accrete matter either by capturing material from the companion star through stellar wind or through Roche lobe overflow of the donor star. The strong magnetic field, close to the neutron star, drives the accretion flow until it falls onto the magnetic poles. This process has a very high efficiency, and due to that, X-ray binaries are the brightest objects in our Galaxy.

Nowadays, the physical knowledge related to these objects is highly improved, but still, many questions need to be answered here. A very interesting case is represented by Her X-1. This source is one of the best studied and best known accreting X-ray pulsars. But, despite this fact, some of its peculiar observational properties are still enigmatic for astronomers. Because of this, after more than 70 years after its discovery as an irregular variable star, an intense study and new observations with the modern X-ray observatories are needed.

The aim of this thesis is to improve our knowledge about Her X-1 making use of both *RXTE* and *INTEGRAL* observatories, in order to explore the physics which governs the observational

properties of this system. To do that, several different analyses have been performed leading to a better understanding of the behavior of this source.

This thesis is organized as follows. Chapter 2 provides a brief introduction to X-ray binaries and the accretion mechanisms. In particular, the characteristics of compact objects, of both High Mass X-ray Binaries (HMXBs) and Low Mass X-ray Binaries (LMXBs) as well as the accretion onto neutron stars are discussed. Chapter 3 and Chapter 4 are dedicated to a short overview of the *RXTE* and *INTEGRAL* observatories and of the system Her X-1/HZ, respectively. In particular, in Chapter 3, the main observational properties of the system as well as the system parameters are summarized. In Chapter 4, the instruments on-board the satellites are described. In Chapter 5, a detailed description of the X-ray flux modulation of Her X-1 is given. In addition, the extracted X-ray light curves to monitor the behavior of the source are shown. Chapter 6 is devoted to the description of the pulse profile variation as function of energy and 35 day phase and to their analysis in order to determine the so-called *turn-on* on the basis of the pulse profile shape. In Chapter 7, one of the most interesting features of the X-ray spectrum of Her X-1, namely the Cyclotron Resonant Scattering Feature (CRSF), is introduced. Using the information about this absorption line from different observations, the positive correlation between the centroid of the line and the bolometric luminosity of the source has been verified. Chapter 8 and 9 are entirely dedicated to the study of the spectral parameters of Her X-1. In Chapter 8, their evolution as function of the 35 day phase is studied. In Chapter 9, the pulse-phase resolved spectroscopy analysis allowed the study of the same spectral parameters as function of pulse-phase of the source. Finally, Chapter 10 summarizes the results obtained in this thesis and describes new physical insights that have been resulted from this work.

2 X-ray binaries and accretion mechanisms

In this chapter, the mechanisms which govern the transfer of matter in X-ray binary systems and the accretion processes onto compact objects are briefly described. Some details about the physics of accretion for X-ray pulsars are given as well. The contents of this chapter are mainly based on Shapiro & Teukolsky 1986 and Longair 2010.

2.1 Compact objects

As reported by Shapiro & Teukolsky (1986), compact objects represent the final stage of stellar evolution as they begin their life when normal stars "die". They consist of three types, white dwarfs, neutron stars and stellar mass black holes, and they differ significantly from normal stars for two main reasons:

1. compact objects have a much smaller size than normal stars. Compared to normal stars with the same mass, compact objects have much smaller radii and also much stronger surface gravitational fields;

2. compact objects have no nuclear fuel available to burn as in the case of normal stars. Because of this, they cannot generate the thermal pressure to maintain hydrostatic equilibrium and support themselves against gravitational collapse. To solve this problem, compact objects use a different kind of pressure called degeneracy pressure. White dwarfs are in fact supported by degenerate electron pressure and neutron stars by degenerate neutron pressure. In the case of black holes, the situation is totally different because they are completely collapsed objects.

Because of the high densities, the physics which describes these objects is closely related to the structure of matter and the nature of the inter-particle forces. For the same reason, and due to the large surface potential, general relativity cannot be neglected.

White dwarfs, because of their very small radii compared to normal stars, are characterized by a higher temperature than normal stars (although at lower luminosity), in order to radiate away their residual thermal energy. Therefore, they appear "whiter" than normal stars. In the case of neutron stars, there is a predominance of neutrons in their interior. This is due to inverse beta decays of electrons and protons. Because of their comparable density to nuclear values (10^{57} baryons), they are essentially big nuclei. Table 2.1 summarizes the characteristics of these objects.

These objects are as common as normal stars in our Galaxy, but not all of them can be directly observed. White dwarfs can be observed directly with optical campaigns during the so-called "cooling epoch". Neutron stars can also be directly observed as pulsating radio sources or accreting X-ray pulsars. On the other hand, black holes can be not directly observed, but the

detection of a compact object with a mass much larger than the maximum possible mass for a neutron star, can be considered as an unequivocal evidence for these compact objects.

To understand whether a normal star will produce either a neutron star, a white dwarf or a black hole after its death, one must consider its mass. White dwarfs are believed to be generated from stars with a mass $\mathrm{M} \lesssim 4\,\mathrm{M}_{\odot}$ and black holes and neutron stars from more massive stars.

Table 2.1: Physical parameters which describe white dwarfs, neutron stars and black holes (Shapiro & Teukolsky 1986).

Object	Mass[1] (M)	Radius[1] (R)	Density (g cm^{-3})	Surface potential ($\mathrm{G}M\,/\,R\mathrm{c}^2$)
Sun	$M_{\odot}$	$R_{\odot}$	1	10^{-6}
White dwarf	$\lesssim M_{\odot}$	$\sim 10^{-2}\,R_{\odot}$	$\lesssim 10^{7}$	$\sim 10^{-4}$
Neutron star	$\sim 1-3\,M_{\odot}$	$\sim 10^{-5}\,R_{\odot}$	$\lesssim 10^{15}$	$\sim 10^{-1}$
Black hole	arbitrary	$2\,\mathrm{G}M\,/\,\mathrm{c}^2$	$\sim M/\,R^3$	~ 1

[1] $M_{\odot} = 1.989 \times 10^{33}$ g and $R_{\odot} = 6.9599 \times 10^{10}$ cm.

2.2 X-ray binaries

A binary system consists of two stars which orbit around each other with respect to the common center of mass (see Figure 2.1). Binary systems represent almost half of the stars in the sky and among this class, a special sub-class is represented by the so-called *X-ray binaries.*

X-ray binaries are binary systems composed of a normal star and a compact object, which could be either a white dwarf, a neutron star or a black hole. The distance between the two stars is relatively small leading to the process of mass transfer from the companion star onto the compact object. During this process, the matter ejected from the normal star is gravitationally captured and then accreted by the compact object. While the matter is falling onto the collapsed star, it gains high kinetic energy. Thus, in the case of a neutron star, when the accelerated material is stopped close to the surface of the neutron star, the gravitational energy is converted into X-ray radiation.

X-ray binaries are usually divided into two classes:

- High Mass X-ray Binaries (HMXBs). This subclass is characterized by a massive companion star ($M \gtrsim 4M_{\odot}$), usually a main sequence star of spectral types O – B, giant or supergiant. The collapsed star is a neutron star or a black hole, and the accretion mechanism is normally through wind accretion (described in section 2.3.1). These sources have an X-ray luminosity of $10^{34} - 10^{38}$ erg s^{-1} and are usually located in the Galactic plane, along the spirals arms where star formation regions are present. Because of this, HMXBs are relative young systems with an age of about 10^{7} years.

- Low Mass X-ray Binaries (LMXBs). In this sub-class, the collapsed star is a black hole or a neutron star. The companion star is normally a main sequence star or either a white dwarf.

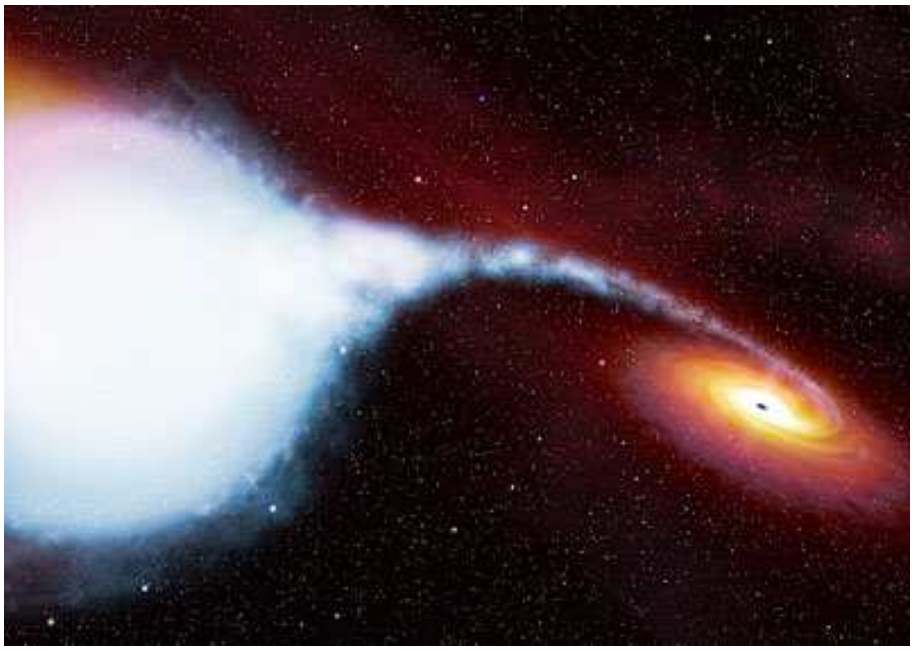

Figure 2.1: Artist's representation of a binary system.

These systems present a huge variability which is, in many cases, related to the so-called *type 1 bursts*, thermonuclear explosions on the surface of the neutron star (in't Zand 2011). Sometimes, also *type 2 bursts* are observed. These are less common than type 1 bursts and are due to accretion instabilities (Lewin et al. 1993). Usually, the optical counterpart is very faint and, because of this, undetectable. LMXBs are concentrated in the direction of the galactic centre and in globular clusters. They are much older than HMXBs for evolutionary reasons (see e.g. Verbunt et al. 2008).

These two sub-classes differ not only in the observational properties given in in Table 2.2, but also in their evolution. This is below described following the overview by Tauris & van den Heuvel (2006).

As mentioned before, HMXB systems are characterized by a massive companion star of spectral type O or B. The companion star emits a strong stellar wind which can be gravitationally captured by the neutron star. A second possibility is that the massive star fills its Roche lobe and starts the mass transfer mechanism. Assuming the compact object as a neutron star, because of the extreme mass ratio, a so-called *spiral in* phase is expected. The neutron star spirals inward into the envelope of the companion. This is due to the fact that drag-forces are created, leading to the dissipation of angular momentum. At the end of this phase, the distance between the two members of the system is quite small. As an outcome of this event, due to gravitational interactions, the envelope can be ejected by the neutron star leading to the formation of a classical high mass X-ray binary. Then, the system can even continue to evolve with the formation of a white dwarf and a millisecond pulsar.

In the case of LMXBs, their evolution is more difficult to understand because there are no clear signature of it in the observations. Also in this scenario, the massive star evolves first, starts mass

Table 2.2: Summary of the main characteristics of HMXBs and LMXBs.

	(HMXBs)	(LMXBs)
Companion star mass	$M > 4\,M_{\odot}$	$M < 1\,M_{\odot}$
Companion star type	O – B	M – K
Type of accretion	Wind, RLO	RLO
Variability	Regular pulsations	mainly Type 1,2 bursts
X-ray Spectrum	power law + cutoff >15 keV	black body dominated <10 keV
X-ray Luminosity (L_x)	$\sim 10^{34} - 10^{38}$ erg s^{-1}	$10^{34} - 10^{38}$ erg s^{-1}
Magnetic Field (B_x)	$\sim 10^{13}$ G	$\sim 10^{13} - 10^{12}$ G
Age	$\sim 10^{7}$ yrs	$\sim 10^{9}$ yrs
Location	Galactic plane arms	Galactic plane/centre globular clusters

transfer mechanism and "captures" the companion with its envelope starting a common envelope stage. Because of the evolution of the massive core, a supernova event can occur. If the core is not too massive, the binary will survive this event, otherwise will be disrupted. The resultant outcome is the formation of a low mass X-ray binary with a companion star of main sequence. Sometimes, the orbit is wide enough that during the supernova event angular momentum is lost. If this is the case, the mass transfer mechanism will start only when the donor evolves away from the main sequence becoming a giant. This is true for companion stars with a mass comparable to the solar mass. If the companion is more massive, as in the case of Her X-1, when it starts to fill its Roche lobe a second spiral-in phase may start, leaving the neutron star orbiting around the core of the companion. Then, the mass transfer ends when the envelope collapses leading to a system made of a degenerate core of a giant star and a compact star. This core can cool into a white dwarf. Then, a phase of common envelope and the consequent restriction of the binary distance can be observed. A second supernova event can occur ending up with the formation of a young pulsar and a so-called recycled pulsar.

2.3 Accretion physics

Accretion is the physical process through which a compact object gravitationally attracts matter from the companion star in the surrounding environment, in the sense that the matter from the companion star is transferred onto the compact object. This process leads to an exchange of mass between the members of the system and can occur in two different modes: (1) Roche lobe overflow, (2) stellar wind.

For a particle with mass m infalling from infinity onto the surface of a neutron star of mass M and radius R, the total energy E_{tot} along the radial trajectory is conserved. Considering a proton as the particle, it will gain kinetic energy along the radial trajectory. This energy is equal to zero at the starting point R_0, so, to conserve the total energy:

$$E_{tot} = \frac{1}{2}mv^2 - \frac{GMm}{R} = 0. \tag{2.1}$$

From Equation (2.1) the velocity of free fall can be derived as:

$$v_{ff}^2 = \frac{2GM}{R}. \tag{2.2}$$

This velocity represents the speed with which the proton arrives to the surface of the neutron star. The proton ends its fall when it is close to the surface of the neutron star and releases its kinetic energy. At a radius $R_I = R + \xi > R$ close to the surface of the neutron star, the proton starts to be decelerated. Thus, the total energy which is dissipated in this process $E_{tot,diss}$ will be:

$$E_{tot,diss} = \frac{GM}{Rc^2} \cdot mc^2. \tag{2.3}$$

For a neutron star this energy is $\simeq 0.1\, m\, c^2$, hence the accretion in neutron stars or black holes is more efficient than nuclear burning of H into He ($\sim$0.007).

The X-ray luminosity produced by the accretion is:

$$L \simeq \frac{GM\dot{M}}{R}, \tag{2.4}$$

where $\dot{M}$ is the mass accretion rate. This formula is extremely important because it gives information about the luminosity, only knowing the characteristics of the compact object such as the radius and the mass. Or, viceversa, it is possible to estimates these two physical parameters only looking at the observed luminosity.

In this framework, there is a limit on the accretion luminosity which can be observed. This is the so-called *Eddington limit*. This limit, also called the *Luminosity of Eddington*, is the maximum luminosity which a source with a spherically symmetric accretion can emit in a steady state. Theoretically, this represents the limit at which the radiation pressure of the source equals its gravitational attraction. Beyond this limit the radiation pressure is greater than the gravitational attraction and the source has to react to this radiation ejecting the outer layers of the object to keep the balance between the inward force of gravity and the outward radiation pressure.

For a fluid element Δm with an acceleration $\mathbf{a}$ the equation of motion is described by:

$$\Delta m \mathbf{a} = \mathbf{F}_{grav} + \mathbf{F}_{rad}, \tag{2.5}$$

where F_{grav} represents the gravitational force acting on an electron-proton pair and can be written as:

$$\mathbf{F}_{grav} = \frac{GM}{r^2}(m_p + m_e) \simeq \frac{GMm_p}{r^2}, \tag{2.6}$$

where m_p and m_e are the mass of the proton and the mass of the electron, respectively. F_{rad} is the radiation force acting on the electron and is given by:

$$\mathbf{F}_{rad} = \sigma_{Th}\, N_{ph}\, p, \tag{2.7}$$

where $\sigma_{Th} = \frac{8}{3}\pi r_e^2$ is the Thomson scattering cross section, N_{ph} is the flux of the photons and p is the momentum exchanged between the photon and the electron in each collision. N_{ph} is given

by:

$$N_{ph} = \frac{L}{4\pi r^2 h\nu}, \tag{2.8}$$

where L is the X-ray luminosity of the source and $h\nu$ the energy of the photons.

Using the expressions for the forces (2.6) and (2.7), the equation of motion becomes:

$$\Delta m\mathbf{a} = -\frac{GM\Delta m}{r^2} + \frac{L}{4\pi r^2 c}\sigma_{Th} = \frac{1}{r^2}\left(-GM\Delta m + \frac{L}{4\pi c}\sigma_{Th}\right). \tag{2.9}$$

From Equation (2.9), assuming $\Delta m = m_p$, it is possible to define the Luminosity of Eddington for which the gravitational force F_{grav} equals the radiation force F_{rad}:

$$L_{Edd} = \frac{4\,\pi\, GMm_p\, c}{\sigma_{Th}} \simeq 1.3 \times 10^{38}\frac{M}{M_\odot} erg\, s^{-1}. \tag{2.10}$$

This formula plays a key role in the physics which governs X-ray binary systems. In particular, L_{Edd} is proportional to the mass in a linear way. This means that assuming a spherically symmetric body in a steady state, this luminosity can provide an estimate of the compact object-characteristics.

Despite the fact that the Eddington limit represents the maximum luminosity for a source under the conditions of spherically symmetric accretion and steady state, some violations to this limit are observed and can be listed as:

1. considering non spherically symmetric accretion;
2. strong variability, for example due to an outburst with the consequent luminosity exceeding the Eddington limit for very short timescales;
3. the presence of relativistic beaming.

2.3.1 Roche lobe overflow (RLO) vs stellar wind accretion

In a binary system the gravitational attraction of both stars and their orbital motion around each other play a key role in determining the potential surfaces of the system. Because of this, the gravitational potential of the two objects has to be added to an extra centrifugal potential which is associated with the binary motion of the system. Thus, assuming two point masses M_1 and M_2 at distances r_1 and r_2 from the centre of mass of the system, the equipotential surfaces are given by:

$$\Phi = \frac{GM_1}{r_1} + \frac{GM_2}{r_2} - \omega^2 r^2 = constant, \tag{2.11}$$

where ω is the angular velocity of the binary system and r the distance to the axis of rotation of the system (Longair 2010).

An example of equipotential surface contours of a binary system is shown in Figure 2.2. Only one of all the gravitational potential surfaces intersects itself. This intersection happens to be in the so-called Lagrangian point L_1. Each region on both the right side and the left side of this point represent the Roche lobes of the two stars. During the evolution of the system, if the companion star evolves and fills its Roche lobe, the mass transfer onto the compact object

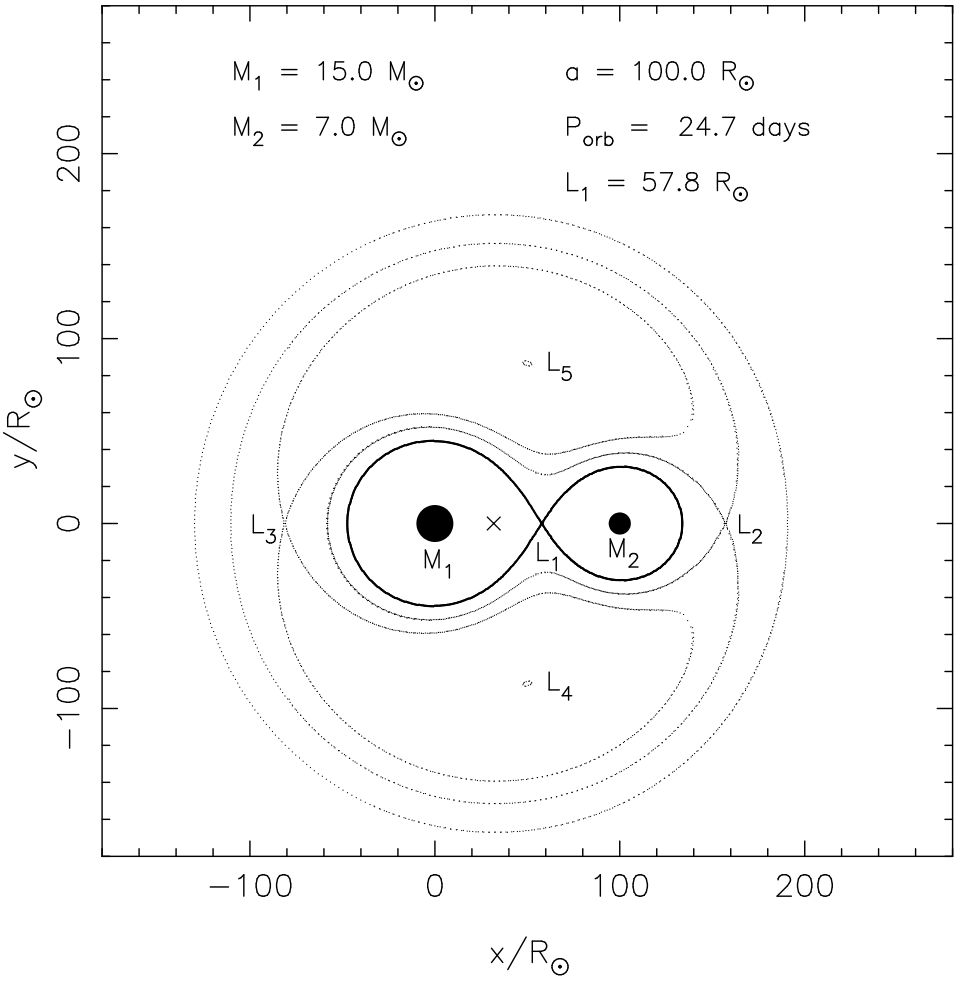

Figure 2.2: Cross-section of the equipotential surfaces for a binary system characterized by two stars of mass $M_1 = 15.0\,M_\odot$ and $M_2 = 7.0\,M_\odot$, respectively. The binary separation a is $100.0\,R_\odot$ and the orbital period $P_{orb} = 24.7$days. The thick curve which crosses through $L_1 = 57.8\,R_\odot$ represents the Roche lobe of the system (Tauris & van den Heuvel 2006).

can start because of the unbalanced pressure at L_1 (Tauris & van den Heuvel 2006). Thus, the matter flows through the Lagrangian point L_1, and the compact object can start to accrete matter through the formation of an accretion disk. The mass transfer through Roche lobe overflow is observed in close binary systems, mostly LMXBs, where the vicinity of the two components of the system influences their evolution (see Figure 2.3).

For *contact binary systems*, where the binary separation ranges between a few times the radius of the companion star to systems with a common envelope even bigger than the Roche lobe, the common envelope lies outside the Roche lobe. On the other hand, for *non-contact close binary systems*, the Roche lobe is not filled by the companion star and the evolution is similar to the evolution of a normal star (Tauris & van den Heuvel 2006).

The situation is totally different for stellar wind accretion. In this case, when the normal star

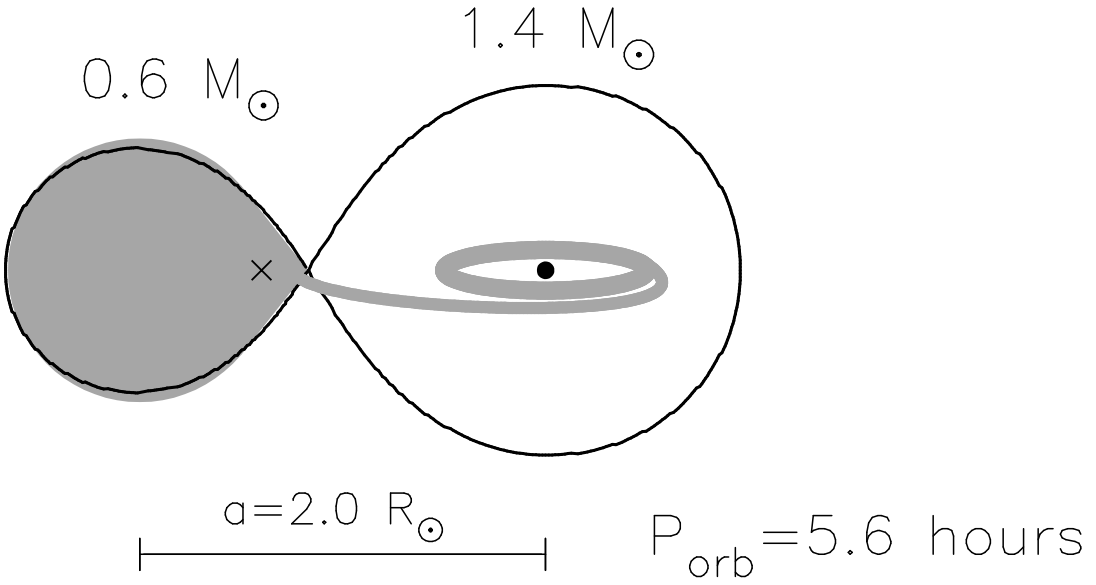

Figure 2.3: Roche lobe overflow for a LMXB with a companion star of $0.6\,M_{\odot}$, a compact object of $1.4\,M_{\odot}$, a binary separation a of $2.0\,R_{\odot}$ and an orbital period P_{orb} of 5.6 hours (Tauris & van den Heuvel 2006).

has strong, outward flowing stellar wind, some of the ejected material can be gravitationally captured and then accreted by the compact object while orbiting the companion star (see Figure 2.4). This process is found in HMXBs where the companion has a strong wind with mass loss rate of $\sim 10^{-6} M_{\odot}/yr$ and supersonic wind with typical velocity of $v_w \simeq 10^3\,\mathrm{km/s}$ (see e.g. Lamers et al. 1976 and references therein).

Accretion in wind-fed X-ray binaries can be described with the Bondi-Hoyle-Lyttleton accretion theory (Hoyle & Lyttleton 1941, Bondi & Hoyle 1944 and Bondi 1952). The stellar wind is ejected by the companion star in all directions, and only some of it is gravitationally captured from a roughly cylindrical region with axes along the wind direction relative to the compact object. The radius of the cylinder is called *accretion radius* and is given by:

$$r_{acc} = \frac{2GM}{v_{rel}^2 + c_s^2}, \tag{2.12}$$

where v_{rel} is the relative velocity between the compact object and the wind, and c_s is the sound velocity through the wind. The mass accretion rate depends on the accretion radius r_{acc} and can be expressed by the following equation:

$$\dot{M} \sim \frac{\dot{M}_w}{4\pi a^2} \cdot \pi r_{acc}^2, \tag{2.13}$$

where $\dot{M}_w$ is the rate of mass loss by the companion star and a is the binary separation. Thus, the factor $\frac{\dot{M}_w}{4\pi a^2}$ is the wind flux at a distance a from the companion and πr_{acc}^2 is the accretion cross section (Lamers et al. 1976).

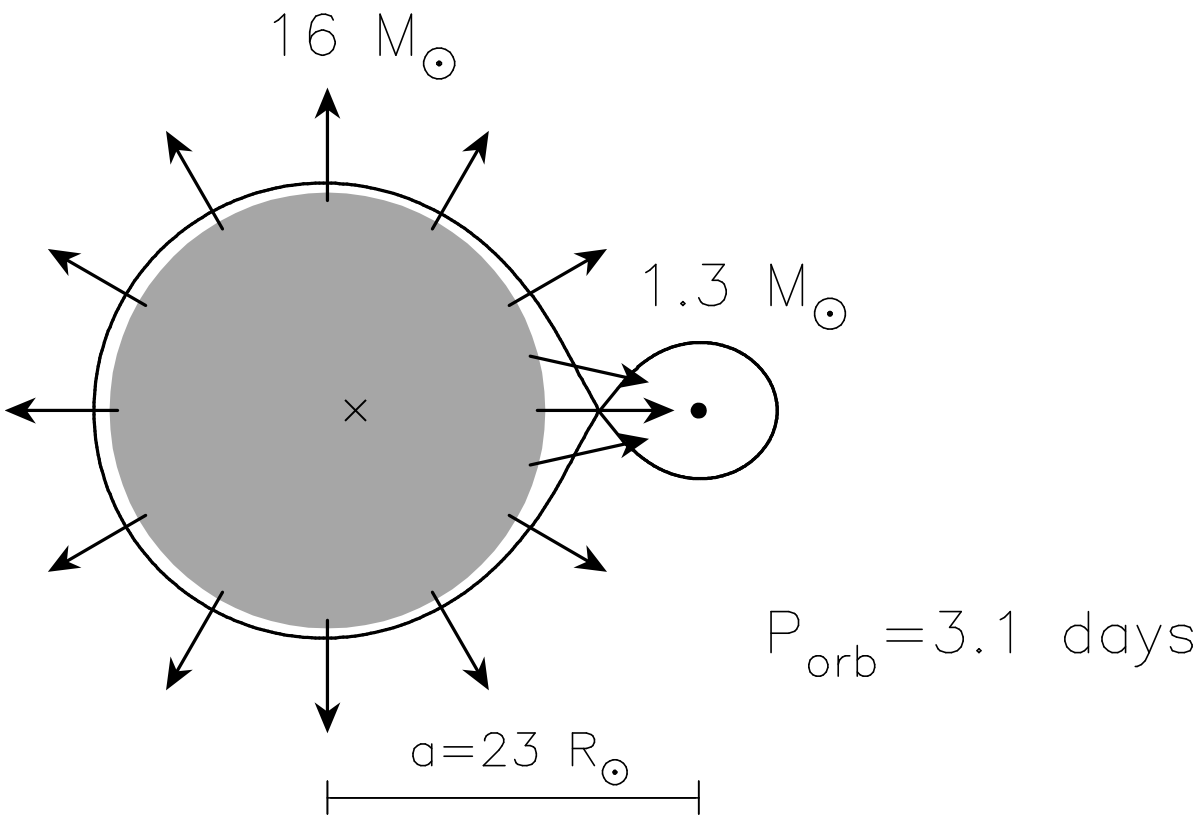

Figure 2.4: Stellar wind accretion for a HMXB with a companion star of $16\,M_{\odot}$, a compact object of $1.3\,M_{\odot}$, a binary separation a of $23\,R_{\odot}$ and an orbital period P_{orb} of 3.1 days (Tauris & van den Heuvel 2006).

2.3.2 The case of the Be star

The Be/X-ray binaries are composed by a neutron star and a rapidly rotating O-B star with an extended circumstellar disk which surrounds its equator (see Figure 2.5). It is believed that in these systems mass transfer is enhanced during periastron passage, when the neutron star accretes matter from the denser region of the circumstellar disk of the Be star, resulting in an X-ray outburst (e.g. Raguzova & Lipunov 1998). The X-ray emission from the Be-star X-ray systems tends to be extremely variable, ranging from complete absence to giant transient outbursts normally lasting days to weeks.

The recurrent X-ray outbursts can be related to the irregular optical outbursts generally observed in Be-stars, which indicate sudden outbursts of mass ejection, presumably generated by rotation-driven instability in the equatorial regions of these stars (see e.g. Slettebak & Snow 1988).

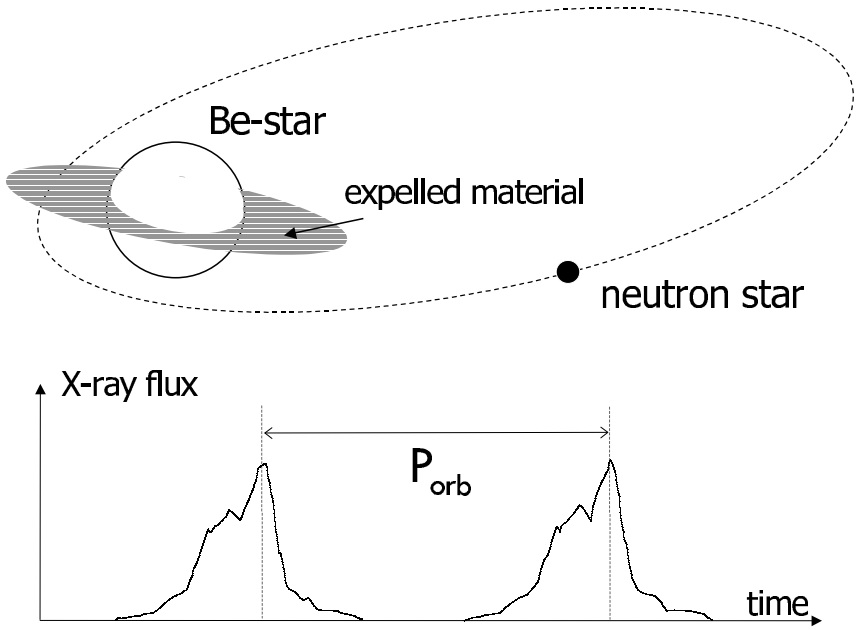

Figure 2.5: Schematic view of a Be/X-ray binary system and its outbursts (Tauris & van den Heuvel 2006).

2.4 Radio-pulsars

A pulsar is defined as a source with a pulsating emission. In particular, radio-pulsars are highly rotating neutron stars with a high magnetic field strength. From the perspective of an observer, these objects seem to pulse at radio and X-ray wavelengths, because of the misalignment between the rotation axis of the source and the axis of its magnetic field. While the neutron star is rotating, the beam of radiation from the poles sweeps in and out of the line of sight of the observer. Main observational properties of pulsars are (Shapiro & Teukolsky 1986):

- the period of pulsars ranges between fraction of seconds to thousands of seconds;
- pulsar periods slowly increase (except for occasional decreases called "glitches");
- pulsars can be considered as good clocks.

These astronomical objects were detected for the first time in 1967 by Jocelyn Bell in the group of Anthony Hewish when they observed stars emitting periodic radio pulses (Hewish et al. 1968). The unusual periodic signal detected was only later associated to rotating neutron stars, with a magnetic filed strength at the surface around 10^{12} G, by Gold (1968).

Gold (1968) also predicted an increase of the period with the loss in rotational energy of the rotating neutron star. This prediction was confirmed by the discovery of the slowdown of the Crab pulsar. Because of this, the model based on a rotational powered neutron star was accepted.

2.5 Accreting X-ray pulsars

Accreting X-ray pulsars differ from radio-pulsars because they accrete material from the companion star. These objects are always in binary systems and are powered by the accretion mechanism. X-ray accreting pulsars accrete matter from the companion through Roche lobe overflow or stellar wind. The flow of matter reaches the magnetosphere of the neutron star and is then channeled along the magnetic field lines onto the magnetic poles of the compact object. To describe this scenario, two different regions have to be considered: the region far from the surface of the neutron star and the region close to its surface.

In the first region, the accretion is spherically symmetric and can be described by:

$$\dot{M} = 4\pi r^2 \rho u, \tag{2.14}$$

where u is the inward radial velocity and ρ the mass density of the gas at a radius r.

As reported by Bondi (1952), Equation (2.14) states how the flow can be described only by the accretion rate $\dot{M}$.

On the other hand, the magnetic field of the neutron star has a strong influence on the flow close to the surface of the source. The matter, in fact, couples to the magnetic field at the so-called *Alfvén radius*. At this radius, the energy density of the magnetic field is comparable to the kinetic energy of the accreting gas and the magnetic field starts to dominate the flow. Thus, the Alfvén radius r_A corresponds to the boundary of the magnetosphere.

The Alfvén radius is defined as the distance from the neutron star where the magnetic field pressure $\frac{B^2(r_A)}{8\pi}$ and the ram pressure of the accreted matter is in equilibrium (Davidson & Ostriker 1973). Equating the magnetic pressure with the ram pressure:

$$\frac{B^2(r_A)}{8\pi} \simeq \frac{1}{2}\rho(r_A)v^2(r_A) \approx \frac{\mu}{r^3} = (10^{12}G)\,\mu_{30}\,R_6^{-3}\left(\frac{R}{r}\right)^3. \tag{2.15}$$

Using Equations 2.12 and 2.14, one can deduce from Equation 2.15:

$$r_A = \left(\frac{\mu^4}{2GM\dot{M}^2}\right)^{1/7} = 3.2\times10^8 \dot{M}_{17}^{-2/7}\,\mu_{30}^{4/7}\left(\frac{M}{M_\odot}\right)^{-1/7}\text{cm}, \tag{2.16}$$

which gives r_A as a function of the mass accretion rate. Using the expression for the total accretion luminosity:

$$L \simeq \dot{M}\frac{GM}{R}. \tag{2.17}$$

Equation (2.16) can be re-written in terms of L in the following way:

$$r_A = \left(\frac{\mu^4 GM}{2L^2M^2}\right)^{1/7} = 3.5\times10^8 L_{37}^{-2/7}\,\mu_{30}^{4/7}\left(\frac{M}{M_\odot}\right)^{-1/7} R_6^{-2/7}\text{cm}, \tag{2.18}$$

where L_{37} is the luminosity in units of 10^{37} erg s^{-1}.

Before the matter reaches this radius, the magnetic field does not penetrate the plasma, but after it, the matter is affected by it and close to the surface of the neutron star starts to be channeled by the magnetic field lines onto the pole on the surface of the neutron star (see Figure

2.6). Accretion structures at the magnetic poles of the neutron star are then created. These are the regions where the X-ray emission originates.

Over the years, many models have been developed to explain how the matter is funneled onto the magnetic poles of the neutron stars, but the picture is still unclear.

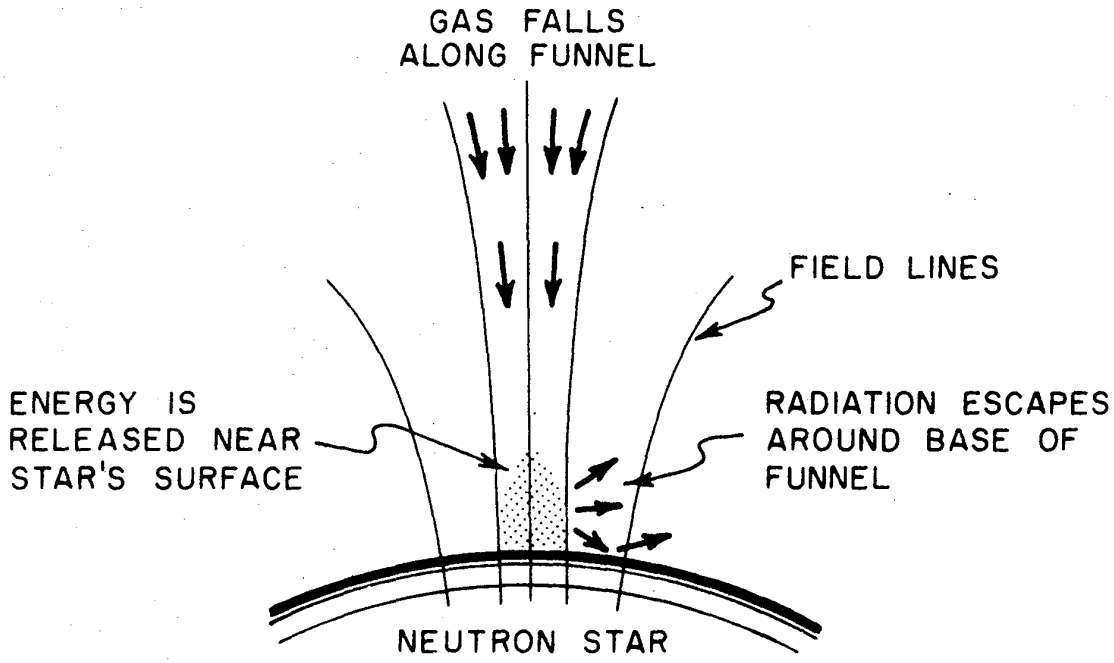

Figure 2.6: Sketch of accretion funnel close to the surface of the neutron star (Davidson & Ostriker 1973).

If an accretion disk is present, which is believed to be the case for Her X-1, the accretion process takes place only under the condition that the angular velocity of the neutron star Ω_s, which coincides to the angular velocity of the magnetosphere, is smaller than the keplerian velocity of the accreted gas at r_A (see details in Illarionov & Sunyaev 1975 or Stella et al. 1986). The distance at which these two velocities are equal is the so-called *corotation radius* r_{co}:

$$r_{co} = \left(\frac{GMP_{spin}^2}{4\pi^2}\right)^{1/3} = \left(\frac{GM}{\Omega_s^2}\right)^{1/3}. \tag{2.19}$$

The accretion mechanism will be inhibited by a centrifugal barrier if $r_A > r_{co}$ which means that the magnetosphere of the pulsar is rotating faster than the Kepler frequency at the inner disk boundary. Accretion will then occur if the magnetospheric radius lies inside the corotation radius.

The influences of the magnetic field and viscosity stress on the flow of matter, can be summarized by Figure 2.7. In particular, the environment around the neutron star can be divided into different "regions".

In the "outer transition zone", far from the surface of the neutron star, the flow is not affected by the magnetic field of the neutron star. This starts to influence the flow within the "boundary

layer" where the magnetic field dominates the viscosity. Thus, when the flow reaches radii smaller than r_A, the magnetic pressure is high and forces the flow to follow the magnetic field lines and fall onto the poles of the neutron star through the accretion column structure.

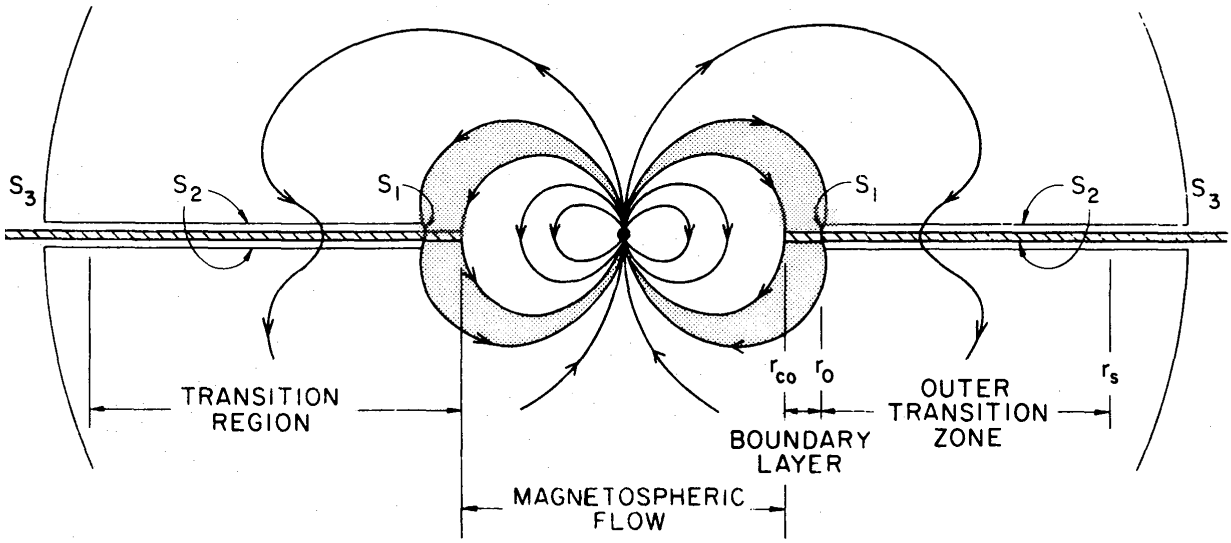

Figure 2.7: Sketch of the different zones close to the surface of the neutron star from Ghosh & Lamb (1979).

2.6 Accretion onto the poles of a neutron star

As mentioned before, when the accreting material is stopped outside the magnetosphere, the magnetic field lines drive the flow onto the poles of the neutron star through the accretion column structure.

Considering an element Δm of matter at a distance r from the neutron star, the lines of a dipole magnetic filed are defined by $sin^2\theta/r=$ constant, where θ is the angle between r and the dipole field. Following the description by Shapiro & Teukolsky (1986), the magnetic pole region is thus delimited by the last field lines which are closed for radii smaller than the magnetosphere radius r_A. At the magnetic pole the angle θ_c formed by the magnetic lines is defined by:

$$sin^2\theta_c = \frac{R}{r_A} \approx \frac{R}{\left(\frac{B_0^2 R^6}{4\dot{M}_{acc}\sqrt{GM}}\right)^{2/7}}, \tag{2.20}$$

with B_0 the magnetic field at the surface of the neutron star, and M and R the mass and the radius of the neutron star, respectively. Thus, the area A of the accretion column at the surface of the neutron star is:

$$A \approx \pi R^2 sin^2\theta_c. \tag{2.21}$$

This area represents only a fraction of the spherical surface of the neutron star and corresponds to the so-called *hot spot*. The physics which describes the fall of the matter onto the hot spot is still unclear. Over the years many models have been suggested, but many questions are still opened (see e.g. Basko & Sunyaev 1976 and references therein). As shown in Figure 2.8, different geometries of the accretion column have been proposed (Meszaros 1984).

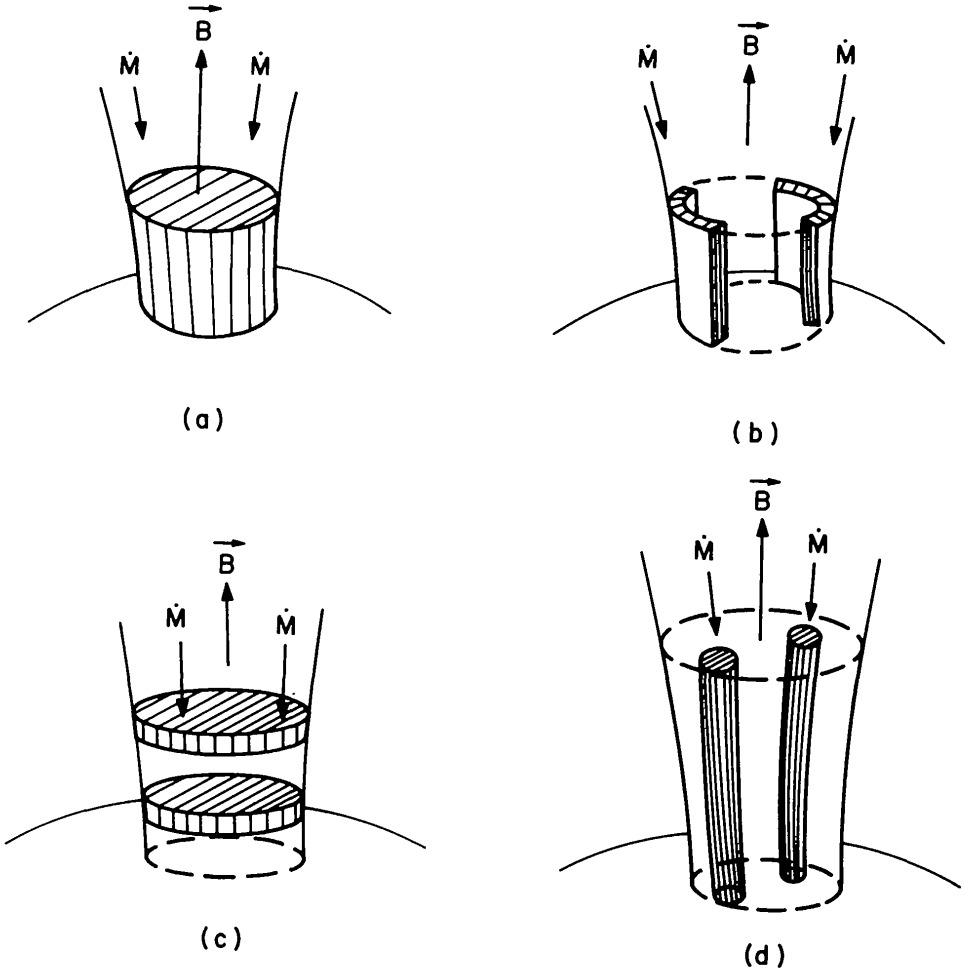

Figure 2.8: Sketch of the different geometry for the accretion columns by Meszaros (1984): a) filled funnel, b) hollow sectional funnel, c) pancake, d) spaghettis.

When the matter reaches the pole, two different scenarios are expected. For low accretion rates, which correspond to luminosity $L \ll L_{Edd}$, the infalling plasma reaches almost freely the surface of the neutron star where it is decelerated by Coulomb interactions with electrons in the atmosphere of the neutron star. Then, X-ray emission leaves the accretion flow vertically leading to the formation of the so called *pencil beam*. This is possible because the amount of plasma infalling onto the pole of the neutron star is small and the accretion is optically thin.

For high accretion rates, the gas pressure is much lower than the radiation pressure which is dominating. The infalling matter looses almost all of its kinetic energy in a radiation dominated

shock through Compton scattering. With an increase of accretion rate, the height of the shock region above the surface of the neutron star rises. Photons are then emitted from the side of the accretion column, in the direction parallel to the surface of the source with the formation of the so-called *fan beam*.

2.7 The transfer of angular momentum

The rotational period of accreting X-ray pulsars is not constant with time and can show fluctuations on different timescales. Normally, it decreases in a linear way leading to the so-called *spin-up* phase. This can be alternate to *spin-down* phases in which the period increases. Spin-up corresponds to an increase of the angular momentum of the neutron star and spin down to a decrease of it (Davidson & Ostriker 1973).

As reported by Ghosh & Lamb (1979) and Nagase (1989), the transfer of angular momentum takes place when the magnetosphere of the neutron star couples magnetically the matter of the disk leading to the formation of torques. This happens close to the boundary layer. In particular, defining the so-called *fastness parameter* as

$$\omega_s = \frac{\Omega_s}{\Omega_k(r_A)} = \left(\frac{r_A}{r_{co}}\right), \tag{2.22}$$

where Ω_k is the Keplerian velocity, if $r_A \ll r_{co}$ ($\omega_s \ll 1$), a spin-up can occur. When ω_s increases, the strength of the spin-up torque becomes weaker and the angular momentum transfer is stopped. Torques leading to a decrease of the angular momentum are produced in the transition region, where the magnetic field treads the disk (see Figure 2.7). On the other hand, if the torques corresponding to spin up and spin down are equivalent, no transfer of angular momentum is observed.

The derivative of the spin period is an important physical parameter because it is proportional to the luminosity L of the accreting object (Rappaport & Joss 1977):

$$-\frac{\dot{P}_{spin}}{P_{spin}} \propto L^{6/7} \cdot P_{spin}. \tag{2.23}$$

The relation between the period derivative and the X-ray luminosity is an helpful tool that provides an indirect measurement of the magnetic field strength and the distance of an accreting neutron star from the Sun. In fact, Equation 2.23 can be also stated as:

$$\frac{\dot{P}_{spin}}{P_{spin}} \propto \mu_{30}^{2/7} P L^{6/7} \mathrm{s/yr}. \tag{2.24}$$

Up to now, many models tried to explain the physics of these torques, but several questions are still open. Details about their formation and the transfer of angular momentum can be found e.g. in Ghosh & Lamb (1979) (and references therein) or in Wang (1987).

3 The high energy observatories RXTE & INTEGRAL

Her X-1 was repeatedly observed by the ***R**ossi **X**-ray **T**iming **E**xplorer* (*RXTE*) and the ***INT**ernational **G**amma-**R**ay **A**strophysics **L**aboratory* (*INTEGRAL*) satellites. In this chapter a small overview of the on-board instruments of these two satellites is given.

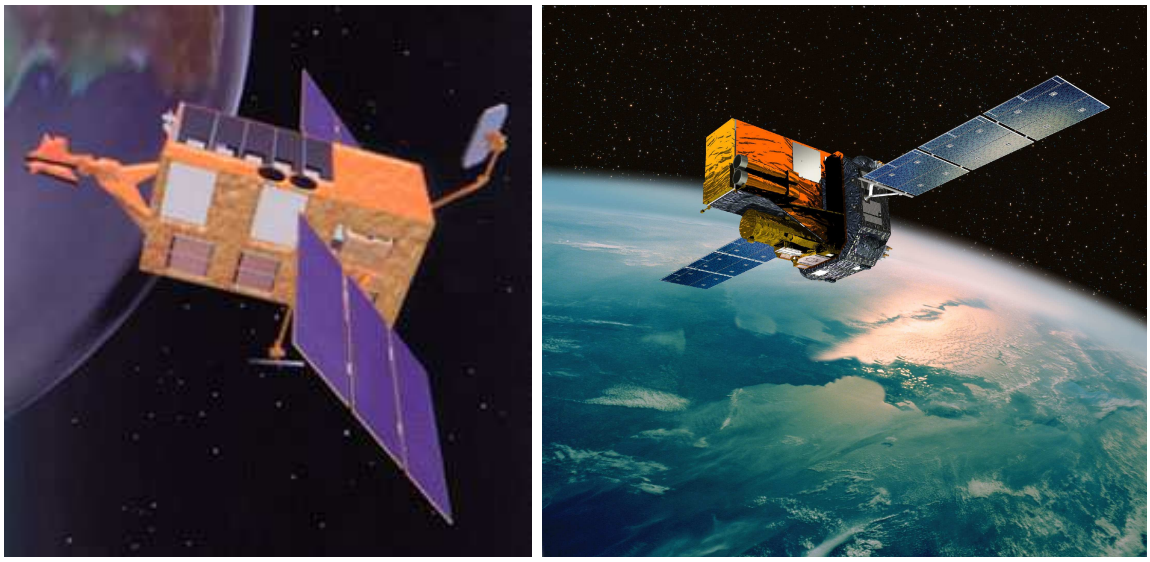

Figure 3.1: Artist's representation of the satellites *RXTE* (left) and *INTEGRAL* (right).

3.1 Rossi X-ray Timing Explorer (RXTE)

The *Rossi X-ray Timing Explorer* (*RXTE*) is a NASA satellite dedicated to X-ray astronomy (see Figure 3.1). This satellite was launched aboard a Delta rocket on December 30, 1995 from NASA's Kennedy Space Center. Its name was originally *X-Ray Timing Explorer*, but later it was changed into *Rossi X-ray Timing Explorer* in honour of the italian astrophysicist Bruno Rossi who is considered one of the pioneers of X-ray astronomy.

It was launched into a low earth circular orbit (LEO) at an altitude of 580 km. This orbit has an inclination of 23 degrees with a period of 90 minutes. On-board this satellite there are two pointed collimated instruments: the Proportional Counter Array (PCA) which works at low energies covering the 2 – 60 keV energy range, and the High Energy X-ray Timing Experiment (HEXTE) which works at higher energies namely the 18 – 250 keV energy range (see Jahoda & PCA Team 1996 and Rothschild et al. 1998). The third instrument is the All Sky Monitor (ASM),

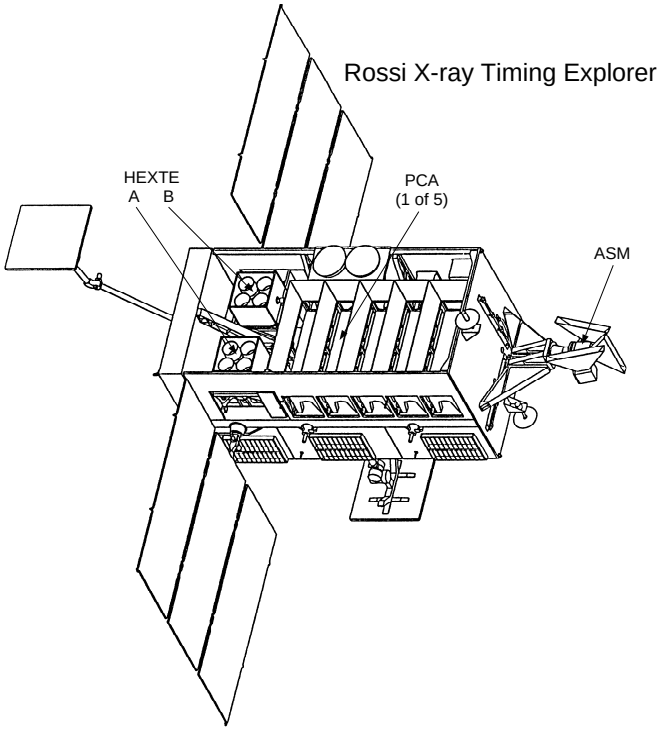

Figure 3.2: Instruments on-board the *RXTE* spacecraft (Rothschild et al. 1998).

a wide field detector which performs a scan of the whole sky every ~ 90 minutes. One of the innovations related to this satellite was the possibility to have these three instruments working simultaneously. The satellite was designed to observe X-ray sources and their variability. For this reason *RXTE* has a good time resolution (down to microseconds) combined with a moderate spectral resolution (3 – 250 keV). After more than 15 years of operation, the satellite will finish its mission early 2012, after a very long period of activity considering its originally planned life time of two years.

In Figure 3.2 a diagram of the spacecraft with its on-board instruments is shown.

3.1.1 Proportional Counter Array (PCA)

The Proportional Counter Array (PCA) is the main science instrument on-board the *Rossi X-ray Timing explorer*. This type of instrument is quite common in X-ray astronomy and over the years many X-ray missions have used such an instrument (e.g. *Uhuru* 1970, *EXOSAT* 1983, *Ginga* 1987 and some others). In the simplest case, the proportional counter is a gas-filled cell with a positively charged wire at the centre. X-ray photons enter the cell and create free electrons ionizing the gas. These electrons are accelerated rapidly towards the wire, at high positive voltage, creating an avalanche of electrons. The multiplication factor between the primary number of electrons and the total number of electrons created in the avalanche is called the *gas gain*. A measurable amount of charge is accumulated at the anode wire. This charge is proportional to the energy of

the original X-ray photon hitting the cell, explaining the name.

The proportional counter array (PCA, Jahoda & PCA Team 1996, Jahoda et al. 2006) consists of five proportional counter units (PCUs) which work independently in the 2 – 60 keV energy range with very good time resolution and a moderate energy resolution. Each PCU has a collecting area of 1600 cm^2 leading to a very large total effective area of 6500 cm^2. These units have a special structure: they are made of five multi-wire, multilayer, proportional counter. Each layer is divided by alternate cells from the amplifier chains in mutual anticoincidence. This division plays a key role in suppressing the background and in the data screening procedure.

Due to its configuration and its one degree-collimator (FWHM), this instrument is limited in flux at about 4 x 10^{-12} erg s^{-1} in the energy range 2–10 keV for an exposure time of 10^5 s, which corresponds to approximately 0.3 counts s^{-1} PCU^{-1}.

Each PCU consists of two different detection layers: the propane volume and the main xenon chamber. The propane volume is an electron veto shield used to reduce the background while the xenon chamber detects the photons coming from the source. An aluminized mylar foil is located in front of each PCU. A second mylar window separates the propane volume and the Xenon chamber. This configuration restricts the lower energy limit of the PCA to >2 keV.

Before they are inserted into the telemetry stream, the events detected by the PCA are processed on-board by the so-called onboard processor *Experiment Data System (EDS)*. This procedure includes a "time-tag" application to each event as well as the event selection and the event data compressions.

In Table 3.1 the technical specifications of the PCA instrument are reported.

Table 3.1: Summary of the technical specifications of PCA.

PCA	
Detector	5 proportional counters
Energy range	2 – 60 keV
Time resolution	1μs
Energy resolution	< 18% @ 6 keV
Spatial resolution	collimator with 1 degree FWHM
Collecting Area	6500 cm^2
Layers	1 Propane veto; 3 Xenon chambers; 1 Xenon veto layer
Sensitivity	0.1 mCrab
Background	2 mCrab

3.1.2 High energy X-ray Timing Experiment (HEXTE)

The High Energy X-ray Timing Experiment (HEXTE) consists of eight scintillation detectors which are divided into two clusters: cluster A and cluster B (Rothschild et al. 1998). Each of these two clusters consists of an array of four detectors in order to detect X-ray emission in the 15 – 250 keV energy range with a resolution of 15% FWHM at 60 keV. The detector units are composed of a collimator, a Na(Tl)/CsI(Na) phoswich detector, a photomultiplier tube, a gain control detector, and the associated electronics needed to keep all these components working

simultaneously. These units are mounted on an external bar and, thanks to this configuration, can be rotated with respect to each other about the nominal source-pointing direction of the satellite. Each cluster is oriented in such a way that they can change their pointing position or "rock" in mutually perpendicular directions. This geometry provides measurements of the background around the observed target. The division into two different clusters is an important characteristic of this instrument as it guarantees useful observations in the case that one of the two clusters shows anomalies. For example, this was the case in March 1996 when cluster B temporally lost its spectral capabilities or in October 2006 when cluster A was fixed in the "on-source" position due to some rocking problems.

The total collecting area of the instrument is ~ 1600 cm^2. The HEXTE's basic properties are summarized in table 3.2.

As in the case of PCA, the events detected by HEXTE are processed on-board before insertion into the telemetry stream. The products of this procedure include event mode, binned spectra, light curves, and a burst-triggered event buffer.

The main advantage of this instrument is the fact that the background can be measured simultaneously to the source observation. This is not the case for the PCA instrument and it is an extremely important aspect because of the high variability of the background. For PCA the problem is solved using a model of the background.

Table 3.2: Summary of the technical specifications of HEXTE.

HEXTE	
Detector	2 clusters (A & B) of 4 NaI/CsI scintillation counters
Energy range	15 – 250 keV
Time resolution	8μs
Energy resolution	15% @ 60 keV
Spatial resolution	1 degree FWHM
Collecting Area	2 times 800 cm^2
Layers	1 Propane veto; 3 Xenon, each split into two; 1 Xenon veto layer
Sensitivity	1 Crab = 360 count/s per HEXTE cluster
Background	50 count/s per HEXTE cluster

3.1.3 All Sky Monitor (ASM)

The All Sky Monitor (ASM) consists of a group of three Scanning Shadow Cameras (SSCs) mounted on a rotating drive assembly (Bradt et al. 1985) which provides a nearly continuous monitoring of the X-ray sky and was designed and manufactured by the Massachusetts Institute of Technology (MIT, USA). Each Camera has a field of view (FOV) of 6×90 degrees and is equipped with proportional counters for a total collecting area of 90 cm^2. Two of the cameras are tilted by ± 12 degrees and look in the same direction while the third one looks in the direction parallel to the ASM drive axis. The proportional counters are position-sensitive in one direction and possess a one-dimensional coded mask. The observations provide a map of the brightest targets in the sky, observing $\sim 80\,\%$ of it every 90 minutes. At the same time, an alert system

reports the discovery of any new X-ray objects. Data are analyzed to give the total source intensity in three to five energy bands. In Table 3.3 the basic properties of the ASM are listed.

As in the case of PCA and HEXTE instruments, events detected by the ASM will be processed on-board by the EDS before they are inserted into the telemetry stream.

Table 3.3: Summary of the technical specifications of ASM.

ASM	
Detector	Xenon proportional counter, position-sensitive
Cameras	3 shadow cameras, each with 6 x 90 degrees FOV
Energy range	2 – 10 keV
Time resolution	80% of the sky every 90 minutes
Energy resolution	15% @ 60 keV
Spatial resolution	3'×15'
Collecting Area	90 cm^2
Sensitivity	30 mCrab

3.2 International Gamma-Ray Astrophysics Laboratory (INTEGRAL)

The *INTErnational Gamma-Ray Astrophysics Laboratory* (INTEGRAL) is an ESA satellite. It was launched from Baykonur (Kazakhistan) on October the 17th 2002 (Winkler et al. 2003). With its highly eccentric orbit ($\sim$3 days) and high perigee (height of perigee: 9000 km, height of apogee: 154000 km), this satellite provides long periods of uninterrupted observations with nearly constant background.

The scientific goal of *INTEGRAL* is to observe celestial X- and gamma-ray sources in the 3 keV – 10 MeV energy range with fine spectroscopy (2.5 keV FWHM @ 1 MeV), fine imaging and accurate positioning with an angular resolution of 3 arcmin FWHM. Thanks to the fine spectroscopy, this mission provides the identification of spectral features and the measurement of line profiles for physical studies of the source region. At the same time, the fine imaging permits the localization and identification of gamma-ray sources as well as of their counterparts at other wavelengths.

The scientific instruments on-board the INTEGRAL spacecraft are the imager IBIS (Imager on-Board INTEGRAL Satellite, Ubertini et al. 2003) for high angular resolution imaging (15 keV – 10 MeV), and the spectrometer SPI (SPectrometer on INTEGRAL, Vedrenne et al. 2003) for high resolution gamma-ray line spectroscopy (20 keV – 8 MeV). These are the two main gamma-ray instruments. In addition, two monitor instruments are present: the X-ray monitors JEM-X (Joint European Monitor for X-ray, Lund et al. 2003) which works in the 3 – 35 keV energy band, and the OMC (Optical Monitoring Camera, Mas-Hesse et al. 2003) in the optical (550 nm) band. All of these instruments operate simultaneously. Figure 3.3 shows where these instruments are located on-board of the satellite.

Because of the strong penetrating power of gamma-rays, it is impossible to focus high-energy photons by using reflecting optics of X-ray telescopes applicable to photons with an energy below

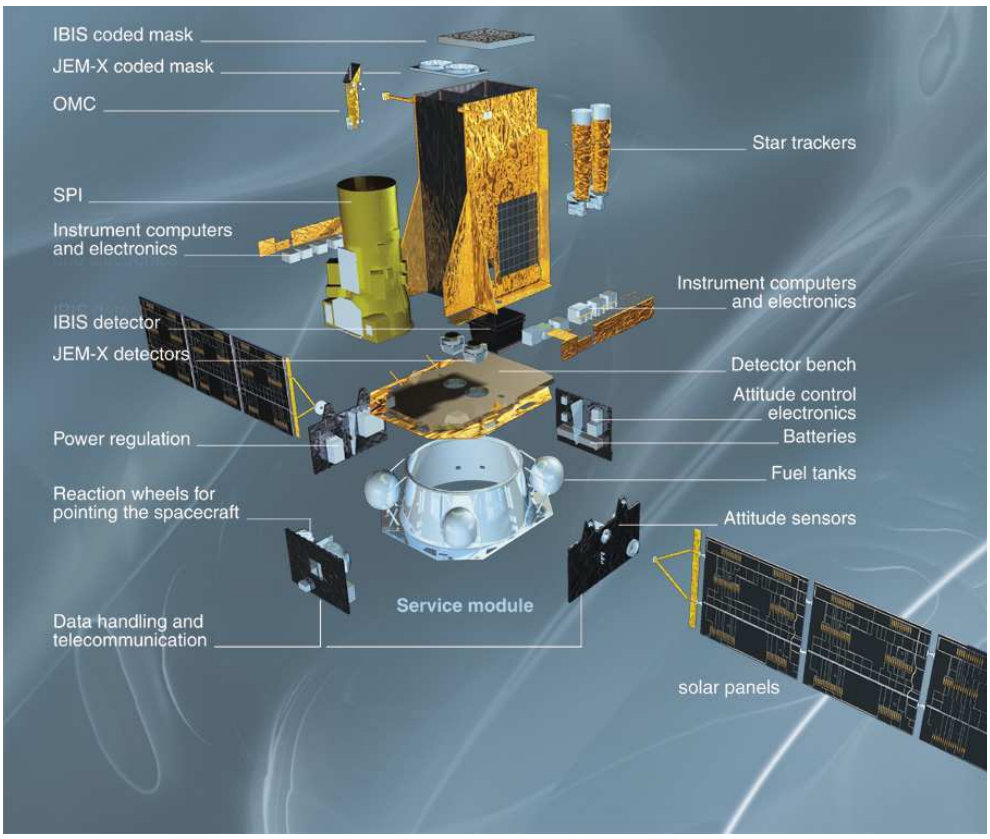

Figure 3.3: Instruments on-board the *INTEGRAL* satellite (Image: ESA).

about 10 keV. Because of this, the high energy instruments such as the spectrometer, the imager and JEM-X on-board of the INTEGRAL satellite make use of the coded mask technique.

The coded mask is made of an absorbing material with several holes, and is located above the detector. The X- or gamma-ray sources create a shadow of the mask on the detector which allows to reconstruct the sky-image. This is due to the particular pattern of the coded mask which is partially transparent and opaque to photons over the rest of the surface. Only part of the radiation can pass the mask and reach the detector. Here, a shadow pattern is created. If the incidence angle of the radiation changes, the shadow pattern is shifted. From the position of the shadow, the position of the sources can be calculated. The resultant shadowgram is an overlapping of several images. This has to be decoded in order to reconstruct the image, taking into account the known orientation of the mask-detector. The reconstruction procedure is designed to give the location and intensity of each source in the field of view [1].

[1]For a detailed description of the coded mask, see Staubert (2008) in: "The Universe in X-rays", J. Trümper and G. Hasinger, Astronomy & Astrophysics Library, Springer 2008, p. 29).

3.2.1 The Imager on-board the INTEGRAL Satellite (IBIS)

IBIS the imager consists of two independent detector arrays: ISGRI (*INTEGRAL* Soft Gamma-Ray Imager, Ubertini et al. 2003), a CdTe solid state array, operating in the 15 – 400 keV energy band, and PICsIT (Pixellated Imaging CaeSium Iodide Telescope, Di Cocco et al. 2003), a CsI scintillator located below ISGRI, which operates in the 180 keV – 2 MeV energy band. These two detectors are located 3.2 m behind the coded mask. The mask of the detector has a size of 1064×1064×16 mm^3 and is made of 95×95 cells of 11.2×11.2 mm^2. Through a coded mask technique, the angular resolution is limited by the size of the detector: ISGRI is made of 16384 CdTe detectors (4×4 mm large, 2 mm thick) and PICsIT is made of 4096 CsI scintillators (9.2×9.2 mm large, 30 mm high). Because of this the Imager uses a detector with many spatially resolved pixels designed as physically distinct elements. The two layers of the detector, the CdTe of ISGRI and the CsI of PiCsIT, are separated by 90 mm and are located on two different layers. The upper layer is occupied by the ISGRI array which is a 2600 cm^2 plane, and the second layer is occupied by the PICsIT array with its 3100 cm^2 plane. This configuration provides to perform a wide energy range and high sensitivity spectroscopy of the target sources. The cells of the mask consist of different materials: 50% of them are made of Tungsten so they are opaque to photons in the IBIS energy range with a 70% opacity at 1.5 MeV. The other 50% of the cells are open with a transparency of 60% at 20 keV.

In Table 3.4 the IBIS technical specifications are reported.

Table 3.4: Summary of the technical specifications of IBIS.

IBIS	
Detector	16384 CdTe (ISGRI); 4096 CsI (PICsIT)
Energy range	20 keV – 8 MeV
Detector area	2600 cm^2 (CdTe); 3100 (CsI)
Spectral resolution	9 keV 100 keV (FWHM)
FOV (fully coded)	9×9 degrees
Angular resolution	12' (FWHM)
Source location	< 1' (radius)
Continuum Sensitivity[1]	2.85×10^{-6} ph/(s cm^2 keV) [3σ in 10^5s (@ 100 keV)]
	1.6×10^{-6} ph/(s cm^2 keV) [3σ in 10^5s (@ 1 MeV)]
Narrow-line sensitivity[1]	1.9×10^{-5} ph/(s cm^2) [3σ in 10^6s (@ 100 keV)]
	3.8×10^{-4} ph/(s cm^2) [3σ in 10^6s (@ 1 MeV)]
Absolute timing accuracy	92 μs (3σ)

[1] The sensitivities are based on in-flight background measurements.

Due to the dimensions of the mask being ~ 2 times larger than the detector, a large field of view (FOV) is provided with respect to the size of its detector. The fact that IBIS is based on a coded mask configuration leads to the possibility to have different projections of the shadowgram on the detector. In the Fully Coded Field Of View (FCFOV) which corresponds to the situation in which the detector is completely illuminated, the recorded shadow is a complete permutation of the mask base pattern. In the case of a Partially Coded Field Of View (PCFOV) when only part of the detector is illuminated, the shadow is only a subset of the complete pattern. At

the same time, the problem of this configuration is the creation of spurious peaks (the so-called "ghost peaks") in the reconstructed images.

3.2.2 Spectrometer on-board INTEGRAL (SPI)

SPI is the spectrometer on-board *INTEGRAL* (Vedrenne et al. 2003) which performs spectral analysis of point and extended gamma-ray sources in the 20 keV – 8 MeV energy range. The energy resolution is 2.2 keV (FWHM) at 1.33 MeV. It consists of 19 hexagonal high purity Germanium detectors which are cooled by a Stirling cooler system to a temperature of 85 K. A coded mask is located 1.7 m above the detection plane in order to construct images of large portions of the sky.

The instrument has a field of view of 16 degrees (fully coded field) and an angular resolution of 2 degrees. A veto anticoincidence system is present in order to reduce the background.

The spectral resolution is fine enough to resolve astrophysical lines and allow spectroscopy in the regime of gamma-rays. The coded mask provides imaging at moderate resolution. Science objectives are nucleosynthesis, relativistic-particle accelerators, and strong-field signatures in compact stars. These are studied through nuclear lines and spectral features in accreting binaries, pulsars, or solar flares, but also through energetic continuum radiation in the 20 keV – 10 MeV range from a variety of cosmic sources, including AGN and gamma-ray bursts. In Table 3.5 the SPI technical specifications are reported.

Table 3.5: Summary of the technical specifications of SPI.

SPI	
Detector	19 Ge Detectors cooled to 85K
Energy range	20 keV – 8 MeV
Detector area	500 cm^2
Spectral resolution	2.3 keV @ 1.3 MeV (FWHM)
FOV (fully coded)	16 degrees (corner to corner)
Angular resolution	2.5 degrees (point source)
Source location	< 1.3 degrees (radius)
Continuum Sensitivity[1]	8.8×10^{-4} ph/(s cm^2 MeV) [3σ in 10^6s (@ 1 MeV)]
Narrow-line Sensitivity[1]	2.4×10^{-5} ph/(s cm^2) [3σ in 10^6s (@ 1 MeV)]
	4.6×10^{-5} ph/(s cm^2) [3σ in 10^6s (@ 511 keV)]
Absolute timing accuracy	129 μs (3σ)

[1] The sensitivities are based on in-flight background measurements.

3.2.3 The Joint European X-ray monitor (JEM-X)

The Joint European X-ray Monitor JEM-X (Lund et al. 2003) plays a key role in the spectral, imaging and timing study of the sources detected by IBIS and SPI. The instrument works simultaneously to the other gamma-ray instruments but it has a narrower field of view (FOV). It provides independent scientific results from sources with a soft spectrum in the 3 – 35 keV energy range with an angular resolution of arcminutes. The instrument consists of two coaligned

coded mask telescopes (JEM-X1 and JEM-X2) which are switched on alternatively during the mission. These are two identical high pressure imaging microstrip gas chambers composed of xenon (90%) and methane (10%). The pattern of the coded mask is composed of 22501 elements with dimensions of 3.3 mm each. The angular resolution is ∼3' and allows better point source location accuracy than IBIS. The mask is located 3.2 m above the detection plane. In Table 3.6 the basic properties of JEM-X are reported.

Table 3.6: Summary of the technical specifications of JEM-X.

JEM - X	
Detector	Microstrip Xe/CH_4 gas detector (1.5 bar)
Energy range	3 keV – 35 keV
Detector area	2×500 cm^2
Spectral resolution	1.2 keV @ 10 keV (FWHM)
FOV (fully coded)	4.8 degrees
Angular resolution	3' (FWHM)
Source location	<30" (radius)
Continuum Sensitivity[1]	1.2×10^{-5} ph/(s cm^2 keV) [3σ in 10^5s (@ 6 keV)]
(single JEM-X unit & isolated source)	1.0×10^{-4} ph/(s cm^2 keV) [3σ in 10^5s (@ 30 keV)]
Narrow-line Sensitivity[1]	1.6×10^{-4} ph/(s cm^2) [3σ in 10^5s (@ 6 keV)]
(single JEM-X unit & isolated source)	1.3×10^{-4} ph/(s cm^2) [3σ in 10^5s (@ 20 keV)]
Absolute timing accuracy	122 μs (3σ)

[1] The sensitivities are based on in-flight background measurements.

4 The accreting binary X-ray pulsar Hercules X-1

In this chapter a short overview of the binary system Her X-1/ HZ Her and its observational properties is given. A more detailed description about the characteristics of this system is discussed in the following chapters.

4.1 Overview of the system

The system Her X-1/HZ Her was historically discovered in 1936, when Hoffmeister (1941) classified it as an irregular variable star. Only in 1972 Tananbaum et al. (1972) classified Her X-1 as an X-ray source during *Uhuru* observations. Since then Her X-1 is one of the brightest, most studied and well-known persistent X-ray accreting pulsars.

The binary system consists of a normal star, the so-called *companion star*, HZ Her and the neutron star Her X-1 (see Figure 4.1 for a representation of the system).

The system exhibits several different periodicities:

1. 1.237 s pulsation (spin of the neutron star);
2. binary 1.7 d (eclipses and doppler-shift of pulses);
3. 35 d (accretion disk precession);
4. 1.62 d dips ("beat" between 1.7 d and 35 d).

Observationally, these four main periodicities are seen as X-ray pulsations, eclipses, the so-called "on-off" cycle of the X-ray flux and the "dips", respectively.

The mass of the neutron star is $1.5\,M_{\odot}$ and the mass of the companion star is $2.3\,M_{\odot}$ (Reynolds et al. 1997). Because of this, it is classified as in the middle between High Mass X-ray Binaries (HMXBs) and Low Mass X-ray Binaries (LMXBs). Usually, X-ray binary systems have a companion star with a mass $< 1M_{\odot}$ for LMXBs and $>5\,M_{\odot}$ for HMXBs. On the other hand, the way to accrete matter from the companion star onto Her X-1 through Roche Lobe Overflow is typical for LMXBs (see Chapter 2 for details about accretion mechanisms). The distance of the system from Earth is $\sim 7\,$kpc (Reynolds et al. 1997) and its orbit is almost circular with an eccentricity of 1.3 x 10^{-4} and a projected orbital radius of $a \cdot sin\,i$ equal to 13.19 lt - s around the common center of mass (Staubert et al. 2009b). The system has also a very high inclination of $83(4)^{\circ}$ and an observer sees the system almost edge-on (Dennerl 1991). This is reflected in the presence of eclipses in the light curve of all the wavelength bands. In table 4.1 an overview of the system parameters is reported.

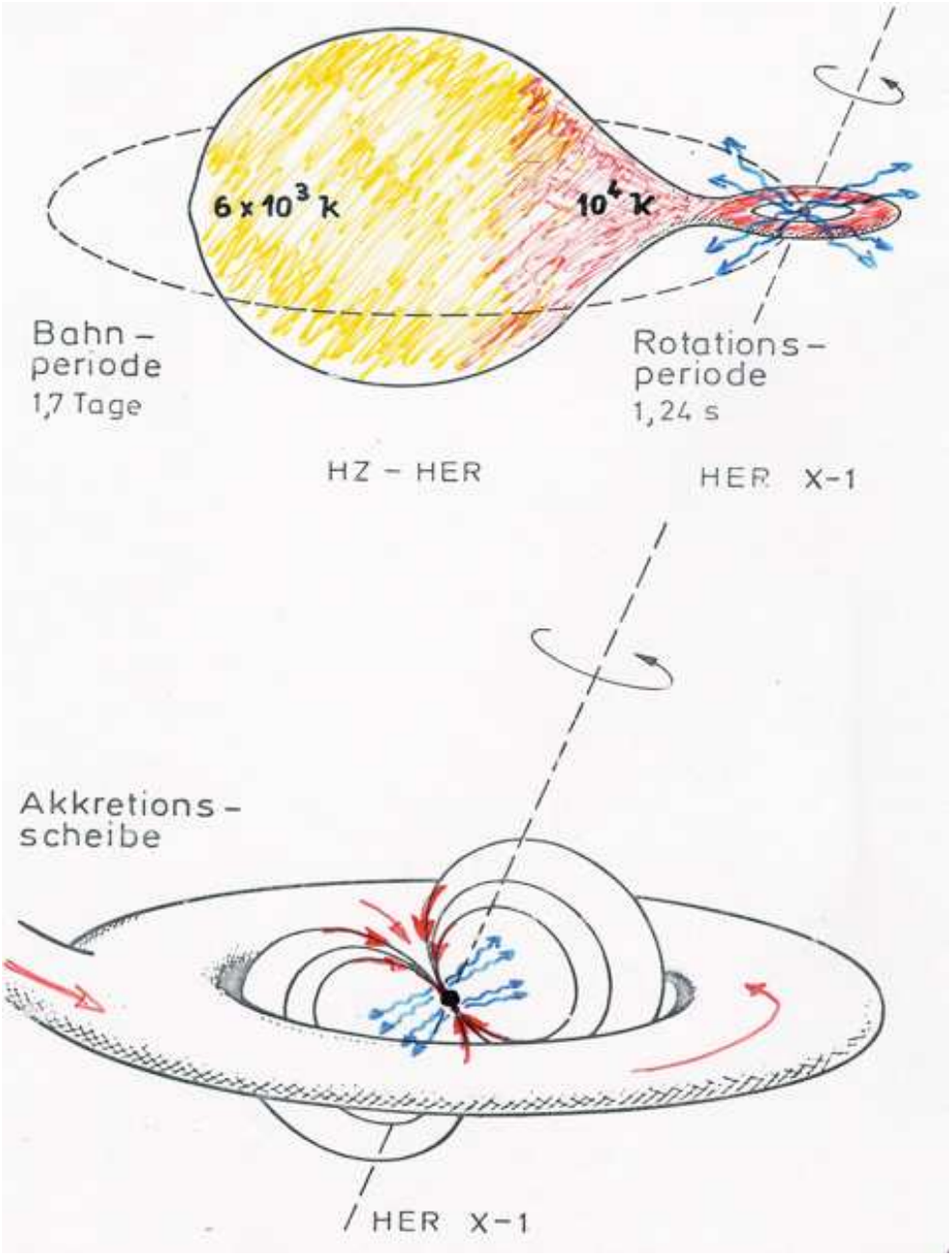

Figure 4.1: *Top*: Representation of the system Her X-1/HZ Her. *Bottom*: Closer view on the neutron star and the accretion disk. Courtesy of Rüdiger Staubert and Joachim Trümper.

Table 4.1: Summary of the binary system Her X-1/HZ Her parameters[1].

Binary system – Her X-1/HZ Her			
Rectascension	$\alpha(2000)$	$6^h\ 57'\ 50'''$	
Declination	$\delta(2000)$	$+35°\ 20'\ 52''$	
Optical magnitude	m_B	13.0	Kukarkin et al. (1971)
Distance	D	6.6 ±0.4 kpc	Reynolds et al. (1997)
Binary orbital period	P_{orb}	1.700167590(2) d	Staubert et al. (2009b)
Orbital period derivative	$\dot{P}_{orb}$	-(4.85±1.3) $\times 10^{-11}$ s s^{-1}	Staubert et al. (2009b)
Projection orbital Radius	$a \cdot \sin i$	13.1831(4) lt - s	Staubert et al. (2009b)
Superior conjunction	$T_{\frac{\pi}{2}}$	MJD 46 359.871940(6)	Staubert et al. (2009b)
Orbit inclination	i	83(4)°	Dennerl (1991)
Eccentricity	e	(4.2±0.8) $\times 10^{-4}$	Staubert et al. (2009b)

Neutron Star – Her X-1			
Mass	M_x	1.5 ± 0.3 $M_\odot$	Reynolds et al. (1997)
Spin Period (MJD 50290.659)	P_{spin}	1.237739612(25) s	Staubert et al. (2009b)
Magnetic Field Strength	B	4.1×10^{12} G	Kuster et al. (2005)
Mass transfer rate	$\dot{M}_{acc}$	$\sim 2 \times 10^{17}$ g s^{-1}	calculated [2]
Radius of Magnetosphere	R_{mag}	≈3000 km	Deeter et al. (1998)

Optical Companion – HZ Her			
Mass	M_{opt}	2.3±0.3 $M_\odot$	Reynolds et al. (1997)
Radius	R_{opt}	4.2±0.2 $R_\odot$	Reynolds et al. (1997)
Spectral Type		B3-B4F	Reynolds et al. (1997)

Accretion Disk			
Mean Precession Period	P_{pre}	34.98 ± 0.01 d	Staubert et al. (2009a)
Inclination	i_{disk}	28°	Howarth & Wilson (1983)
Inner Radius	$R_{disk,in}$	10^8 cm	Cheng et al. (1995)
Outer Radius	$R_{disk,out}$	2×10^{11} cm	Cheng et al. (1995)
Inner edge Temperature	$T_{disk,in}$	1.0×10^4 K	Cheng et al. (1995)
Outer edge Temperature	$T_{disk,out}$	9.5×10^6 K	Cheng et al. (1995)

[1] Table based on a previous version given in M. Kuster PhD thesis (Kuster 2003).
[2] This value has been calculated assuming that the radiative efficiency of the accretion is about 10%. Using the value for the X-ray luminosity $L_x \sim 2 \times 10^{37}$ erg s^{-1} for a distance D of 6.6 ±0.4, $\dot{M}_{acc}$ is estimated by $L \sim 0.1 \dot{M} \cdot c^2$ (D. Klochkov PhD Thesis, Klochkov 2007).

4.2 Observational properties

The system Her X-1/HZ Her presents several phenomena which occur at different timescales. The properties of the system studied in this work are summarized below:

- the 35 day modulation of the X-ray flux;
- the systematic variation of the pulse profile as function of the 35 day phase and energy;
- the cyclotron absorption feature in the X-ray spectrum and its positive correlation with the bolometric luminosity of the source;
- the systematic variation of the cyclotron line energy with pulse phase.

The 35 day cycle

This modulation, originally known as the "35 day on-off cycle", is very well-known since the discovery of the system and it was attributed to the counter-clock precession of a tilted and twisted accretion disk which covers temporarily the X-ray emitting region. Because of the changing in the obscuration of the neutron star, the emission region is occulted, totally or partially, by the accretion disk. This leads to a clear modulation of the X-ray flux as function of the precession of the accretion disk. Within this modulation it is possible to identify two on-states at those 35 day phases where high X-ray flux is detected. These two on-states are separated by two off-states in which the X-ray flux is very low or even not detected. Even more interesting is the fact that the on-states are of two different types: the *Main-On* and the *Short-On*. The necessity to distinguish the two on-states comes from the difference in X-ray flux (and because of different pulse profiles). The flux of the Main-On is higher than the flux of the Short-On by a factor of four to five. The transition between the off-state and the Main-On is called *turn-on* and it is used to count the 35 day cycles (see Figures 5.1, 5.2 and 5.4).

The pulse profile variation

The system shows a systematic and repeating variation of the pulse profiles shape as function of energy and time. Each 35 day cycle, the same evolution of the pulse profile shape is observed. This is a unique scenario among X-ray accreting pulsars and, it is known since the discovery of the system. The variation of the pulse profile with energy is quite common for X-ray pulsars, but the systematic changes with precession phase are noticed only in Her X-1. These changes are reflected in a variation of the individual components of which the X-ray pulse profile consists. The typical double-peaked structure of the Her X-1 pulse profile varies into a single peak structure with an increase of energy or precession phase. Other smaller changes are also observed for the interpulse component.

Cyclotron line energy / luminosity correlation

Her X-1 was also the first X-ray accreting pulsars for which a Cyclotron Resonance Scattering Feature (CRSF) was discovered (Trümper et al. 1978). This absorption-like feature is observed around 40 keV and played a key role in the estimation of the magnetic field of neutron stars. In

fact, using the formula $B_{12} = (1+z)\ E_{cyc}/11.6\,\mathrm{keV}$ (where B_{12} is the magnetic field strength in units of 10^{12} Gauss, z is the gravitational redshift and E_{cyc} is the energy of the cyclotron line; see e.g. Lipunov 1987), the first direct measurement of its magnetic field was found. The source shows a positive correlation between the centroid of the cyclotron line energy and the bolometric luminosity (Staubert et al. 2007, Vasco et al. 2011). This is a unique scenario, because other studies on bright, super-Eddington transient pulsars such as V0332+53 and 4U 0115+63 have shown the opposite behavior (Mihara et al. 1998, Mowlavi et al. 2006, Nakajima et al. 2006). This is believed to be due to a transition between two different accretion regimes. For high luminosity transients, when the accretion rate increases, the height of the radiative shock above the neutron star increases as well, leading to a decrease of the magnetic field strength, which is reflected in a decrease of the cyclotron line energy (Tsygankov et al. 2006). On the other hand, in the sub-Eddington regime, as in the case of Her X-1, the scattering region is located closer to the neutron star surface because of the dynamical pressure of the infalling material which pushes down this region. This leads to an increase in the magnetic field strength and an increase in the observed cyclotron line energy (Staubert et al. 2007).

Systematic variation of the cyclotron line energy with pulse phase

Her X-1 shows a systematic variation of the centroid of the cyclotron line as function of the pulse phase. Pulse phase resolved spectroscopy analyses have been performed over the years with different instruments (see e.g. the latest by Klochkov et al. 2008). The centroid of the cyclotron line follows the shape of the pulse profile: higher values of the cyclotron line are observed at those phases corresponding to the pulse peak, and lower values at the rest of the pulsation.

The system has been repeatedly observed by the main X-ray missions, from *Uhuru* to the most recent *Suzaku* (Enoto et al. 2008). In this work data from both *RXTE* and *INTEGRAL* satellites have been used. In particular more than a decade for *RXTE*, from July 1996 to July 2010 and two years (2005 and 2007) for *INTEGRAL*.

In this chapter, the source and only a few main observational properties, on which this work is based, have been introduced. More detailed descriptions and explanations of the observational properties of the system are given in the following chapters. In particular, the 35 day modulation of the X-ray flux is described in Chapter 5, the pulse profiles variation in Chapter 6, the cyclotron line energy feature and the positive correlation with the luminosity in Chapter 7, and the X-ray spectrum in Chapter 8.

5 Monitoring of the source: the X-ray light curves of Her X-1

In this chapter the very well-known 35 day periodicity of Her X-1 is described. This is a peculiar modulation of the X-ray flux which is one of the main and interesting characteristics of this source. Some physical explanations of this observational property are also discussed. Finally, the collection of X-ray light curves from *RXTE*/PCA and *INTEGRAL*/ISGRI archival data are presented.

5.1 Observational features of the X-ray light curve

5.1.1 The 35 day modulation

The X-ray light curve of Her X-1 shows a clear and strong modulation of the flux over a super-orbital period of about 35 days. The occurrence of two distinct X-ray high-states within the 35 day cycle is very well known and has been attributed to obscuration of the central X-ray source by a tilted, twisted and counter-precessing accretion disk which temporarily covers the X-ray emitting region of the neutron star (Petterson 1975, 1977).

This modulation has a peculiar shape due to the alternation of so-called *on-states*, during which high X-ray flux is detected, and *off-states*, during which the X-ray flux is very low and almost no flux is detected. The description of variable X-ray flux becomes even more complicated because of the presence of two different *sub* on-states: the so called *Main-On* and *Short-On*. A high X-ray flux is observed for both these two on-states, however the flux of the Main-On is higher than the flux of the Short-On by a factor of four to five.

The Main-On state is known since the first observation of the source (Tananbaum et al. 1972; Giacconi et al. 1973), but the Short-On state was found only later with observations by the Copernicus satellite (Fabian 1973). Many studies have been dedicated to the 35 day periodicity of the X-ray flux in Her X-1, leading to a quite complicated picture of the 35 day cycle which can be summarized as follows: the modulation of the X-ray flux consists of two on-states (the Main-On and the Short-On) of about 7 and 5 orbital cycles ($\sim$11 and $\sim$8 days), respectively, separated by two off-states of about 4 to 5 orbital cycles (see Figure 5.1).

These two states also show a huge variability in flux. This is due to the presence of dips which correspond to a decrease in the X-ray flux (see the next section for more details) and the brightness variability of the source itself which is around a factor of two in flux. The resultant shape of the X-ray light curve is asymmetric. During the Main-On the intensity of the X-ray flux increases very rapidly for $\sim$1.2 to $\sim$2 orbital cycles until it reaches a maximum and remains at this flux intensity for $\sim$2.5 orbital cycles, decreasing into a minimum in the following three orbital revolutions. This is also reflected in some spectral parameters such as the absorption. At the beginning of the Main-On while the X-ray flux is increasing, the X-ray spectrum is dominated by

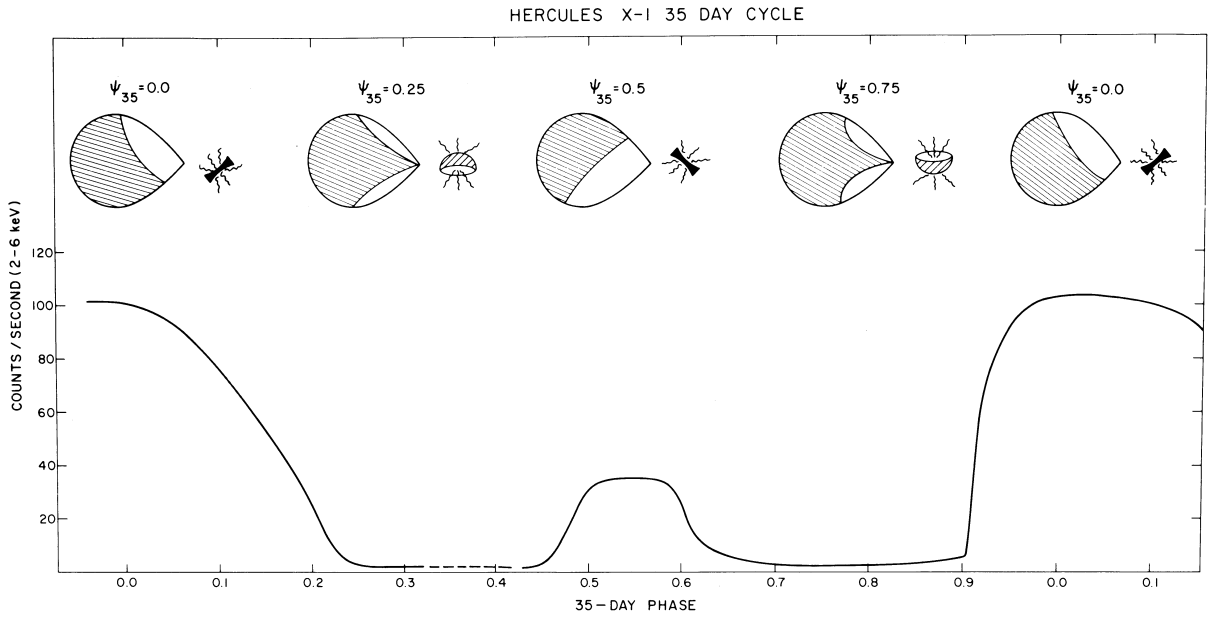

Figure 5.1: Modulation of the X-ray flux of Her X-1 covering the entire 35 day cycle. In the upper portion of the figure, the configuration of the precessing disk orientation corresponding to the on- and off-state of the source is reproduced (*Uhuru* observations, Jones & Forman 1976).

a strong low energy absorption (Kuster et al. 2005). However when the X-ray flux is decreasing after the maximum, the absorption is relatively weak (Shakura et al. 1998).

After the Short-On, the sharp transition from the off-state to the Main-On is called the *turn-on* and it is normally used to count the 35 day cycles. Sometimes the transition between the off-state and the Short-On is called the *secondary turn-on*. Historically the 35 day "phase-zero" corresponds to the beginning of the 35 day cycle and occurs at the time of the turn-on, when the X-ray flux reaches $\sim$10% of the maximum Main-On flux. A more detailed study of the X-ray light curve of Her X-1, reported by Scott & Leahy (1999), shows how the Main-On covers 35 days phases $0-0.31$ and the Short-On covers 35 day phases $0.56-0.76$. The Main-On and the Short-On peaks are separated by ~ 0.50 in 35 day phase. In the same way the two off-state minima are also consistent with a separation of 0.50 in 35 day phase (Scott & Leahy 1999).

The duration of each 35 day cycle is not always the same and shows a variation from cycle to cycle of 20, 20.5 or 21 times the orbital period. The turn-on occurs at fixed binary orbital phases 0.3 or 0.7 (Staubert et al. 1983).

The traces of this periodicity have also been found in the optical window studying HZ Her, the companion star of Her X-1. A clear optical modulation of the 1.7 day pulsation has been reported by Kurochkin (1972), and later by Boynton et al. (1973) and Howarth & Wilson (1983). In general, the companion star HZ Her is strongly heated by X-rays coming from Her X-1, but it shows only small variations in total magnitude (Gerend & Boynton 1976, Deeter et al. 1976). On the other hand, optical pulsations produced by the re-procession of the X-ray flux of the neutron star during both the two on-states have been observed (Middleditch & Nelson 1976, Middleditch 1983). These results lead to the conclusion that the X-ray emission from Her X-1 is relatively constant and that a variation in the accretion rate cannot explain the 35 day modulation of the

light curve of the source (Scott et al. 2000).

5.1.2 Eclipses and dips

The X-ray light curve of Her X-1 shows eclipses and sudden decreases in X-ray flux, the so-called *X-ray dips*. Eclipses are a common feature for X-ray binaries and correspond to an obscuration of the neutron star by the companion star each orbital revolution. In the case of Her X-1, eclipses are observed every 1.7 days and they are normally anticipated by the so-called *pre-eclipse dip*. This feature in the X-ray light curve of Her X-1 plays an important role to understand the geometry of the system especially in the low-state. Choi et al. (1997) have reported that the eclipse ingress and egress in the extended low-state is underlined by a small variation in the X-ray flux on a timescale of about three hours. The X-ray dips are an enigmatic feature of the source. They can be divided into two different classes: the *pre-eclipse dips* and the *anomalous dips*. Pre-eclipse dips are generally observed at orbital phases of $0.6-0.9$, and move from the eclipse toward earlier orbital phases. These dips also show a periodicity with a period of ~ 1.62 days smaller than the orbital one of $\sim$1.7 day. Anomalous dips, instead, occur randomly at orbital phases $0.45-0.65$ within one orbital period after the turn-on (Shakura et al. 1999). Normally, the dropping of the X-ray flux intensity is very rapid, about a factor of four in few seconds. The duration is different from dip to dip but on average is comparable to the duration of the eclipse (~ 6 hours). Within this time interval, quasi periodic oscillation QPOs are observed (Boroson et al. 2000).

Occasionally a third feature is also observed: the so-called *post-eclipse recoveries* which correspond to a delay of a few hours of the egress from the eclipse which occurs in the first orbit after the turn-on (Shakura et al. 1999).

All of these features produce drastic changes in the spectral parameters, essentially due to high photoelectric absorption. The physics which explains this phenomenon is still not clear and despite the fact that several models have been suggested, the X-ray dips in the light curve of Her X-1 remain an enigmatic feature (see e.g. Crosa & Boynton 1980, Vrtilek & Halpern 1985 and Bochkarev 1989).

5.2 The main actor of the show: the accretion disk

As mentioned in the previous section, the observational properties of the X-ray light curve of Her X-1 can be physically explained by the presence of the accretion disk which temporarily covers the X-ray emitting regions of the neutron star. This is why the 35 day modulation can be considered as the best evidence for an accretion disk which happens to be warped, tilted and counter-precessing. Thanks to the huge observing coverage with different X-ray missions of both the Main-On and the Short-On states, it has always been clear that the accretion disk should play a key role in the modulation of the X-ray flux and explain the occurrence of the two on-states. This was attributed by Petterson (1975, 1977) to the obscuration of the neutron star by an accretion disk which is modeled as being geometrically thin and consisting of many rings, tilted with respect to the orbital plane and twisted with respect to each other (Petterson 1977). In this scenario, the two on-states are explained when the line of sight of the observer is close to the orbital plane and the neutron star is emerging from behind the outer rim of the accretion disk. In particular, at both Main-On and Short-On the accretion disk is "open" to the line of sight of the observer with a different angle for the two on-states with the angle at the

Main-On being larger than in the Short-On. Then, the dropping of the X-ray flux at the end of the on-states produces the configuration in which the line of sight of the neutron star is moving close to the inner edge of the accretion disk (see bottom panel of Figure 5.2, Scott et al. 2000).

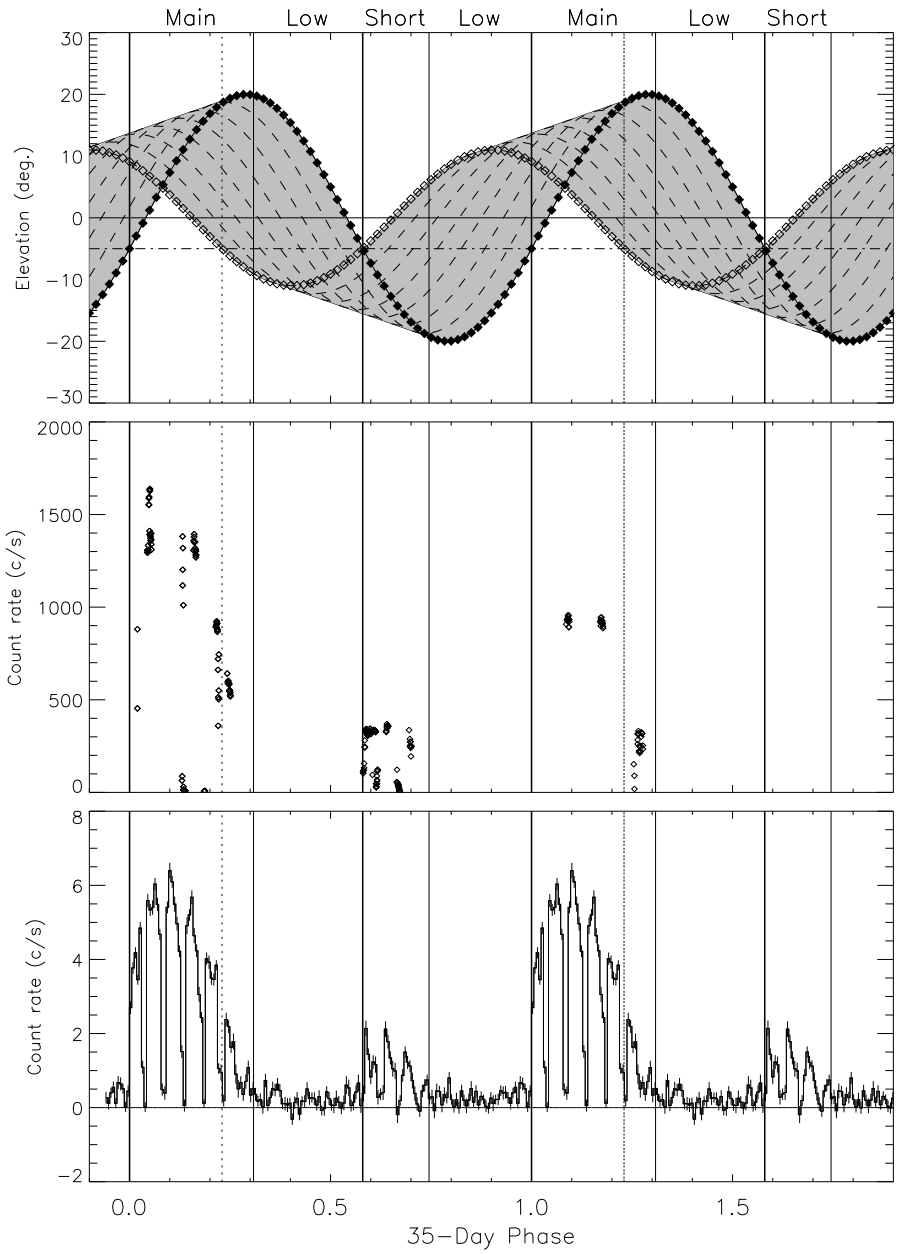

Figure 5.2: *Top*: View of the disk as seen from the surface of the neutron star. The horizontal dash-dotted line represents the elevation of the observer which is -5 degrees. Bold solid lines represent the turn-ons. An observer sees the neutron star Her X-1 as a point source from the outer disk rim, but as an extended source at the inner disk rim. *Middle*: Ginga light curve of Her X-1 from observations in 1989 in the 1 − 37 keV energy range. *Bottom*: Comparison with the *RXTE*/ASM light curve. Picture taken form Scott et al. (2000).

On the other hand, the counter-precessing nature of the accretion disk has been explained on the basis of optical observations as well as theoretical considerations. Systematic changes observed in the optical light curve of the companion star reported by Deeter et al. (1976) can be reproduced only with a retrograde direction of the disk precession by the combination of the disk emission and the occultation of the companion HZ Her (Gerend & Boynton 1976). This is also confirmed by theoretical studies for which a tilted disk is forced to precess in a counter-precessing direction (Katz 1973).

Detailed descriptions of the X-ray flux modulation and the geometry of the accretion disk have been proposed by several authors (see e.g. Priedhorsky & Holt 1987). For example, the following description is from the review of Scott et al. (2000).

X-ray pulsations are observed during the increasing of the flux at those 35 day phases after the turn-on which correspond to the transition between the off-state and the Main-On. Usually X-ray pulsations are also accompanied by some spectral changes in the X-ray spectrum of Her X-1, namely the presence of cold matter absorption (Parmar et al. 1980). In the next one to four days a factor of 20 –50 % increase in flux is observed as the result of observing the neutron star through a hot and dense lower corona located above the outer disk surface. The obscuration is decreasing with an increase of the elevation of the observer line of sight with respect to the plane of the outer disk. Historically the presence of a second corona, larger than the first one and with a lower density of scattering, has been introduced to explain a short and rapid decrease of the flux of about 5% of the Main-On flux peak (Choi et al. 1997, Mihara et al. 1991). This was also studied by Schandl & Meyer (1994) where a theoretical model was proposed. This describes the behavior of the outer disk which plays a key role at the beginning of the on-state (both Main-On and Short-On). On the other hand, the inner disk influences the scenario at the end of the on-state where a gradual decrease of the flux is observed. This is not as rapid as the increase of the flux after the turn-on. This situation can be explained only with a tilted an twisted accretion disk. A tilted planar accretion disk would introduce a clear cutoff in the flux at the end of the Main-On. In this configuration the azimuthal angle between the outer disk and the inner one is larger than 90 degrees. This implies a slow and gradual coverage of the X-ray emission region by the hot, inner region of the disk reproducing the decrease in flux at the end of the on-states. Figure 5.2 illustrates the geometry of the disk as seen from the neutron star and the resultant modulation of the flux.

Leahy (2002) has also modeled the 35 day periodicity of the X-ray flux of Her X-1 modeling the geometry of the accretion disk. The twisted, tilted and counter-precessing disk consists of a set of different rings tilted to each other with increasing radius. This is shown in Figure 5.3 supposing an observer at 35 day phase 0.06 and 5 degrees above the orbital plane. In this picture, the neutron star as well as the central part of the disk are totally visible only at phase 0.06. The rings in the intermediate region of the disk are very important because they are responsible for blocking the line of sight to the neutron star before the two on-states and after the Main-On and Short-On decays.

During the Main-On state, at 35 day phase very close to the turn-on, the outer disk edge starts to “free” the line of sight of the observer, uncovering the neutron star which appears as a very small object compared to the large structure of the disk. The brightness of the central region is extremely variable. This is due to the fact that the view is opening and closing through the tilted ring which surrounds the neutron star. The emission from the inside surface of the ring varies owing to the changing occultation by the rest of the ring. The variability is also due to

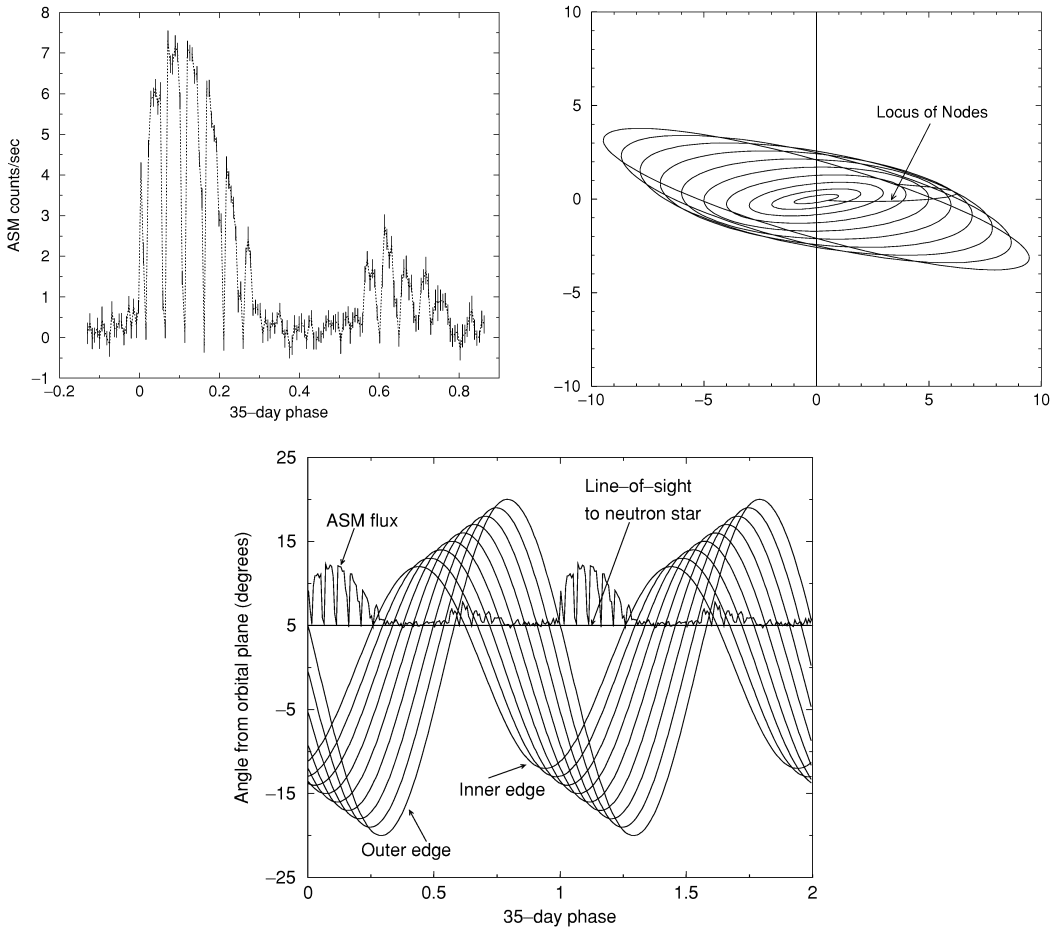

Figure 5.3: *Top left*: *RXTE*/ASM light curve of a complete 35 day cycle. *Top right*: View of the twisted and tilted disk as seen from an observer at 5 degrees above the orbital plane. *Bottom*: Changing of the line of sight to the neutron star because of the presence of the accretion disk and comparison with *RXTE*/ASM light curve. Figures taken form Leahy (2002).

the decrease and increase of both ring emission and of the central source emission on different timescales.

For the Short-On state the situation is similar. In this case the maximum emission from the inside of the tilted ring is very close to what is observed in the Main-On state. This is the result of a relative high inclination of the system geometry. In this configuration most of the inside of the ring is visible in the case the ring axis is tilted toward the observer. The resultant configuration is the emerging of the source from behind the outer disk ring, followed by the partial obscuration by the inner disk edge at phases $0.546 - 0.676$. Then, the occultation by the rest of the ring increases up to phase 0.790. The ring emission is now much more important because in the Short-On it is the dominant one.

5.3 Constructing the X-ray light curves of Her X-1

To monitor the source and describe the modulation of the X-ray flux and its peculiar 35 day periodicity, *RXTE* light curves of observations from 1996 to 2010, as well as *INTEGRAL* light curves of observations in 2005 and 2007, have been analyzed.

5.3.1 RXTE light curves

The *RXTE* satellite has repeatedly observed Her X-1 from 1996 up to 2011, its final year of activity. To have a complete collection of the light curves of Her X-1 over this 15 years period, *RXTE*/PCA data were analyzed and the X-ray light curve of each observation constructed. Table 5.1 lists the Main-Ons and the Short-Ons of all observations taken with *RXTE*.

To have a time resolution of 16 seconds provided by the PCA instrument `standard_2f` data products were used. As described in Chapter 3, the PCA instrument on-board *RXTE* consists of five different proportional counter units (PCUs). Every unit is a different detector and the X-ray PCA light curve for each pointing can be composed of different combinations of PCUs. For this reason PCA light curves have to be normalized for the number of PCUs switched on during the observation. To correct the count rate of the extracted light curves for the number of PCUs and subtract the background, the `lcmath` routine was used. Table 5.2 lists the approximate fractions for each PCU of the total (with all the five PCUs switched on) effective area. These values are taken from NASA Goddard Space Flight Center [1] and are determined comparing the individual count rates during Crab observations.

Using the values reported in Table 5.2, a multiplicative factor has been calculated to normalize the count rate of each light curve to a reference. In this work, PCU0 was chosen as the value to which the count rate are normalized. This procedure consists of weighting the light curves by the approximate effective areas of the PCU, which are on during the observations in order to determine the weight for a particular combination of PCU, taking the inverse of the sum of the corresponding fractions. The choice is arbitrary (the same correction could have been done for any PCU). In particular, the correction factor (F) has been calculated in the following way:

$$C^{norm} = C \cdot F = C \cdot \frac{A_0}{\sum_{i=1}^{N} A_i}, \tag{5.1}$$

where C^{norm} is the normalized count rate, C the original count rate of the light curve, A_0 the fraction of effective area related to PCU 0 and A_i is the number of active PCUs during the observation taken into account. Using Equation 5.1, the normalization factors for all the cases encountered in the PCA analysis for Her X-1 are the following:

$$F_{1\,off} = \frac{A_0}{A_0 + A_2 + A_3 + A_4}, \quad F_{3\,off} = \frac{A_0}{A_0 + A_1 + A_2 + A_4},$$

$$F_{4\,off} = \frac{A_0}{A_0 + A_1 + A_2 + A_3}, \quad F_{1,3\,off} = \frac{A_0}{A_0 + A_2 + A_4},$$

$$F_{1,4\,off} = \frac{A_0}{A_0 + A_2 + A_3}, \quad F_{3,4\,off} = \frac{A_0}{A_0 + A_1 + A_2},$$

[1] http://heasarc.nasa.gov/docs/xte/recipes/pcu_combine.html#extract

Table 5.1: Summary of the *RXTE*/PCA Main-On and Short-On observations between 1996 and 2010 used to construct the X-ray light curves of Her X-1.

Cycle number[1]	Date of observation	Time interval of observation (MJD)	On-state
252	January 1996	50114.135 – 50114.225	Main-On
257	July 1996	50290.026 – 50291.449	Main-On
258	September 1996	50340.989 – 50345.950	Short-On
259	September 1996	50356.136 – 50365.360	Main-On
268	August 1997	50690.309 – 50694.215	Short-On
269	October 1997	50705.046 – 50713.217	Main-On + Short-On
271	November 1997	50773.871 – 50774.899	Main-On
277	July 1998	51000.266 – 51007.848	Short-On
288	May 1999	51370.831 – 51373.974	AL3
295	March 2000	51621.336 – 51623.148	AL3
302	November 2000	51869.160 – 51869.245	Main-On
303	December 2000	51895.196 –51901.755	Main-On
304	January 2001	51933.514 – 51933.812	Main-On
307	May 2001	52032.979 – 52039.774	Main-On
308	June 2001	52068.639 – 52073.818	Main-On + Short-On
313	December 2001	52243.591 – 52246.585	Main-On + Short-On
319	July 2002	52454.192 – 52460.929	Main-On
320	August 2002	52492.779 – 52493.136	Main-On
323	November 2002	52595.060 – 52603.646	Main-On
324	December 2002	52633.782 – 52634.148	Main-On
333	November 2003	52950.029 – 52950.390	Main-On
336	February 2004	53045.289 – 53058.961	Main-On
340	July 2004	53199.031 - 53202.104	Main-On
343	October 2004	53300.774 – 53301.131	Main-On
351	July 2005	53576.352 – 53576.387	Main-On
352	July 2005	53578.251 – 53582.149	Main-On

[1] Cycle numbering reflect the common notation used by Staubert et al. (2009a).

Table 5.2: Approximation fractions of the total (all PCUs switched on) effective area used to correct the count rate and normalize it to the number of PCUs switched on during the observation (PCU0 was chosen as the reference).

PCU	Fraction of effective area
0	0.204
1	0.204
2	0.206
3	0.194
4	0.191

$$F_{1,3,4\,off} = \frac{A_0}{A_0 + A_2}, \quad F_{0,1,2\,off} = \frac{A_0}{A_3 + A_4},$$

where A_0, A_1, A_2, A_3 and A_4, are the fraction of the total effective area for PCU0, PCU1, PCU2, PCU3 and PCU4, respectively, and F_i are the corresponding factor for a particular combination of PCUs switched on. For example $F_{3\,4}$ is the conversion factor for an observation in which both PCU3 and PCU4 were switched off. These different conversion factors have to be multiplied by the count rate to normalize all the combinations of PCUs for different observations. These values are listed in Table 5.3.

Table 5.3: Conversion factor calculated to normalize the count rate for each light curve to the effective area for PCU0.

PCU-off	PCUs-on	Correction Factor
1	0 2 3 4	0.256604
3	0 1 2 4	0.253416
4	0 1 2 3	0.252475
1 3	0 2 4	0.339434
1 4	0 2 3	0.337748
3 4	0 1 2	0.332480
1 3 4	0 2	0.497561
0 1 2 4	3	1.051546

Usually two important conditions in extracting *RXTE*/PCA data are the so-called "electron-ratio" and the time interval after the passage of the South Atlantic Anomalies (SAA). The former gives an indication of the particle background and corresponds to the threshold number above which the background is considered too strong and data are not to be considered. The second parameter is the time in minutes after the SAA which takes into account a possible influence to the data because of the presence of radioactivity produced in the detectors at the SAA-passage. In particular, the "electron-ratio" condition is very important for soft sources or for a deep spectral analysis. This is not the case of Her X-1 which is a very bright source. For this reasons,

no particular settings were used, but the default values for both the electron-ratio and the time after the SAA. For the electron-ratio, the default threshold is equal to 0.10 which is rather small, but does not influence the X-ray light curve extraction. In the case of the SAA passage, the default value corresponds to 30 minutes. This is clearly a very conservative time interval which permits the radioactivity described before to decay completely. In addition to the correction for the number of PCUs, the original light curves were background subtracted in order to have the real (net) source count-rate.

The `standard_2f` mode used is a type of binned mode with a time resolution of 16 seconds that runs for all observations. The energy range adopted to construct the light curves is 2 – 60 keV which corresponds to all the energy channels available for the PCA instrument.

Using the extracted light curves, it has been possible to monitor the behavior of the source for several 35 day cycles. Unfortunately, there is not a good coverage for all the cycles by the PCA instruments. The two cycles with the highest statistics are cycle number 313 and cycle number 323. In particular, the latter shows an entire coverage of the Main-On. An interesting cycle is cycle number 269 for which both the Main-On and the Short-On states have been observed. The light curve, shown in Figure 5.4 shows nicely the 35 day modulation described in the previous sections with the two on-states. The Main-On starts around MJD 50705.0 and the Short-On around MJD 50724.5.

This cycle is also a good example to study the features present in the X-ray light curve of Her X-1, namely the presence of eclipses and dips (both types of dips: normal dips and anomalous dips). In particular, a close up of the light curve close to the turn-on is reproduced in Figure 5.5. Here, the normal dip is indicated with the letter D, the anomalous dip with the letters AD and the eclipse with the letter E. The figure reproduces exactly the nature of the dips. The normal dip occurs when the X-ray flux is decreasing before the eclipse takes place. On the other hand, the anomalous dip occurs randomly at 35 day phases close to the turn-on which is, in the case of cycle number 269, around MJD 50705 near orbital phase $\sim$0.5.

The *RXTE*/PCA X-ray light curves of the other cycles are given in Figure 5.6 (cycle numbers 252, 257, 258, 259, 268, 269, 271 and AL3 cycle 288), 5.7 (cycle numbers 302, 303, 304, 307, 308, 313, 319 and 320) and 5.8 (cycle numbers 323, 324, 333, 336, 340, 343 and 351) for the Main-On states and in Figure 5.9 for the Short-On states (cycle numbers 258, 268, 269, 277, 308, 313 and AL3 cycle 295). Also in these cases the dotted lines represent the eclipses.

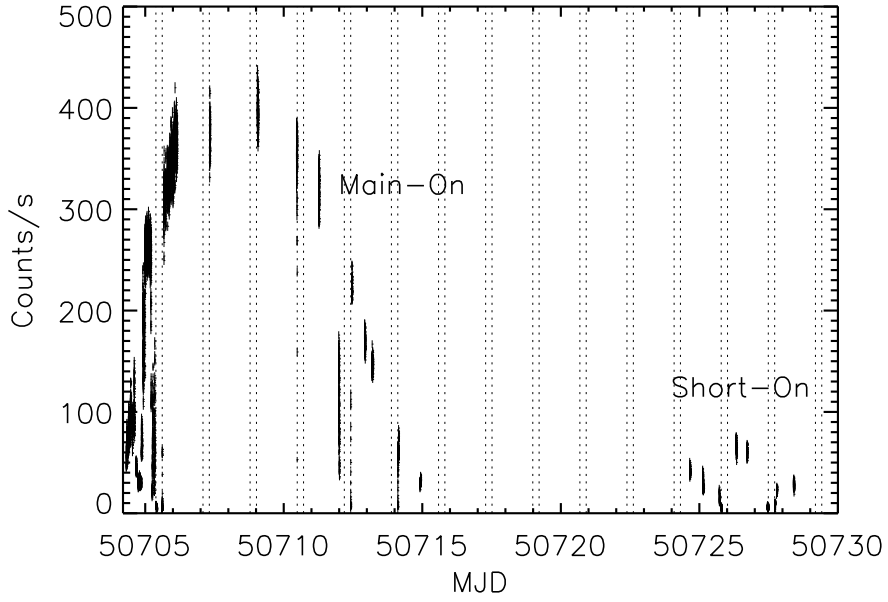

Figure 5.4: *RXTE*/PCA X-ray light curve of cycle 269. The dotted lines corresponds to those time intervals for which an eclipse is expected.

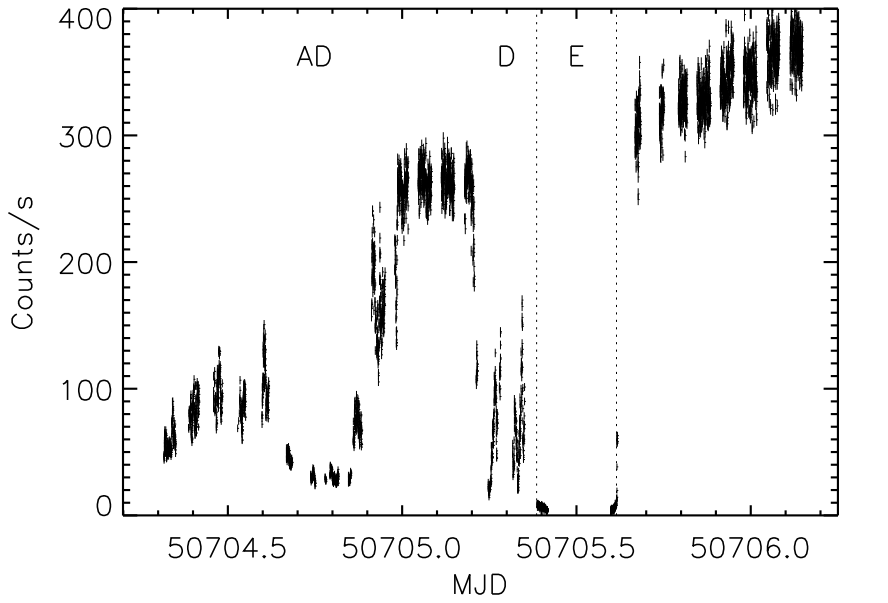

Figure 5.5: Close up view of the beginning of cycle 269. In the picture the features explained in section 5.1.2 are reported. Letter E indicates eclipse, D a normal dip and AD an anomalous dip.

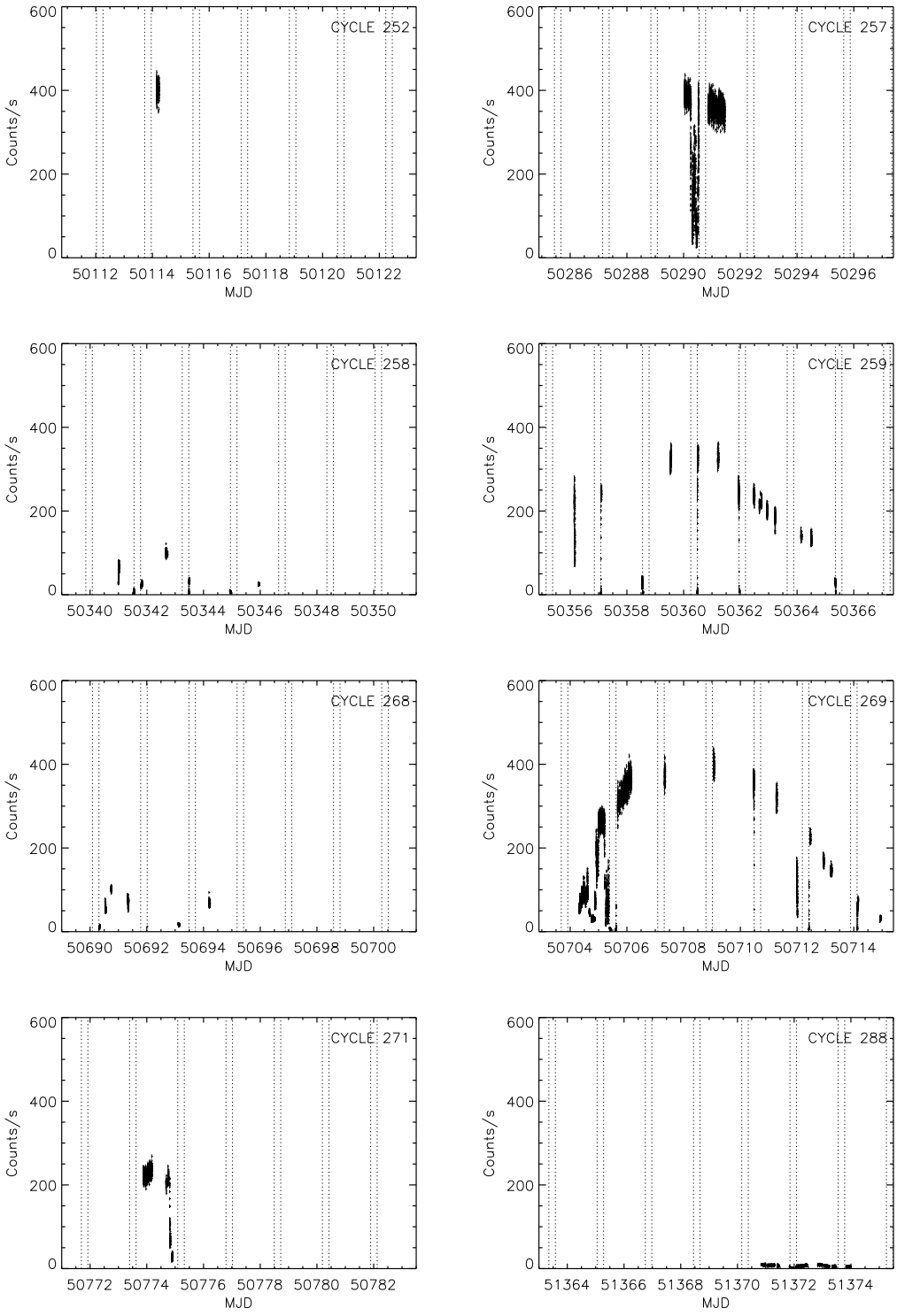

Figure 5.6: *RXTE*/PCA Main-On light curves of Her X-1 of cycles 252, 257, 258, 259, 268, 269, 271 and of the AL3 cycle 288.

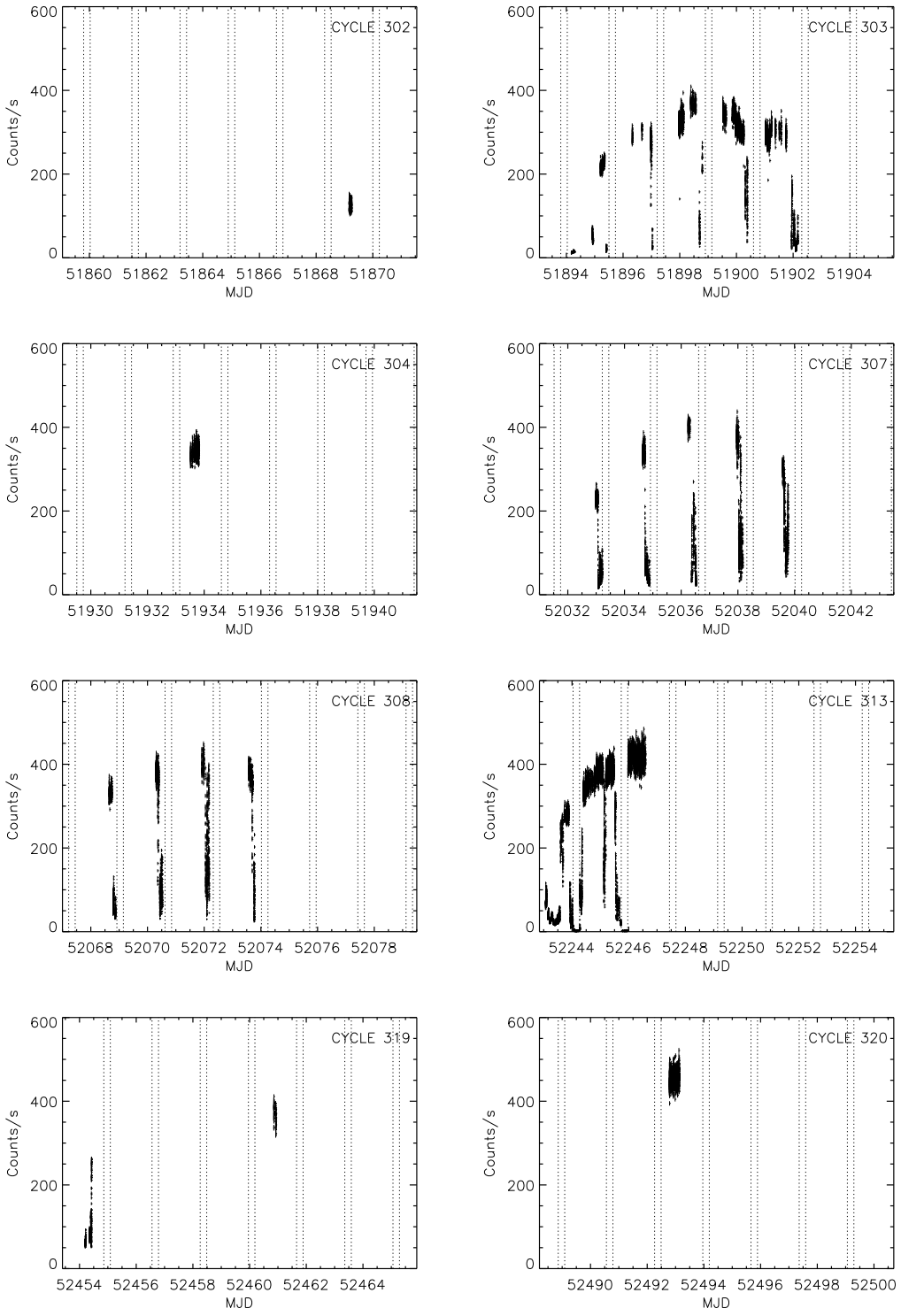

Figure 5.7: *RXTE*/PCA Main-On light curves of Her X-1 of cycles 302, 303, 304, 307, 308, 313, 319 and 320.

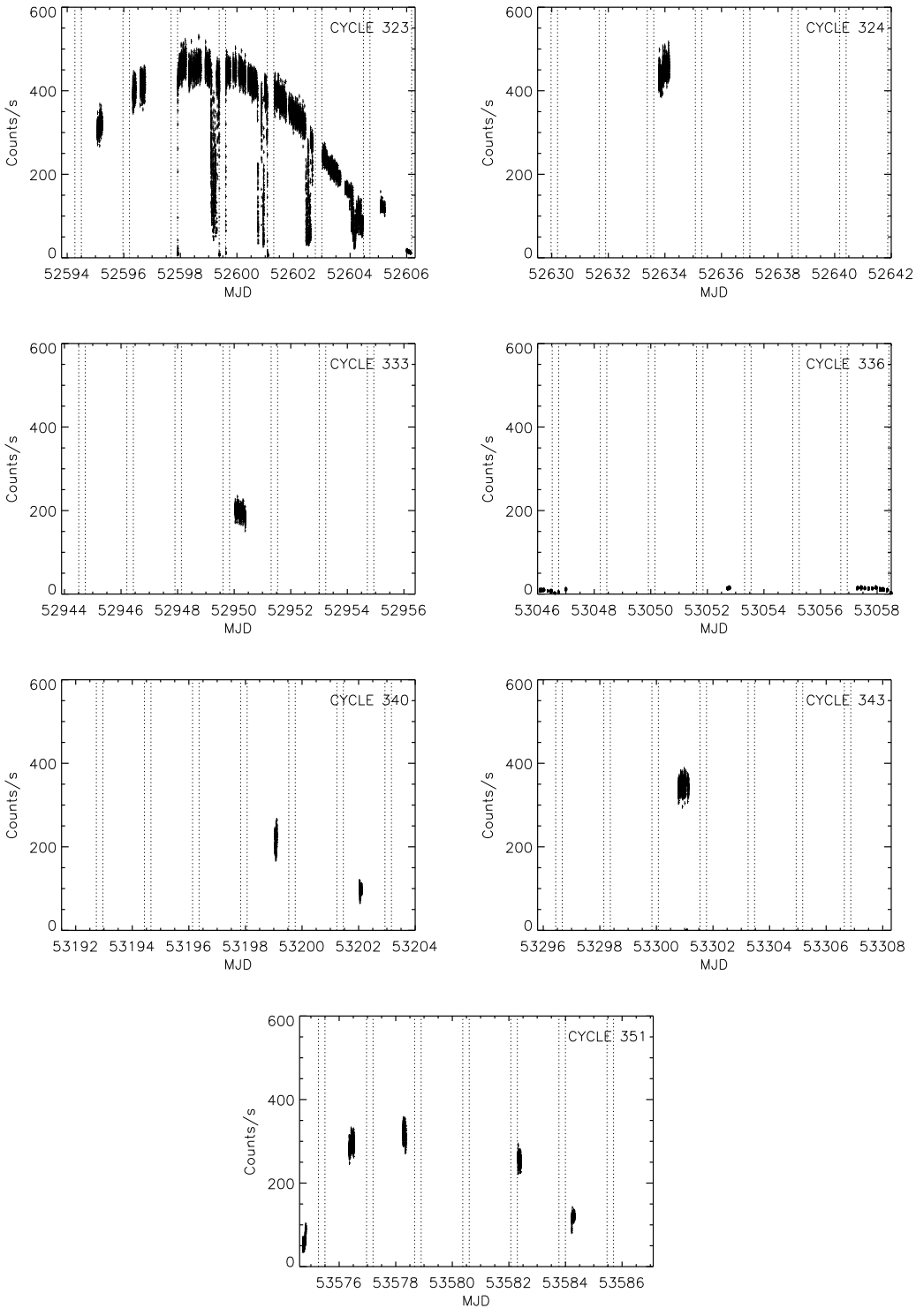

Figure 5.8: *RXTE*/PCA Main-On light curves of Her X-1 of cycles 323, 324, 333, 336, 340, 343 and 351.

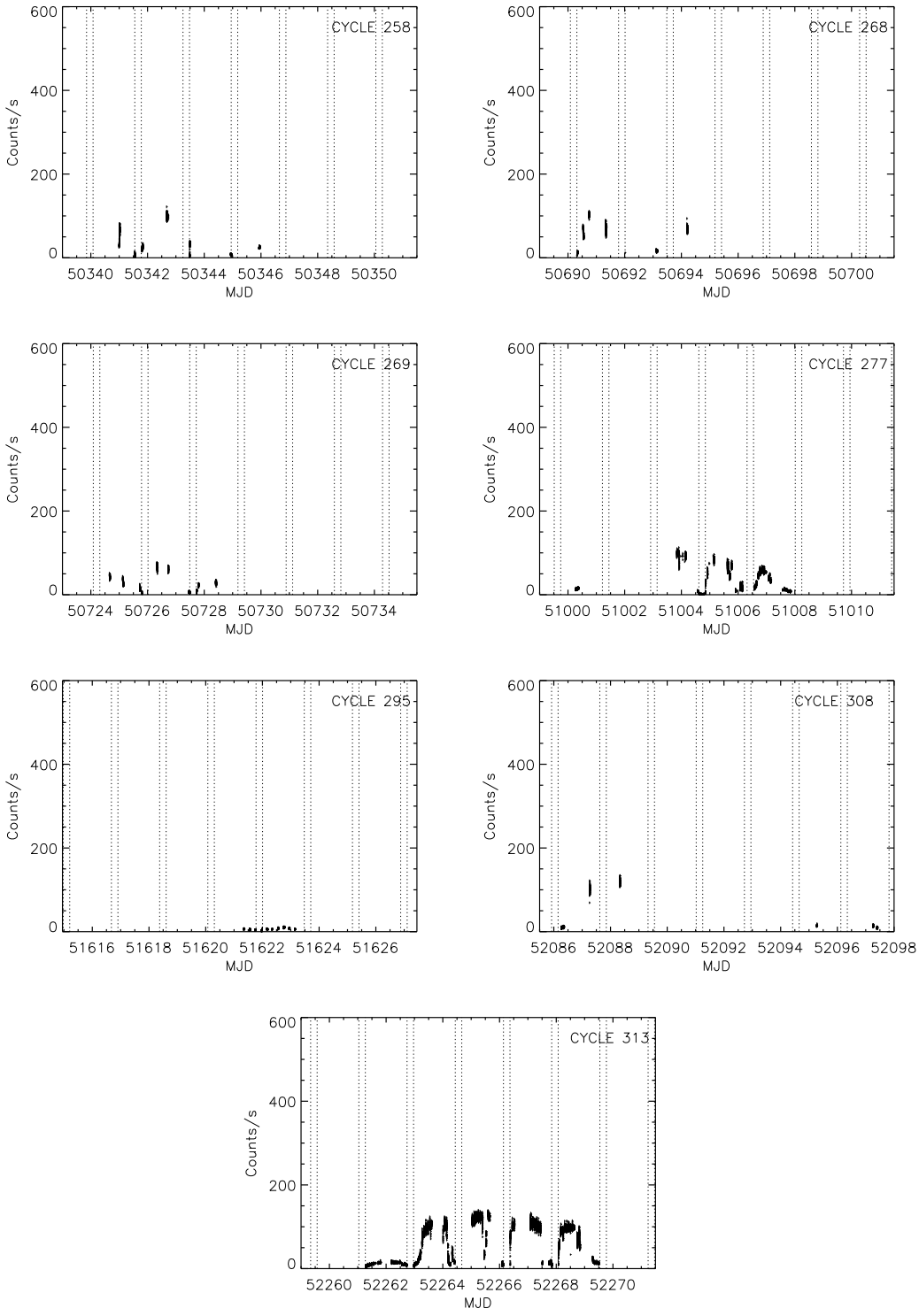

Figure 5.9: *RXTE*/PCA Short-On light curves of Her X-1 of cycles 258, 268, 269, 277, 308, 313 and of the AL3 cycle 295.

5.3.2 INTEGRAL light curves

X-ray light curve of Her X-1 were also extracted for the *INTEGRAL* observations. In this case, the observations are from two years: 2005 and 2007 (see table 5.4). The coverage period is not as long as in the case of *RXTE*, nevertheless the *INTEGRAL*/ISGRI light curves can provide information about the 35 day flux modulation. In particular, the energy range is 20 – 100 keV with a time resolution of ∼2000 seconds.

In Figure 5.10 the X-ray light curve of Her X-1 from July 2005 observations is shown. This X-ray light curve provides a good example to show the amplitude and the shape of the Main-On flux. This corresponds to cycle 351, the turn-on of which is observed around MJD 53573. In the same way, the light curve from 2007 is shown in figure 5.11. In this case the cycle number is 373 with an observed turn-on around MJD 54346.

Table 5.4: Summary of the *INTEGRAL*/ISGRI observations in 2005 and 2007 used to construct the X-ray light curves of Her X-1.

Number of cycle	Date of observation	Time interval of observation (MJD)	On-state
351	July 2005	53572.858 – 53584.872	Main-On
373	September 2007	54346.100 – 54351.633	Main-On

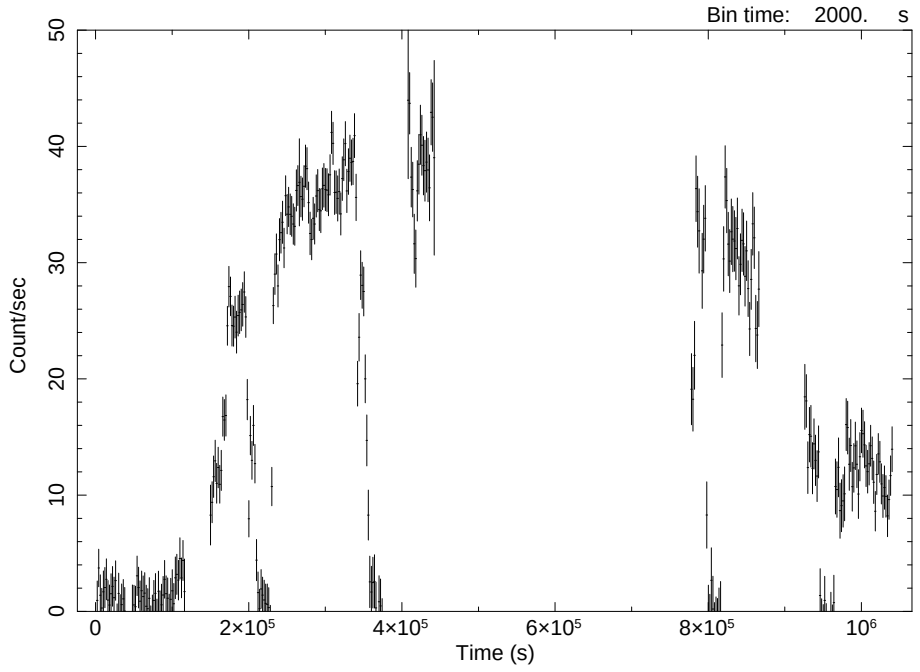

Figure 5.10: *INTEGRAL*/ISGRI Main-On light curve of Her X-1 of cycle 351. Start time in MJD: 53572.858.

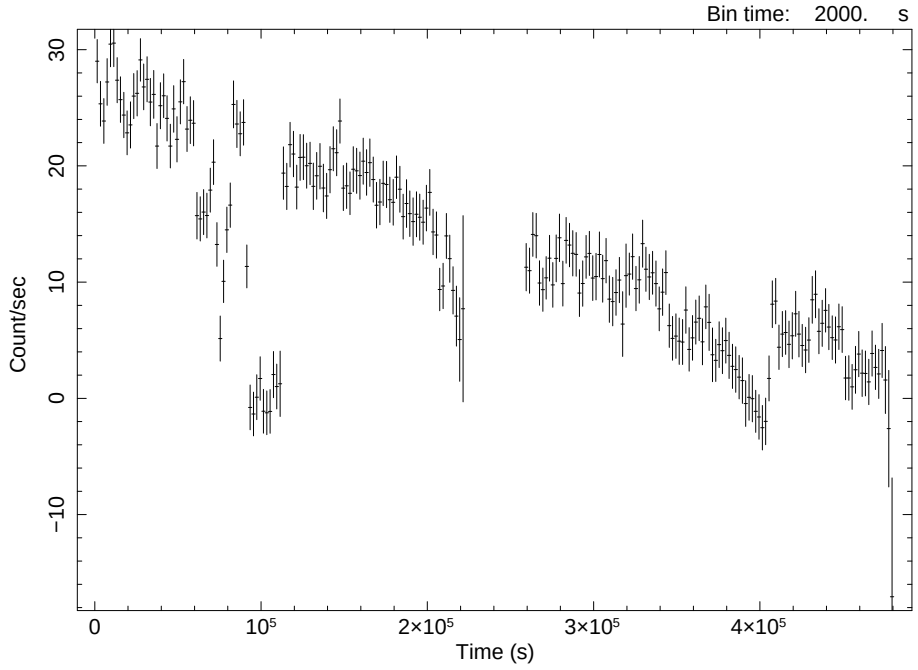

Figure 5.11: *INTEGRAL*/ISGRI Main-On light curve of Her X-1 of cycle 373. Start time in MJD: 54346.100.

6 The pulse profile evolution

The pulse profile shows the modulation of the X-ray flux as function of the rotation phase of the neutron star. A repeating, systematic evolution of the pulse profiles is a phenomenon currently known to exist only in Her X-1. In this chapter a description of the pulse profile shape and its features and the evolution as function of 35 day phase and energy, mostly based on a review by Scott et al. (2000), is reported. At the end, an analysis of the turn-on history based on the pulse profiles of the source is described as well.

6.1 Pulse profile properties

The study of the pulse profile evolution is important to investigate the emission geometry of accreting X-ray pulsars. This class of objects shows a huge variety of pulse profile shapes. The simplest case is a sinusoidal-like profile, but in many cases a more complex structure is observed. This scenario becomes even more complicated studying the evolution of the pulse profile shape as function of energy and time.

Since the first detection of Her X-1, repeated observations of the source, mostly with the Large Area Counter (LAC) on *Ginga* and the Proportional Counter Array (PCA) on *RXTE*, have shown a precise evolution of the pulse profile: its features change throughout the 35 day phase and with energy in a systematic way. The result of these changes is a repeating energy- and 35 day phase-dependent modulation of the pulse profile shape which repeats every 35 days. These systematic changes are a very well-known phenomenon since the observations with *EXOSAT* in 1984 (Trümper et al. 1986) and have been identified in several observations by Joss et al. (1978), Gruber et al. (1980), Ohashi et al. (1984), Kahabka (1987), Oegelman & Trümper (1988), Soong et al. (1990b), Scott et al. (2000) and represent a unique feature within X-ray accreting pulsars.

In Figure 6.1 a typical X-ray pulse profile for Her X-1, with the nomenclature adopted by Deeter et al. (1998) for its features, is shown. In the main high-state (Main-On) it consists of a double peaked structure: a main, relatively large pulse and a smaller interpulse. Usually, depending on the energy range, the main pulse exhibits a hard peak which represents the maximum intensity, two small soft shoulders (the so-called *soft leading* and *soft trailing* shoulders) and a huge pre-interpulse minimum. For the short high-state (Short-On), the situation is somewhat different, but a similar double-peaked structure is still observed: a big soft peak and a second small one. In addition, several minor substructures, mostly close to the interpulse, appear.

To distinguish the different components, a study of the pulse profile variation with energy is required (Blum & Kraus 2000). This has been done for example for other X-ray accreting pulsars such as 4U 1676–67 and 4U 1538–52 in the work by Kii et al. (1986) and Bulik et al. (1992), respectively.

Based on *Ginga* observations, Deeter et al. (1998) have suggested that the small, spectrally hard feature in the Short-On can be identify with the more prominent spectrally hard feature in the Main-On. This leads to a stable and persistent aspect of the pulse profile deserving considerations

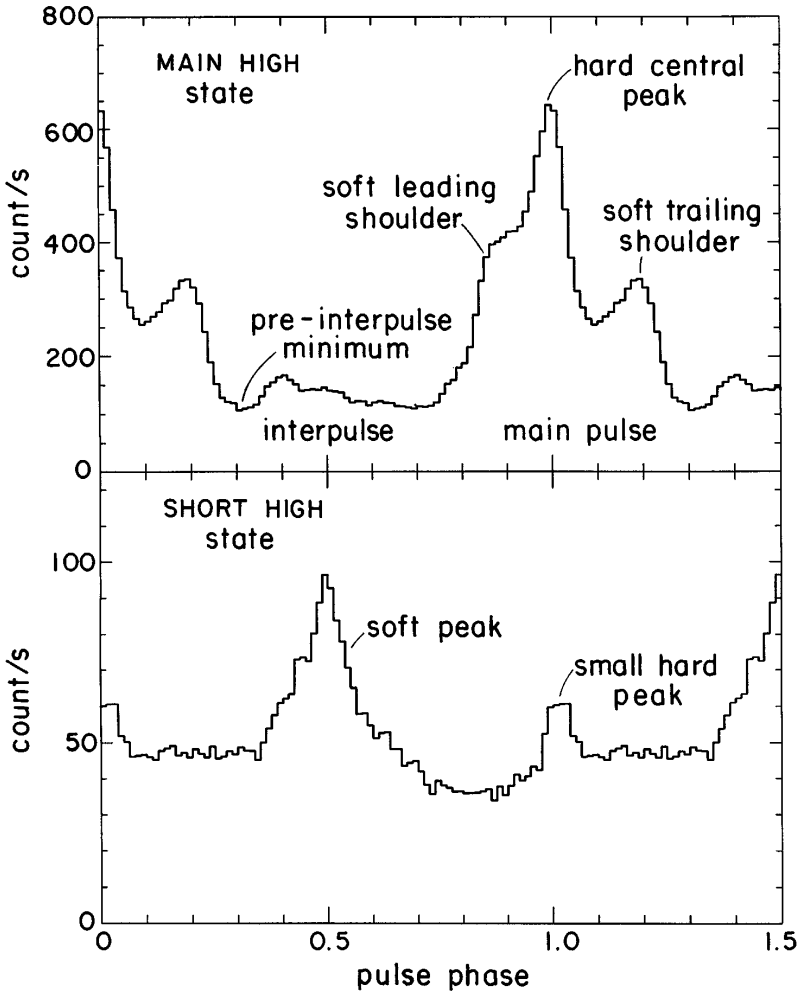

Figure 6.1: Typical X-ray pulse profile for Her X-1 with the nomenclature adopted for features. Top panel: Main-On pulse profile. Bottom panel: Short-On pulse profile. This sample of pulses is taken from *Ginga* observations by Deeter et al. (1998).

about two different components. The spectrally hard central peak has been suggested to be an independent component with a different origin and not only an extension of the adjacent shoulder. In the same way, the different evolution of the two shoulders suggests a number of separately obscured or formed pulse components. The resultant picture is very complicated and suggests a complex evolutionary cycle. Despite this fact, the shape of the pulse profile is well described in the literature. For detailed reviews on this topic see for example Deeter et al. (1998) and Scott et al. (2000).

All of these features are normally explained with the oblique rotator model by Lamb et al. (1973). In this model, the matter coming from the binary companion travels through an accretion disk and then along the magnetic field lines to finally fall onto the two magnetic poles of a highly magnetized and rotating neutron star producing X-ray emission. The "pulsations" are produced by an anisotropic radiation which is originating in the accretion columns close to the surface of

the neutron star due to the misalignment between the magnetic axis and the rotation axis of the source. Because of this, the shape of the pulse profile contains important information on the geometry of the emission region close to the magnetic poles of the neutron star where the accretion process is concentrated. A detailed description of the mechanism is still unknown, but theoretical models explain the pulse formation as a consequence of the continuously changing beam visibility. At the same time, many questions about the geometry of the radiation pattern need to be answered. For Her X-1, the observed profiles suggest the superposition of two different beams: the so-called *pencil beam*, defined as the emission coming from the beam perpendicular to the surface of the neutron star (assumed to be parallel to the magnetic axis), and the so-called *fan beam*, defined as the emission coming from the direction parallel to the surface of the neutron star. Some solutions were proposed by Wang & Welter (1981) and Leahy (1991) without giving a definitive answer because any observed feature can be interpreted as a fan/or pencil beam and different interpretation could all be correct (Deeter et al. 1998).

Now it is believed that the beamed emission and complex pulse profile structures could be the result of the effects of the interaction between the magnetic field of the neutron star and the infalling material. On the other hand, the preferred beam direction depends on the regime in which the accretion occurs. For high luminosity (super - Eddington regime), a radiative shock is expected to form. In this case photons will escape preferentially from the sides of the accretion column leading to the formation of a fan beam pattern. In contrast, for lower luminosities (sub - Eddington regime), the infalling material might be decelerated in a collisionless shock above the polar cap. In this case the emission region is closer to the surface of the neutron star and radiative transfer effects in the $\sim 10^{12}$ G magnetic field will constrain the photons escaping in the direction of the field lines, therefore giving rise to a pencil beam pattern. More complicated models are presented in Section 6.4.

6.2 Pulse profile evolution as function of energy and time

Following the review by Scott et al. (2000), a description of the main features of the pulse profile and its evolution for both the Main-On and the Short-On in Her X-1 is reported below.

Main-On.
The energy-dependent evolution of the Main-On pulse profile is shown in Figure 6.2. At low energies the high-state pulse profile has a double-peaked structure which consists of a large main pulse with two unequal shoulders and a smaller interpulse. At higher energies, this complicated double structure of the main pulse changes into a unique central peak which grows with energy and dominates entirely the main pulse around 20 keV (Soong et al. 1990b). In the same way, the 35 day phase-dependent evolution of the Main-On is shown in Figure 6.3 and can be summarized in three different steps: (1) the deepening and widening of a "gap" in the underlying component near the pulse phase of the interpulse minimum. This feature, visible early in the main high-state until the end of it has been observed in *Ginga*, *Uhuru*, *HEAO 1* and *RXTE* pulse profiles studies by Scott et al. (2000), Joss et al. (1978) and Scott et al. (1997), respectively; (2) the first real change of the main pulse which consists of the disappearance of the leading and trailing shoulders. Before this, the main pulse remains relatively constant. This behavior has been reported in many previous works (e.g. Soong et al. 1990b, Joss et al. 1978, Kahabka 1989, Sheffer et al. 1992, Scott

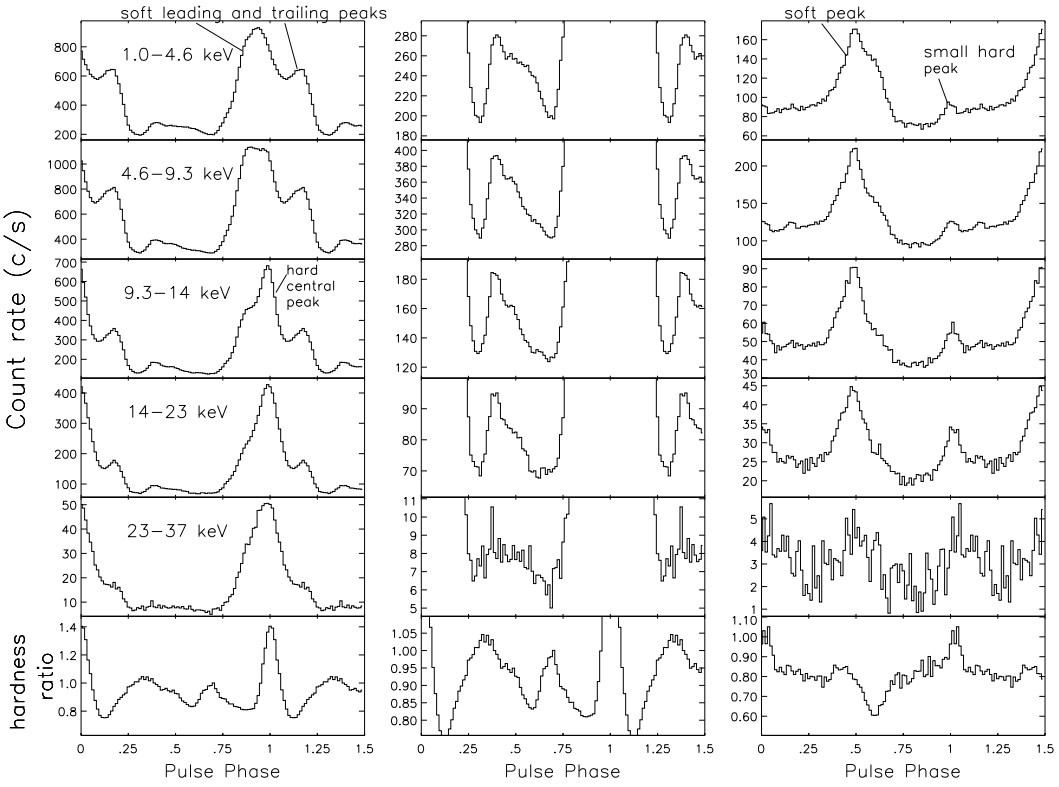

Figure 6.2: Evolution of the pulse profile as function of energy reported by Scott et al. (2000). The sample is from *Ginga* observations of Her X-1 and reproduces pulse profiles in five different energy bands. The energy increases from top to bottom: 1.0 - 4.6, 4.6 - 9.3, 9.3 - 14, 14 - 23, and 23 - 37 keV. The panels at the bottom display a hardness ratio (9.3 - 23 keV / 1.0 - 4.6 keV). The main pulse occurs at phase interval 0.75 - 1.25 and the interpulse at phase interval 0.3 - 0.7. In the middle panel a zoom of the interpulse is reported. In the right panel the evolution for the Short-On is reported with the same scale as the middle panel.

1993, Scott et al. 1997 and Deeter et al. 1998); (3) the disappearance of the spectrally hard peak of the main pulse after a rapid decay (Scott et al. 2000 for *Ginga* observations and Soong et al. 1990b for *HEAO 1* observations).

Short-On.
For the short high-state there are not so many observations as for the main high-states. To get a good statistics which allows a consistent study of the pulse profile evolution, those observations have to be combined with other shorter and fragmentary observations from different short high-states. Here, the pulse profile is significantly different because of a decrease in flux with respect to the Main-On of about a factor of four. Two peaks, separated by 180 degrees, are observed: a small spectrally hard peak and a larger spectrally soft one (see Figure 6.3). This is in contrast to what has been observed with *EXOSAT* by Kahabka (1987) and Kahabka (1989). In these analyses the presence of a small hard peak larger than the soft one is claimed, but *Ginga*

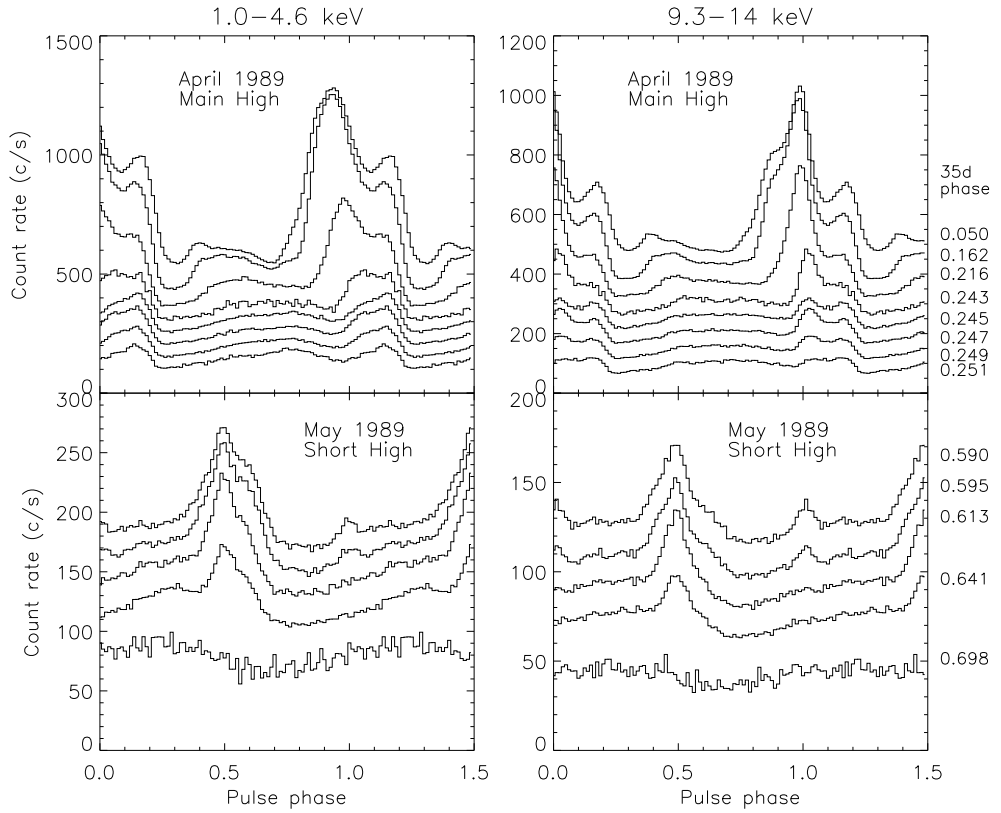

Figure 6.3: Evolution of the pulse profile as function of 35 day phase. The evolution of the Main-On pulse profile in April 1989 (top panels) and May 1989 (bottom panels) is shown in two different energy bands: 1.0-4.6 keV and 9.3-14 keV. Picture from Scott et al. (2000).

observations showed the small hard peak increasing with energy without exceeding the soft one. At the same time, the small hard peak disappears as function of energy within one day after the secondary turn-on and the soft peak declines in flux but slower, disappearing three or four days after the secondary turn-on. On the other hand, the amplitude of the pulse profile decreases with later 35 day phases. Sometimes it is also possible to distinguish a softer peak (Scott et al. 2000, Kahabka 1987 and Kahabka 1989) which is visible as long as the main soft peak is present.

In conclusion, the variations of the pulse profile and its evolution can be summarize as follows: the main high-state pulse profile evolves with the decay of the leading edge of the main pulse and the decay of the interpulse and the formation of multiple substructures; the short high-state, instead, evolves with the decay and disappearance of the two peaks (see Figures 6.2 and 6.3). This leads to the consistent idea of a repeating, stable and systematic variation of the pulse profile shape.

6.3 The free precession model

The variations of the pulse profiles have been explained with the free precession of the neutron star.

To define *free precession* for a rotating neutron star, some assumptions have to be taken into account:

1. the neutron star is not perfectly spherically symmetric, but slightly elongated (or contracted) along a direction which does not coincide (and not even parallel or perpendicular) to the spin axis;

2. the neutron star can be considered as a "two-axial" body where two axes of inertia are equal, but differ from the third one: $I_1 = I_2 \neq I_3$;

3. I_3 does not coincide with the spin axis.

Under these conditions, a rotating neutron star can undergo free precession.

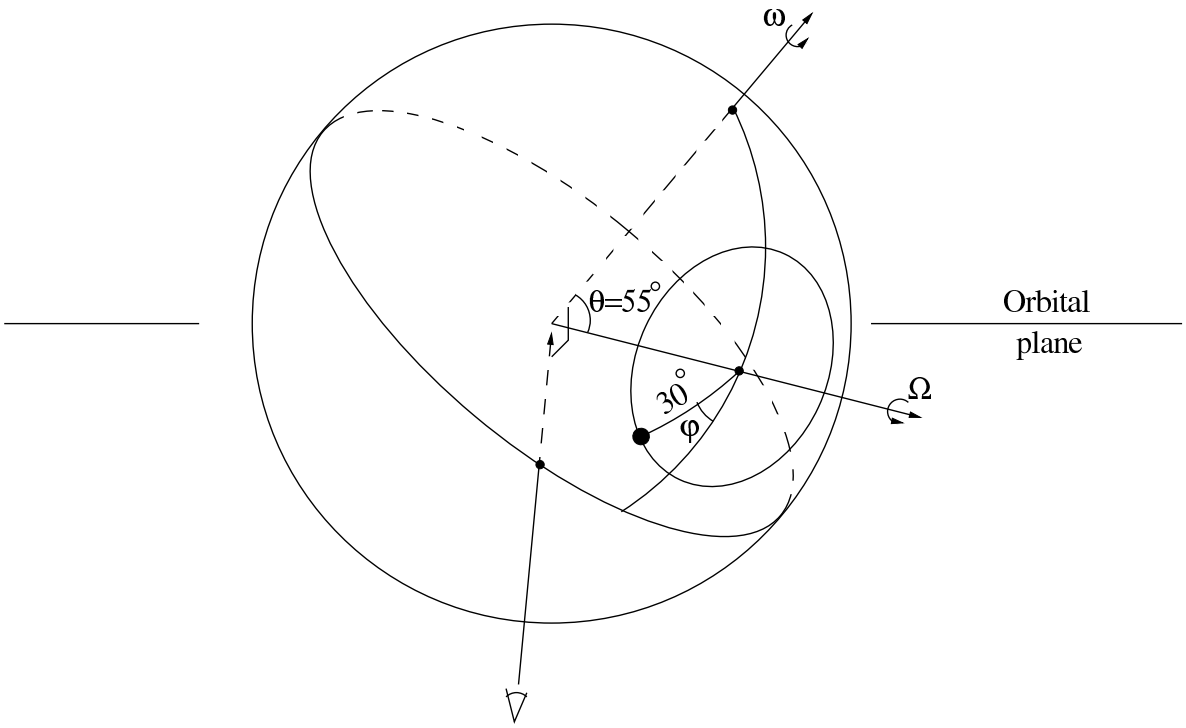

Figure 6.4: Schematic representation of the geometry for a freely precessing biaxial neutron star with axes of inertia $I_1 = I_2 \neq I_3$. ω is the axis of angular momentum, Ω the axis around which the precession occurs and ϕ is the phase of precession. Picture from Klochkov (2007).

In Figure 6.4, ω is the angular momentum of the neutron star which almost coincides with the spin axis. With this geometry, the neutron star is rotating with a P_{spin} (in Her X-1 1.24 s),

but it is also rotating around the axis of symmetry Ω. The orientation of the symmetry axis differs from the orientation of the axis of angular momentum by the angle θ. The black spot on the figure represents the magnetic pole wich rotates around the axis of symmetry with a $P_{prec} \simeq$ 35 days. In particular, the period of the precession P_{prec} is proportional to the period of the pulsation P_{spin} in the following way:

$$P_{prec} = P_{spin}/(\Delta I/I cos\theta), \tag{6.1}$$

where $\Delta I = I_3 - I_{1,2}$. Finally, the angle ϕ characterizes the phase of the precession.

This configuration leads to the fact that while the neutron star is freely precessing, the viewing conditions of the X-ray emitting regions change leading to the systematic variations of the pulse profile observed as function of the 35 day phase.

As reported by Link & Epstein (2001), free precession has been considered by many authors for most treatments of pulsar precession. Historically, free precession was introduced to explain the 35 day modulation of the X-ray flux (see e.g Pines et al. 1973, Lamb et al. 1975), and only later it was taken into account as possible mechanism to produce the observed variations in the pulse profiles shape.

A first suggestion for free precession in Her X-1 was proposed by Brecher (1972). This idea was introduced to explain the 35 day cycle, but also the complex structure of the pulse profiles. In particular, at that time, the existence of an interpulse was suggestive because there was only one other confirmed X-ray pulsar (associated to the radio pulsar NP 0532 in the Crab nebula) for which a similar shape was observed.

Free precession in Her X-1, was also later suggested by Trümper et al. (1986), Kahabka (1987), Kahabka (1989), Prokhorov et al. (1990), Shakura et al. (1998), Ketsaris et al. (2000) and Wilms et al. (2003). According to Trüemper et al (1986), the free precession model was used to explain not only the changing in amplitude of the pulse profiles, but also the pulse widths and several substructures. The interpretation proposed was that pulse and interpulse represent the polar beams of the X-ray emission seen from an observer at changing angles. In this frame, during the Main-On, one of the two poles is seen pole-on while the interpulse is produced by the second one which is only barely visible during the Main-On. Viceversa, during the Short-On, the second pole becomes prominent and the primary first pole is barely visible.

Up to now, the free precession model is still questionable and there is not a definitive answer to its validity. On the other hand, different models have been proposed without explaining in a concrete and uniform way the variation of pulse profiles in Her X-1.

6.4 Alternative models

Until a couple of years ago, the most quoted model to explain the evolution of the pulse profile was the free precession model (Trümper et al. 1986). This model was applied to some objects to explain the variation of the pulse profile shape, pulse amplitude or pulse residuals as a consequence of the changing viewing angle, because of the precession of the star. Within this sample there are radio pulsars such as the Crab pulsar, the Vela pulsar, PSR 1828-11 and PSR 1642-03, isolated neutron star (RX J0720.4-3121) and X-ray accreting pulsars like Her X-1. Trümper et al. (1986) suggested for the first time this model to explain the variation of the pulse profile and the difference in shape between the Main-On and Short-On light curves. The same model

was elaborated later by Kahabka (1989) and was noted that pure free precession of the neutron star cannot totally explain the high-low cycle. The beam needed to model the high-state would be too wide for a complete disappearance during the low-state. This is also supported by the fact that the unpulsed component must be produced by a wide beam or an unbeamed emission, but in both cases it is impossible to explain the disappearance of the pulsed component at the end of the high-state. On the other hand, cold matter absorption observed close to the turn-on in both high-states is not explained (Scott et al. 2000). To avoid this problem a model which takes into account both the free precession of the neutron star and the precession of the accretion disk was proposed. In this scenario an accretion disk, which occults the neutron star, and the free precession of the star itself work together. This solution proposed by Kahabka (1989) esplained the changes in the pulse profile shape of the *EXOSAT* observations. The resulting picture of the Her X-1 pulse profiles was inconsistent with the observed one.

There are some suggestions in the literature of how to explain at least some of the observed pulse profile features based on the free precession model (see e.g Shakura et al. 1998).

Taking into account all these considerations and excluding the free precession of the neutron star as the unique or primary cause for the pulse profile evolution, the precessing inner disk could be, most probably, responsible for the observed variations of the pulse profiles. The precession of the accretion disk could, in fact, be responsible for the 35 day cycle and the changing structure of the accretion column and the consequent evolution of the pulse profiles because of a change in the pattern by which matter couples to the magnetic field lines (Scott et al. 2000).

Other explanations of the variation of the pulse profile shape have been proposed, but still without solving the problem. Examples are a change in the disk orientation suggested by Scott et al. (2000), or an obscuration of the source due to the presence of "flaps" of matter at the meeting point between the magnetosphere and the tilted accretion disk by Patterson et al. (1991).

Finally, Scott et al. (2000) presented a model which consists of an occultation of the source because of the presence of the tilted and precessing inner edge of the disk. If a pencil beam surrounded by a fan beam cannot explain the leading edge decay of the main pulse, an opposite geometry where the fan beam is emitted in the antipodal direction to the pencil beam, can reproduce the decay only by an occultation. With the same motivation, the evolution of the Short-On pattern is explained. In this model the gravitational light bending is also taken into account, suggesting that the fan beam could be produced from those photons backscattered from a cyclotron resonance. Figure 6.5 summarizes the emission regions on which this model is based. In the left top panel the pulse profiles are reproduced with a central pencil beam (labelled by letter C) and a surrounded fan beam (labelled with letter B). Then, other three components are present (labelled with letter A, D, and E) which correspond to coronal emission and two isotropic emissions in the accretion column, respectively. The middle top panel shows the locations of the emission components. The right top panel shows just a larger vision to identify the locations of components D and E. The bottom panels reproduce the same situation as before, but with the accretion column on the opposite position, on the "back" of the neutron star. The main problem of the model by Scott et al. (2000) is that it needs a radius of the inner edge of the accretion disk which is much smaller than generally assumed.

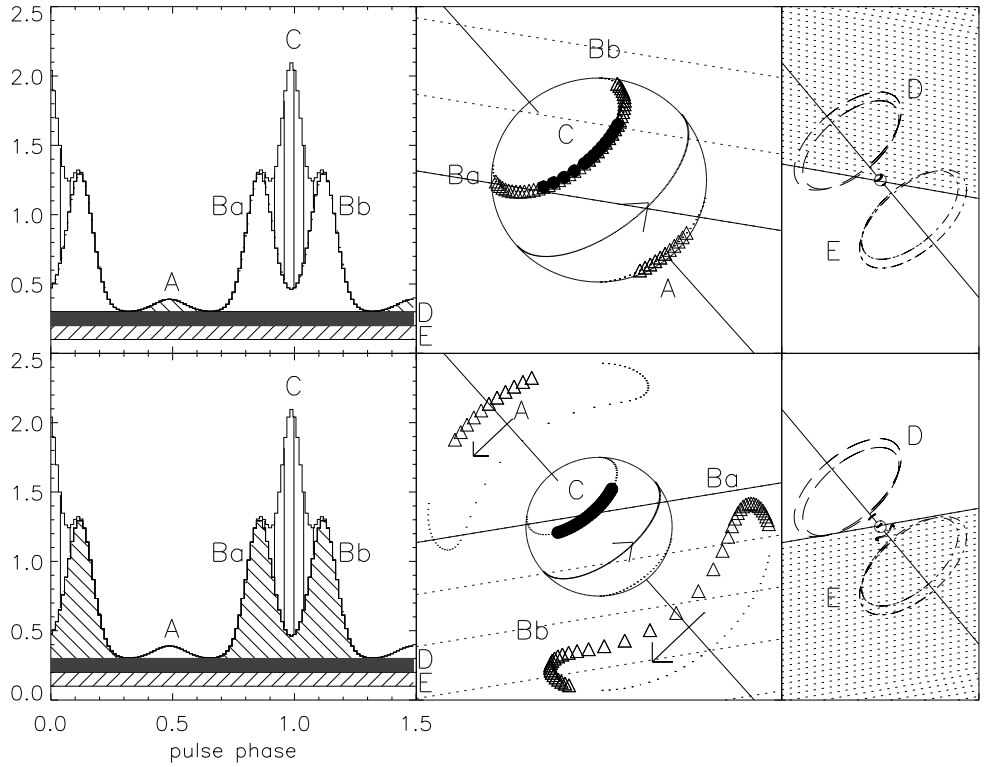

Figure 6.5: Schematic representation of the model presented by Scott et al. (2000). For details see the text.

6.5 Analysis of the pulse profiles and determination of turn-ons

The turn-on and the (O - C) diagram

As reported in Chapter 5, the so-called *turn-on* represents the transition between the off-state and the on-state and can be used to count the 35 day cycles. The behavior of the 35 day super-orbital period can be described by the so-called *(O - C) diagram* in which the difference between the observed turn-ons and the calculated ones under the assumption of a constant period is plotted. This diagram tracks the history of the 35 day period as function of time in MJD (or cycle number).

As shown in Figure 6.6 there is a clear variation of the 35 day period as function of time. Each change in direction plotted in Figure 6.6 reproduces a change in the period. A horizontal line would correspond to the situation in which there are no variations of the turn-on period. In the (O - C) diagram the interval in time between the different turn-ons is a half-integer number of the orbital cycles, but, in general, the 35 day turn-on clock is irregular: any individual cycle could have a length of 20.0, 20.5, or 21.0 times the orbital period (Staubert et al. 2006). In Figure 6.6, a period of 20.5 binary orbits, corresponding to a super-orbital period of 34.85 d, was used to calculate the turn-ons.

In Figure 6.6 also the so-called *anomalous low (AL)* periods are shown. These are those periods

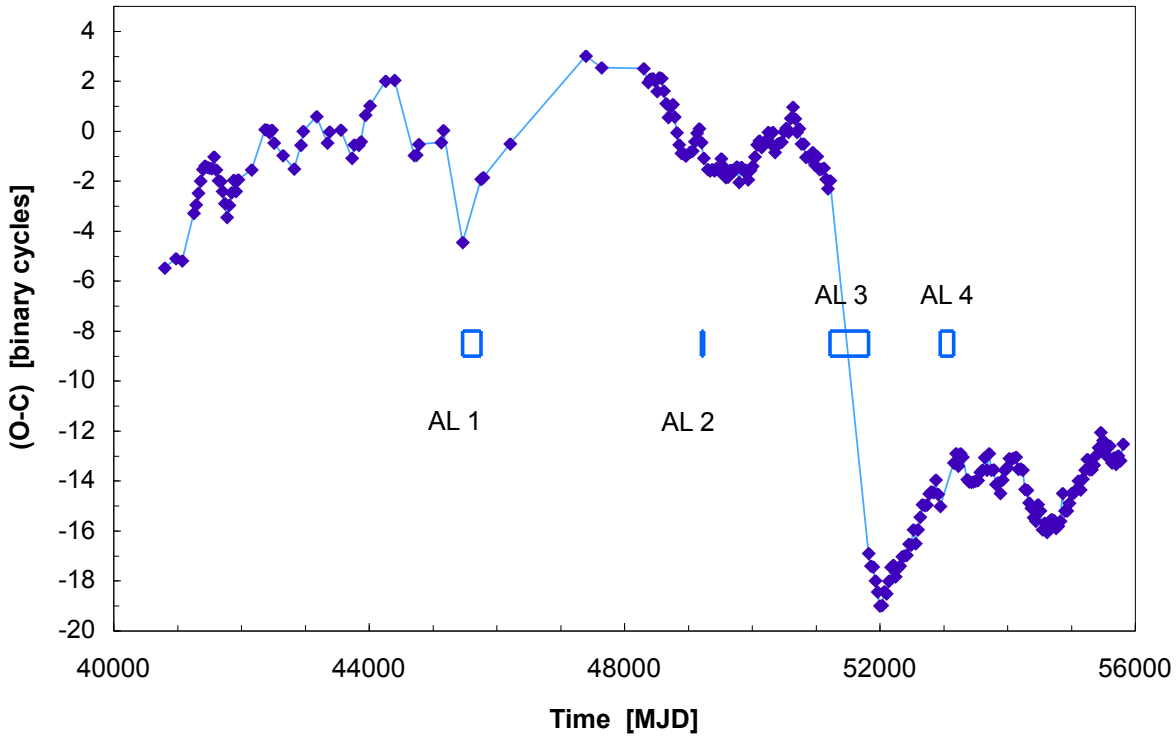

Figure 6.6: (O - C) diagram: the history of the turn-ons since the discovery of Her X-1 (Staubert, priv. comm. 2011; update of Figure 3 of Staubert et al. 2009a).

for which the X-ray flux is very low or even not observed and, consequently, the turn-on is not observed. The first AL was detected in June 1983 (Parmar et al., 1985) and lasted up to March 1984. Then, other ALs were detected in August 1993 (Vrtilek et al. 1994, Mihara et al. 1994), in the late months of 1997, in April 1999 (see e.g. Parmar et al. 1999 and Coburn et al. 2000) and, the most recent, in the late months of 2003 (Boyd et al. 2004). Each of these ALs lasts from one 35 day cycle (AL2) to several 35 day cycles (Still et al., 2001a) and seems to be due to a strong change in the inclination of the accretion disk which becomes very low with respect to the plane of the disk. This particular configuration leads to a total coverage of the X-ray emission region. During these periods a rapid spin-down of the pulse period was observed (see e.g. Parmar et al. 1999 and Coburn et al. 2000). The third anomalous low (AL3) which is centered at $\sim$ MJD 51500 is studied in details in Staubert et al. (2009a). During this period the number of 35 day cycles could be either 17 or 18 (see Figure 6.7). The solution of 18 cycles seems to be the correct physical interpretation for the continued precession of the accretion disk. On the other hand, taking into account 17 cycles, the mean duration of this period is longer and it has been associated to a regular clock: the free precession of the neutron star.

The modulation in flux and the turn-on history, described through the (O - C) diagram, is related to the accretion disk and its covering of the X-ray emitting region of the neutron star. On the other hand, the variation in shape of the pulse profiles, described in the previous sections, was

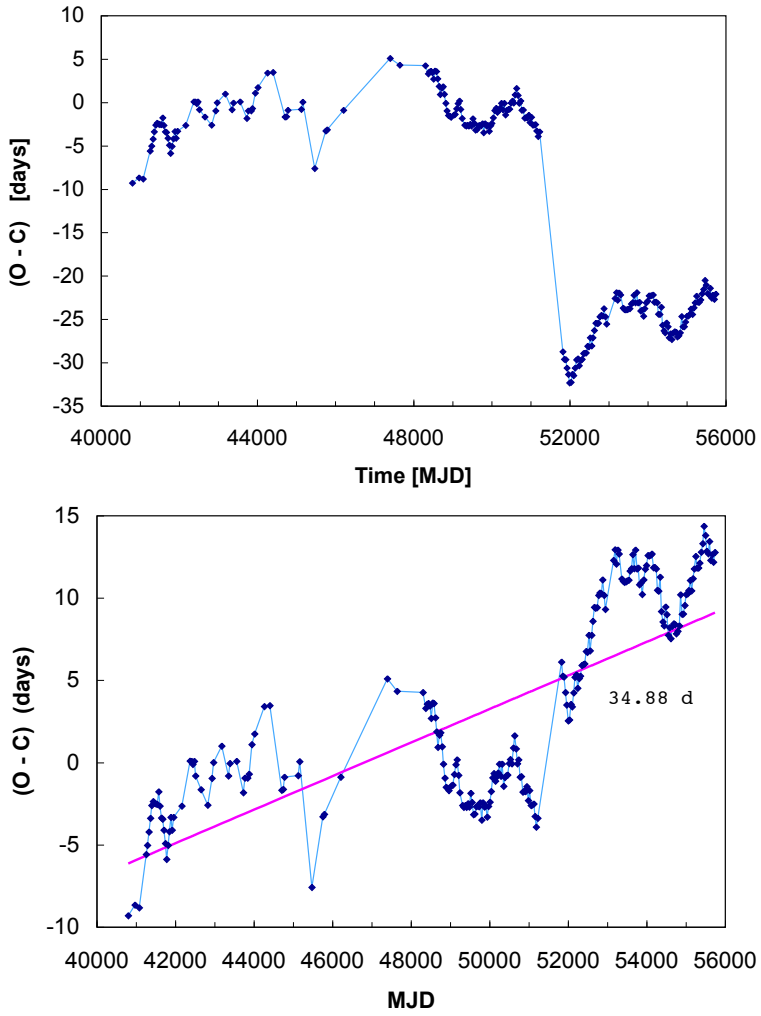

Figure 6.7: (O - C) diagram. *Top panel*: under the assumption of 18 cycles during the AL3 (third anomalous low); *Bottom panel*: under the assumption of 17 cycles (Staubert et al. 2010c).

suggested to be due to the free precession of the neutron star. In 2009, Staubert et al. (2009a) have suggested the existence of two different "clocks" in the Her X-1/HZ Her binary system. This comes from the observational fact that the 35 day cycles can be counted through the turn-on history and the relative On/Off cycle, as well as through the variation of the pulse profile shape which re-appears regularly every 35 days.

These two clocks, which are assumed to represent the precession of the accretion disk and the free precession of the neutron star, respectively, are synchronized and both have a period of about 35 days. This configuration explains the modulation of the X-ray flux as well as the variation in shape of the pulse profiles. In fact, the precession of the accretion disk blocks the line of sight to the X-ray emitting region close to the polar caps of the neutron star, leading to the observations of the turn-on, while the free precession of the neutron star changes the orientation of the X-ray emission leading to the variation of the pulse profile shape (Staubert et al. 2009a). The fact that the two clocks have nearly the same period suggests a strong correlation between them and

a strong physical feedback in the system which explains the synchronization. Staubert et al. (2009a) have proposed that the "master clock" is the free precession of the neutron star. This is because this clock is much more stable than the "accretion disk clock". This is clear from Figure 6.7 bottom, where the magenta line represents the free precession clock and the green line the accretion disk clock. The variation observed in the precession of the accretion disk is due to some torques which act on it such as tidal forces, the influence of the magnetosphere of the neutron star, viscous forces and dynamical forces from the interaction between the accretion stream and the illumination by the X-ray beam (Shakura et al. 1998, Klochkov et al. 2006).

The resultant picture is a free precession of the neutron star and a mildly slaved accretion disk precession. These two clocks are connected by a strong feedback based on the mass transfer rate of the companion star (here described following Staubert et al. 2009a). The X-ray emission from the neutron star heats the surface of HZ Her enhancing the mass transfer. The precessing disk is responsible for the X-ray flux modulation leading to an irregular heating of the optical component of the system. This means that if the inner part of the accretion disk follows the free precession of the neutron star due to the interaction with the magnetosphere, the shadowing of the companion star reflects the mass transfer with the period of the neutron star free precession. The resultant accretion stream hits the accretion disk and applies a force which influences the precession of the disk and its tilt (Shakura et al. 1999; Klochkov et al. 2006). At the end, the variability of the mass transfer rate is reflected in the variability of the mass accretion rate and consequently in the X-ray luminosity. This luminosity is the same one which is responsible for the heating of the optical star and for the illumination of the accretion disk where torques are possibly produced (Schandl & Meyer 1994). Finally, the variable heating of the companion star by the X-ray beam closes the loop.

Determination of the turn-ons on the basis of the pulse profiles

To verify the evolution of the pulse profiles and the existence of the two clocks reported in the previous section, a deep investigation of the pulse profile shape has been done using all the RXTE observations from 1996 and 2005. This study, reported in Staubert et al. (2010a,b,c), allowed to describe the systematically repeating features. A timing analysis of the archived data was performed in order to generate pulse profiles in the 9 – 13 keV energy range. This was done after the correction of the time to the solar system barycenter and for the binary orbital motion. In particular, *RXTE* `standard_2f` data products were extracted and `generic events` (`E_250us_128M_0_1s`, `E_1ms_128M_50_1s` and `B_16ms_16B_0_49_H`) as well as `GoodXenon`[1] observational modes of the PCA for the high resolution analysis were used. High resolution light curves were extracted with a resolution of 2 ms. The orbital parameters needed for the pulse profile extraction were taken from Staubert et al. (2009b): $T_{\frac{\pi}{2}} = 46\,359.871940$, P_{orb}=1.700167590 and $dP_{orb}/dt = -(4.85 \pm 1.3) \times 10^{-11}$. The so-called "time zero" which corresponds to the starting time of the folding procedure was chosen a couple of days before the start time of the light curve for each cycle.

The observations used for this analysis and the corresponding pulse periods for several Main-Ons are listed in table 6.1.

Within each Main-On, several short time intervals of a few hours were selected, then for

[1] http://heasarc.gsfc.nasa.gov/docs/xte/abc/pca_issues.html#configs_modes

Table 6.1: Summary of the observations and relative P_{spin} used to work on this analysis.

Cycle number[1]	Observation date	P_{spin} [s]
252	January 1996	1.23773985
257	July 1996	1.2377396
259	September 1996	1.2377377
269[2]	October 1997	1.2377294
269[3]	October 1997	1.2377298
271	November 1997	1.2377340
277	July 1998	1.2377276
288	May 1999	1.2377460
302	November 2000	1.2377710
303	December 2000	1.2377698
304	January 2001	1.2377724
307	May 2001	1.2377701
308	June 2001	1.2377694
313[2]	December 2001	1.2377677
313[3]	December 2001	1.2377670
320	August 2002	1.2377650
323	November 2002	1.2377620
324	December 2002	1.2377747
333	November 2003	1.2377650
340	December 2004	1.2377640

[1] Cycle numbering reflect the common notation used by Staubert et al. (2009a).
[2] Main-On [3] Short-On

each of these intervals the pulse profile was constructed. The result of this procedure is a huge collection (where the statistics was good enough to permit to recognize the shape of the pulse profile) of pulse profiles at different 35 day phases. This was the first step to start a detailed model-independent investigation of the periodic pulse profile variations. The second step was to construct a template, which represents a "mean" pulse profile in the $9-13$ keV energy range, summing up data of Main-Ons of cycles 313 and 323, which provide a good and uniform coverage of the 35 day phase range -0.05 and 0.22. These two cycles are those cycles with the highest statistics. The result is a 3D matrix of 128 bins in pulse phase and 28 bins in 35 day phase, as shown in Figure 6.8 (Staubert et al. 2010b,c). The resolution of the template is of 0.01 in phase. Then, the final step was to compare the other extracted pulse profiles with this template.

All of the pulse profiles observed in the same energy range can be in fact compared with the template and through this comparison it is possible to determine the corresponding 35 day phase. This process is done with a χ^2 minimization. To do this comparison, a "reference feature" as time marker is needed. This is the "sharp-edge" feature at the trailing edge at the decay of the main pulse right shoulder which goes into a minimum (Staubert et al. 2009b). The choice to use this feature as the phase marker is due to the fact that it is generally well defined and easy to identify and, secondly, because this feature happens to be the sharpest and most stable one.

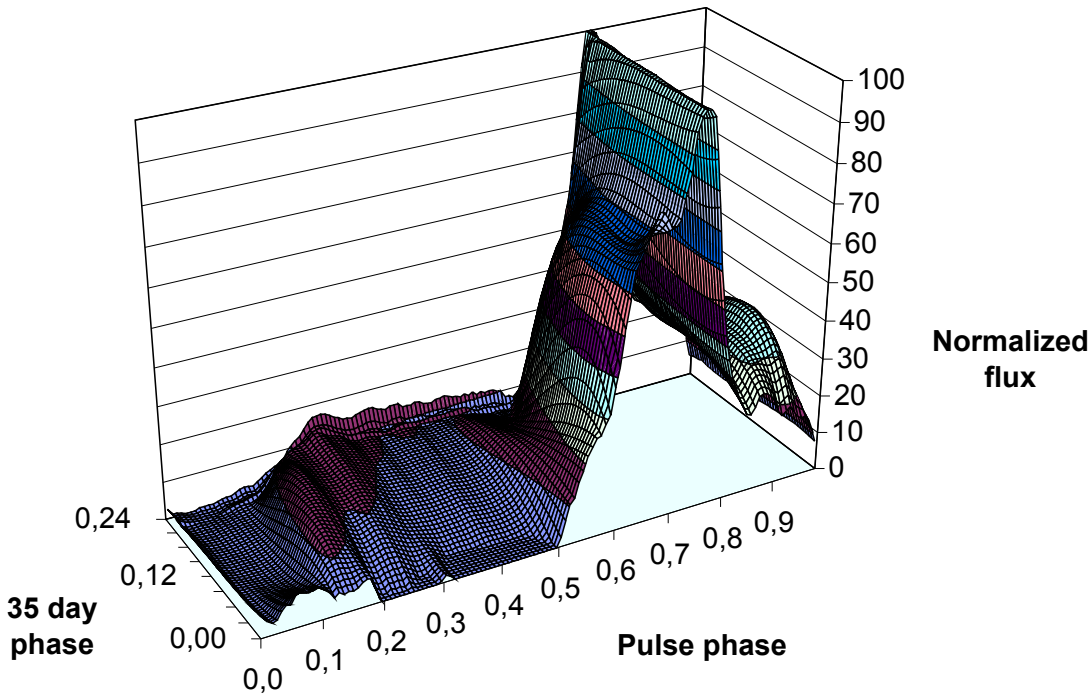

Figure 6.8: 3D representation of the template which represents a mean Main-On pulse profile in the 9-13 keV energy range for Her X-1 (Staubert et al. 2010b,c).

Once the 35 day phase for each observed pulse profile is determined, the so-called "phase-zero" for the corresponding cycle can be extrapolated. This phase represents the transition between the on-state and the off-state and consequently between two cycles in the same way as the turn-on. This is so by definition, since the template was constructed using data of cycle 313 for which the flux turn-on was well observed. The "phase zero" is found by a linear fit of the 35 day phases, corresponding to each pulse profile, estimated by the comparison with the template and using a period 34.85 day. For cycles 313 and 323, which are those cycles used to construct the template, the "phase-zero" are identical values by definition, for all the other cycles it can be determined by the process described before. In Figure 6.9 an example of the "phase-zero" extrapolation for cycle 257 is reported. The data represented in the plot are the 35 day phases obtained through the comparison between the observed pulse profiles and the template. The slope of the line used to fit these data is equal to the fixed period of 34.85 d. Then, the "phase-zero" value is represented by the point where this line intersects the x-axis which correspond to "0" in 35 day phase.

This procedure can be summarized as follows:

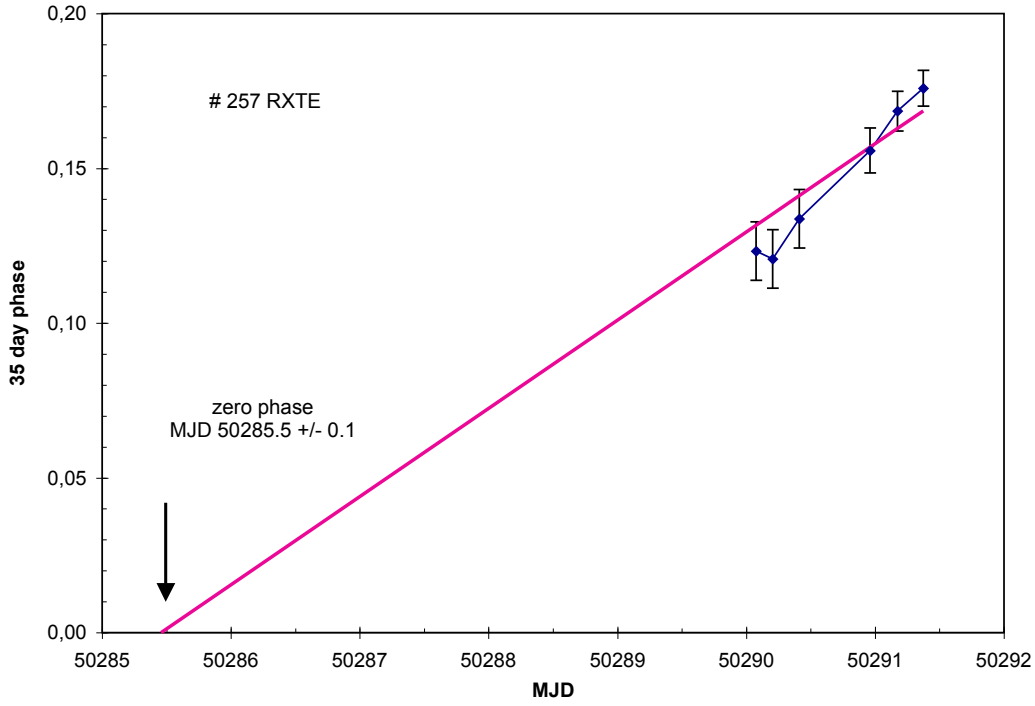

Figure 6.9: Example of the linear extrapolation of the "phase-zero" for cycle 257.

- extraction of the Main-On pulse profiles in the 9 – 13 keV energy range;
- construction of the template from data of cycles 313 and 323;
- comparison of pulse profiles of other cycles with the template to determine the corresponding 35 day phase;
- linear extrapolation to find the so-called "phase-zero" which represents the transition between two different cycles.

The determination of the "phase-zero" provides a different way to count the 35 day cycles which is based only on the observed pulse profiles of the source. This is very important because it represents an alternative option for the counting of cycles to the common one based on the observed turn-ons. The last step is to compare these two different ways. This comparison is shown in Figure 6.10 in which both the "phase-zero" ("phase-zero" based on the observed turn-ons) and the "pulse profile phase-zero" ("phase-zero" based on the pulse profiles) are reported. The green points connected by the solid line represent the observed turn-on times and the red points are determined on the basis of the pulse profile analysis. It is clear from this plot that the history of the different turn-ons track each other perfectly: taking into account statistical uncertainties the times for the turn-ons obtained on the basis of the pulse profile analysis are identical to those from the observed turn-ons due to the obscuration of the precessing disk. Considering the "flux turn-ons" as a clock and the "pulse profile turn-ons" as a different clock, as suggested by Staubert

et al. (2009a), this picture leads to the conclusion that there are not two synchronized clocks, but just one which governs both turn-ons.

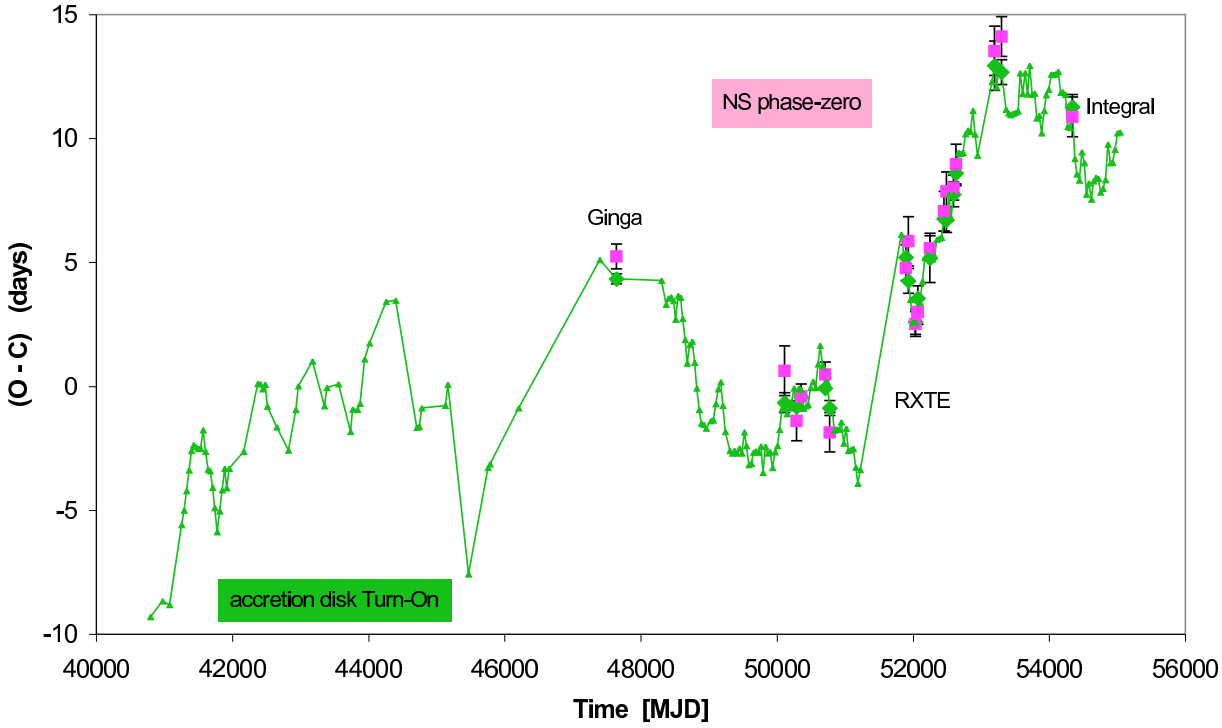

Figure 6.10: (O - C) diagram for both the observed turn-ons and the turn-ons generated from the pulse profile analysis (Staubert et al. 2010c).

These results introduce a new vision about the physical process, which governs the variation of the pulse profile shape. As already noted, the evolution of the pulse profiles with 35 day phase have been associated to free precession of the neutron star, but if the observed turn-ons and the ones obtained on the basis of the pulse profiles are identical, the question whether the free precession is really responsible for the variations of the pulse profiles or whether a different model should be developed still needs an answer. The picture is not clear, but if the free precession would be the only cause for the variation of the pulse profiles, then how it is possible that the neutron star changes its precessional period on very short timescales remains an unsolved problem. Another point which is equally difficult to explain is how the neutron star could transmit its precessional motion to the accretion disk. Staubert et al. (2009a) have suggested a strong feedback in the binary system which could explain this mechanism. These conclusions seem to be in line with the model proposed by Scott et al. (2000) (described before) in which the pulse profile shape variations are explained only with the precession of the accretion disk. Because of this, a detailed model which explains these variations, at least qualitatively, is a crucial point for the understanding of the physics which governs these phenomena in Her X-1.

7 An absorption line - like feature: the cyclotron line

The X-ray spectrum of Her X-1 shows an absorption line-like feature around ∼40 keV: the so-called *cyclotron line* (Trümper et al. 1978). In this chapter a description about the physical meaning of this feature is reported as well as some observational properties related to the cyclotron line. The results reported in this chapter can also be found in Vasco et al. (2011).

7.1 The physics behind the cyclotron line

For magnetic fields with a strength $B \geq 10^{12}$ Gauss, the electrons perpendicular to the magnetic field have energies quantized into the so-called *Landau levels*. The allowed energies of these Landau electrons are given by:

$$E_n = m_e c^2 \sqrt{1 + \left(\frac{p}{m_e\, c}\right)^2 + 2\, n \frac{B}{B_{crit}}}, \tag{7.1}$$

where n = 0,1,2,3,... is an integer number and corresponds to the principal quantum number, p is the electron moment parallel to the magnetic field, and B/B_{crit} is the strength of the magnetic field expressed in units of the critical magnetic field $B_{crit} = m_e^2 c^2 / e\hbar = 4.414$ x 10^{13} Gauss (for a detailed description see Harding & Daugherty 1991). The difference between two allowed "eigenstates" is the so-called *cyclotron line energy* E_{cyc} and can be approximated as:

$$E_{cyc} = E_{n+1} - E_n = \hbar\, \omega_c = \frac{e\hbar}{m_e} \cdot B \approx 11.6\,\mathrm{keV} \cdot B_{12}, \tag{7.2}$$

where B_{12} is the magnetic field in unit of 10^{12} Gauss. Assuming $B \ll B_{crit}$, an electron which occupies the ground state ($n = 0$) can be excited to a higher state ($n > 0$) by photons with energies equal to n times the energy of the cyclotron line $E = n\, E_{cyc}$. The life time of the Landau levels is very short and, because of this, excited electrons which occupy states $n > 1$ return almost instantaneously to the ground state emitting a resonant photon in the same way of a resonant scattering process leading to the formation of a resonance line (see Figure 7.1). This line is a an absorption-like feature, now referred to as *cyclotron resonant scattering feature* (CRSF), and can be observed at energies equal to n times E_{cyc}.

In the case of $B \approx B_{crit}$, relativistic corrections should be taken into account. Under this assumption, the cyclotron line energy E_{cyc} depends on the angle between the primary photon and the axis of the magnetic field. Assuming this angle θ, Harding & Daugherty (1991) caculated the energy E_n as:

$$E_n = m^2 c^2 \sin^2\theta \sqrt{1 + 2n \frac{B}{B_{crit}} sin^2\theta - 1}. \tag{7.3}$$

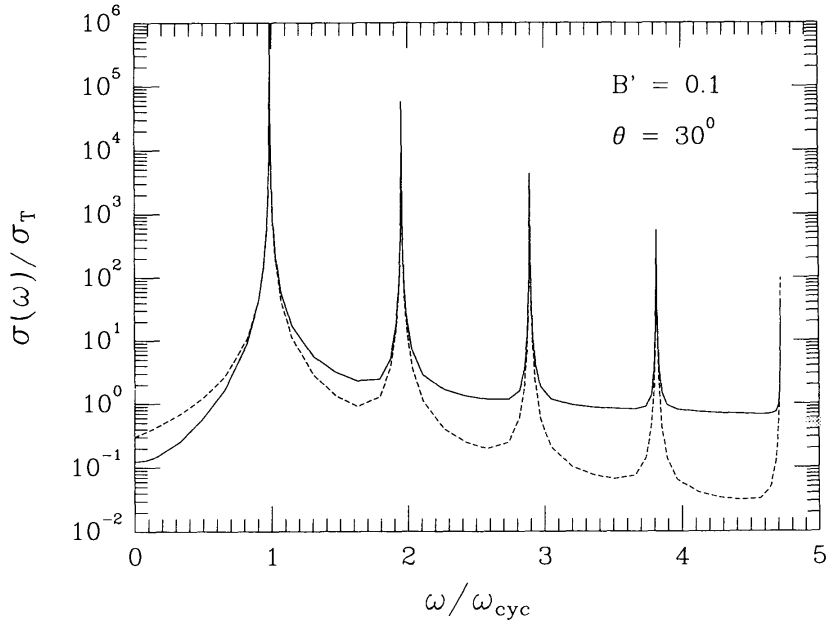

Figure 7.1: Landau levels from Harding & Daugherty (1991).

Equation 7.3 shows how the shape of the cyclotron line is influenced by the magnetic field. For X-ray binaries with a neutron star as compact object and magnetic fields up to $B \geq 10^{12}$ Gauss, gravity cannot be neglected leading to the following formula for the cyclotron line energy E_{cyc}:

$$E_{cyc,z} = \frac{E_{cyc}}{(1+z)} = \sqrt{1 - \frac{2\,GM}{R\,c^2}}, \tag{7.4}$$

where $E_{cyc,z}$ is the cyclotron line energy E_{cyc} gravitationally redshifted, M and R the mass and the radius of the neutron star, respectively. Using both Equation 7.2 and Equation 7.4, the cyclotron line energy E_{cyc} can be written as:

$$E_{cyc} = 11.6\,\mathrm{keV}\ \cdot\ B_{12}(1+\mathrm{z}) \tag{7.5}$$

and consequently:

$$B_{12}(1=z) = \frac{E_{cyc}}{11.6\,\mathrm{keV}}. \tag{7.6}$$

This formula is very important for X-ray binary systems because it provides a direct way to estimate he magnetic field of the neutron star.

7.2 The cyclotron line feature in the X-ray spectrum of Her X-1

In 1975 for the first time a line - like feature in the X-ray spectrum of Her X-1 was discovered. This discovery was based on a balloon observation of a collaboration between the *Max-Planck-Institut für Astronomie* (MPI) Garching and the *Astronomische Institut Tübingen* (AIT) (Trümper et al.

1978). The spectrum was modeled by an exponential but there was evidence of a strong line-like feature which was fitted with a Gaussian emission line (see Figure 7.2). This phenomenon was new for X-ray astronomy and was explained as a cyclotron line. Because of this, Her X-1 is the first X-ray accreting pulsar for which a cyclotron line was discovered.

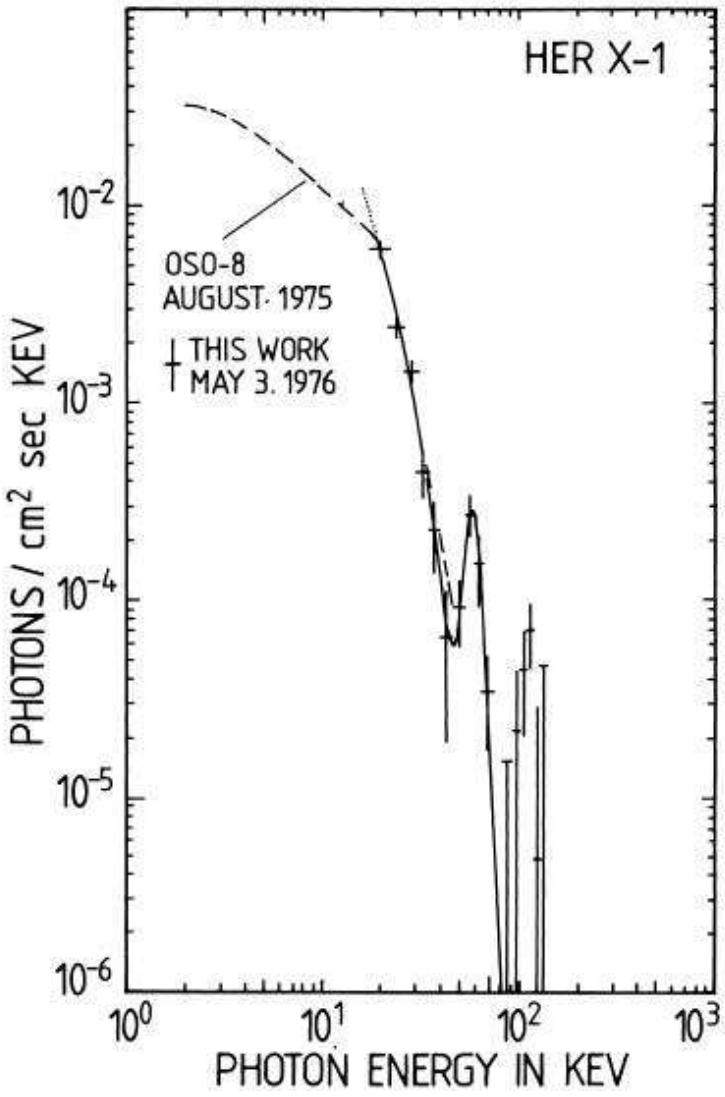

Figure 7.2: X-ray spectrum of Her X-1 from Trümper et al. (1978). *Solid line*: best-fitting exponential spectrum with a Gaussian emission line to the data points. In the plot also the spectrum of Her X-1 observed by OSO-8 during the 1975 August on-state is shown.

By theoretical considerations (Nagel 1980) and finally by observations (Kunz et al. 1996) it has become clear that the line is a feature in absorption. Nowadays, it is believed to be present in several X-ray binaries, transient as well as persistent sources and it seems to be quite common in accreting X-ray pulsars (Coburn et al. 2002). This is why during the last years cyclotron line

astronomy became quite important and the list of objects for which a cyclotron line has been discovered in the X-ray spectrum continues to increase. In Table 7.1 the sources for which this feature has been discovered are listed.

Table 7.1: Cyclotron line sources based on Wilms et al. (2009).

Source	E_{cyc} (keV)	Reference
Swift J1626.6 - 5156	10	DeCesar et al. (2009)
4U 0115 + 63	14, 24, 36, 48, 62	Wheaton et al. (1979)
4U 1907 + 09	18 ,38	Heindl et al. (1999); Santangelo et al. (1999)
4U 1538 - 52	22, 47	Cusumano et al. (1998)
Vela X - 1	24, 52	Kendziorra et al. (1992); Kreykenbohm et al. (2002)
V0332 + 53	27, 51, 74	Makishima et al. (1990)
Cep X - 4	28	Mihara et al. (1991)
Cen X - 3	29	Heindl & Smith (1998); Santangelo et al. (1998)
X Per	29	Coburn et al. (2001)
MXB 0656 - 072	33	Heindl et al. (2003)
XTE J1946 + 274	36	Heindl et al. (2001)
4U 1626 - 67	37	Orlandini et al. (1998); Heindl & Smith (1998)
GX 301 - 2	37	Mihara et al. (1995)
Her X - 1	41	Trümper et al. (1978)
A0535 + 26	50, 110	Kendziorra et al. (1992); Maisack et al. (1997)
1A1118 - 61	55	Doroshenko et al. (2010)
GRO J1008 - 57	88	Shrader et al. (1999)
RX J0440.9 + 4431	32	Tsygankov et al. (2012)
GX 304 - 1	54	Yamamoto et al. (2011)

Some of these objects exhibit also higher harmonics. This is for example the case of 4U 0115+64 for which five cyclotron lines have been discovered (Santangelo et al. 1999; Heindl et al. 1999). This feature can also be broad and complex depending on many factors such as the temperature of the electrons and the viewing angle with respect to the magnetic field, however higher harmonics show a simpler absorption line structure (Kretschmar et al. 2001).

As mentioned before, the cyclotron line plays a very important role in the measurement of the magnetic field. Using in fact Equation 7.6, a direct estimation of the magnetic field of Her X-1 can be found in the following way:

$$B_{12,\,\mathrm{HerX-1}}(1+z) = \frac{E_{cyc,\,\mathrm{HerX-1}}}{11.6\,\mathrm{keV}} \simeq 3.4 \times 10^{12}\,\mathrm{G}, \tag{7.7}$$

where $B_{12,\mathrm{HerX-1}}$ is the magnetic field strength in units of 10^{12} Gauss of Her X-1, z is the gravitational redshift (estimated for a neutron star with R=10 km and M=1.4 $M_{\odot}$) and $E_{cyc,\mathrm{HerX-1}}$ is the energy of the cyclotron line in keV observed for Her X-1 ($\sim$ 40keV).

7.3 Relation between the cyclotron line and the luminosity

The cyclotron line feature of a few high luminosity transient sources shows a variation of its position in the X-ray spectrum related to the change in the X-ray luminosity. Studies of some bright, super-Eddington transient pulsars show that this correlation is negative: the cyclotron line energy is reduced when the X-ray luminosity of the source increases. This is what was found for sources such as 4U 0115+63 and V 0332+53 observed by *Ginga* and *RXTE* (Mihara et al. 1998). This behavior is explained as due to the change in height of the emission region above the surface of the neutron star with the changing mass accretion rate. This has been suggested by Burnard et al. (1991), based on a previous work of Basko and Sunyaev (1976), in which an increase of the accretion column height h_{top} with increasing luminosity is predicted theoretically as:

$$h_{top} \approx L. \tag{7.8}$$

The correlation between the centroid of the cyclotron line and the luminosity of the source is true on long timescales as well as on time scales of single pulses (Klochkov et al. 2011), but our knowledge about the physics of the accretion column and the height of the cyclotron generating region is poor and open questions need to be answered. What is known about the physics of these phenomena is strongly related to the details of the mass accretion. Under a radiation pressure dominated regime, applicable to high-luminosity sources, an increase of the mass accretion rate leads to an increase of the radiative shock height and, consequently, to a decrease of the effective magnetic field in the cyclotron line generating region. In the gas pressure dominated case, realized for low luminosity sources, due to the increased pressure of the infalling material, the cyclotron line generating region gets closer to the surface of the neutron star where the magnetic strength is higher (Staubert et al. 2007).

In the case of 4U 0115+63 and V 0332+53 a negative correlation between the energy of the cyclotron line and the luminosity of the source has been clearly observed (Kreykenbohm et al. 2005, Tsygankov et al. 2006, Mowlavi et al. 2006 and Nakajima et al. 2006). For Her X-1 the picture is different: repeated measurements of the cyclotron line energy with *RXTE* have instead shown a *positive* correlation. These results have been reported by Staubert et al. (2007) and the correlation is shown in Figure 7.3. In this case the maximum Main-On flux as measured by *RXTE*/ASM (see section 3.1.3) is taken as a measurement of the bolometric luminosity of the source for the particular 35 day cycle.

In particular, in the case of low luminosity, the relation between the cyclotron line and the luminosity L can be described by:

$$\frac{\Delta E_{cyc}}{E_{cyc}} = 3\frac{l_*}{R}\frac{\Delta L}{L}, \tag{7.9}$$

where l_* is the height of the characteristic region above the surface of the object and R the radius of the neutron star (Staubert et al. 2007). This means that the change in cyclotron line energy can be directly proportional to the change in luminosity.

Currently, there are a few sources for which a dependence of the CRSF energy on the luminosity has been observed (Her X-1, 4U 0115+63, V0332+53, A0535+26 and Cen X-3), but this sample of sources is not enough to develop the corresponding theoretical models. Among these sources,

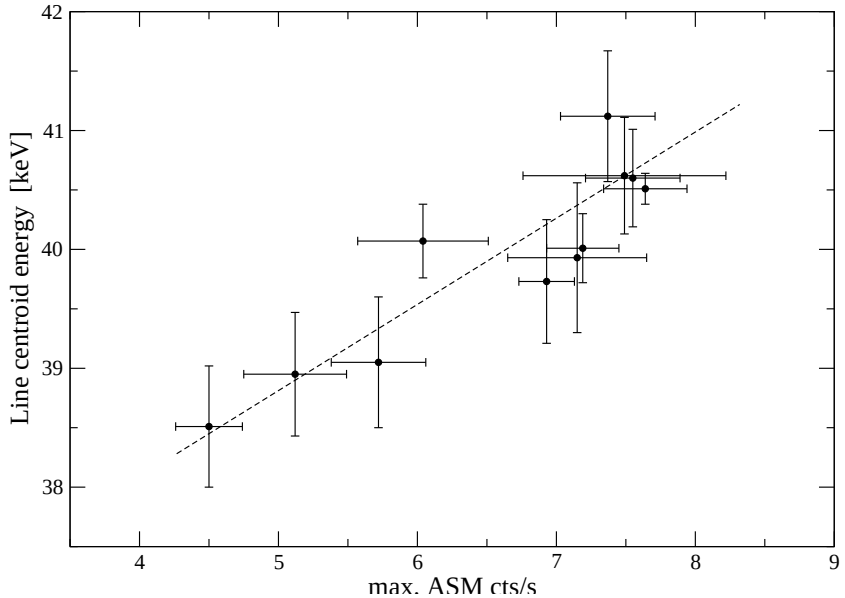

Figure 7.3: Correlation between the energy of the cyclotron line and the luminosity of Her X-1 from Staubert et al. (2007).

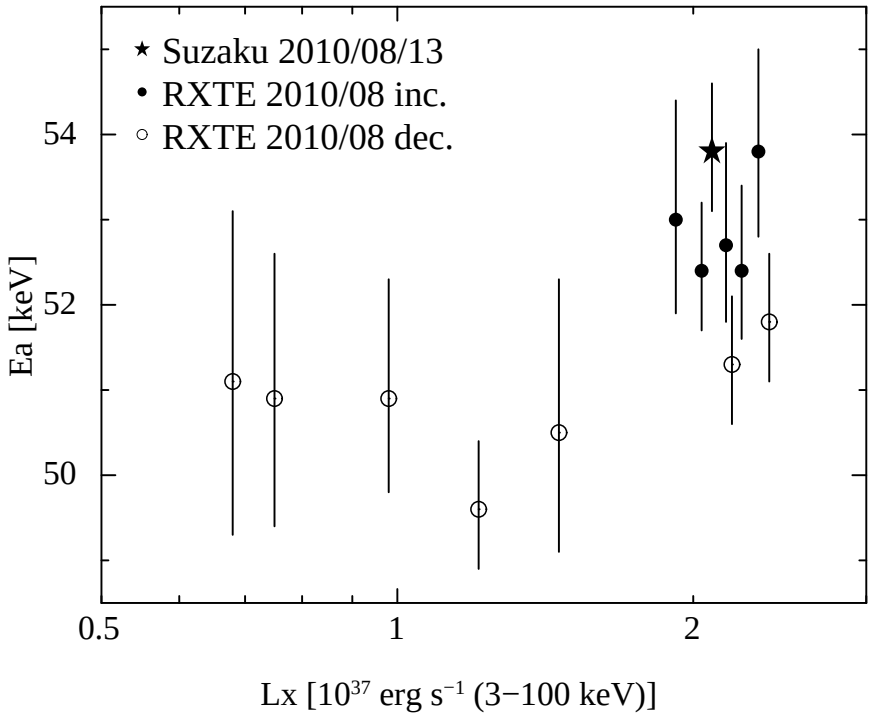

Figure 7.4: Correlation between the energy of the cyclotron line and the luminosity of GX 304-1 from Yamamoto et al. (2011).

a dependance of the cyclotron line energy on the luminosity is still questionable for A0535+26 and Cen X-3 (see e.g. Caballero et al. 2008). On the other hand, only Her X-1 shows a clear positive correlation between the centroid of the cyclotron line and the bolometric luminosity of the source.

Recently, two other sources have been suggested as possible candidates for such a positive correlation: GX 301-2 and GX 304-1. For both sources a marginal indication of a positive luminosity-dependance was claimed by La Barbera et al. (2005), Yamamoto et al. (2011) and Klochkov 2012 (private comm.), but the statistics is not enough to allow a deep spectral analysis as function of the luminosity of the source (see Figure 7.4). In addition, the positive correlation found by Staubert et al. (2007) has been confirmed by Vasco et al. (2011).

7.4 Redetermination of the the cyclotron line / flux correlation in Her X-1

The aim of this work was to question whether the ASM flux is really an accurate measure of the bolometric luminosity of the source and re-determine the positive correlation between the cyclotron line and the luminosity of the source found by Staubert et al. (2007).

As mentioned in Chapter 4, Her X-1 has been repeatedly observed by *RXTE* since 1996. Using *RXTE* observations of eleven 35 day Main-Ons with photon statistics of sufficient high quality to allow a spectral analysis have been analyzed. Those cycles (nos.) 257, 269, 303, 304, 307, 308, 320, 323, 324, 343 and 351 (cycle no. 313 was not included, despite the high quality statistics, because no ASM observations were available). For the definition of cycle counting we refer to Staubert et al. (2009b). All of these observations cover a period of ten years from July 1996 (cycle number 257) to July 2005 (cycle number 351) as shown in Table 7.2.

Table 7.2: Details of *RXTE* observations of Her X-1 used for the spectral analysis.

Observation month/year	35 day Main-On cycle number [1]	Center MJD
July 96	257	50290.75
September 97	269	50707.06
December 00	303	51897.69
January 01	304	51933.67
May 01	307	52035.48
June 01	308	52071.16
August 02	320	52492.96
November 02	323	52599.32
December 02	324	52634.01
October 04	343	53300.95
July 05	351	53577.35

[1] Cycle numbering according to Staubert et al. (2009a).

7.4.1 Spectral analysis

For this work data from both *RXTE* instruments were used. In particular, data of PCA in the 3.5 – 60 keV energy range, and of HEXTE in the 20 – 75 keV energy range. For the spectral analysis, `XSPEC`[1] (12.6.0) and spectra for all observed Main-Ons, summing all available data were generated. For each spectrum (one for each Main-On), two quantities were determined: the central energy $E_{\rm cyc}$ of the cyclotron absorption feature (pulse phase averaged) and the integrated flux in the range 3.5 – 60 keV (in units of erg cm^{-2} s^{-1}). Also in this case, `standard_2f` data products were used with some initial conditions (see section 5.3.1). The time in minutes after the SAA which takes into account a possible influence to the data because of the presence of radioactivity produced in the detectors at the SAA-passage, was set to 10 minutes (instead of the default value of 30 minutes) and only PCU 2 was used to ensure maximum uniformity in the data set, analyzed in a uniform way. In particular only the top layer of this detector was taken into account. This condition permits to avoid any problem with background particles generated inside the detector and with the re-normalization needed because of the different combination of PCUs switched on during the observations (see section 5.3.1).

To fit the data, the `highecut`[2] model (based on a power-law continuum with an exponential cut-off) and a multiplicative *Gaussian* absorption line for the cyclotron resonant scattering feature (CRSF) has been used. The model was used in previous analyses on the same object, such as Coburn et al. (2002) and Staubert et al. (2007).

In the spectral analysis, both the iron line feature and cold material absorption were taken into account in each fit. In particular, the iron line was fitted with a Gaussian and all values of the absorption were consistent to within two standard deviations with the mean value of $N_H = 1.08 \times 10^{22}\,\mathrm{cm}^{-2}$.

The goal of this work was to compare these results with those of Staubert et al. (2007). This consists in a re-determination of the cyclotron line (an "update") and of the flux of the source to estimate the bolometric luminosity. Because of this, a uniform analysis was performed with slight differences to the original one. In particular, in the original analysis PCA data were used only up to 25 keV to define the continuum at the lower energies. New response matrices are now available[3] that allow to use the PCA up to ∼50 keV. But the PCA instrument can in fact be used up to 60 keV to contribute information about the cyclotron line around 40 keV. This choice is confirmed by the agreement between the PCA and HEXTE spectra in the overlapping region of the two instruments (40 – 60 keV). This is also confirmed in the analysis by Rothschild et al. (2011) of RXTE observations of Cen A in which PCA data were successfully used up to 60 keV. A second difference is related to the uncertainties. In this work uncertainties of 0.5% (which are recommended for use with the new response matrices[2]) were added, while in the original analysis by Staubert et al. (2007) 1% uncertainty was taken into account.

Figure 7.5 shows an example of a spectral fit to data of July 1996 (cycle no. 257). The observation is centered at MJD 50290.75 and the total integration time is 31 ks for PCA/PCU2 and 10 ks for each of the two HEXTE clusters.

The maximum X-ray flux of Her X-1 varies as a function of 35 days phase because of variable absorption by the accretion disk. To take into account this variation, the bolometric flux for the

[1] http://heasarc.gsfc.nasa.gov/docs/xanadu/xspec/
[2] http://heasarc.gsfc.nasa.gov/docs/xanadu/xspec/manual/XSmodelHighecut.html
[3] http://www.universe.nasa.gov/xrays/programs/rxte/pca/doc/rmf/pcarmf-11.7/

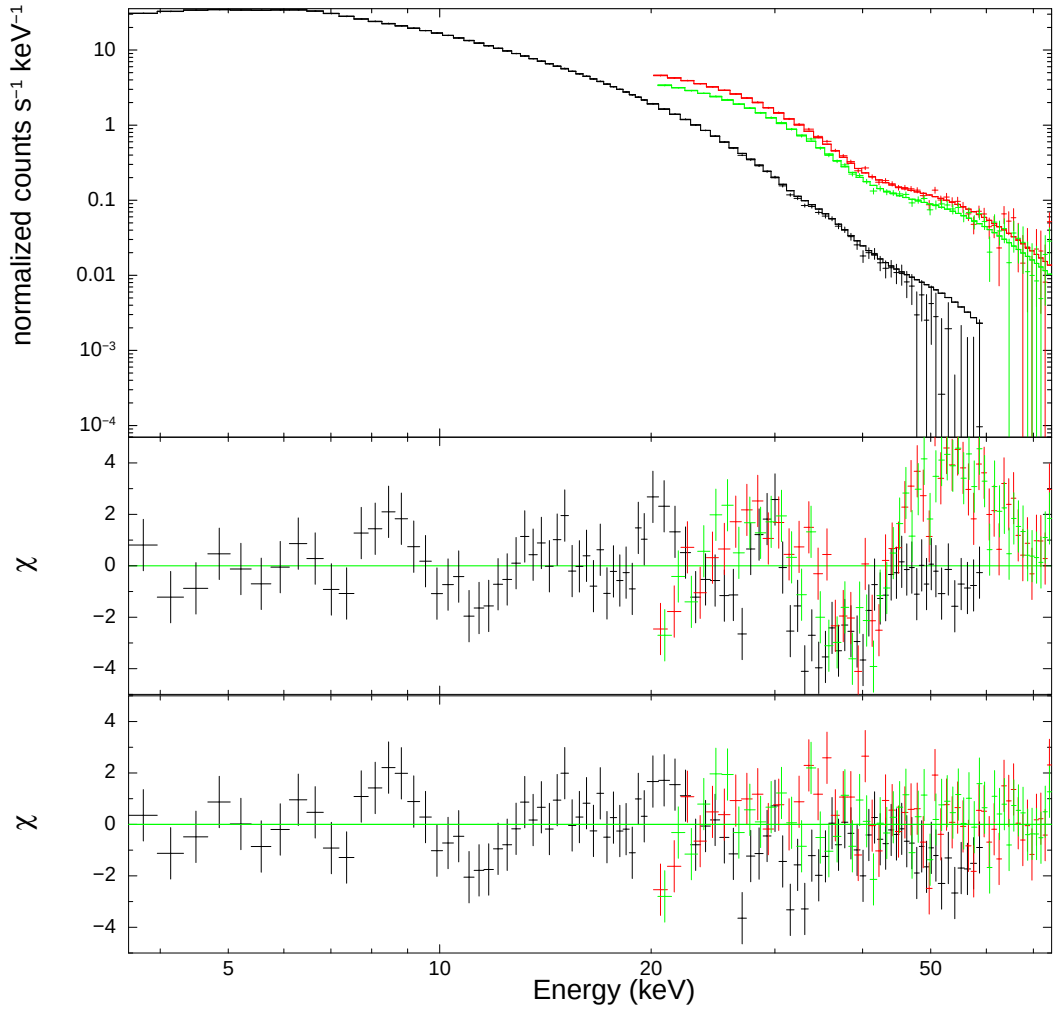

Figure 7.5: Example of a spectral fit to an *RXTE* observation of Her X-1 in July 1996 (cycle no. 257). The observation is centered at MJD 50290.75 and the integration time is 31 ks for PCA and 10 ks for each of the two HEXTE clusters. Black: PCA, red: HEXTE-A, and green: HEXTE-B, respectively; *top*: count rate spectra; *middle*: residuals with respect to a fit of a continuum model; *bottom*: residuals with respect to a fit which includes a cyclotron line.

individual spectra was found by integrating the fit function (over the 3.5 – 60 keV range), using the `XSPEC` routine `flux`[4]. This is the main difference between this analysis and the original one by Staubert et al. (2007). In that case, the ASM maximum flux is taken as a measurement of the bolometric luminosity of the source. The choice to use the ASM maximum flux is based on two reasons: (1) physically, the maximum of the ASM flux is believed to represent the bolometric luminosity of the source because it corresponds to the configuration in which no accretion disk

[4] http://heasarc.gsfc.nasa.gov/xanadu/xspec/manual/XSflux.html

(or a very small part of it) covers the X-ray emission region of the neutron star; (2) the maximum of the ASM flux is the easiest feature to recognize and consequently to use as a reference.

The sampling of the various Main-Ons in groups of pointed observations was rather different from one Main-On to the next, and the fluxes determined from the spectra are mean values of the observations, which happened to be made at different phases of the 35 day modulation. These fluxes cannot directly be compared to the *maximum X-ray flux* of the respective Main-On. To find the comparable bolometric fluxes in the 3.5 – 60 keV range that represent the *maximum flux* for the particular cycle, it was necessary to scale the fluxes found in the individual spectra to the *maximum flux*. The scaling factor is the ratio of the *maximum flux* to the mean flux used to generate the spectra. To find the *maximum flux*, all observed *RXTE*/PCA light curves were fitted by a function representing a template of the mean 35 day Main-On modulation, the shape of which was taken from an overlay of many 35 day light curves observed by *RXTE*/ASM (see e.g. Klochkov et al. 2006). For this procedure, we are only interested in the overall 35 day modulation, that is without eclipses and dips, which is described by the analytical function:

$$f(t) = A_0 \left(1 - \frac{A_1}{1 + \exp\left(B_1(t - C_1)\right)}\right) \frac{1}{1 + \exp\left(B_2(t - C_2)\right)},$$

under the condition that negative functional values are set to zero. Here $f(t)$ is the flux as a function of time t in MJD, A_0 is the amplitude in units of (3 – 20 keV) PCA cts s^{-1} per PCU, A_1=1.25, B_1=1.87, and B_2=0.80 are fixed functional parameters, C_1 is the time reference in MJD, and C_2=C_1+8.4 d is the offset that represents the length of the standard Main-On. The time of reference C_1 was fixed to the MJD of the turn-on that had been determined from the corresponding ASM light curve. The *amplitude* A_0 is the only free fitting parameter. The maximum of the fitting function (on average found to be equal to A_0-5.4 cts s^{-1}) is then taken as the *maximum flux* (in units of PCA cts s^{-1}) for this cycle. Dividing this *maximum flux* by the corresponding mean flux from all the photons that are also used in generating the corresponding spectrum leads to a scaling factor. Multiplying the 3.5 – 60 keV flux found from the spectra by this scaling factor then leads to the *maximum bolometric flux* (in units of erg cm^{-2} s^{-1}). These bolometric flux values can now be compared to the *maximum ASM flux* values used in the earlier work by Staubert et al. (2007).

To test whether the above procedure in determining the maximum bolometric fluxes could be influenced by systematic changes of the spectral shape over the 35 day phase, we have investigated spectra of cycle no. 323 which provides a good coverage of a complete Main-On. Systematic changes were only found in one spectral parameter, the power-law index, with a magnitude of ±3%, which corresponds to a negligible relative change of the integrated flux of less than 5×10^{-2}%.

The uncertainties in the bolometric flux values are dominated by the uncertainties in the scaling factors, which in turn are dominated by systematic uncertainties in determining the maximum Main-On flux in fitting the observed light curve by the common analytical function. These systematic uncertainties are estimated to be 3%, the main contributions being the uncertainty in the turn-on time and the fluctuations in the shape of the modulation from cycle to cycle.

Table 7.3 compares the results of this re-analysis (Vasco et al. 2011) to those of the original analysis by Staubert et al. (2007).

Table 7.3: Phase-averaged cyclotron line energies $E_{\rm cyc}$ and *maximum fluxes* reproduced from Staubert et al. (2007) (1) and from the spectral re-analysis of this work (2) (Vasco et al. 2011).

35 day cycle number[1]	$E_{\rm cyc}(1)$ [keV]	*max. flux* (2 – 10 keV) ASM [cts s^{-1}]	$E_{\rm cyc}(2)$ [keV]	*max. flux* (3.5 – 60 keV) [2] [10^{-9} erg cm^{-2} s^{-1}]
257	41.12 ± 0.55	7.37 ± 0.34	40.61 ± 0.34	7.99 ± 0.45
269	40.62 ± 0.49	7.49 ± 0.73	40.45 ± 0.41	8.02 ± 0.46
303	40.07 ± 0.31	6.04 ± 0.47	39.81 ± 0.24	7.27 ± 0.41
304	39.05 ± 0.55	5.72 ± 0.34	38.72 ± 0.31	7.14 ± 0.40
307	39.93 ± 0.63	7.15 ± 0.50	39.78 ± 0.49	8.26 ± 0.47
308	39.73 ± 0.52	6.93 ± 0.20	40.04 ± 0.33	8.18 ± 0.46
320	40.01 ± 0.29	7.19 ± 0.26	39.94 ± 0.29	9.55 ± 0.36
323	40.51 ± 0.13	7.64 ± 0.30	40.16 ± 0.11	9.37 ± 0.44
324	40.60 ± 0.41	7.55 ± 0.34	40.37 ± 0.35	9.16 ± 0.52
343	38.51 ± 0.51	4.50 ± 0.24	38.26 ± 0.43	7.05 ± 0.40
351	38.95 ± 0.52	5.12 ± 0.37	39.28 ± 0.60	6.61 ± 0.38

[1] Note that for 35 day cycle numbers 303 and larger the corresponding numbers in Staubert et al. (2007) are larger by 1. This reflects the observation that there must have been an extra cycle during the long *anomalous low* before cycle 303. However, using the numbers as given here allows to use them in an ephemeris for a rough prediction of the 35 day turn-ons using a mean period of 35.88 d. We do not doubt the physical reality of the extra cycle found by Staubert et al. (2009a).
[2] The flux in Col. 5 represents the 35 day *maximum flux* in the 3.5 – 60 keV range (see text).

7.5 The "new" correlation between the luminosity and the centroid of the cyclotron line

In Figure 7.6, the newly determined cyclotron line energies are plotted against those from the original analysis. Overall, there is very good agreement between the new values for $E_{\rm cyc}$ and those from the original analysis: considering the respective uncertainties, the differences are smaller than 0.79 standard deviations for ten of the eleven values and 2.1 standard deviations for one value (cycle number 323).

In Figure 7.7, the 3.5 – 60 keV maximum bolometric fluxes are plotted against the corresponding ASM fluxes of the original analysis.

There is a good linear relationship between the two fluxes: the slope (taking the uncertainties in both variables into account) is 0.88±0.15 (10^{-9} erg cm^{-2} s^{-1}) / (ASM cts s^{-1}), and the Pearson correlation coefficient is 0.82, corresponding to a chance probability of no correlation of $P < 10^{-3}$. This demonstrates that the *maximum ASM flux* can be taken as a good measure of the *maximum bolometric X-ray flux* (and luminosity) of Her X-1 during the respective 35 day cycle. The variation in flux from one 35 day cycle to the next is small, such that the maximum observed flux of a particular 35 day Main-On can be considered a good measure of the luminosity of the source during this particular cycle. Because of this, the maximum ASM flux was used as a reference in

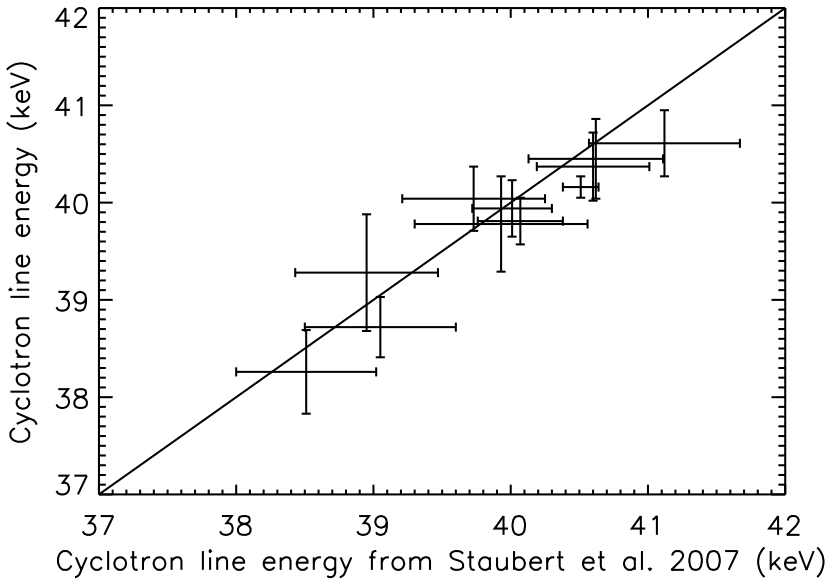

Figure 7.6: $E_{\rm cyc}$ from the spectral re-analysis (Vasco et al. 2011) versus $\rm E_{cyc}$ from the original analysis (Staubert et al. 2007). The Pearson correlation coefficients are 0.95.

the original analysis by Staubert et al. (2007).

With the newly determined values of both the cyclotron line and the flux, it is possible to reconstruct the final correlation between the cyclotron line energy and the X-ray flux. This is given in Figures 7.8 and 7.9 in two ways: we correlate $E_{\rm cyc}$ from the re-analysis with the *scaled 3.5 – 60 keV maximum Main-On flux* (Figure 7.8), as well as the *maximum ASM flux* (Figure 7.9). The corresponding slopes of the linear fits to these data (taking the uncertainties of both variables into account) and the corresponding Pearson correlation coefficients r are: (i) for the Main-On flux presented in Figure 7.8 slope = 0.62±0.19 (keV)/(10^{-9} erg cm^{-2} s^{-1}) and r = 0.62 (P=2×10^{-2}); (ii) for the maximum ASM flux presented in Figure 7.9 slope = 0.67±0.14 (keV)/(ASM cts s^{-1}) and r = 0.90 (P=10^{-4}).

The correlation seen in Figure 7.8 is somewhat less convincing than that of Figure 7.9 (and that in the original analysis of Staubert et al. 2007). This is attributed to the unavoidably larger uncertainties associated mainly with the scaling of the bolometric flux measured for the individual spectrum to the flux that does describe the maximum flux of the particular 35 day cycle. The originally used maximum ASM fluxes are, in contrast, simple direct measurements.

From this analysis, it is possible to conclude that the maximum ASM flux used in the original analysis (Staubert et al. 2007) can really be taken as a measure of the luminosity of the source because it scales well with the maximum 3.5 – 60 keV flux estimated through the spectral analysis. This is evident from Figure 7.7 that shows that there is a good linear relationship between the bolometric 3.5 – 60 keV flux with the 2 – 10 keV flux measured by *RXTE*/ASM (both fluxes refer to the *maximum 35 day Main-On flux*).

The information contained in Figures 7.6, 7.7, 7.8 and 7.9 provide an internally consistent

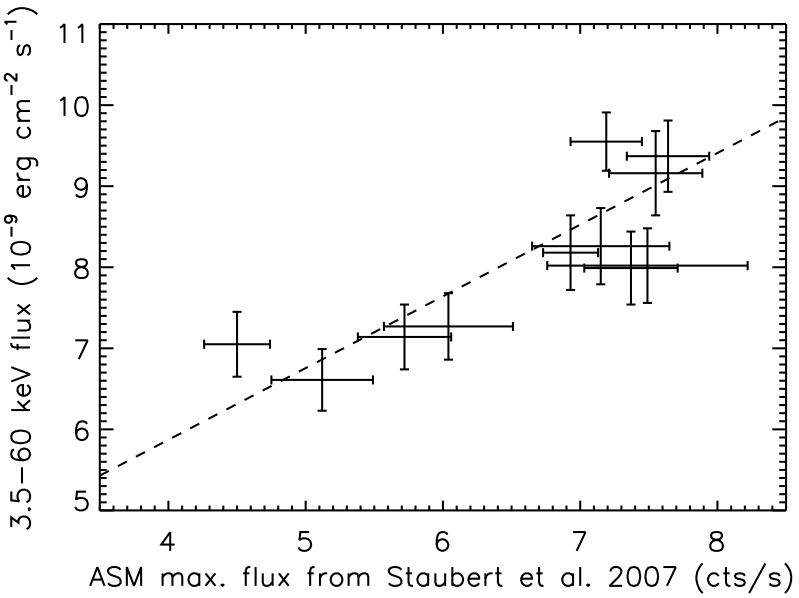

Figure 7.7: Scaled maximum 3.5 – 60 keV flux (in units of 10^{-9} erg cm^{-2} s^{-1}) from the spectral re-analysis versus the maximum 2 – 10 keV ASM flux (in units of cts s^{-1}) from the original analysis. The Pearson correlation coefficients are 0.82.

picture. Considering the combined evidence of all the correlations shown before, the correctness of the positive correlation between the cyclotron line energy and source luminosity as suggested in Staubert et al. (2007) is not questionable. A direct comparison to the original analysis can be made by considering Figure 7.9: the slope of the linear best fit is determined to (0.67 ± 0.14) keV/(cts s^{-1}), which is in good agreement with the (0.66 ± 0.10) keV/(cts s^{-1}) found in the original analysis. The final and confirmed result with respect to this correlation can then be stated as follows: *the value of the cyclotron line energy $E_{\rm cyc}$ increases by ∼7% for a change in flux of a factor of two.*

This is consistent with the physics described in section 2.3 and with the recent analysis of Klochkov et al. (2011) which supports the physical correlation between the cyclotron line energy and the luminosity of three sources: 4U 0115+63, V 0332+53, and Her X-1. In this analysis data from a short time interval were used, and spectra were generated by summing up photons belonging to individual pulses in selected ranges of pulse amplitude. In this *pulse-to-pulse variability* study, the variations in X-ray flux (source luminosity) occur on timescales comparable to the duration of the individual pulses (the period of rotation of the neutron star). The previously found correlations (based on flux variations on much longer timescales) between the cyclotron line energy and the X-ray flux are reproduced: that is a *negative* correlation for the super-Eddington transient sources 4U 0115+63 and V 0332+53, and a *positive* correlation for the sub-Eddington source Her X-1.

Up to now, there is not a theoretical model which describes in details the physical background needed to explain the transition between the two regimes or to model the geometry of the accretion

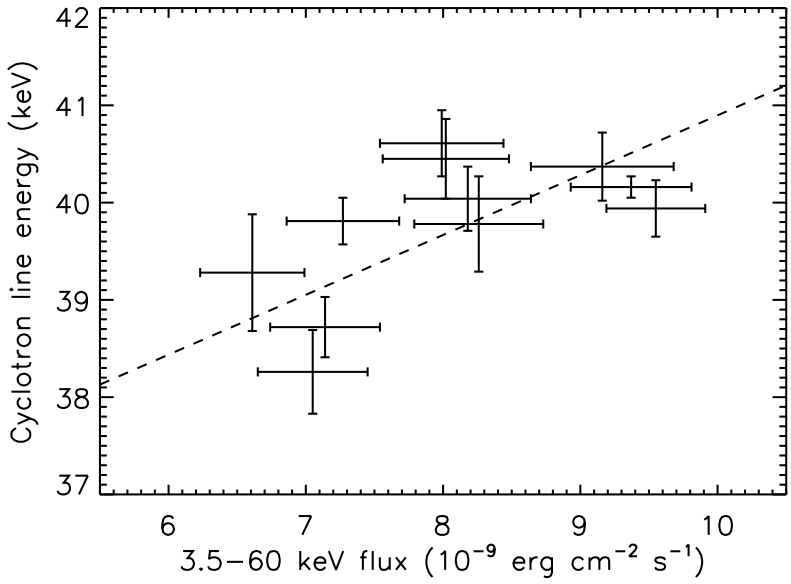

Figure 7.8: $E_{\rm cyc}$ from the spectral re-analysis (Vasco et al. 2011) versus the scaled maximum 3.5 – 60 keV flux (in units of 10^{-9} erg cm^{-2} s^{-1}).

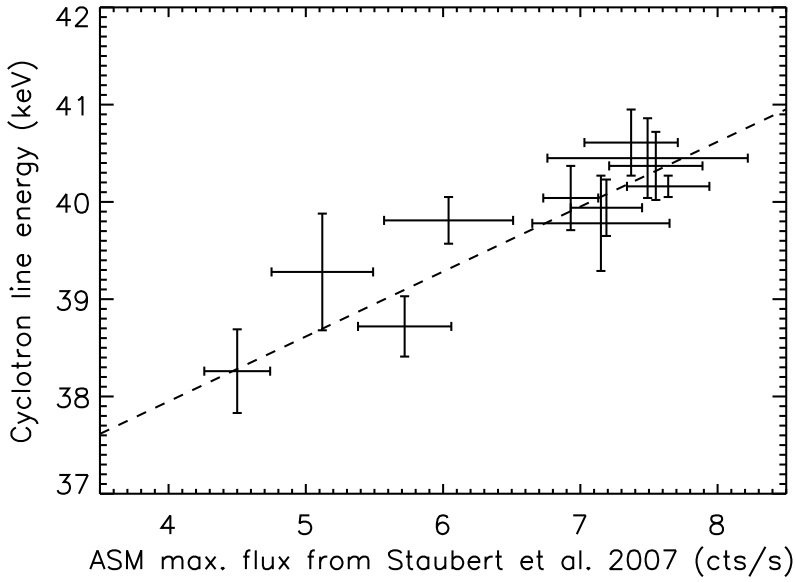

Figure 7.9: $E_{\rm cyc}$ from the spectral re-analysis versus the maximum 2 – 10 keV ASM flux (in units of cts s^{-1}) from the original analysis.

column which is responsible for the mechanisms involved. Despite this fact, several models have been proposed. This is the case of the self consistent model of binary pulsar emission suggested by Becker & Wolff (2007). In Ferrigno et al. (2009) this model was applied to 4U 0115+63 successfully. The high energy emission related to the pulse profile peak is produced by thermal and bulk Comptonization of the cyclotron emission. This represents the main channel for the cooling of the accretion column. For lower energies an extended halo formed by the continuum is due to thermal Comptonization of black body radiation. This leads to a quite complicated picture in which the photons are generated by cyclotron cooling above the surface of the neutron star and then scattered by electrons in the accretion column. In this configuration, the radiation leaves the column laterally, from the walls of the column, close to the neutron star surface.

8 Spectral analysis of Her X-1

This chapter summarizes the results related to the spectral analysis of Her X-1. The X-ray spectrum of the source has been studied using data of *RXTE* observations. In particular, thanks to the good spectral resolution, it has been possible to analyze the evolution of the individual spectral parameters as function of the 35 day phase. Due to the complex picture about the iron line and the column density in the X-ray spectrum of the source, a deeper study of these two components is also presented in this chapter.

8.1 The X-ray spectrum of pulsars

As reported by White et al. (1983), spectra of X-ray pulsars are described by different components. Some of these components, such as the cyclotron line, depend on the source, but most of them are common to all X-ray pulsars and can be used to model the X-ray spectrum of these sources. These components are:

1. a black body type thermal emission at very low energies;
2. cold material absorption at low energies;
3. a power law with index Γ at low energies;
4. an exponential cutoff E_{cut} at higher energies;
5. an iron line emission feature between 6 and 7 keV;
6. other absorption/emission line-like features (e.g. cyclotron lines).

These are the components normally needed to fit the data and to obtain a good value of χ^2 performing a spectral analysis. Sometimes, additional absorption or emission line-like features to take into account noise generated by the instruments have to be added. Early examples of fitted X-ray spectra of X-ray pulsars can be found in e.g. Pravdo et al. (1977a), Pravdo et al. (1977b), Pravdo et al. (1978), Pravdo et al. (1979), Swank et al. (1976) and Becker et al. (1976). From these analysis, it is clear how almost all these feature are model-independent, except of narrow line-like features which can be influenced by the model adopted. Normally, the power law index Γ ranges between $0.8 \lesssim \Gamma \lesssim 1.5$, the high energy cutoff E_{cut} between $10-30\,\mathrm{keV}$ and the folding energy E_{fold} between $10-40\,\mathrm{keV}$, respectively (Nagase 1989 and White et al. 1983). These values are common for a standard X-ray spectrum of a pulsar, but some sources exhibit different spectral parameters. This is the case, for example, of X Per which shows a softer spectrum characterized by a lower value of Γ (White et al. 1983) or 1E $2259+586$ with an extremely hard spectrum described by $\Gamma \approx 3.7$ (Koyama et al. 1987). In Figure 8.1 some example of X-ray spectra of pulsars are shown.

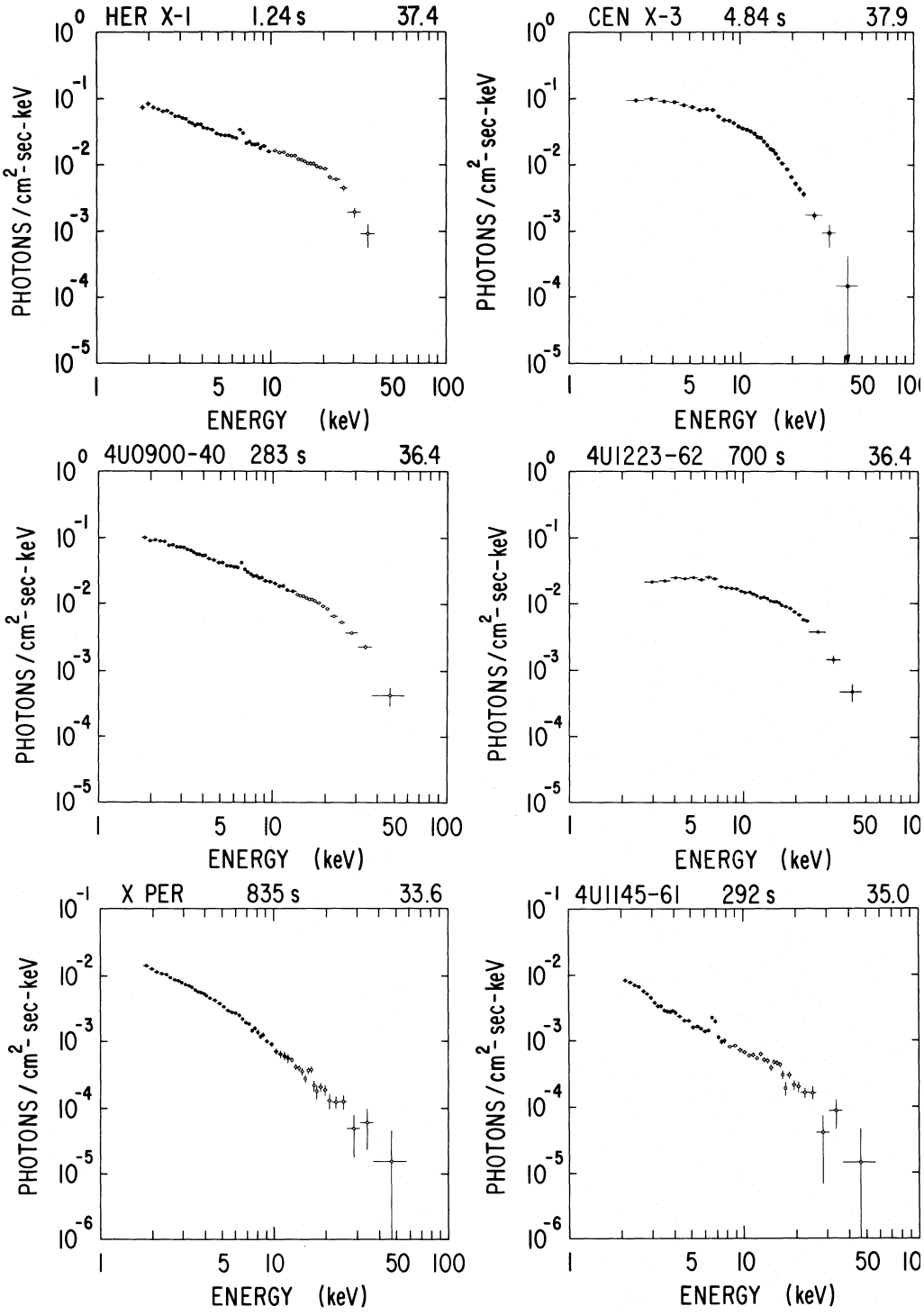

Figure 8.1: Phase-averaged spectra of X-ray pulsars from White et al. (1983).

A recent study of the continuum formation for X-ray pulsars has been proposed by Becker & Wolff (2007). This model was successfully applied to Her X-1, Cen X-3 and LMC X-4. As shown in Figure 8.2, in the accretion column a radiation dominated shock is formed and the photons are emitted at the base of the column as black body radiation as well as in the column as bremsstrahlung or cyclotron emission. Generally, bulk Comptonization dominates the transfer of energy from the gas to the photons. On the other hand, thermal Comptonization is responsible for the transfer of energy from high to low energy photons. This explains both the flattering of the X-ray spectrum at low energies and the cutoff at higher energies.

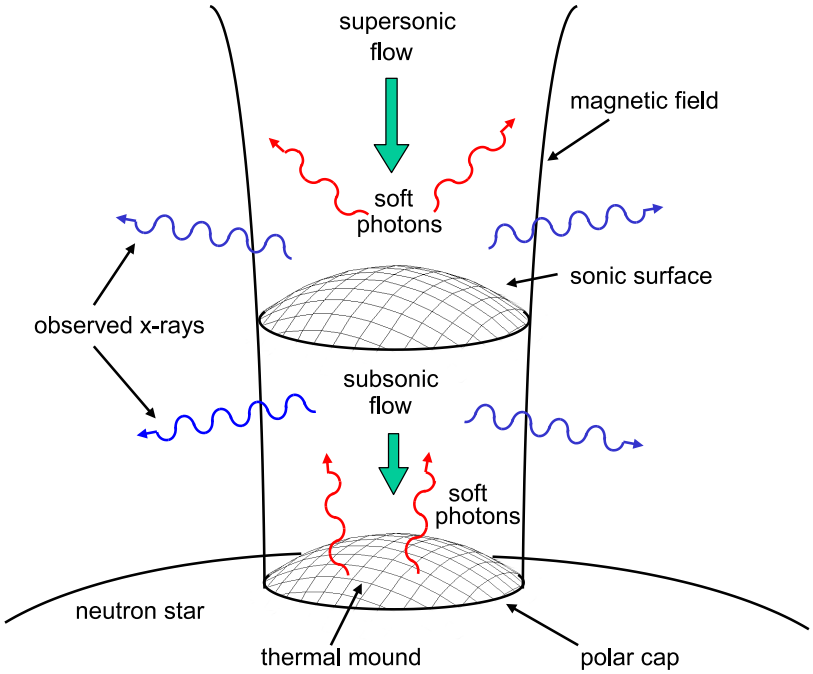

Figure 8.2: Sketch of the accretion column for neutron stars in the model proposed by Becker & Wolff (2007).

One has to mention that the spectral functions used for the fitting process are only mathematical functions without a physical meaning. Over the years, some models based on physical assumptions have been proposed. This is the case for `comptt` or `diskbb`[1] (and some other used) to try to model Comptonization of soft photons in a hot plasma or an accretion disk consisting of multiple blackbody components, e.g. Titarchuk (1994) and Mitsuda et al. (1984) respectively.

[1]For details see the `XSPEC` manual at http://heasarc.nasa.gov/xanadu/xspec/manual/Additive.html and references therein.

8.2 The X-ray spectrum of Her X-1

The X-ray spectrum of Her X-1 has the shape of a typical X-ray spectrum of an accreting binary pulsar described in the previous section, and can be modeled by the following components: (1) a thermal blackbody emission with $kT_{BB} \approx 0.1$ keV (E < 1 keV) which dominates completely the X-ray spectrum at very low energies; (2) a power law with a photon-index $\Gamma \approx 0.95$-1.0 up to 10 keV; (3) a folding energy $E_{fold} \approx 10$ keV and a drop in the X-ray flux after the cutoff energy $E_{cut} \simeq 20$ keV; (4) an emission feature corresponding to the iron line at energy $E_{Fe} \sim 6.5$ keV; (5) and a cyclotron resonant scattering feature (CRSF) with energy $E_{cyc} \sim 40$ keV. Usually, cold matter absorption is also taken into account for the fitting process.

Coburn et al. (2002) have analized the X-ray spectrum of Her X-1 with *RXTE* observations using only data corresponding to the peak of Main-On states and rejecting those observations corresponding to dips and eclipses. The spectral parameters obtained through this analysis are listed in Table 8.1 and a typical X-ray spectrum of Her X-1 is shown in Figure 8.3.

Table 8.1: Spectral parameters of Her X-1 from Coburn et al. (2002).

Γ	E_{cut}	E_{fold}	E_{cyc}
$0.93^{+0.01}_{-0.02}$	$22.0^{+1.4}_{-0.8}$	$10.8^{+0.2}_{-0.3}$	$40.4^{0.8}_{-0.3}$

These values agree with previous analyses (e.g. Gruber et al. 2001) made on the same observations. Coburn et al. (2002) also claimed that there is no evidence for a second harmonic for the cyclotron line around 80 KeV as suggested by *Beppo-SAX* and *Suzaku* observation and the presence of a small deviation about 8% in the residuals close to 10 keV as shown in Figure 8.3, which influences the final χ^2, but not the values of the spectral parameters found by the fit. The "10 keV feature" is not only seen in Her X-1, but it seems to be a common feature of X-ray spectra of accreting pulsars.

Thanks to the huge collection of Her X-1 data, spectral analyses of this object have been done with different instruments providing a very good spectral statistics of the source in both high- and low-states. Taking into account the individual components of the X-ray spectrum of Her X-1, it was attempted to describe the physical meaning of each component and their evolution with time.

The blackbody thermal emission was observed for the first time by Shulman et al. (1975). This has been interpreted as matter which gravitates near the magnetosphere of the neutron star or as thermal emission coming from the the inner part of the accretion disk. This was confirmed in several analyses over the years: e.g. McCray et al. (1982); Dal Fiume et al. (1998); Endo et al. (2000). Oosterbroek et al. (1997) suggested that the blackbody emission is originated in the same region as the iron line component. This is suggested by the fact that for this feature a strong correlation is observed with pulse phase with the same flux observed for the blackbody emission. The cutoff around 20 keV is very well described in the analysis of Coburn et al. (2002), however none of the models suggested over the years could explain the dropping in flux. Finally, the cyclotron scattering resonant feature has been discovered by Trümper et al. (1978) (see discussion in Chapter 7).

Usually, spectral parameters show a variation as function of time. For Her X-1, this modulation

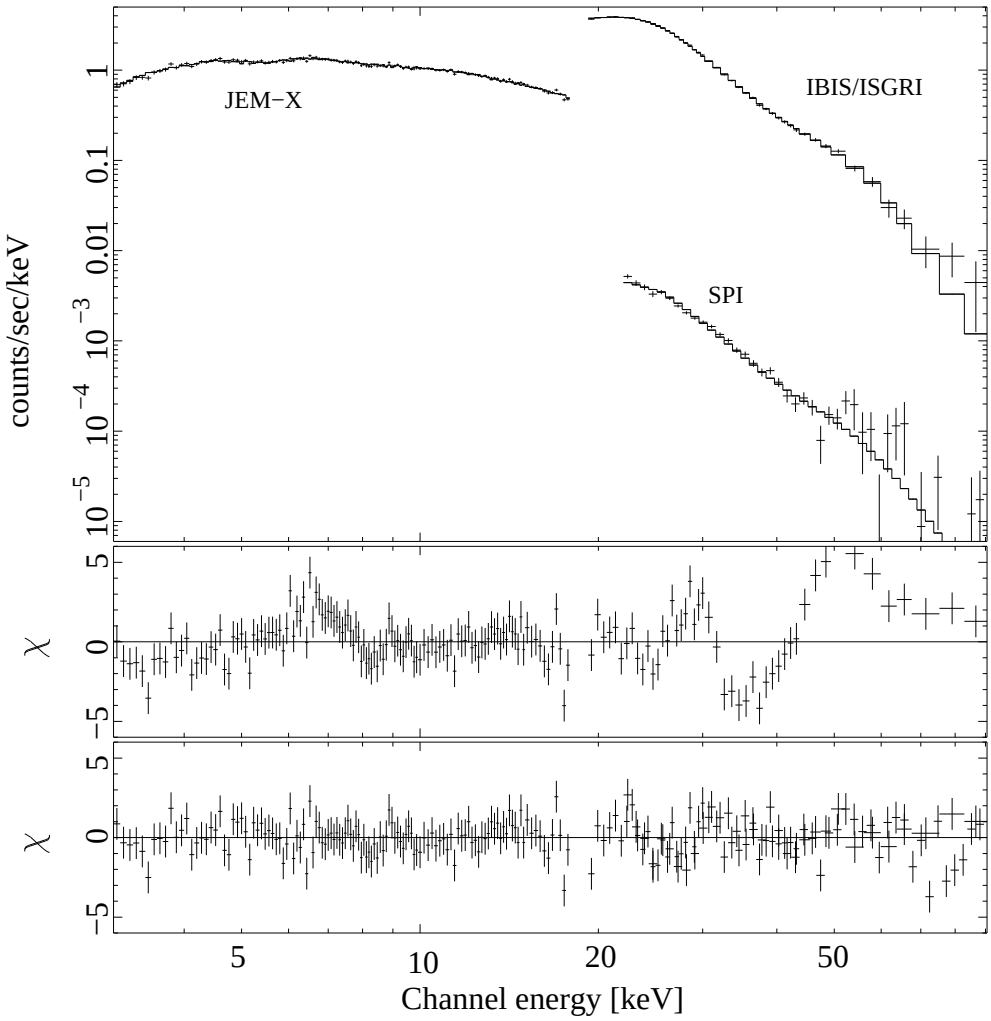

Figure 8.3: *RXTE* Phase-averaged spectra of Her X-1 from Klochkov et al. (2008).

has been observed as function of the 35 day phase. This variation of the spectral parameters was explained as the influence of the corona and the accretion disk on the X-ray spectrum of the source. Changes of spectral parameters are normally observed during the dips where the absorption N_H is higher and the photon-index Γ is drastically reduced.

For the spectral analysis, to model the X-ray spectrum of Her X-1, the `highecut`[2] model from `XSPEC`[3] was used. This consists of a power law with an exponential cutoff as described by the following formula:

$$I_{cont} = I_{1\,keV} \cdot \begin{cases} E^{-\Gamma}, & \text{if } E \leq E_{cut} \\ E^{-\Gamma} \cdot \exp\left(\frac{E-E_{cut}}{E_{fold}}\right), & \text{if } E > E_{cut} \end{cases} \tag{8.1}$$

[2]http://heasarc.gsfc.nasa.gov/docs/xanadu/xspec/manual/XSmodelHighecut.html
[3]http://heasarc.nasa.gov/xanadu/xspec/

where E is the energy of the photon, Γ the photon-index, E_{cut} is the energy of the cutoff, and E_{fold} the corresponding folding energy. Equation 8.1 has to be multiplied by a Gaussian component to model the cyclotron line absorption feature around 40 keV and an iron emission line around 6.5 keV has to be added to reproduce the X-ray spectrum of Her X-1. This leads to a final function I_{tot} (in units of photons $\cdot$ cm^{-2} $\cdot$ s^{-1} $\cdot$ keV^{-1}) used to model the X-ray spectrum:

$$I_{tot} = I_{cont} \cdot \exp\left\{-\tau_{cyc} \cdot \exp\left(-\frac{(E-E_{cyc})^2}{2\sigma_{cycl}^2}\right)\right\} + K \cdot \frac{1}{\sqrt{2\pi}\sigma} \cdot \exp\left(-\frac{(E-E_{Fe})^2}{2\sigma_{Fe}^2}\right), \quad (8.2)$$

where E_{cyc}, E_{Fe}, σ_{cyc}, σ_{Fe} are the cyclotron line energy, the iron line energy, the width of the cyclotron line and the width of the iron line, respectively. K is a numerical constant corresponding to the strength of the iron line.

This model permits to compare the results presented in this work with previous analyses such as those by Coburn et al. (2001) and Staubert et al. (2007), but it is not the only one which fit nicely the data leading to a good χ^2 for *RXTE* and *INTEGRAL* observations of Her X-1. For example, Enoto et al. (2008) model the cyclotron line absorption feature multiplying the continuum with a factor e^{-S} where S is the cross section of the cyclotron scattering and is given by a Lorentzian profile:

$$S = \frac{DE^2}{(E-E_a)^2 + W^2} \text{ x } \left(\frac{W}{E_a}\right)^2, \quad (8.3)$$

where E is the energy of the photons, and E_a, D, W are the energy, the depth and the width of the resonance according to Clark et al. (1990) and Makishima et al. (1999).

Note that, due to the different functional form, E_a and E_{cyc} are not directly comparable: E_a is about 1.5 keV lower than E_{cyc} (Makishima et al. 1999).

8.3 Spectral parameters evolution with RXTE data

As mentioned before, spectral parameters can change as function of the time, or in the case of Her X-1, as function of the 35 day phase, contributing information about the behavior of the source. To perform a detailed analysis of the evolution of spectral parameters as function of the 35 day phase, a spectral analysis of small time intervals within the Main-On of cycle 323 has been performed.

The spectral analysis, was made using both PCA and HEXTE (cluster A and B) data. PCA and HEXTE data were used in the 3.5 – 60 keV and 20 – 75 keV energy range, respectively. Also in this case only data from the top layer of PCU2 were used. The initial condition related to the SAA was set to 10 minutes (see section 4.3.1). To fit the data with the model described before, `XSPEC`[4] (12.6.0) was used. A systematic error of 0.5% was added to the PCA data.

After avoiding those observations corresponding to dips in the X-ray light curve of Her X-1, several time intervals were chosen in order to have a complete coverage of the Main-On of cycle 323 and study in details the variation of the spectral parameter as function of the 35 day phase. These interval are listed in Table 8.2 with their start and stop time and the corresponding 35

[4] http://heasarc.gsfc.nasa.gov/docs/xanadu/xspec/

Table 8.2: List of the time intervals within the Main-On of cycle 323 for which the spectral analysis has been performed.

Interval	Start time (MJ)	End time (MJD)	35 day phase
a	52595.145	52595.229	0.010
b	52596.365	52596.414	0.045
c	52596.659	52596.743	0.053
d	52598.046	52598.192	0.093
e	52598.504	52598.719	0.106
f	52598.961	52599.043	0.119
g	52599.790	52599.962	0.143
h	52600.179	52600.294	0.154
i	52600.570	52600.747	0.166
j	52601.525	52601.734	0.193
k	52601.993	52602.143	0.206
l	52602.419	52602.666	0.219
m	52603.101	52603.175	0.238
n	52603.276	52603.328	0.243
o	52603.474	52603.591	0.249

day phase. The latter is estimated taking into account the center of the individual intervals and the observed turn-on for cycle 323 at MJD 52594.8.

8.4 Variation of the spectral parameters as function of the 35 day phase

Using the values of the spectral parameters obtained through this spectral analysis, it was possible to understand whether there are some components such as the photon-index Γ, the cutoff energy E_{cut} and the folding energy E_{fold} show a modulation as function of the 35 day phase. In Figure 8.4 (top panel) it is clear that there is no evidence for a modulation of the cutoff energy E_{cut} and the folding energy E_{fold}. Under the spectral fit conditions "all parameters free", which corresponds to the situation in which there are no fixed parameters in the spectral model used to fit the data, E_{fold} is relatively constant around 10 keV and E_{cut} around 20 keV (see Table 8.3).

In particular the mean value for E_{fold} is 10.22 ± 0.07 and 21.16 ± 0.15 for E_{cut}. It has also been noted a tendency for a slight decrease with 35 day phase in the case of E_{fold}, but the statistics is not good enough to claim it. These values are consistent with previous analyses on Her X-1 (e.g. Coburn et al. 2002, Staubert et al. 2007) and follow the general picture which characterizes X-ray spectra of accreting pulsars reported in section 8.1.

In the case of the photon-index Γ, a clear modulation with 35 day phase is observed: Γ is constant high before phase 0.15 (with a mean value of 0.93 ± 0.01) and constant low (harder spectrum) between phase 0.17 and 0.23 (with a mean value of 0.84 ± 0.01) with some deviation for the last two points. In other words, the spectrum becomes harder for higher 35 day phases

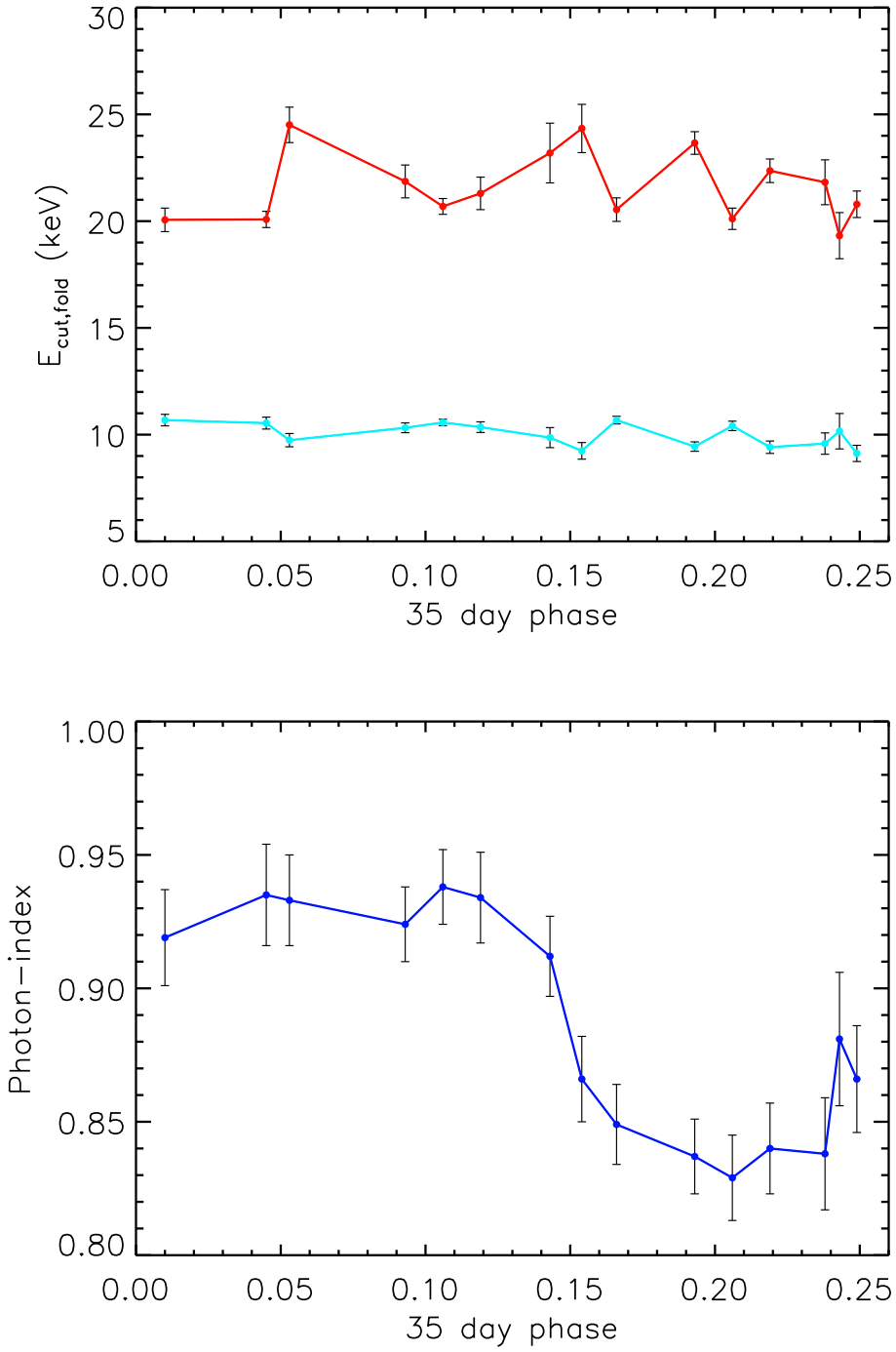

Figure 8.4: Modulation of E_{cut} (red) and E_{fold} (light-blue) in the upper panel, modulation of the photon-index Γ (blue) in the bottom panel.

(after 35 day phase 0.17). This is shown in Figure 8.4 (bottom panel) where the photon-index varies with 35 day phase in a sinusoidal-like shape.

Table 8.3: Spectral parameters values for N_H, Γ, E_{cut} and E_{fold} for cycle 323.

Interval	N_H (10^{22} cm^{-2})	Photon-index Γ	E_{cut} (keV)	E_{fold} (keV)
a	1.14 ± 0.33	0.919 ± 0.018	20.06 ± 0.55	10.68 ± 0.27
b	1.27 ± 0.36	0.935 ± 0.019	20.08 ± 0.38	10.54 ± 0.28
c	0.99 ± 0.33	0.933 ± 0.017	24.51 ± 0.83	9.74 ± 0.31
d	0.93 ± 0.28	0.924 ± 0.014	21.86 ± 0.77	10.32 ± 0.23
e	1.16 ± 0.27	0.938 ± 0.014	20.69 ± 0.37	10.57 ± 0.15
f	1.05 ± 0.31	0.934 ± 0.017	21.30 ± 0.76	10.35 ± 0.25
g	0.143 ± 0.89	0.29 ± 0.912	23.19 ± 1.40	9.86 ± 0.47
h	0.154 ± 0.29	0.29 ± 0.866	24.34 ± 1.13	9.24 ± 0.39
i	0.28 ± 0.29	0.849 ± 0.015	20.54 ± 0.55	10.68 ± 0.18
j	0.14 ± 0.27	0.837 ± 0.014	23.66 ± 0.53	9.44 ± 0.22
k	0.15 ± 0.31	0.829 ± 0.016	20.11 ± 0.50	10.41 ± 0.22
l	0.50 ± 0.31	0.840 ± 0.017	22.36 ± 0.55	9.41 ± 0.29
m	0.42 ± 0.39	0.838 ± 0.021	21.82 ± 1.05	9.58 ± 0.50
n	1.38 ± 0.45	0.881 ± 0.025	19.32 ± 1.08	10.16 ± 0.83
o	1.01± 0.37	0.866 ± 0.020	20.79 ± 0.62	9.12 ± 0.38

8.5 The iron line feature

Another spectral parameter which has been studied as function of the 35 day phase is the iron line intensity.

The presence of an iron emission line in the X-ray spectrum is a common feature for X-ray pulsars. This is associated to fluorescence produced by iron ions and has been observed for many objects (see e.g. Nagase 1989).

For Her X-1, the iron line feature has been detected by several instruments. An iron line complex was clearly detected at ∼6.5 keV (Leahy 2001 and references therein). Furthermore, Endo et al. (2000) with *ASCA* observations resolved this feature into two different components at ∼ 6.4 and ∼6.7 keV. Then, Zane et al. (2004) reported the detection of a distinct component around 7 keV with *XMM-Newton* observations.

The fluorescent iron line is produced when a K- or L-shell electron of an iron atom is ejected following photoelectric absorption of an X-ray. This happens in binary systems where a fraction of the X-ray emission is absorbed by plasma which surrounds the compact source, the photosphere of the companion star and the outer layer of the accretion disk. X-ray photons are absorbed in these regions of gas through photoeffect primarily on K-electrons and consequently a fluorescent photon can be emitted (Basko 1978). Depending on the transition, the photons are classified as follows. When the transition occurs from the $n = 2$ to $n = 1$ levels, 6.4 keV $K\alpha$ photons are

produced. When the transition is between the $n = 3$ and the $n = 1$ levels, 7 keV $K\beta$ photons are produced. On the other hand, transitions to the $n = 2$ or L-shell are designated as $L\alpha$ ($n = 3$ to $n = 2$) and $L\beta$ ($n = 4$ to $n = 2$). In particular:

$$K_\alpha : L \rightarrow K;\ K_\beta : M \rightarrow K;\ L_\alpha : M \rightarrow L;\ L_\beta : N \rightarrow L. \tag{8.4}$$

There are two contributions to this phenomenon. The main one is due to the reflection or backscattering of photons when the X-ray beam illuminates the accretion disk or the plasma in the vicinity of compact objects. The second one, much weaker, is due to the scattering with the medium in the direction of the observer.

In Her X-1 the iron line feature was discovered for the first time by Pravdo et al. (1977a). Using the *GSFC X-ray spectroscopy experiment (CXS)* on-board *OSO-8*, a double structured emission feature in all the high-state spectra near the $K\alpha$ iron line energy was detected. The latter was attributed to fluorescence originated in an opaque region at the Alfvén radius. One year later, Pravdo et al. (1978) found the same feature also in the low-state with *HEAO-1*.

Up to now it is not entirely clear where this feature originates. For Her X-1, the production of the iron line has been associated to different sites (Choi et al. 1994):

- the outer edge of the accretion disk extended in the vertical direction;
- a corona of the accretion disk;
- the atmosphere of the companion star;
- a surface at the Alfvén radius.

Pravdo et al. (1977a) excluded the hypothesis of the companion atmosphere because of geometrical reasons. For a neutron star, the solid angle subtended is too small to explain the equivalent width of the iron line observed during the Main-on ($\sim$0.2 keV). This was also confirmed by Basko (1978) and Bai (1980). On the other hand, it is difficult to distinguish whether this fluorescence originates in the disk edge or at the Alfvén surface because all the suggestions proposed in previous studies are based on different data sets. For example, the accretion disk site was suggested by Bai (1980) and Mihara et al. (1991) with observations of the low-state. Instead, the Alfvén surface site was suggested using observations of the Main-On state. One has also to take into account that there could be a change in the site of the production as function of the 35 day phase. This would explain the change in the intensity over the 35 day super-orbital period reported by Choi et al. (1994): the iron line intensity is typically smaller during the Short-on of a factor of 10% with respect to the Main-On.

Choi et al. (1994) has also suggested that a contribution to the Fe $K\alpha$ may come from cold material associated to a disk wind as observed for cataclysmic variables by Drew (1997). This could be the case also for Her X-1 (Zane et al. 2004) since a possible wind material from the companion star has been reported by Anderson et al. (1999) and Boroson et al. (2001).

Zane et al. (2004), improving a previous analysis by Ramsay et al. (2002), studied the variation of the iron line as function of the 35 day phase with *XMM-Newton* observations and found a prominent fluorescent line at all phases. The iron line energy varies between $\sim$6.4 and $\sim$6.6 keV and is higher during the Main-On. They also detected a second component around $\sim$7 keV

visible only outside of the Main-On. This represents another evidence for a variation over the 35 day phase. They also noticed that no double structures, previously reported by Endo et al. (2000), in the Main-On or at any other 35 day phases were detected (as was also reported before by Ramsay et al. 2002). On the other hand, the ∼7 keV complex has been observed with *XMM-Newton* at different 35 day phases. This feature was later confirmed with *Chandra* observations by Jimenez-Garate & Khu (2004). Probably, this line comes from photoionized plasma which could be a trace for the hot external layers of the corona of the disk (Zane et al. 2004).

Another study of the iron line intensity as function of the 35 day phase has been done by Leahy (2001) using *Ginga* observations. In this analysis, it was found that the mean of the iron line energy during the Main-On is higher than during the eclipses or dips (6.60 ± 0.02 keV versus 6.41 ± 0.03 keV with 90% error). This mean value is also higher than the intensity detected during the Short-On dips/eclipses and during the off-state where the mean energy is marginally lower than 6.6 keV.

Leahy (2001) also suggested that the different energies reported by several authors can be explained as a mixture of the two different components resolved by Endo et al. (2000) and that the iron line detected is the result of reprocessing in material highly ionized, which plays a key role all the time during the 35 day cycle. Assuming the reprocessing and taking into account the accretion column model of Scott et al. (2000), both the pencil beam and a scattered component close to the neutron star in a highly ionized accretion column is implied. Leahy (2001) also reported that during the low-state, the iron line energy is marginally smaller. This is explained as follows. In this state the emission comes from scattering by an extended region located far from the pulsar. This scattering plays a key role for the iron line energy. In particular, the iron line intensity is reduced when scattering by cold material occurs, and it is increased when there is scattering by hot material. The decrease observed indicates scattering by cold matter. This led to the conclusion that the low-state emission is dominated by scattering in cold matter and not, for example, in a hot accretion disk corona (Leahy 2001).

Naik & Paul (2003) confirmed what was suggested by Leahy (2001) and introduced new information about the region in which the iron line is originated: the reprocessing of X-rays is important for all the states of Her X-1 and the major source for the production of the iron line is the accretion column. Probably, the 6.6 keV feature is produced in the accretion column and the 6.4 keV component with the reprocessing in the accretion disk. This scenario perfectly fits with the accretion column model by Scott et al. (2000).

Despite this, these two ideas are in contrast to White et al. (1983) where it has been noticed that the accretion column plasma is too hot and the iron ions are totally ionized.

To complicate the picture, there are some cases in which no iron line feature in the X-ray spectrum of Her X-1 was found. This is the case of McCray et al. (1982) using the spectrometer on the *HEAO 2 Einstein Observatory* and of Choi et al. (1994) during a study of the eclipses. This underlines how the emission of Her X-1 is very complicated and its origin is not clearly understood. Most probably several emission regions can contribute to the total emission like the pencil beam, the fan beam, the accretion column as well as scattering with the surface of the disk, the disk corona or the surface of the companion star (Leahy 2001).

As mentioned before, for Her X-1 a strong correlation between the iron line intensity and the continuum intensity has been observed. This property was reported by several authors (see e.g. Choi et al. 1994, Leahy 2001, Naik & Paul 2003 and Zane et al. 2004).

This correlation was also studied by Leahy (2001), İnam & Baykal (2005) and Ji et al. (2009).

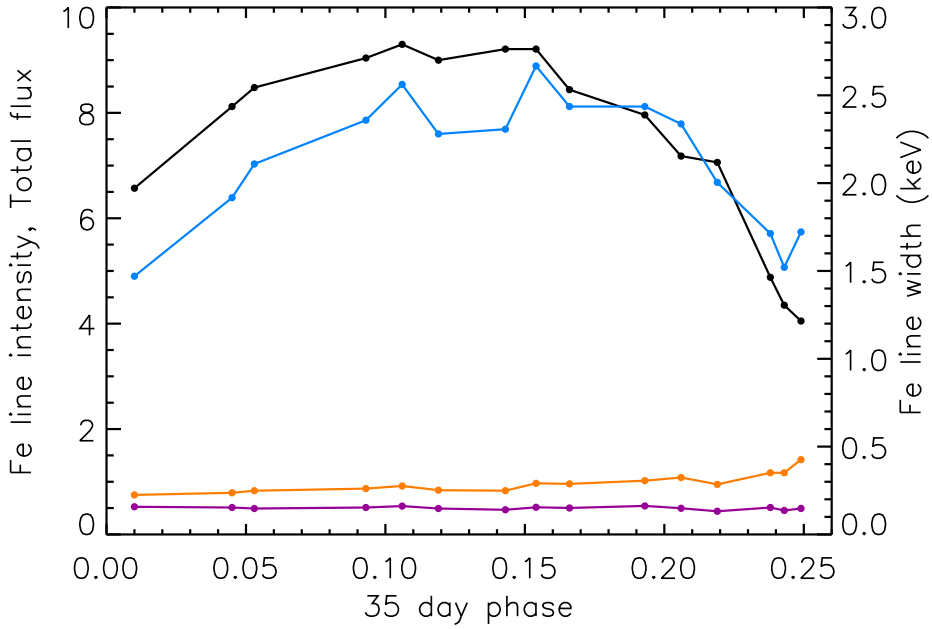

Figure 8.5: Modulation of the iron line intensity (pure in light-blue, left axis; in ratio to the 3.5 – 60 keV in orange, left axis) and of the iron line width (purple, right axis) as function of the 35 day phase. The 3.5 – 60 keV flux is plotted in black. The intensity of the iron line is scaled in order to have all the parameters in the same plot. For the same reason the errorbars are too small and not visible.

Leahy (2001) divided the continuum normalization in an absorbed component and an unabsorbed component. In this analysis, it has been found that the iron line is correlated with both of these two components. At the same time, no correlation was found during dips or eclipses. İnam & Baykal (2005) found the positive correlation studying the off-state and the Short-On of the source and noticed that with *RXTE* it is not possible to distinguish and resolve the line at 7 keV detected by Zane et al. (2004).

Ji et al. (2009) suggested that this positive correlation should be reflected in an increase of the iron line intensity also with the edge flux. Most of their observations confirmed this suggestion except of few cases at the end of the Main-On state when the absorption dominates.

In Figure 8.5 the analysis of the iron line intensity presented in this thesis is shown. In particular, the intensity (pure and scaled to the flux) and the σ of the iron line are compared to the 3.5 – 60 keV total flux. From this figure it is evident how the iron flux roughly follows the modulation of the total flux increasing up to 35 day phase 0.15 and decreasing at higher phases in correspondence with the drop in flux at the end of the Main-On. This confirmed the idea of a variation of the iron line intensity as function of the 35 day phase within the Main-On. The σ of the iron line remains instead almost constant with some deviation at those phases which correspond to the end of the Main-On. In Figure 8.6 the positive trend with *RXTE* data used in this thesis is shown. Thanks to the good resolution of *RXTE*, it is possible to distinguish two

different branches: one for 35 day phases below 0.15 and the other one for 35 day phases above 0.15.

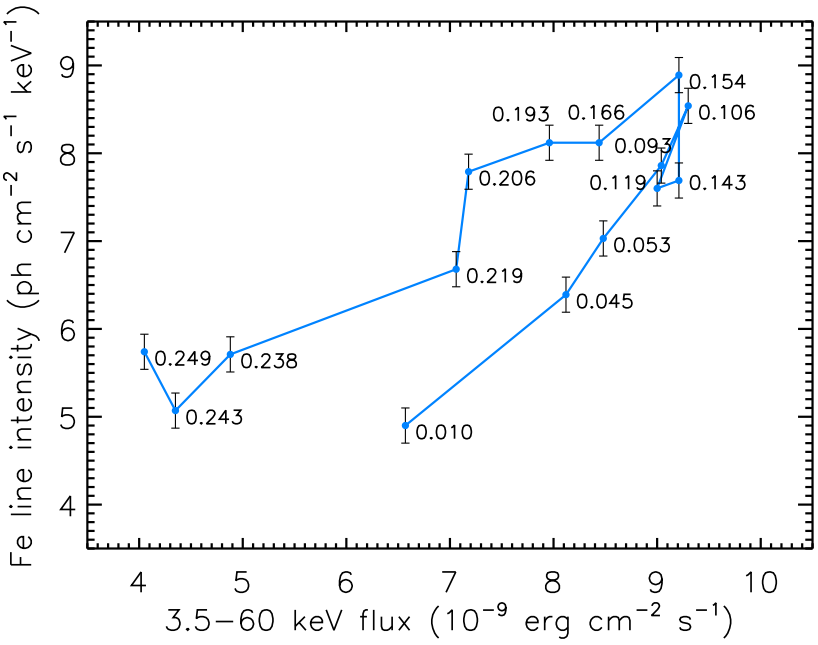

Figure 8.6: Correlation between the iron line intensity and the continuum (3.5 – 60 keV) intensity for 35 day cycle 323. In the plot, the correspondent 35 day phase is also shown.

8.6 The coupling between the photon-index and the absorption column density

A similar case to the variation of the photon-index is the modulation of the cold matter absorption N_H. Under the same conditions, this spectral parameter shows a very similar modulation with the 35 day phase to the one observed for Γ. These two spectral parameters are strongly coupled by the fitting process. This is shown in Figure 8.7: both smaller Γ and smaller N_H lead to "harder" spectra.

To reproduce in fact the observed photon-index, a similar variation with time of N_H is needed. This strong correlation is also confirmed by the "general" one between these two parameters shown in Figure 8.8. Here, the Γ/N_H correlation is shown for the complete collection from all available Main-Ons used for the analysis reported in Chapter 7, in particular for cycles number 257, 269, 303, 304, 307, 308, 320, 323, 324, 343, 351 (see Staubert et al. 2009a for the cycle numbering). The slope of the linear correlation is of the order of 0.054 units in Γ per $10^{22}\,\mathrm{cm}^{-2}$ in N_H.

In addition, an analysis of the N_H spectral parameters using the raw spectra has been performed. In this analysis the variation of N_H as a function of 35 day phase was also found. N_H

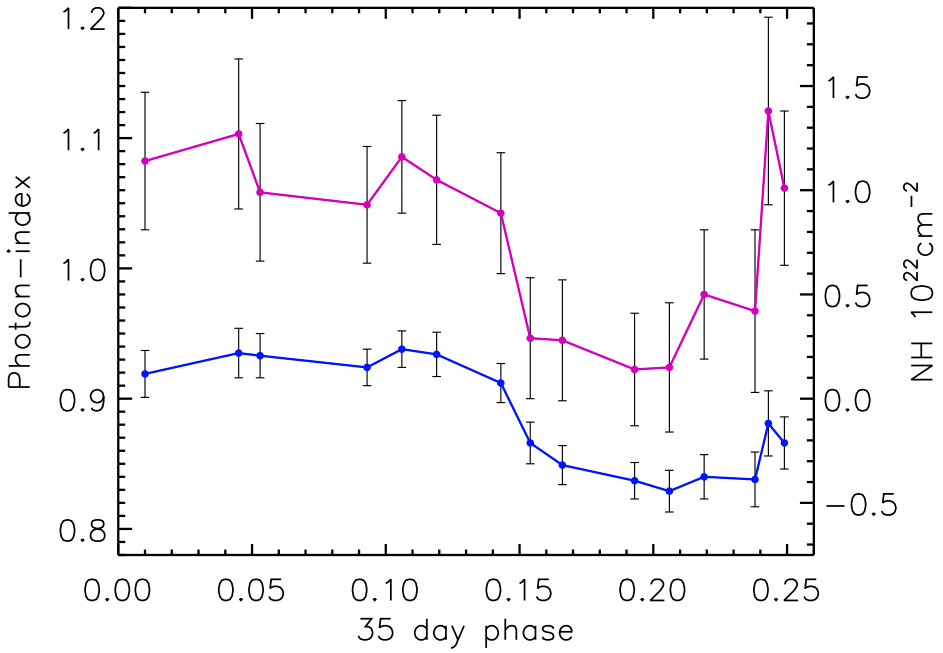

Figure 8.7: Modulation of Γ (blue, left axis) and N_H (lilla, right axis).

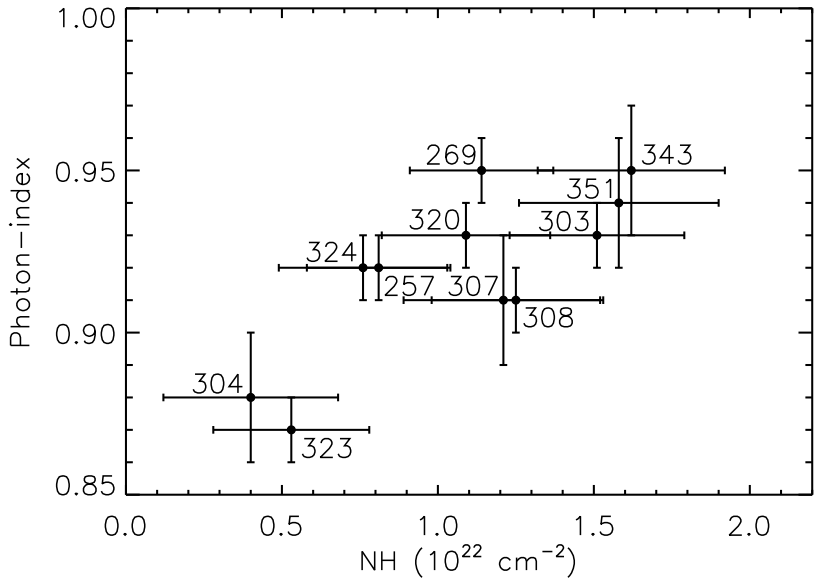

Figure 8.8: General correlation between Γ and N_H from all data of the corresponding Main-Ons.

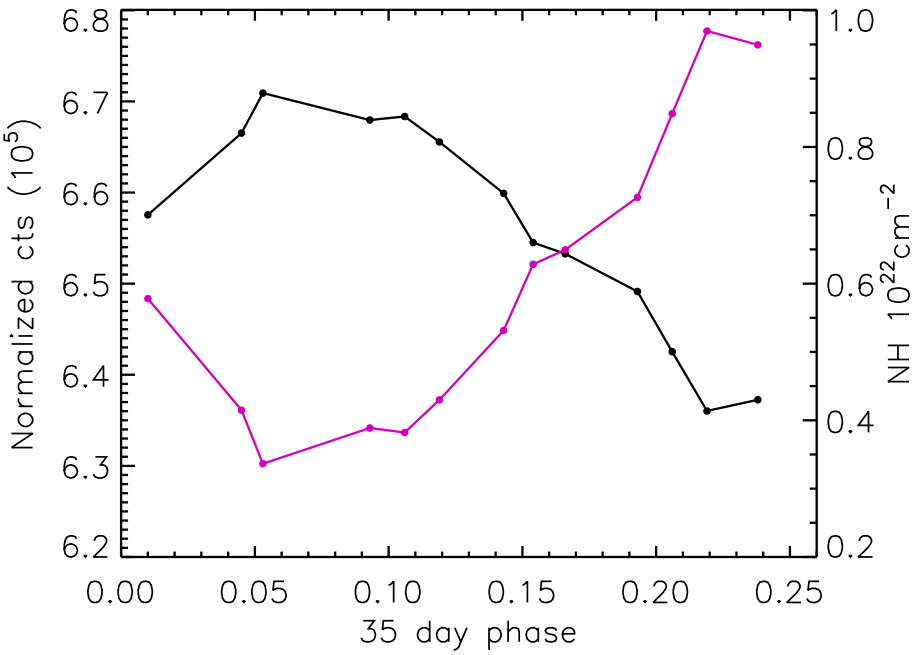

Figure 8.9: Flux modulation (black, left axis) and N_H modulation (lilla, right axis) with 35 day phase.

is found to initially decrease to a roughly constant minimal level of about 0.41×10^{22} cm^{-2} until 35 day phase 0.15 and then to increase while the Main-On flux is dying out. This makes physical sense if we assume that the flux modulation during a Main-On is (at least in part) due to a variable column thickness of cold material (see Figure 8.9).

To verify whether the photon-index modulation is not influenced by the modulation of the N_H, the spectral analysis of the same intervals with different initial conditions has been done. In particular, all the intervals have been re-analyzed fixing the value of N_H to the limiting values of 0 and 1.08 (mean of N_H). In Figure 8.10 Γ as function of the 35 day phase is plotted for different initial conditions. For spectral analysis where N_H is fixed to 1.08 (black line) as well as where N_H is fixed to 0 (green line), the modulation is the same. In the middle, the red line corresponds to N_H with values determined from the raw spectra in order to obtain the observed value of Γ. Using this N_H evolution as input to the spectral fitting ("all parameters free, except N_H") leads to a dependence of Γ on 35 day phase which is qualitatively the same as before, however with a smaller amplitude of modulation (red line). A particularly interesting fit condition is E>7 keV (orange points): here the spectra are fitted by using only events with energy above 7 keV. At this energy N_H should not play any role. It is not really clear why the photon-index is so high for 35 day phases below 0.13 (as for N_H=1.08 or "all free parameters"). It is reassuring, however, that the general evolution of Γ is always the same and that the solution for it using the N_H from the raw spectra analysis is roughly centered between N_H=0 and N_H=1.08. The drop in Γ around 35 day phase 0.15 is, in any case, highly significant (see Table 8.4).

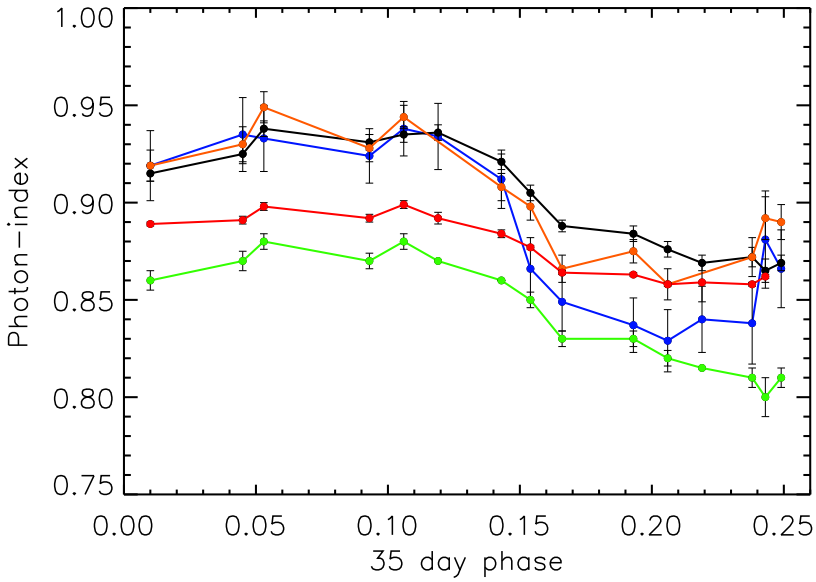

Figure 8.10: Photon-index modulation under different assumptions for N_H. In particular, N_H=0 (green), N_H=1.08 (black), spectra only for $E > 7$ keV and N_H from raw spectra (red). The case "all parameters free" is plotted in blue. Values from Table 1.4.

Table 8.4: Spectral parameters values for N_H for cycle 323 under different assumptions of N_H.

Interval	Photon-index (N_H=0)	Photon-index (N_H=1.08)	Photon-index (E >7 keV)	Photon-index (N_H from raw spectra)
a	0.860 ± 0.005	0.915 ± 0.004	0.919 ± 0.008	0.889 ± 0.001
b	0.870 ± 0.005	0.925 ± 0.005	0.930 ± 0.009	0.891 ± 0.002
c	0.880 ± 0.004	0.938 ± 0.004	0.949 ± 0.008	0.898 ± 0.002
d	0.870 ± 0.004	0.931 ± 0.004	0.928 ± 0.007	0.892 ± 0.002
e	0.880 ± 0.004	0.935 ± 0.004	0.944 ± 0.006	0.899 ± 0.002
f	0.870 -	0.936 ± 0.004	-	0.892 ± 0.003
g	0.860 -	0.921 ± 0.004	0.908 ± 0.007	0.884 ± 0.002
h	0.850 ± 0.004	0.905 ± 0.004	0.898 ± 0.007	0.877 ± 0.001
i	0.830 ± 0.004	0.888 ± 0.003	0.866 ± 0.007	0.864 ± 0.001
j	0.830 ± 0.004	0.884 ± 0.004	0.875 ± 0.006	0.863 ± 0.001
k	0.820 ± 0.004	0.876 ± 0.004	0.858 ± 0.008	0.858 ± 0.001
l	0.815 -	0.869 ± 0.004	-	0.854 ± 0.001
m	0.810 ± 0.005	0.872 ± 0.005	0.872 ± 0.010	0.859 ± 0.010
n	0.800 ± 0.010	0.865 ± 0.006	0.892 ± 0.011	0.858 ± 0.001
o	0.810 ± 0.005	0.869 ± 0.004	0.890 ± 0.009	0.862 ± 0.001

8.7 The complicated case of the column density

The variation of the N_H reported in section 8.6 have been compared with previous studies. The *RXTE* data analysis of Her X-1 here presented shows that the Main-On of cycle 323 requires an absorbed component to fit nicely the X-ray spectra. The column density ranges roughly between 0.1 and 1.5 $\times 10^{22}$ cm^{-2} (see Table 8.3). This is consistent with previous analyses obtained with the same instrumentation (see e.g. Naik & Paul 2003). On the other hand, Dal Fiume et al. (1998), using *BeppoSAX* observations, adopted a column density of 5.1×10^{19} cm^{-2}, consistent with the interstellar value, and Leahy (2001), with *Ginga*, found about 10^{24} cm^{-2}. Both of these two values are significantly different from the values listed in Table 8.3.

In Table 8.5 a collection of previous analyses with the corresponding N_H values is shown. The huge variation of N_H evident in the table is most likely due to the different data sets (different 35 day phases) and the different spectral models used to fit the observations. Two interesting examples are the following ones. Ramsay et al. (2002) observed Her X-1 with *XMM-Newton*. To fit the X-ray spectrum, a neutral hydrogen component at 5×10^{22} cm^{-2} to take into account the interstellar absorption towards Her X-1 was used. At the same time, an additional partial covering component in the case of bad fits was added. With this model a high value of N_H was found when the source is at low intensity, and a low value of N_H when the source is at high intensity. Another example comes from Kuster et al. (2005) that studied the turn-on of cycle 269 of Her X-1. In this analysis two different components were taken into account: an "uneffected" component and a component modified by scattering and absorption. In particular, photons which reach directly the observer and photons which undergo photoelectric absorption and Thomson scattering were both accounted. This model is required because the influence of photoelectric absorption at the beginning of the turn-on cannot be ignored. This is taken into account on the model by the scattering on free electrons ($\sigma_{Thomson}$ which is not energy dependent) and by the photoabsorption (σ_{bf} which is energy dependent and scales with E^{-3}). A second component is also introduced to represent the unaffected radiation (partial covering model).

To investigate the X-ray spectra of Her X-1 analyzed in this thesis, several models have been used: 1) without any absorption component ($N_H = 0$); 2) with absorption component 3) the partial covering model 4) a combination of the partial covering model and a normal absorption component. These can be summarized as:

$$I_1 = N \cdot CONT \tag{8.5}$$
$$I_2 = Ne^{-N_H\sigma} \cdot CONT \tag{8.6}$$
$$I_3 = N(1 + c \cdot e^{-N_H\sigma}) \cdot CONT \tag{8.7}$$
$$I_4 = Ne^{-N_{H1}\sigma}(1 + c \cdot e^{-N_{H2}\sigma}) \cdot CONT, \tag{8.8}$$

where $CONT$ is the continuum, N_H the column density, c the covering factor and σ the relative cross-section. Not all of these models fitted nicely the spectra. In the first two cases (I_1 and I_2), it has been possible to fit the data with reasonable values of χ^2 with $\chi^2_{I_2}$ slightly smaller than $\chi^2_{I_1}$. Instead, in the third[5] and fourth case, it was not possible to estimate correctly the uncertainties on the individual fit parameters.

[5]The same of $I_3 = N((1-f) + f \cdot e^{-N_H\sigma}) \cdot$ CONT with covering factor f=[0,1].

Up to now it is not clear whether the values for the column density can be converted in a physical model which explains the complex geometry of the system. Despite this, some attempts have been proposed.

Leahy (2001) suggested that all the different states of Her X-1 (main-high, short-high, and low-states) require two different components to model the continuum: a small absorbed component and a large unabsorbed component. Adopting the model of Scott et al. (2000) for the accretion column, the absorbed component is explained as follows. There is a pencil beam with radius comparable with the radius of the neutron star and two backscattered fan beam components with a radius almost twice the radius of the neutron star. A much more extended scattered component is also taken into account. The inner edge of the accretion disk covers the scattered component at all times. For this reason, at the beginning of the Main-On, the disk edge covers first one of the fan beam, then the pencil beam and finally the second fan beams. The result of this coverage is a highly absorbed continuum component in the X-ray spectrum of Her X-1. From all of the emission covered by the disk, only a small percentage contributes to the absorbed component because the rest of the emission is completely blocked from the line of sight of the observer. This leads to the strong dependance of the absorbed component on the size of the blocking region and the width of the edge of the disk. This leads to the conclusion that it is not possible to trace a clear modulation of the N_H as function of the 35 day phase.

A similar picture can be drawn looking at Table 8.5. The values of the N_H range within a huge interval. This could be due to variability on long timescales and/or because of the variation of the column density as function of the 35 day phase. The N_H appears to be higher during the Short-On than during the Main-On and much higher during the off-state. This makes physical sense. During the Main-On the accretion disk covers only partially the X-ray source leading to a small column density. On the other hand, an increase of the coverage by the accretion disk in the Short-On leads to an increase of the column density. The latter reaches the maximum when during the off-state, the accretion disk covers completely the compact object blocking the X-ray emission, only some scattered and highly absorbed radiation may be seen.

The examples reported before underline that it is possible to treat the N_H component in different ways. The results reported in section 8.5 are consistent with analyses of the same data set with the same instrumentation, but to compare them with previous works, it is important to take into account other parameters such as the spectral model used for the analysis and the corresponding 35 day phase of the data set. Because of this, it is difficult to extrapolate from these information a correct picture of the physics which governs the modulation of the N_H as function as the 35 day phase.

Table 8.5: Summary of different observations of Her X-1 and relative N_H observed.

Satellite	Time of Obs.	35 day phase	State[1]	N_H(unit of $\times 10^{22}\,\mathrm{cm}^{-2}$)	Model	References
RXTE	July 1998	0.63 – 0.74	SO	(0 – 80)	partial covering	Still et al. (2001b)
	July 1999	0.339 – 0.470	AL	16×10^2	partial covering	Still et al. (2001a)
	September 96	0.674, 0.603, 0.201	OS, SO. MO	$1.7 \times 10^{-2} < N_H < 7.3$	un- ab-sorbed comp.	Naik & Paul (2003)
	December 01	0.515	OS	1.25	normal abs.	Inam & Baykal (2005)
		0.745	SO	1.54	plus partial covering	
		-	AD	1.80		
		-	ND	2.45		
	September 97	-0.011	TO to MO	3.6 – 77 $\times 10^2$	Scatt. plus abs.	Kuster et al. (2005)
OSO-8	August 75	-	prior TO	~ 0	norm. abs.	Becker et al. (1977)
		0.059	mid TO	6.2×10^2		
			post TO	1.0×10^2		
			ND	2.9×10^2		
	August 75	0.059	MO			Pravdo et al. (1977a)
HEAO-1	February 78	0.083	HS	0.72	norm. abs.	Pravdo et al. (1978)
		0.399	LS	0.18		Pravdo et al. (1978)
HEAO-2	February 79	0.139	MO	$< 3 \times 10^{-2}$	norm. abs.	McCray et al. (1982)
	March 79	0.115	MO	1.5 – 2.7$\times 10^{-2}$		
EXOSAT	March 84	0.335	MO	0.2 ... 30	norm. abs.	Voges et al. (1985)
	April 84	0.129				
		0.227				
Ginga	August 88	0.742	MO	$log(N_H) < 21$	norm. abs.	Mihara et al. (1991)
	September 01	0.742	LS	$log(N_H) \sim 24$		
		0.172	ND	$log(N_H) \sim 24$		
	August 88	0.059	MO	< 1 up to 120	norm. abs.	Choi et al. (1994)
	April 89	0.109	MO	$log(N_H) < 21.5$		Choi et al. (1994)
	May 89	0.654	SO	$log(N_H) < 22$		Choi et al. (1994)
	April 89	0.059	ND	$22.2 < log(N_H) < 24.4$	partial covering	Leahy et al. (1994)
	May 89	0.568	SO	$log(N_H) < 23.5$	partial covering	Leahy et al. (2000)
	April 89	0.683				
	April – July 89	-0.006 up to 0.626	all states	close to 100		Leahy (2001)
BeppoSAX	July 96	0.077 – 0.162	MO	0.33×10^{-2}	interstellar	Oosterbroek et al. (1997)
	August 94	0.742	MO	5.1×10^{-3}		Dal Fiume et al. (1998)
	April 96					
ASCA	August 93	0.187	MO	-	interstellar	Choi et al. (1997)
		0.617	SO	-		
			E	< 0.04		
	August 94	0.129	MO	0.4	norm. abs.	Endo et al. (2000)
	April 96	0.077	MO	47...78		
ROSAT	August 90	0.668 – 0.728	SO	(1.5...3.6) $\times 10^{-2}$	interstellar	Mavromatakis (1993)
Many Sat.	August 93	0.116		$log(N_H) = 23.96$	norm. abs.	Vrtilek et al. (1994)
		0.220		$log(N_H) = 23.91$		

[1] MO = Main-On, SO = Short-On, HS = high-state, LS = low-state, ND = normal dip, E = Eclipse, AD = anomalous dip, TO = turn-on

8.8 Summary

The spectral analysis reported in this section led to the conclusion that within the Main-On of cycle 323, some spectral parameters remain constant as function of the 35 day phase and some spectral parameters show a modulation over this super-orbital period. In particular:

- E_{fold} and E_{cut} remain constant with 35 day phase around 10 keV and 22 keV, respectively;
- the photon-index Γ shows a clear modulation as function of the 35 day phase;
- a strong coupling due to spectral fit is observed for the absorption parameter N_H and the photon-index Γ;
- the modulation of the photon-index Γ is confirmed by the raw spectral analysis with different conditions for N_H and by the raw spectra analysis;
- N_H first decreases, then increases with respect with the 35 day phase;
- to first order, the intensity of the iron line fluorescence feature scales with the intensity of the continuum (3.5 – 60 keV), however, the ratio of those values increases slightly with progressing 35 day phase.

9 RXTE pulse phase resolved spectroscopy of Her X-1

In this chapter the results of the pulse phase resolved spectroscopy of Her X-1 are reported. This analysis completes the picture already started in Chapter 8 about the evolution of the spectral parameters. This chapter is also based on results which are going to be submitted early 2012.

9.1 Spectral parameters as function of the pulse phase

A special method to study the spectral evolution of pulsating sources is pulse phase resolved spectroscopy. This analysis provides important information about the evolution of spectral parameters as function of the pulse phase of the source through the study of separated spectra of individual portions of the pulse profile. The pulse profile is a representation of the radiation received from the source and, because of this, the pulse phase resolved spectroscopy gives information about the X-ray emission characteristics of the source.

The observed changes of the spectral parameters with pulse phase are quite common among the class of accreting pulsars and are attributed to the change in the viewing angle of the emission region (see e.g. Kreykenbohm et al. 2004 and references therein). For Her X-1, the dependence of the spectral parameters on the pulse phase have been observed by several missions. Early examples are Pravdo et al. (1978) with *OSO 8*, Pravdo et al. (1979) and Soong et al. (1990a) with the *A-4* experiment of *HEAO-1* and McCray et al. (1982) with *HEAO 2* the *Einstein Observatory*. Later examples are Xu et al. (1995) and Endo et al. (2000) with *ASCA*, Zane & Ramsay (2001) with *XMM Newton*, Lutovinov et al. (2000) with the *ART-P* telescope on-board of *GRANADA* and Klochkov et al. (2008) with *INTEGRAL*.

From these previous analyses it is clear, that the spectral parameters show a strong variation at those phases corresponding to the peak of the X-ray pulse profile. As reported by Klochkov et al. (2008), this is the case, for example, of the photon-index Γ and the folding energy E_{fold}. These two spectral components show dramatic changes in correspondence with the peak of the pulse profile.

In the case of the photon-index Γ, the behavior as function of the pulse phase was reported by Lutovinov et al. (2000). The decrease of Γ at the peak of the pulse profile (hardening of the X-ray spectrum) can be explained as a change of the optical depth and of the angle between the magnetic field lines and the line of sight of the observer (Pravdo et al. 1977b).

A similar behavior is observed for the folding energy E_{fold}. The folding energy is in fact higher at the peak of the pulse profile than at other phases. Rybicki & Lightman (1979) have reported how this parameter should be proportional to the temperature of the plasma which characterizes comptonized X-ray spectra, as in the case of accreting pulsars. When the plasma is originated in the region close to the surface of the neutron star, its temperature is typically higher than the

temperature of plasma originated far from the surface of the neutron star. As for the photon-index, at the peak of the pulse profile, the optical depth is higher suggesting that the radiation comes from the base of the accretion column, which corresponds to the region where the plasma has a higher temperature.

In the case of the centroid of the cyclotron line energy, the situation is different and much more interesting. This spectral parameter shows a strong variability within the pulsation of the neutron star and seems, to first approximation, to follow the shape of the pulse profile. Its centroid is in fact higher at those pulse phases corresponding to the peak of the pulse profile and much lower in correspondence of the minimum observed after the interpulse component. The physical interpretation is still unclear and cannot be related to a change of the height of the emission region in the accretion column. This is because in Her X-1, the accretion column is believed to be relatively short (Staubert et al. 2007) and a change in the height of the emission region cannot produce the observed strong variability. Shakura et al. (1991) and Panchenko & Postnov (1994) have suggested that this variability can be due to the complex shape of the multipole magnetic field structure. In particular, the presence of a quadrupole component of the magnetic field near the surface of the neutron star is claimed. This peculiar shape would be responsible for the X-ray anisotropic emission of Her X-1 and, consequently, of the changes of the centroid of the cyclotron line pulse phase.

9.2 Results of earlier pulse phase resolved spectroscopy

The pulse phase resolved spectroscopy analysis has been performed several times using different instruments. Here, some of the most important examples are discussed in order to compare earlier analyses with the new *RXTE* pulse phase resolved spectroscopy reported in this thesis.

A first example is the analysis by Voges et al. (1982). Using a balloon experiment of a collaboration between the MPI Garching and the AIT Tübingen, a study of phase-dependent spectra showed how spectral parameters such as the cyclotron line energy and the exponential folding energy vary during the main pulse. In particular, this variation was explained as a consequence of the changing angle of the line of sight with respect to the magnetic field direction, confirming previous findings by Rothschild et al. (1981). This is shown in Figure 9.1 (left and right). In particular, Figure 9.1 (left) shows the modulation of the folding energy and the cyclotron line energy as function of 1.238 s pulse phase fitted by a sinusoidal function. Figure 9.1 (right) shows the modulation of the energy of the cyclotron line with pulse phase of combined *HEAO 1* A-4 data taken from Rothschild et al. (1981) and MPI/AIT balloon flight data. Also in this case, the best sinusoidal fit to the data is given.

Another important work for the pulse phase resolved spectroscopy has been done by Soong et al. (1990a). In Figure 9.2 the variations of spectral parameters as function of the pulse phase is shown. In particular, the left panel shows the modulation for an absorption model and the right panel for an emission model. From Figure 9.2 it is clear that the centroid of the cyclotron line energy follows the trend of the pulse intensity. For other parameters, such as the exponential folding energy, this is true only in the case of an absorption model.

In 1996, pulse phase resolved spectroscopy with the *Mir HEXE* instrument was performed by Kunz (1996). Figure 9.3 shows the intervals used for this analysis and Figure 9.4 the variation of different spectral parameters as function of the pulse phase.

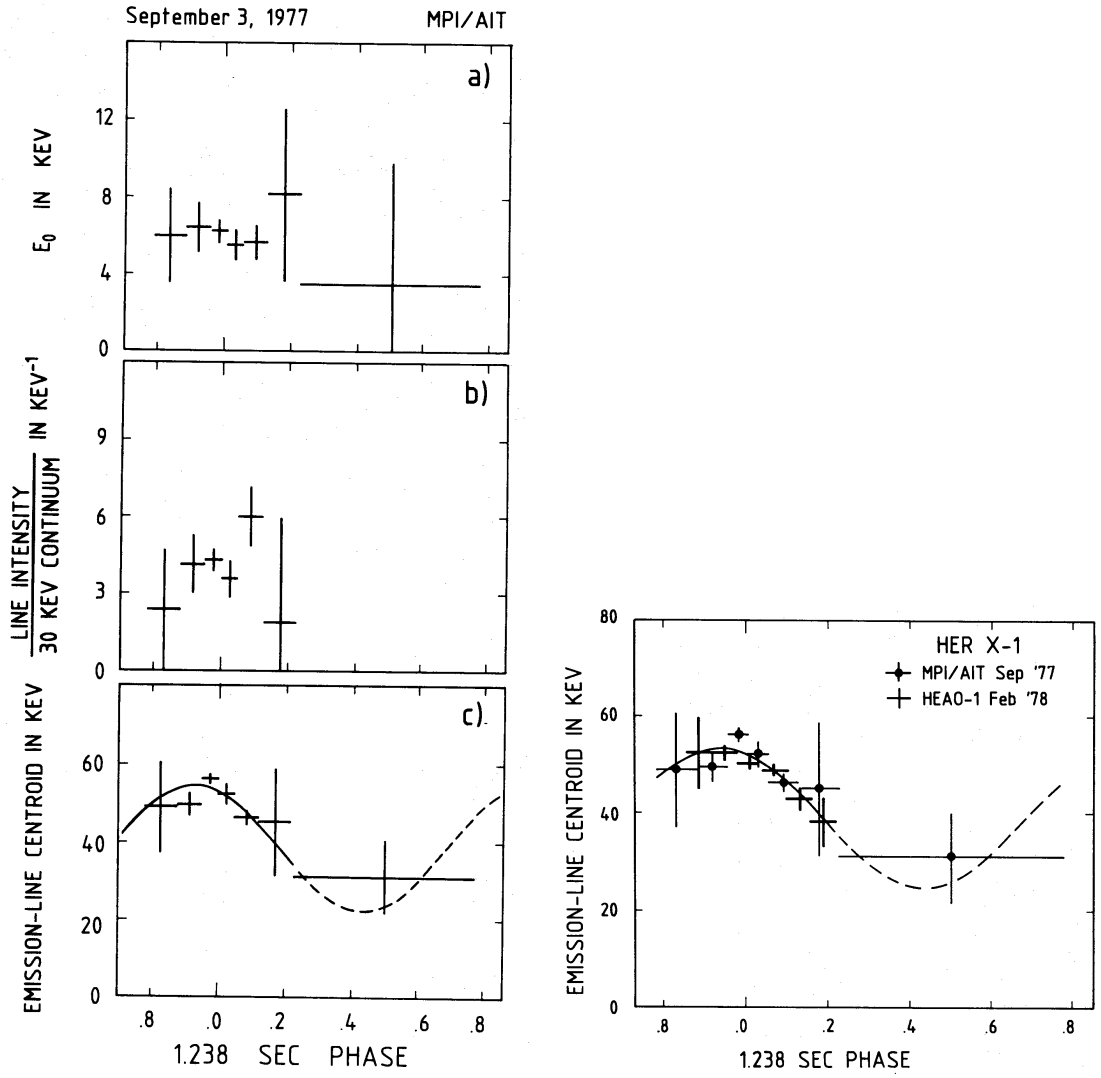

Figure 9.1: *Left panel*: Folding energy, ratio of line and continuum intensities and cyclotron line energy as function of pulse phase. The solid curve indicates the best sinusoidal fit (Voges et al. 1982). *Right panel*: Cyclotron line energy profile from the combined *HEAO 1* A-4 (taken from Rothschild et al. 1981) and MPI/AIT balloon flight (from Voges et al. 1982). Note: here the cyclotron line energy is from fits with an emission line model.

Finally, a more recent example is reported in Klochkov et al. (2008) based on *INTEGRAL* data for revolution 339, 340 and 341. The results are consistent with the fact that the centroid of the cyclotron line varies as the intensity of the pulse profile. This is shown in Figure 9.5 and 9.6.

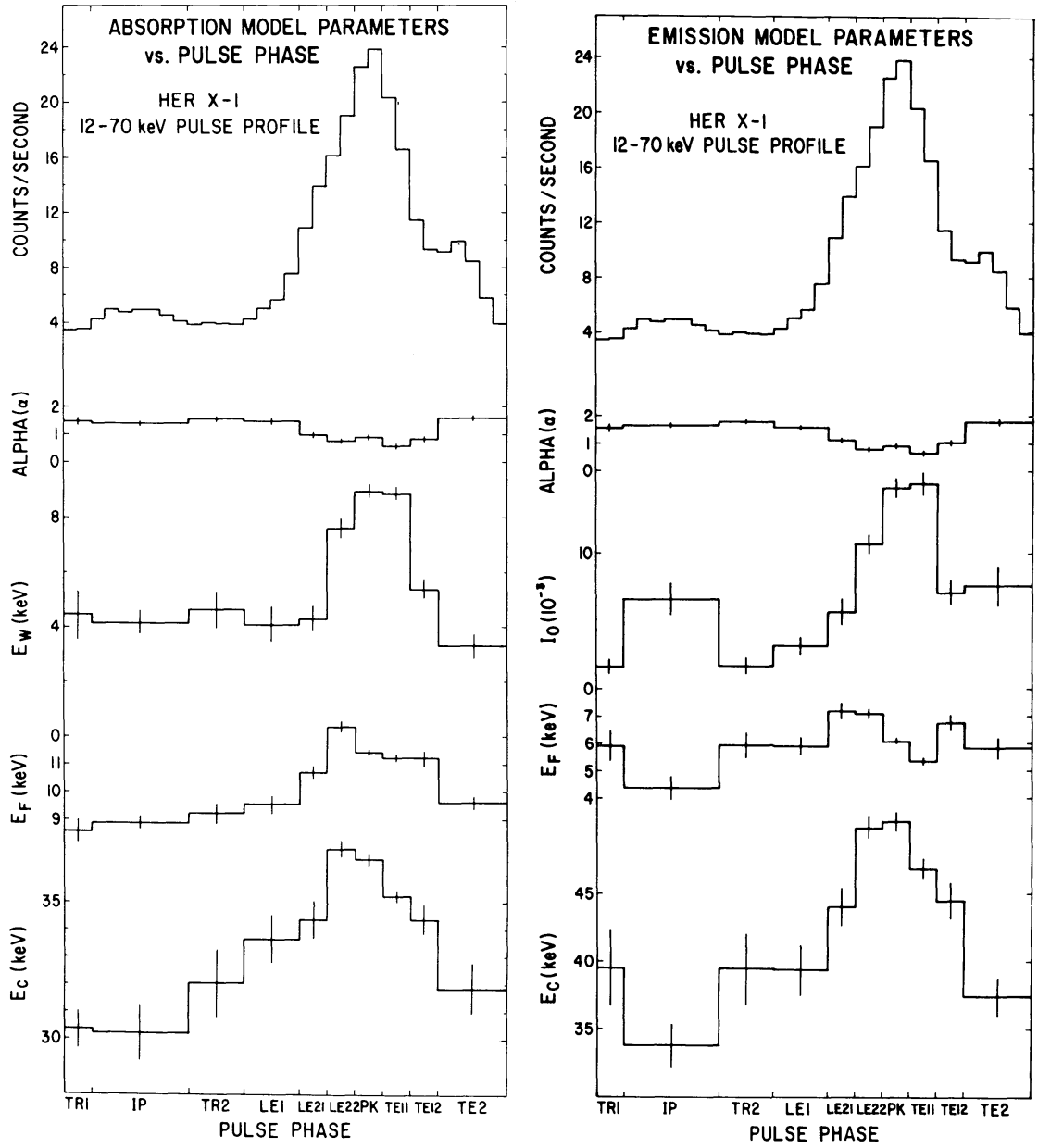

Figure 9.2: Variation of spectral parameters as function of the pulse phase for an absorption model (left) and an emission model (right) based on data from the *HEAO* A-4 experiment (Soong et al. 1990a).

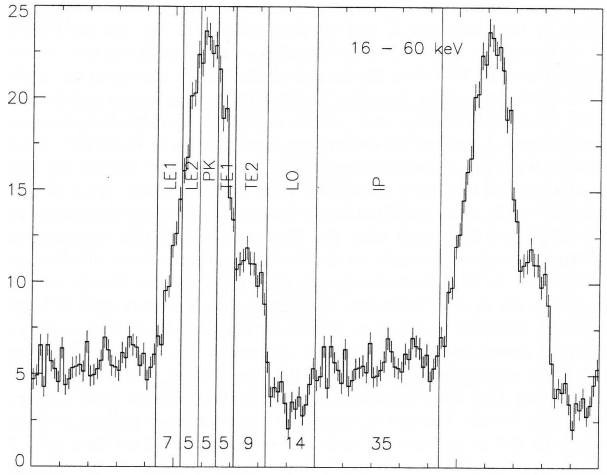

Figure 9.3: Division of the pulse profile in pulse phase bin intervals by Kunz et al. (1996).

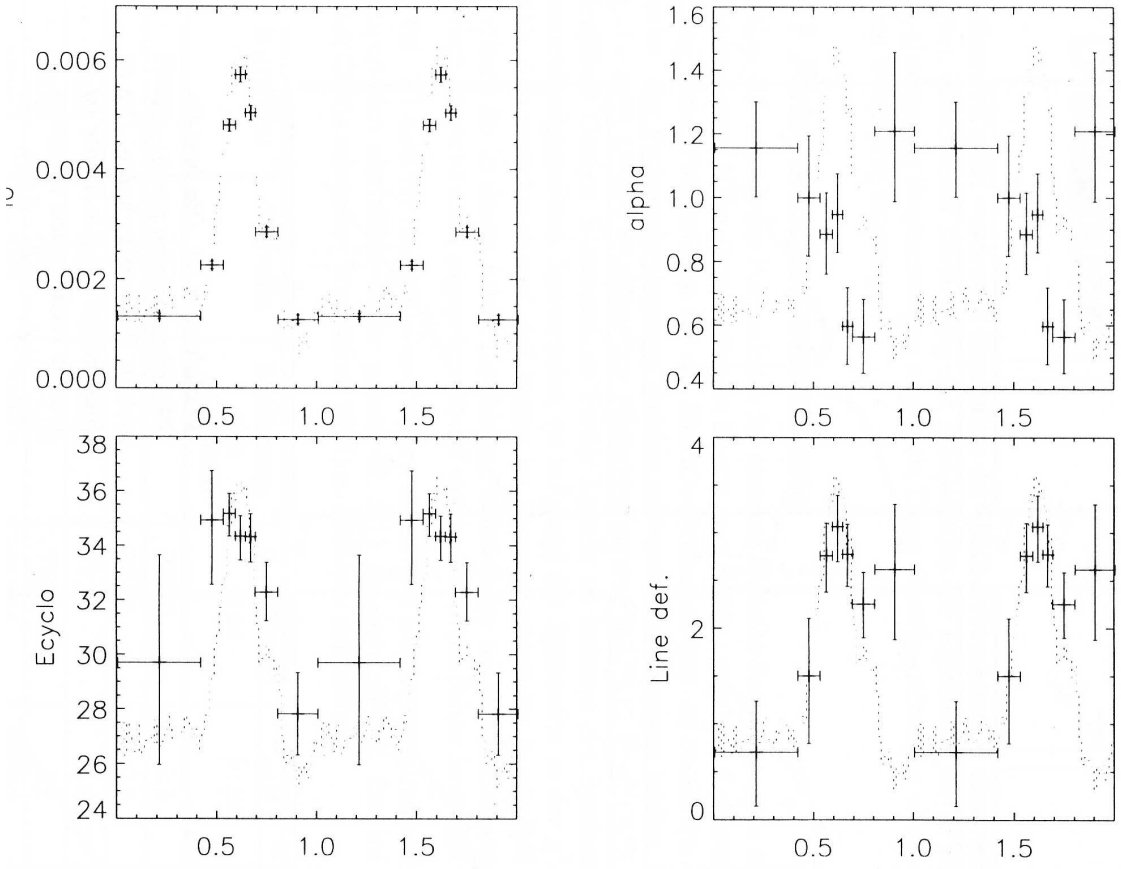

Figure 9.4: Variation of different individual spectral parameters as function of the pulse phase with *Mir HEXE* by Kunz et al. (1996). Note: here the cyclotron line energy is from fits with an absorption line model.

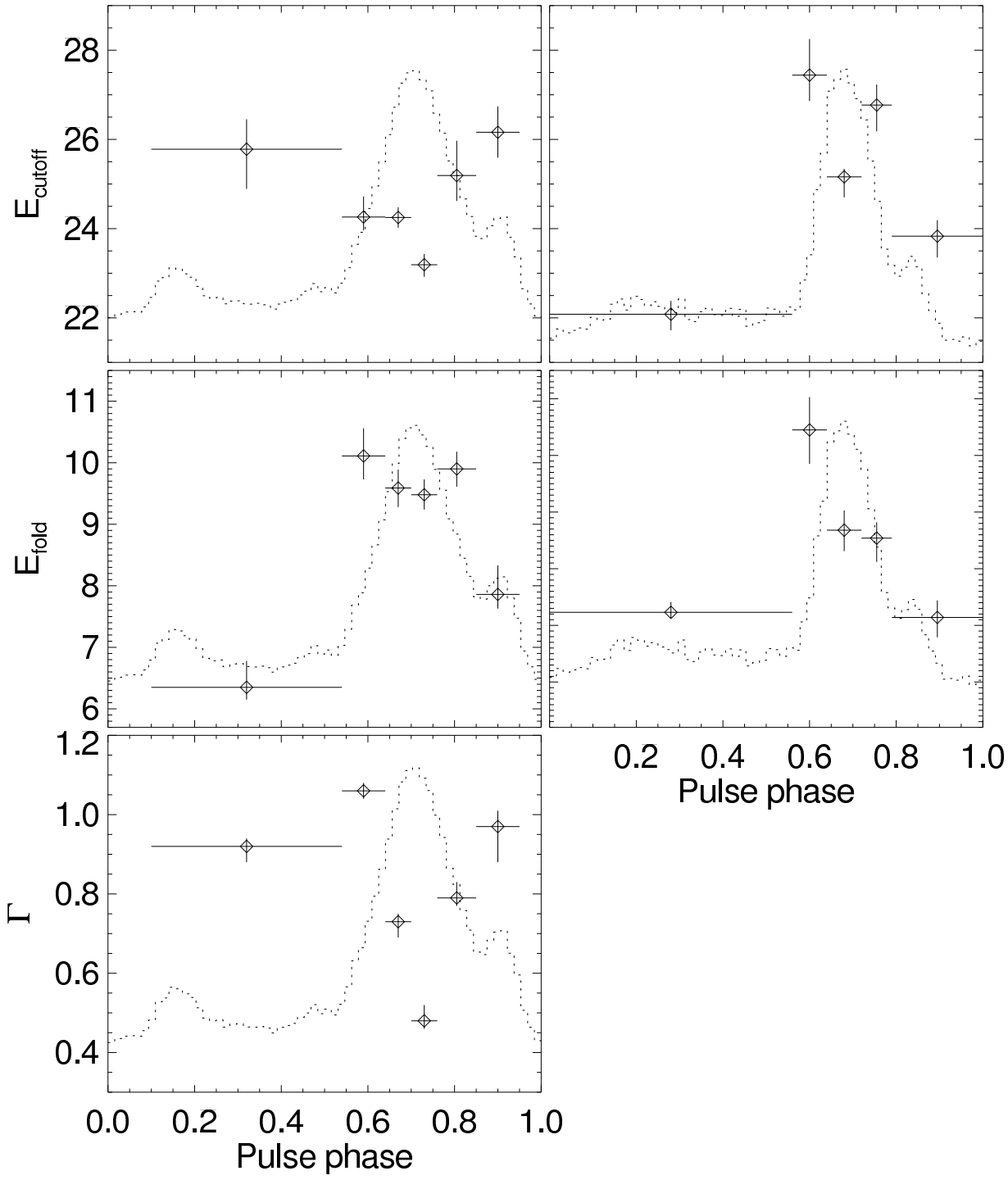

Figure 9.5: Variation of spectral parameters as function of the pulse phase with *INTEGRAL* by Klochkov et al. (2008), I. In particular, these results are obtained for revolution 339 and 340 (left) and 341 (right). Again, an absorption line model was assumed.

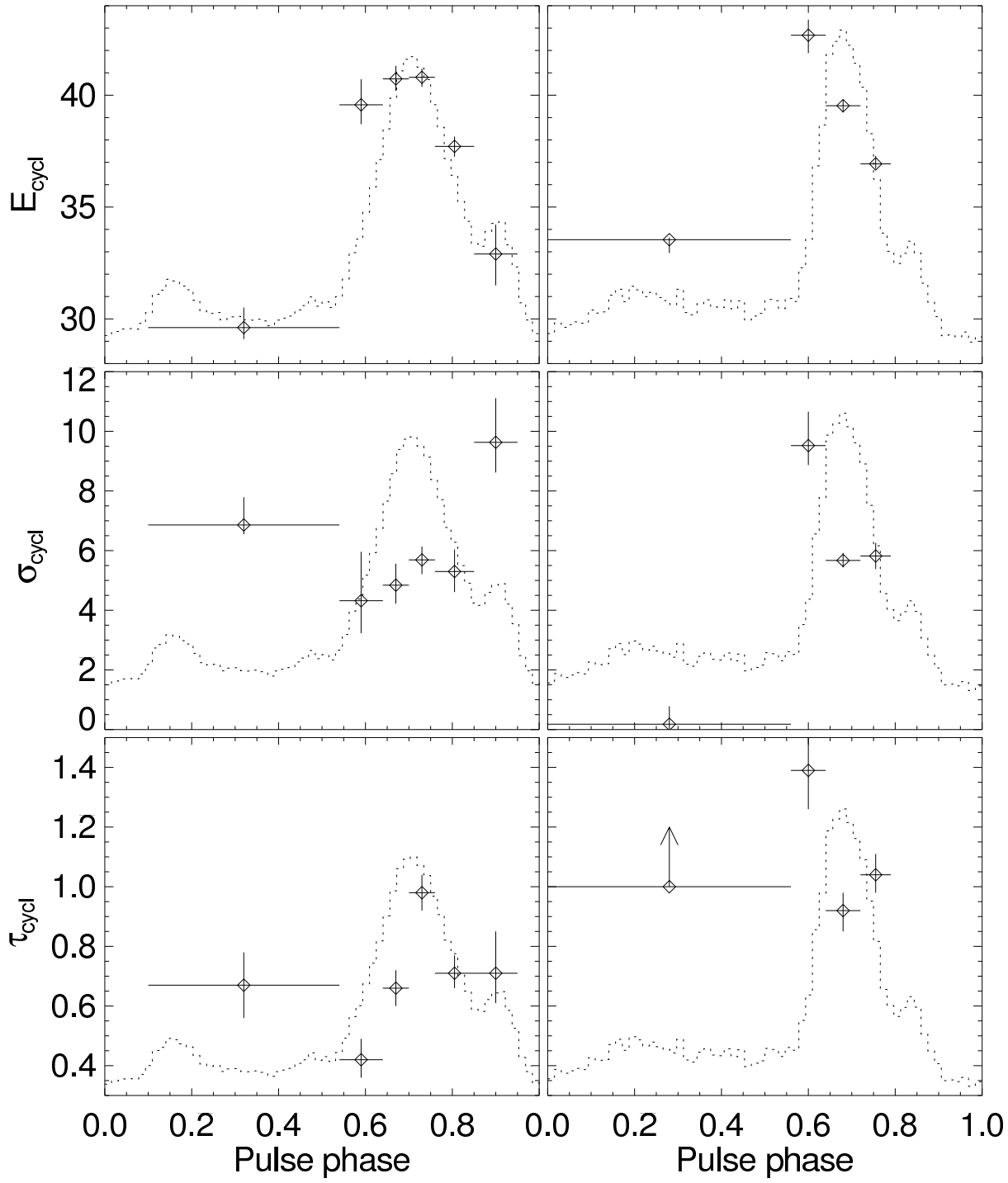

Figure 9.6: Variation of spectral parameters as function of the pulse phase with *INTEGRAL* by Klochkov et al. (2008), II. In particular, these results are obtained for revolution 339 and 340 (left) and 341 (right).

9.3 Pulse phase resolved spectroscopy of Her X-1

To carry out this analysis, observations of Her X-1 with *RXTE* performed in November 2002 were used. These observations correspond to cycle number 323 centered at MJD ∼52599.32. Within this cycle, observations from four selected time intervals at different 35 day phases were analyzed in order to have a good coverage of an entire Main-On avoiding dips and eclipses. All of the intervals last approximately one day (see section 5.3.1 for the X-ray light curves of cycle 323). From now on, for simplicity, these interval are referred as Interval 1, Interval 2, Interval 3 and Interval 4. In table 9.1 the time intervals and the corresponding 35 day phases are listed.

Table 9.1: Summary of the four intervals used for this analysis. In the table are listed: the number of the interval (first column); the interval time in MJD (second column), and the corresponding 35 day phase (third column).

Interval	MJD	35 day phase
1	52595.060 - 52596.743	0.03
2	52597.959 - 52598.719	0.10
3	52599.603 - 52600.726	0.15
4	52601.316 - 52602.406	0.20

To apply the barycentric and binary correction to the light curves before extracting the pulse profiles, orbital parameters from Staubert et al. (2009a) were used. In particular, the orbital period P_{orb}=1.700167287 s, the derivative of the orbital period $P_{orb} = +(2.8 \pm 0.2) \times 10^{-12} ss^{-1}$, the projection of the orbital radius $a \cdot \sin i$=13.1831 as well as the superior conjuction $T_{\frac{\pi}{2}}$=52599.486440.

To produce all pulse profiles in phase, a reference time following Staubert et al. (2009b) for the "phase zero" was used. This is the "sharp-edge" feature at the trailing edge corresponding to the decay of the main pulse of the right shoulder which goes into a minimum. To do that, a t_0=52594.869900091 MJD for the folding and the spin period P_{spin}=1.237761809 s were used.

As for the analyses presented in Chapter 7 and 8, both the PCA and HEXTE instruments were used in a uniform way; PCA was used in the energy range 3.5 – 60 keV and HEXTE in the energy range 20 – 75 keV. The data have been analyzed with `XSPEC` 12.6.0[1] using the `highecut`[2] model (based on a power law continuum with an exponential cut-off around 20 keV) to reproduce the continuum of the X-ray spectrum of Her X-1. In addition, a multiplicative *Gaussian* absorption line for the Cyclotron Resonant Scattering Feature (CRSF) around 40 keV and an additional one for the iron line emission feature around 6.5 keV were added. This model is the same one used in earlier analysis (see e.g. Coburn et al. 2002 and Staubert et al. 2007). As mentioned before, the choice to use PCA data up to 60 keV instead of up to 50 keV, as suggested from the PCA team with the new response matrices, is based on the fact that PCA data up to 60 keV can definitively contribute to improve the statistics around the energies which correspond to the cyclotron line absorption feature. The same choice has been used in previous analysis (see e.g. Ferrigno et al. 2011) and it was confirmed by Rothschild et al. (2011) on *RXTE* observations of Cen A. The

[1] http://heasarc.gsfc.nasa.gov/docs/xanadu/xspec/
[2] http://heasarc.gsfc.nasa.gov/docs/xanadu/xspec/manual/XSmodelHighecut.html

`recorn` spectral component was also added to the model to normalized the background at higher energies.

On PCA data an uncertainty of 1% was added, which is slightly higher than the recommended 0.5%. In order to avoid problems in cases where the background dominates at low energies, the iron line energy was fixed to the value of 6.45 keV and the width of the line to 0.5.

Also for this analysis, *RXTE* `standard_2f` data products were extracted and `generic events` (`E_250us_128M_0_1s`, `E_1ms_128M_50_1s` and `B_16ms_16B_0_49_H`) and `GoodXenon` [3] observational modes of the PCA for the high resolution analysis were used.

As mentioned before, with the pulse resolved spectroscopy analysis, it is possible to generate spectra from different phase intervals within the pulse. For this analysis, the pulse profile has been divided in 14 pulse phase bins. The size of these bins is not always the same because of the variable statistics. In particular, smaller bins correspond to those phases where the peak of the pulse profile is observed. This division is listed in Table 9.2 and shown in Figure 9.7.

9.4 Pulse phase variability

This analysis is highly interesting in order to investigate the physical properties of Her X-1. It is the first time that pulse phase resolved spectroscopy was done with such a fine resolution for the best set of *RXTE* observations (cycle 323). The division in 14 bins of the pulse profile provides a unique picture about the evolution of the spectral parameters. This is confirmed, for example, by the identification of the left shoulder in the cyclotron line energy profile for the first time ever. In all of the following an absorption line model was used for the spectral fits.

Table 9.2: Pulse phase bins used to divide the pulse profile.

Range of the bin	Center of the bin
0.000 - 0.200	0.1000
0.200 - 0.400	0.3000
0.400 - 0.500	0.4500
0.500 - 0.600	0.5500
0.600 - 0.650	0.6250
0.650 - 0.700	0.6750
0.700 - 0.725	0.7125
0.725 - 0.750	0.7375
0.750 - 0.775	0.7625
0.775 - 0.800	0.7875
0.800 - 0.850	0.8250
0.850 - 0.900	0.8750
0.900 - 0.950	0.9250
0.950 - 1.000	0.9750

[3] http://heasarc.gsfc.nasa.gov/docs/xte/abc/pca_issues.html#configs_modes

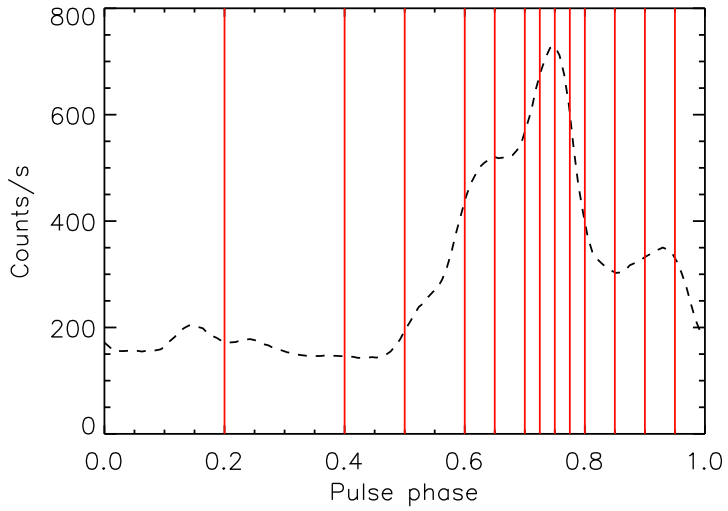

Figure 9.7: Division of the pulse profile in 14 bins for the pulse phase resolved spectroscopy analysis (see Table 9.2).

9.4.1 Pulse profiles

In Figure 9.8 the 9 –13 keV pulse profiles of all four intervals are shown. In particular, Interval 1 is plotted in black, Interval 2 in green, Interval 3 in red and Interval 4 in blue.

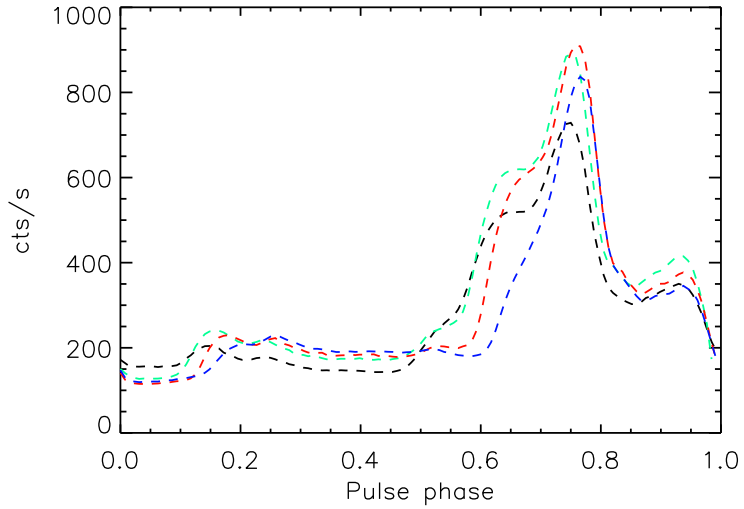

Figure 9.8: Pulse profiles for the four intervals: Interval 1 (black), Interval 2 (green), Interval 3 (red) and Interval 4 (blu). The reference feature for the phase zero is the "sharp-edge" feature at the trailing edge at the decay of the main pulse right shoulder which goes into a minimum (Staubert et al. 2009b).

The fact that the shape of the pulse profiles changes with energy and with 35 day phase is well known for Her X-1. The variation with energy is well described in Chapter 6 and the variation with 35 day phase can be deduced from Figure 9.8. The left shoulder structure (see section 6.1 for a detailed description of the features of the pulse profile) seen for Intervals 1 and 2 (black and green) is slowly decaying and disappears completely for Interval 4 (blue). With the definition of "phase zero" reported in the previous section, the center of the main pulse peak is close to pulse phase 0.75 and increases leading to a slight shift of its position after 35 day phase 0.1. This variation in shape of the pulse profile is consistent with previous analysis (e.g. Scott et al. 2000) and it has been also discussed in Chapter 6.

9.4.2 Cyclotron line energy

As is shown in Figure 9.9, the value of the centroid of the cyclotron line varies between 33.89 ± 0.86 and 41.75 ± 0.39 for Interval 1, between 35.52 ± 1.03 and 41.62 ± 0.27 for Interval 2, between 31.92 ± 0.73 and 41.48 ± 0.14 for Interval 3 and between 32.99 ± 1.13 and 41.69 ± 0.14 for Interval 4.

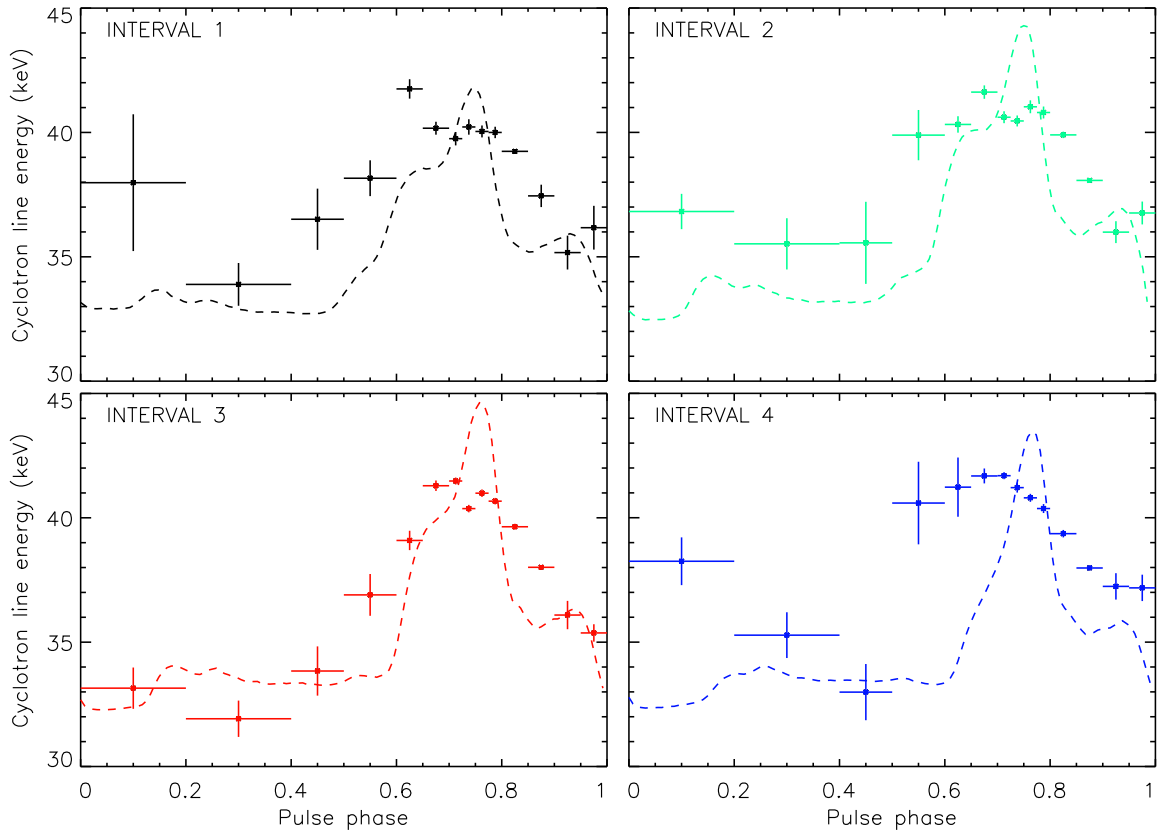

Figure 9.9: Cyclotron line energy profiles as function of the pulse phase for Interval 1(*top left*), Interval 2 (*top right*), Interval 3 (*bottom left*) and Interval 4 (*bottom right*).

This modulation roughly follows the shape of the pulse profile: the maximum value for the centroid of the cyclotron line is observed for all intervals in correspondence with the peak of the

pulse profile. This increase towards the pulse profile peak around pulse phase 0.75 is explained by the idea that at that phase the X-rays are originated closer to the surface of the neutron star, where the magnetic field strength is higher.

As mentioned before, from Figure 9.9 it is possible to identify the left shoulder around pulse phase 0.675.

The profiles of the four intervals show some fluctuations. The cyclotron line energy profile of Interval 1 is somewhat lower than the other profiles, and the profile of Interval 3 at phases closer to the left shoulder is shifted to the right with respect to the profiles of the other intervals. At low pulse phases, in the 0.0 – 0.40 pulse phase interval, there are the largest deviations within the four intervals. On the other hand, after pulse phase 0.75 which corresponds almost to the pulse peak, the profiles of the cyclotron line track each other very well. This is given in Figure 9.10 where it is clear that the mean shape of the profile remains constant over the 35 day phase.

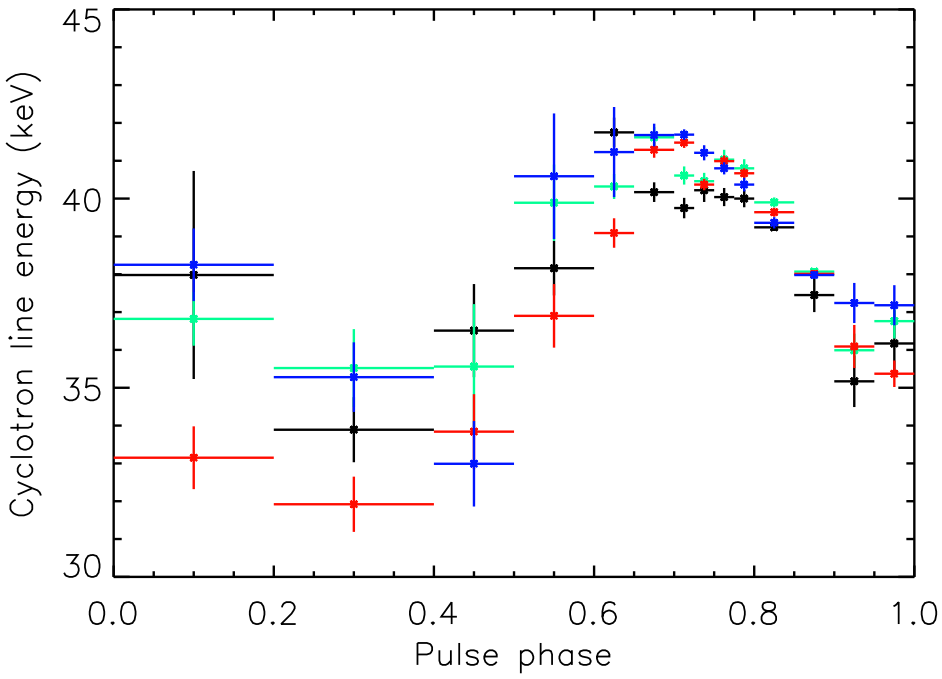

Figure 9.10: Overlay of the cyclotron line energy profiles as function of the pulse phase for all the intervals. Interval 1 is plotted in black, Interval 2 in green, Interval 3 in red and Interval 4 in blue.

9.4.3 Photon-index

In Figure 9.11 the profiles of the photon-index as function of the pulse phase are shown. As in the previous case, Interval 1 is plotted in black, Interval 2 in green, Interval 3 in red and Interval 4 in blue.

This parameter is relatively constant for pulse phases up to 0.6 (showing a small tendency to increase with increasing pulse phase), but shows large fluctuations at those phases which

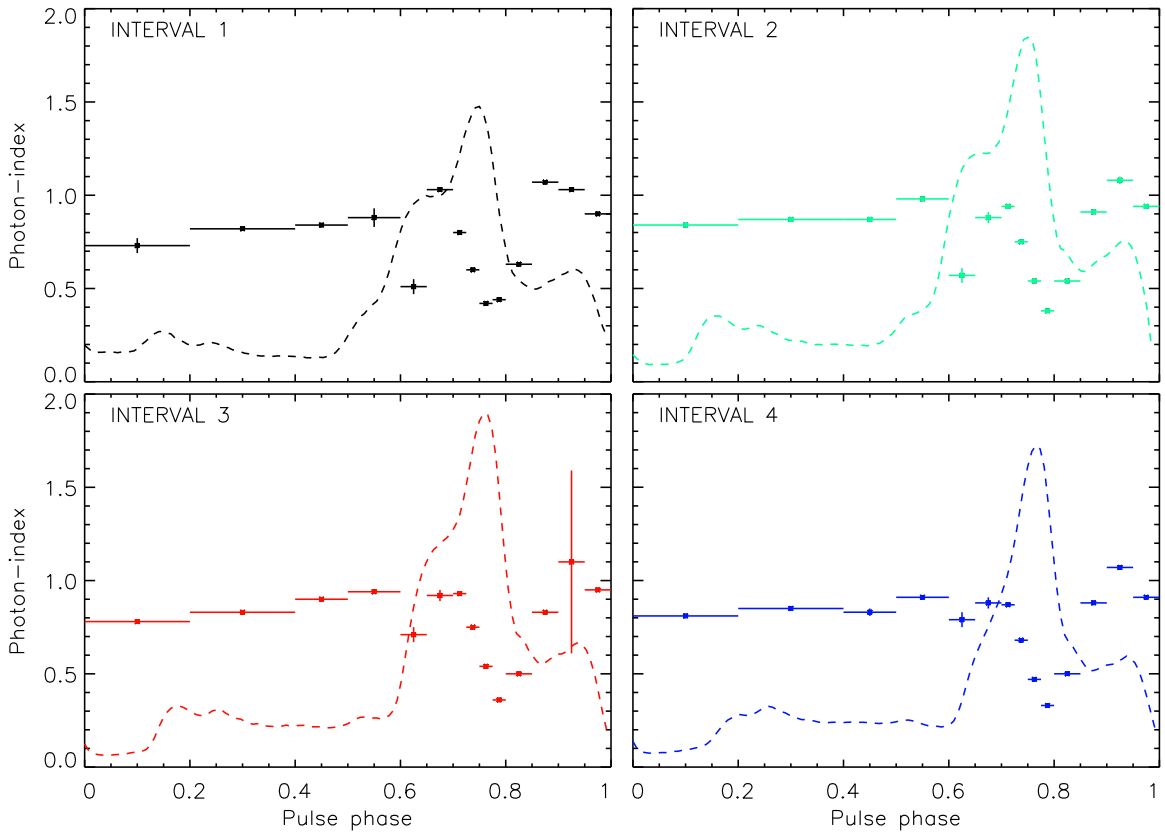

Figure 9.11: Photon-index profiles as function of the pulse phase for Interval 1(*top left*), Interval 2 (*top right*), Interval 3 (*bottom left*) and Interval 4 (*bottom right*).

correspond to the pulse peak. In particular, the photon-index ranges between 0.42 ± 0.01 and 1.07± 0.01 for Interval 1, between 0.54 ± 0.01 and 1.08 ± 0.02 for Interval 2, between 0.36 ± 0.01 and 1.10 ± 0.49 for interval 3 and between 0.33 ± 0.01 and 1.07 ± 0.01 for Interval 4.

This is consistent with the hardening of the X-ray spectrum in correspondence with higher luminosity at the peak of the emission. The photon-index profiles show how Γ decreases during the peak of the pulse profile almost in a symmetric way, following its sharpening. As reported before, this reflects the dependence of the optical depth on the angle between the direction of the magnetic field and the line of sight of the observer.

As, in the case of the cyclotron line energy profile, also the photon-index profile seems to be constant in shape and not dependent of 35 day phase (see Figure 9.12).

9.4.4 The iron line normalization

Another spectral parameter which shows a clear modulation as function of the 35 day phase is the iron line normalization. The latter shows a small increase up to pulse phase 0.7. Then, the normalization of the iron line drops down into a minimum around pulse phase 0.8 before reaching a constant value at pulse phase 0.9. In particular, the minimum is coincident with the peak of the X-ray pulse (see Figure 9.13). The modulation presented here is consistent

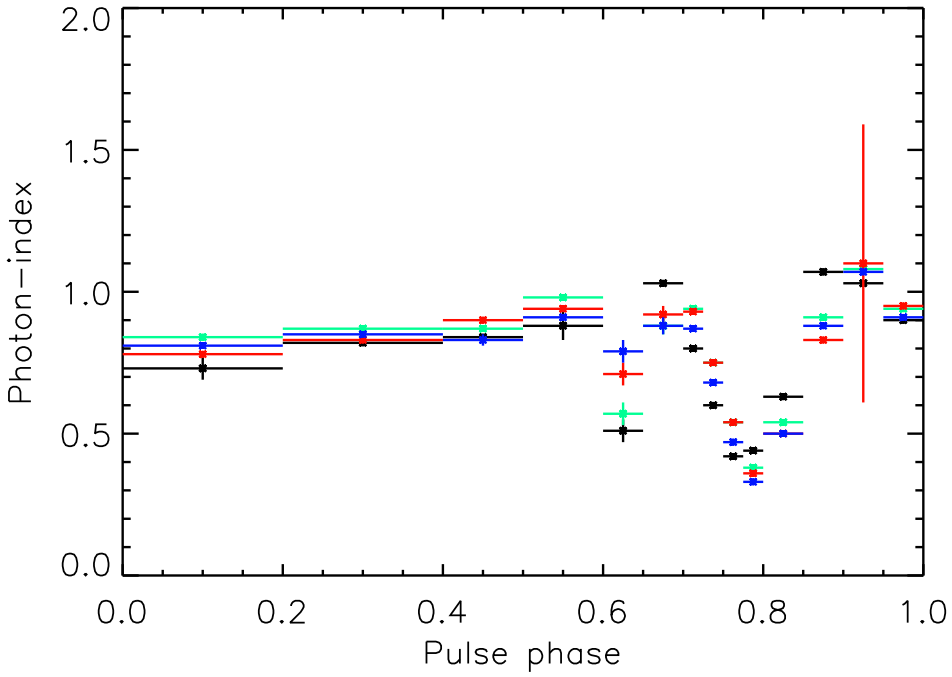

Figure 9.12: Overlay of the photon-index profiles as function of the pulse phase for all the intervals. In particular, Interval 1 is plotted in black, Interval 2 in green, Interval 3 in red and Interval 4 in blue.

with previous analyses. An example is the study of Oosterbroek et al. (1997) shown in Figure 9.14. Unfortunately, the comparison has to be done with the $Fe-L$ normalization because in Oosterbroek et al. (1997) the $Fe-K$ was not treated due to the bad quality of the data. They also suggested that the iron line, both K and L are expected to be originated in a similar region where also the soft component comes from. Oosterbroek et al. (2000), studying the Short-On of Her X-1 with *BeppoSAX* observations, presented the variation of both the $Fe-K$ and $Fe-L$ normalization during the Main-On and the Short-On. In this analysis, the $Fe-L$ normalization appears to be relatively constant, on the other hand the $Fe-K$ normalization shows a small variation, but not very well defined. The last example comes from Zane et al. (2004) with *XMM-Newton* observations. Also in this case, there is a variation of the $Fe-K$ normalization similar to what is shown in Figure 9.13, even if the resolution is worse.

This modulation is very interesting from a physical point of view. Taking into account the shape of the pulse profile, the minimum of the iron line normalization corresponds to the peak of the X-ray emission. It is believed that the pencil beam corresponds to the situation in which the observer looks at the neutron star directly into the beam. On the other hand, a minimum in the normalization of the iron line means that there is no material which can be responsible for the production of fluorescence. This can provide some constraints on the geometry of the accretion column. The only geometry which allows this situation is the hollow cone (see Figure 2.8). The

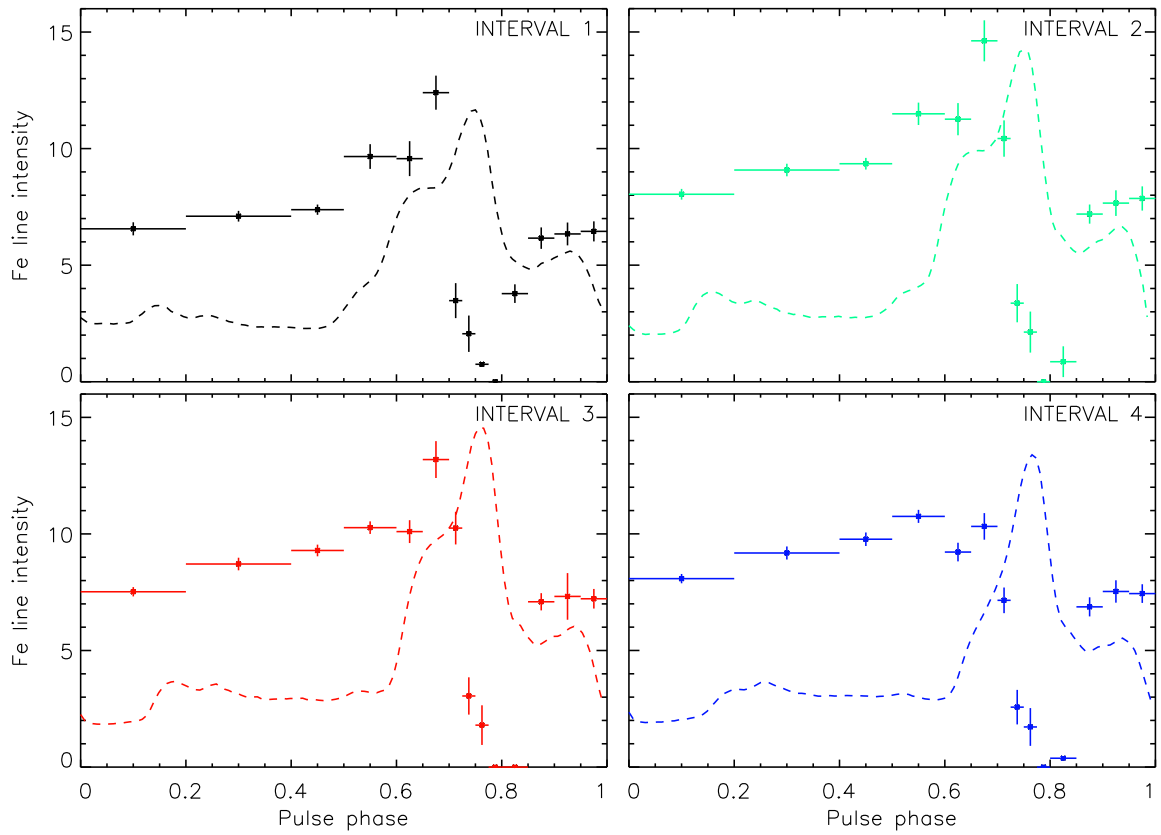

Figure 9.13: Iron line intensity profiles as function of the pulse phase for Interval 1(*top left*), Interval 2 (*top right*), Interval 3 (*bottom left*) and Interval 4 (*bottom right*).

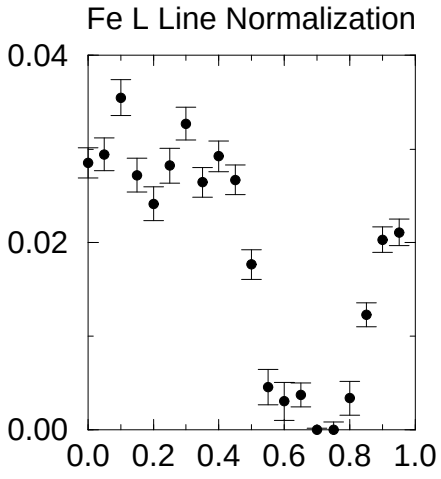

Figure 9.14: $Fe - L$ normalization as function of the pulse phase from Oosterbroek et al. (1997).

only questionable fact to this conclusion is the temperature of the plasma in the region of the accretion column. As discussed in Chapter 8, White et al. (1983) suggested that in the accretion column the plasma is too hot to allow any transition between the levels and no fluorescence can be produced. On the other hand, some authors have advocated in the accretion column as the most probably site for the production of the iron line (see e.g. Leahy 2001 and İnam & Baykal 2005). This suggestion matches with the modulation of the $Fe-K$ normalization presented here.

9.4.5 Other spectral parameters

Other spectral parameters such as E_{cut} or E_{fold} show a different behavior as that of the cyclotron line energy or the photon-index. Figures 9.16 and 9.17 show how these parameters also dramatically change at the pulse peak. Other phases values are much more scattered and they cannot be considered constant as in the case of the cyclotron line energy and the photon-index. This is also the case for the width (σ_{cyc}) and the depth (τ_{cyc}) of the cyclotron line absorption feature (see Figures 9.18 and 9.19).

All the values of the spectral parameters for all of the intervals are listed in Tables 9.3, 9.4, 9.5, 9.6, 9.7 and 9.8.

9.5 Residuals at pulse phase range 0.80-0.85

Throughout this analysis a singular behavior of the continuum has been noted. All the residuals of the X-ray spectrum for the bin 0.80 - 0.85 of the pulse phase corresponding to the trailing edge of main peak in the pulse profile show huge fluctuations around 8 keV. This is also the case of few a neighbouring pulse phase bins (e.g. 0.85 - 0.90). The fact that this behavior is repeated always at the same pulse phase bin (0.80 - 0.85) for all the intervals leads to the conclusion that there should be a physical explanation. In Figure 9.15 an example of residuals of pulse phase bin 0.80 - 0.85 for Interval 3 is shown. Unfortunately, so far no explanations are proposed.

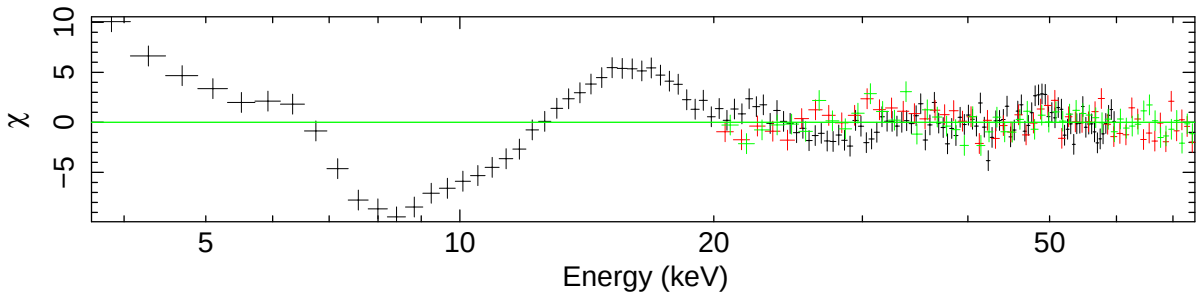

Figure 9.15: Residuals of the X-ray spectrum of pulse phase bin 0.80 - 0.85 for Interval 3.

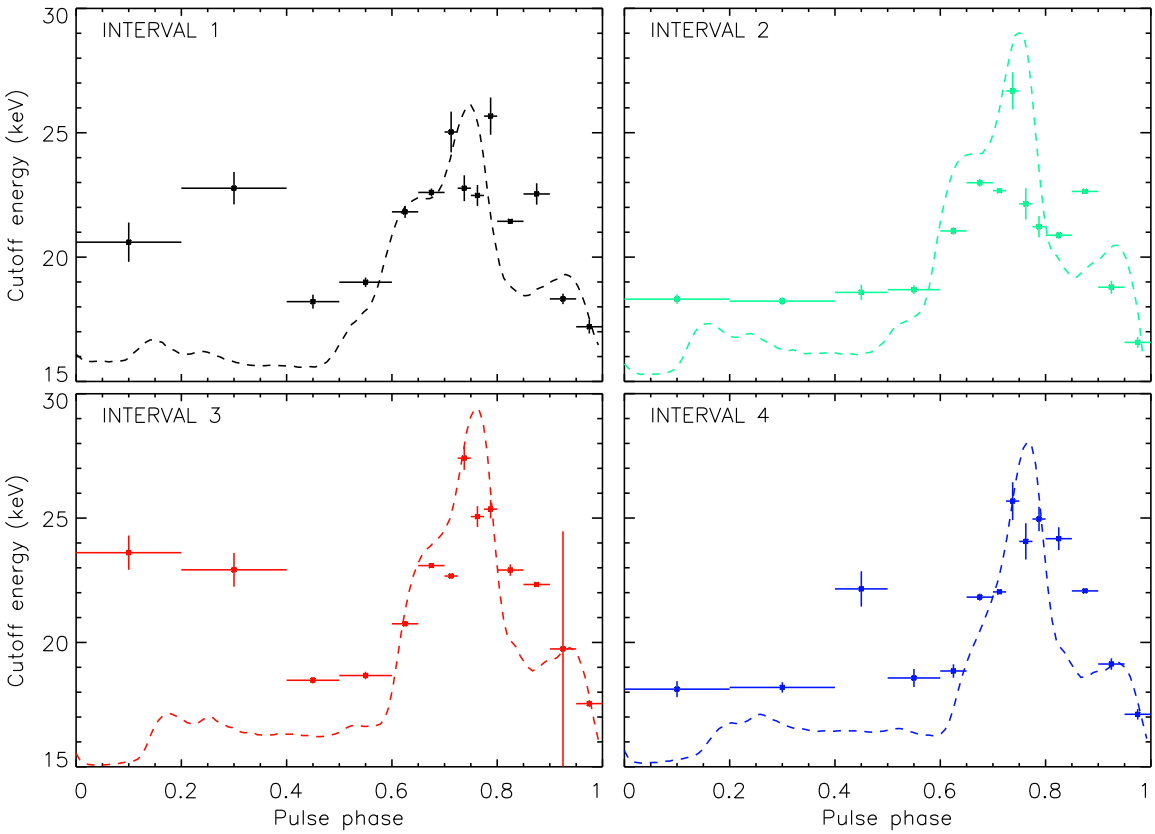

Figure 9.16: Cutoff energy profiles as function of the pulse phase for Interval 1(*top left*), Interval 2 (*top right*), Interval 3 (*bottom left*) and Interval 4 (*bottom right*).

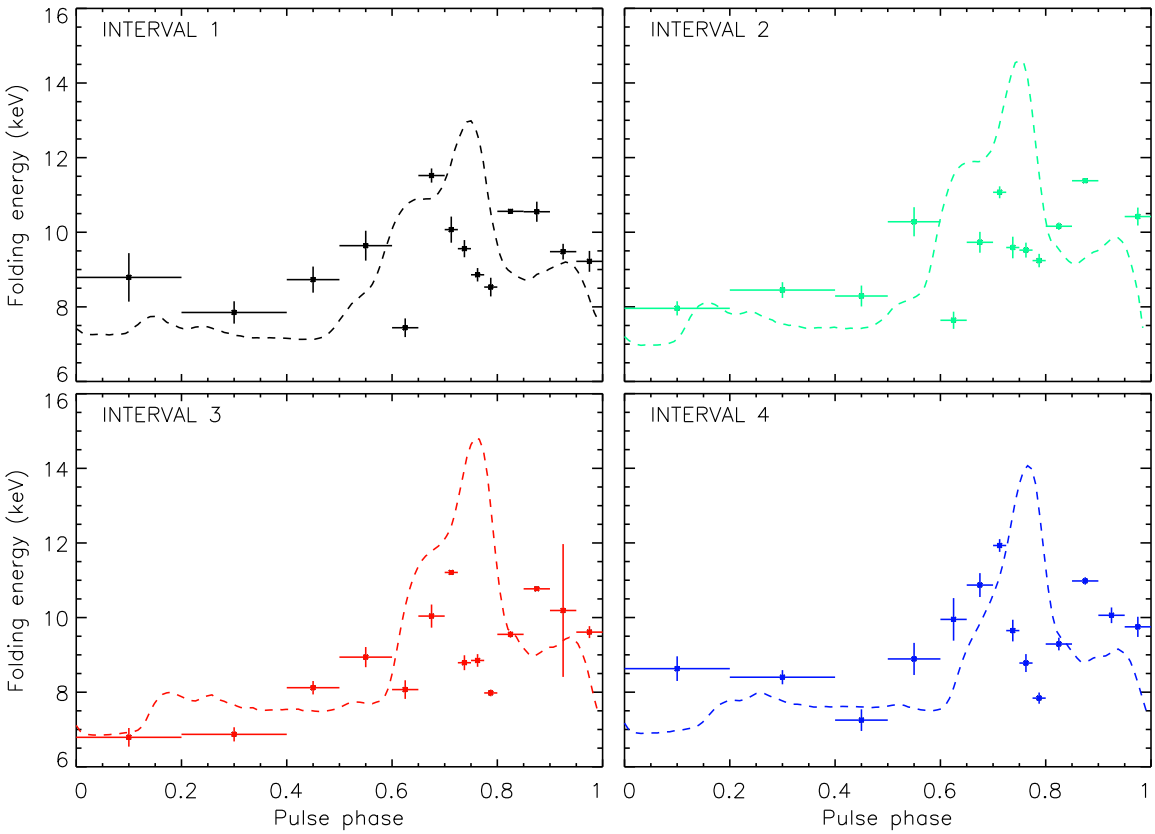

Figure 9.17: Folding energy profiles as function of the pulse phase for Interval 1(*top left*), Interval 2 (*top right*), Interval 3 (*bottom left*) and Interval 4 (*bottom right*).

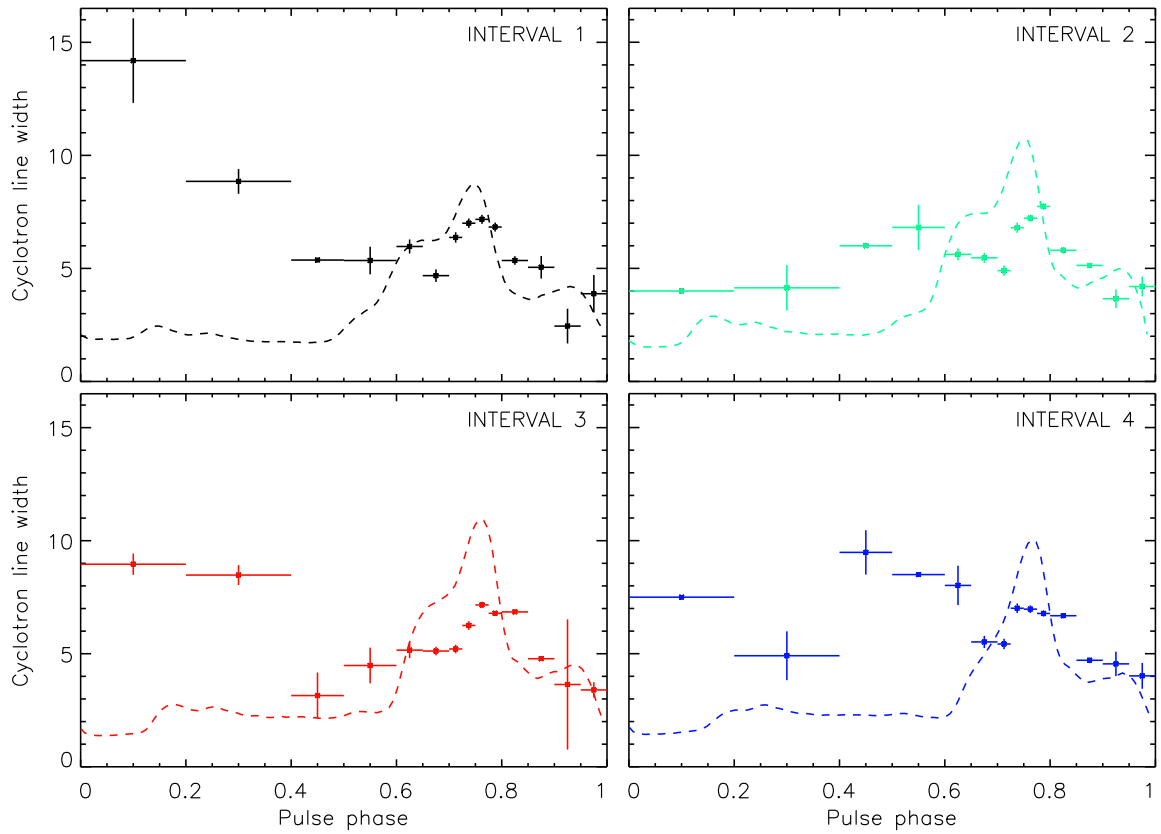

Figure 9.18: Width (σ) of the cyclotron line profiles as function of the pulse phase for Interval 1(*top left*), Interval 2 (*top right*), Interval 3 (*bottom left*) and Interval 4 (*bottom right*).

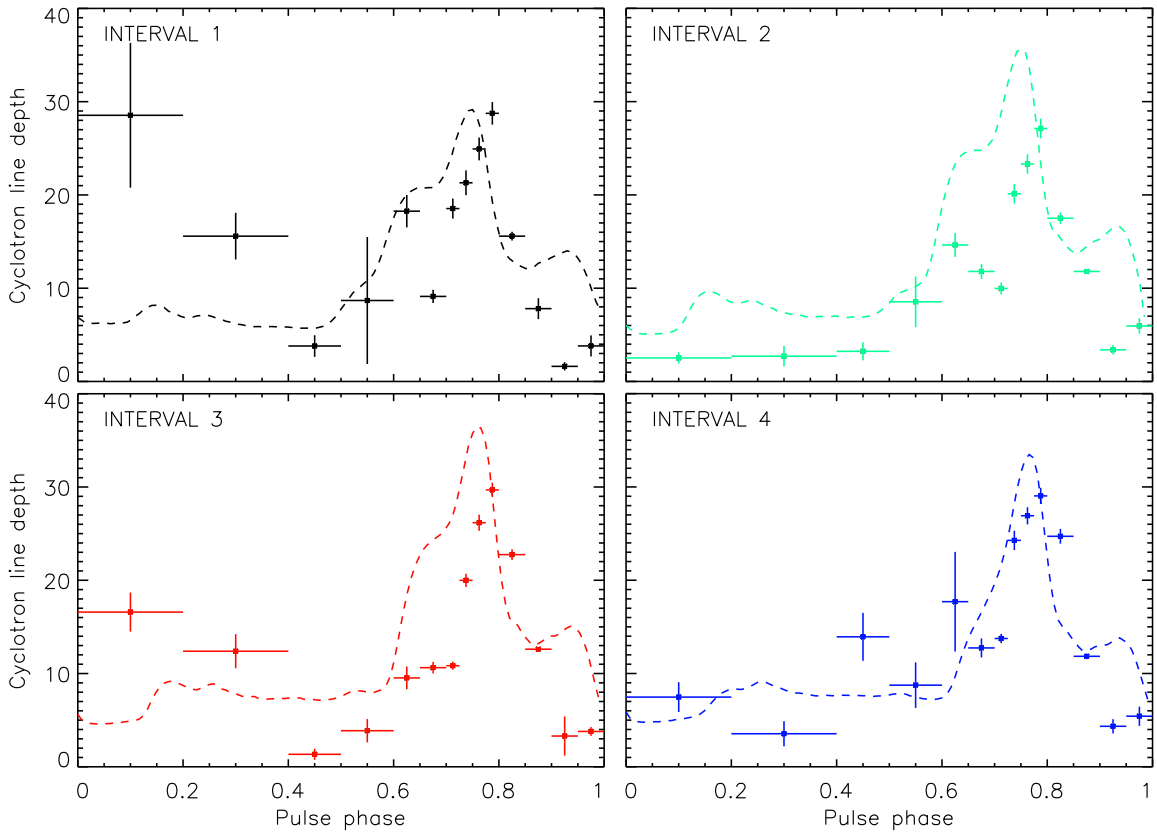

Figure 9.19: Depth (τ) of the cyclotron line profiles as function of the pulse phase for Interval 1(*top left*), Interval 2 (*top right*), Interval 3 (*bottom left*) and Interval 4 (*bottom right*).

Table 9.3: Summary of the spectral parameters for Interval 1.

Bin center	E_{cyc} (keV)	Photon-index Γ	E_{cut} (keV)	E_{fold} (keV)	Iron line norm. (10^{-3})
0.1	37.98 ± 2.75	0.73 ± 0.04	20.60 ± 0.79	8.79 ± 0.65	6.56 ± 0.28
0.3	33.89 ± 0.86	0.82 ± 0.01	22.77 ± 0.65	7.85 ± 0.30	7.10 ± 0.23
0.45	36.51 ± 1.23	0.84 ± 0.01	18.21 ± 0.28	8.73 ± 0.35	7.38 ± 0.22
0.55	38.16 ± 0.72	0.88 ± 0.05	18.99 ± 0.19	9.64 ± 0.40	9.66 ± 0.53
0.625	41.75 ± 0.39	0.51 ± 0.04	21.82 ± 0.24	7.44 ± 0.25	9.57 ± 0.75
0.675	40.17 ± 0.26	1.03 ± 0.005	22.60 ± 0.16	11.52 ± 0.19	12.40 ± 0.73
0.7125	39.75 ± 0.27	0.80 ± 0.01	25.03 ± 0.82	10.07 ± 0.35	3.48 ± 0.75
0.7375	40.22 ± 0.31	0.60 ± 0.01	22.77 ± 0.52	9.56 ± 0.23	2.06 ± 0.78
0.7625	40.04 ± 0.24	0.42 ± 0.01	22.48 ± 0.42	8.86 ± 0.18	$0.75 \pm$ -
0.7875	40.00 ± 0.23	0.44 ± 0.01	25.67 ± 0.75	8.53 ± 0.25	$0.00 \pm$ -
0.825	39.24 ± 0.08	0.63 ± 0.003	21.44 ± 0.05	10.56 ± 0.07	3.78 ± 0.40
0.875	37.45 ± 0.45	1.07 ± 0.01	22.54 ± 0.43	10.55 ± 0.27	6.16 ± 0.46
0.925	35.17 ± 0.68	1.03 ± 0.01	18.32 ± 0.21	9.48 ± 0.21	6.34 ± 0.49
0.975	36.17 ± 0.88	0.90 ± 0.01	17.20 ± 0.27	9.22 ± 0.28	6.45 ± 0.43

Table 9.4: Summary of the spectral parameters for Interval 2.

Bin center	E_{cyc} (keV)	Photon-index Γ	E_{cut} (keV)	E_{fold} (keV)	Iron line norm. (10^{-3})
0.1	36.82 ± 0.71	0.84 ± 0.01	18.31 ± 0.19	7.96 ± 0.19	8.04 ± 0.23
0.3	35.52 ± 1.03	0.87 ± 0.01	18.23 ± 0.15	8.45 ± 0.21	9.08 ± 0.27
0.45	35.56 ± 1.65	0.87 ± 0.01	18.58 ± 0.30	8.29 ± 0.28	9.35 ± 0.25
0.55	39.89 ± 1.01	0.98 ± 0.01	18.69 ± 0.18	10.28 ± 0.39	11.49 ± 0.48
0.625	40.32 ± 0.33	0.57 ± 0.04	21.05 ± 0.15	7.64 ± 0.23	11.26 ± 0.69
0.675	41.62 ± 0.27	0.88 ± 0.03	22.99 ± 0.16	9.73 ± 0.28	14.62 ± 0.88
0.7125	40.61 ± 0.24	0.94 ± 0.004	22.67 ± 0.07	11.07 ± 0.16	10.43 ± 0.78
0.7375	40.46 ± 0.22	0.75 ± 0.01	26.68 ± 0.75	9.59 ± 0.29	3.37 ± 0.82
0.7625	41.03 ± 0.26	0.54 ± 0.01	22.14 ± 0.63	9.52 ± 0.20	2.13 ± 0.88
0.7875	40.80 ± 0.24	0.38 ± 0.01	21.22 ± 0.43	9.24 ± 0.18	$0.00 \pm$ -
0.825	39.90 ± 0.13	0.54 ± 0.01	20.88 ± 0.14	10.16 ± 0.10	0.86 ± 0.66
0.875	38.07 ± 0.09	0.91 ± 0.003	22.64 ± 0.08	11.38 ± 0.07	7.19 ± 0.41
0.925	35.99 ± 0.44	1.08 ± 0.02	18.79 ± 0.26	20.34 ± 0.21	7.66 ± 0.55
0.975	36.76 ± 0.46	0.94 ± 0.01	16.57 ± 0.22	10.42 ± 0.24	7.86 ± 0.52

Table 9.5: Summary of the spectral parameters for Interval 3.

Bin center	E_{cyc} (keV)	Photon-index Γ	E_{cut} (keV)	E_{fold} (keV)	Iron line norm. (10^{-3})
0.1	33.15 ± 0.83	0.78 ± 0.01	23.61 ± 0.69	6.79 ± 0.25	7.52 ± 0.20
0.3	31.92 ± 0.73	0.83 ± 0.01	22.92 ± 0.68	6.87 ± 0.19	8.71 ± 0.27
0.45	33.84 ± 0.99	0.90 ± 0.01	18.48 ± 0.13	8.12 ± 0.18	9.29 ± 0.25
0.55	36.90 ± 0.84	0.94 ± 0.01	18.67 ± 0.15	8.94 ± 0.27	10.27 ± 0.27
0.625	39.09 ± 0.39	0.71 ± 0.04	20.75 ± 0.11	8.07 ± 0.25	10.10 ± 0.49
0.675	41.29 ± 0.21	0.92 ± 0.03	23.09 ± 0.09	10.04 ± 0.31	13.19 ± 0.79
0.7125	41.48 ± 0.14	0.93 ± 0.004	22.67 ± 0.06	11.21 ± 0.05	10.25 ± 0.70
0.7375	40.37 ± 0.15	0.75 ± 0.005	27.41 ± 0.47	8.79 ± 0.20	3.05 ± 0.80
0.7625	40.99 ± 0.15	0.54 ± 0.01	25.06 ± 0.42	8.85 ± 0.17	1.80 ± 0.85
0.7875	40.67 ± 0.13	0.36 ± 0.01	25.36 ± 0.37	7.98 ± 0.09	$0.00 \pm$ -
0.825	39.64 ± 0.12	0.50 ± 0.005	22.91 ± 0.23	9.55 ± 0.09	$0.00 \pm$ -
0.875	38.01 ± 0.06	0.83 ± 0.003	22.33 ± 0.02	10.77 ± 0.05	7.09 ± 0.37
0.925	36.09 ± 0.57	1.10 ± 0.49	19.74 ± 4.73	10.19 ± 1.78	7.32 ± 1.00
0.975	35.37 ± 0.35	0.95 ± 0.01	17.54 ± 0.14	9.61 ± 0.16	7.22 ± 0.42

Table 9.6: Summary of the spectral parameters for Interval 4.

Bin center	E_{cyc} (keV)	Photon-index Γ	E_{cut} (keV)	E_{fold} (keV)	Iron line norm. (10^{-3})
0.1	38.25 ± 0.96	0.81 ± 0.01	18.12 ± 0.32	8.63 ± 0.33	8.08 ± 0.20
0.3	35.28 ± 0.92	0.85 ± 0.01	18.19 ± 0.21	8.40 ± 0.19	9.18 ± 0.28
0.45	32.99 ± 1.13	0.83 ± 0.02	22.15 ± 0.71	7.25 ± 0.29	9.77 ± 0.29
0.55	40.59 ± 1.66	0.91 ± 0.01	18.57 ± 0.36	8.89 ± 0.43	10.75 ± 0.28
0.625	1.23 ± 1.19	0.79 ± 0.04	18.85 ± 0.27	9.95 ± 0.57	9.22 ± 0.40
0.675	41.68 ± 0.30	0.88 ± 0.03	21.82 ± 0.14	10.87 ± 0.32	10.32 ± 0.57
0.7125	41.69 ± 0.14	0.87 ± 0.004	22.03 ± 0.05	11.93 ± 0.17	7.15 ± 0.55
0.7375	41.21 ± 0.20	0.68 ± 0.01	25.68 ± 0.76	9.65 ± 0.29	2.57 ± 0.74
0.7625	40.80 ± 0.16	0.47 ± 0.01	24.06 ± 0.73	8.78 ± 0.24	1.72 ± 0.81
0.7875	40.37 ± 0.18	0.33 ± 0.01	24.96 ± 0.49	7.84 ± 0.15	$0.00 \pm$ -
0.825	39.36 ± 0.15	0.50 ± 0.01	24.17 ± 0.46	9.29 ± 0.17	$0.38 \pm$ -
0.875	37.98 ± 0.10	0.88 ± 0.005	22.07 ± 0.06	10.98 ± 0.10	6.87 ± 0.41
0.925	37.24 ± 0.53	1.07 ± 0.01	19.13 ± 0.23	10.06 ± 0.21	7.53 ± 0.48
0.975	37.18 ± 0.53	0.91 ± 0.01	17.11 ± 0.21	9.75 ± 0.27	7.44 ± 0.40

Table 9.7: Summary of the values of σ_{cyc} and τ_{cyc} for intervals 1 and 2.

Bin center	Interval 1		Interval 2	
	σ_{cyc} Interval 1	τ_{cyc} Interval 1	σ_{cyc} Interval 2	τ_{cyc} Interval 2
0.1	14.19 ± 1.87	28.54 ± 7.76	4.00 -	2.52 ± 0.60
0.3	8.85 ± 0.55	15.58 ± 2.50	4.14 ± 1.01	2.71 ± 1.09
0.45	5.37 ± 0.00	3.80 ± 1.16	6.00 -	$3.23, \pm 0.96$
0.55	5.35 ± 0.61	8.68 ± 6.81	1.00 ± 1.87	8.54 ± 2.71
0.625	5.97 ± 0.31	18.26 ± 1.74	5.62 ± 0.26	14.63 ± 1.28
0.675	4.68 ± 0.28	9.12 ± 0.71	5.47 ± 0.22	11.79 ± 0.79
0.7125	6.37 ± 0.23	18.54 ± 1.07	4.90 ± 0.23	9.97 ± 0.64
0.7375	7.00 ± 0.21	21.30 ± 1.33	6.80 ± 0.23	20.12 ± 1.05
0.7625	7.17 ± 0.20	24.93 ± 1.22	7.22 ± 0.15	23.31 ± 1.04
0.7875	6.83 ± 0.20	28.75 ± 1.21	7.74 ± 0.15	27.12 ± 1.06
0.825	5.35 ± 0.19	15.58 ± 0.47	5.80 ± 0.15	17.50 ± 0.63
0.875	5.05 ± 0.50	7.81 ± 1.12	5.13 ± 0.07	11.79 ± 0.20
0.925	2.45 ± 0.77	1.62 ± 0.45	3.66 ± 0.41	3.39 ± 0.51
0.975	3.88 ± 0.83	3.81 ± 1.13	4.20 ± 0.44	5.95 ± 0.84

Table 9.8: Summary of the values of σ_{cyc} and τ_{cyc} for intervalas 3 and 4.

Bin center	Interval 3		Interval 4	
	σ_{cyc}	τ_{cyc}	σ_{cyc}	τ_{cyc}
0.1	8.96 ± 0.47	16.59 ± 2.10	7.5 -	7.47 ± 1.60
0.3	8.48 ± 0.44	12.39 ± 1.83	4.91 ± 1.08	3.54 ± 1.35
0.45	3.15 ± 1.02	1.34 ± 0.59	9.48 ± 0.98	13.93 ± 2.57
0.55	4.48 ± 0.79	3.87 ± 1.25	8.5 -	8.75 ± 2.44
0.625	5.16 ± 0.35	9.53 ± 1.22	8.02 ± 0.87	17.70 ± 5.34
0.675	5.12 ± 0.19	10.63 ± 0.62	5.52 ± 0.27	12.74 ± 1.02
0.7125	5.21 ± 0.19	10.84 ± 0.43	5.35 ± 0.28	13.36 ± 0.87
0.7375	6.25 ± 0.19	19.99 ± 0.71	7.01 ± 0.21	24.27 ± 1.04
0.7625	7.16 ± 0.14	26.17 ± 0.86	6.97 ± 0.17	26.91 ± 0.92
0.7875	6.79 ± 0.11	29.69 ± 0.77	6.78 ± 0.14	29.04 ± 0.87
0.825	6.85 ± 0.09	22.75 ± 0.57	6.68 ± 0.12	24.71 ± 0.79
0.875	4.78 ± 0.06	12.61 ± 0.16	4.71 ± 0.13	11.84 ± 0.30
0.925	3.64 ± 2.88	3.30 ± 2.10	4.55 ± 0.54	4.34 ± 0.76
0.975	3.40 ± 0.34	3.79 ± 0.47	4.02 ± 0.57	5.42 ± 1.03

10 Summary and conclusions

The results presented in this work contribute to the advance of our knowledge of the accreting binary X-ray pulsar Her X-1. Despite the fact that this system is one of the best studied objects, the huge collection of archival data available and new observations permit to investigate deeply both the phenomenology of the source and the physics which governs its observational properties.

In particular, making use of *RXTE* and *INTEGRAL* archival data, several analyses have been performed:

- extraction of X-ray light curves of Her X-1;
- determination of the turn-ons on the basis of the pulse profiles;
- re-determination of the positive correlation between the cyclotron line energy and the bolometric luminosity of the source;
- study of the X-ray spectrum of Her X-1 and the evolution of spectral parameters as a function of the 35 day phase;
- study of the evolution of the spectral parameters as a function of the pulse phase through the pulse phase resolved spectroscopy analysis.

10.1 X-ray light curves of Her X-1

This analysis has been performed with the aim to monitor the behavior of the source and observe the well known "on-off cycle". In particular, X-ray light curves of Her X-1 have been constructed with both *RXTE* (observations from 1996 until 2010) and *INTEGRAL* (observations in 2005 and 2007) archival data. This first analysis has been highly important to understand which 35 day cycles could provide a good photon statistics for subsequent analyses.

10.2 Determination of the turn-ons from the pulse profiles

The extraction of the pulse profiles from *RXTE* archival data allowed to determine the turn-ons on the basis of the pulse profile shape and give an alternative way to construct the (O-C) diagram (see section 6.5).

This analysis permitted first to verify the variation of the pulse profile as a function of 35 day phase and then to determine the "35 day phase zero", which corresponds to the transition between the off-state and the Main-On (the so-called turn-on). This represents an alternative way for the counting of the 35 day cycles based only on the pulse profiles shape and not on the modulation of the X-ray flux.

Comparing the turn-ons obtained through the pulse profile analysis and the observed turn-ons, it is clear how their histories track each other perfectly. This is described in section 6.5 where it is shown how the "phase-zero" based on the observed turn-ons and the "phase-zero" based on the pulse profiles analysis are identical within statistical uncertainties (see Figure 6.10).

Staubert et al. (2009a) have suggested the presence of two different synchronized clocks in Her X-1, one related to the accretion disk and responsible for the observed turn-ons, and a second one related to the free precession of the neutron star responsible for the variations of the pulse profiles. The new analysis of the pulse profiles led to the conclusion that there is only one clock in Her X-1 which is responsible for both turn-ons.

These results opened new questions about the pulse profiles variations. Assuming the free precession as responsible for the variation of the pulse profiles and for those times of the turn-ons, there are two main arguments which are difficult to explain. The first one is related to the change of the precessional period by several percent on short timescales of about 100 days (Staubert et al. 2009a). This would need external forces strong enough to change it. Torques to the axis of inertia have to be excluded to reproduce such variations, but the physics of the interior of the neutron star can be taken into account. In particular, the complex configuration with the crust and the liquid core can be responsible for phenomena where a strong time variability is observed. Another possibility is related to the occurrence of glitches (Staubert et al. 2009a). The second argument is about the role of the free precession on the accretion disk. Assuming that the turn-ons are due to the precession of the accretion disk, how the free precession can slave the accretion disk is unclear. Staubert et al. (2009a) have proposed a feedback in the system where the neutron star represents the "master clock" because of its relatively stability, but the synchronization reported in the results of this work makes this feedback questionable. This led to the conclusion that the free precession model cannot explain the observed variations of the pulse profiles shape with the 35 day phase

On the other hand, if there is no free precession for Her X-1, an explanation to the observed variations of the pulse profiles and the synchronization of the turn-ons is needed. A model has been proposed by Scott et al. (2000) using *Ginga* and *RXTE* observations where these variations are due to a combination of changes in the accretion geometry and occultation of the X-ray emitting region by the precessing accretion disk. Despite this suggestion, a model which explains the multi-structured pulse profile of Her X-1 with its variations as function of 35 day phase is still necessary.

10.3 Re-determination of the Luminosity / cyclotron line energy correlation

This analysis is an update of the original one presented by Staubert et al. (2007). The aim was to confirm the positive correlation between the bolometric luminosity of the source and the energy of the cyclotron line. This work confirmed the positive correlation and allowed to answer the question whether the maximum of the $2-10\,\mathrm{keV}$ flux monitored by *RXTE*/ASM can be taken as a measure of the bolometric luminosity of the source. The good agreement between the flux used in the original analysis and the flux calculated in this work, gave a positive answer to the question.

In particular, the maximum ASM flux used in the original analysis scales well with the max-

imum 3.5 – 60 keV flux estimated in this work. This is shown in section 7.4 and 7.5 where the correlations between the fluxes and the energies of the cyclotron line are reported. A direct comparison to the original analysis can be made considering the slope of the linear fit for the correlation between the luminosity and the cyclotron line energy. The slope of the linear best fit is determined to (0.67 ± 0.14) keV/(cts s^{-1}), which is in good agreement with the (0.66 ± 0.10) keV/(cts s^{-1}) found in the original analysis (see Figures 7.3, 7.8 and 7.9). This confirms what was found in Staubert et al. (2007) and can be summarized as follows: the value of the cyclotron line energy E_{cyc} increases by ∼7% for a change in flux of a factor of two.

This is consistent with the physics described in section 2.3. The *negative correlation* (the decrease of E_{cyc} with luminosity), which has been repeatedly observed for high luminosity transients such as V 0332+53 and 4U 0115+63 (Mihara et al. 1998, Mowlavi et al. 2006, Nakajima et al. 2006 and Tsygankov et al. 2006), has been interpreted in the following way: when the mass accretion rate (and hence the luminosity) increases, the height of the radiative shock above the neutron star surface increases, leading to a decrease in the effective magnetic field strength in the scattering region and therefore to a decrease in E_{cyc}. This is in line with theoretical considerations about accretion in the (locally) super-Eddington regime (Burnard et al. 1991). In the sub-Eddington regime, however, believed to be realized in Her X-1, the deceleration of the accreted material is thought to be due to Coulomb drag and collective plasma effects (Nelson et al. 1993). In this case, under an increased accretion rate the atmosphere is compressed by the ram pressure of the infalling material and the scattering region moves closer to the neutron star surface. This is equivalent to an increase in effective field strength and an increase in E_{cyc}, hence to a *positive correlation* with luminosity (Staubert et al. 2007). These results have been published in Vasco et al. (2011).

The recent analysis of Klochkov et al. (2011) supports the same correlation on short time intervals for three different objects: 4U 0115+63, V 0332+53, and Her X-1.

10.4 Spectral analysis

The spectral analysis performed with *RXTE* allowed a deep investigation of the behavior of the spectral parameters as a function of the 35 day phase. This analysis showed that some spectral parameters such as the cutoff energy and the folding energy remains constant with 35 day phase. In particular, the cutoff energy is constant around 21.16 ± 0.15 keV and the exponential folding energy around 10.22 ± 0.07 keV (see Figure 8.4, top panel).

On the other hand, the photon-index does show a modulation with 35 day phase. Before 35 day phase 0.15 it is constant high around 0.93 ± 0.01 and between 35 day phases 0.17 and 0.23 it is constant low around a mean value of 0.84 ± 0.01 (see Figure 8.4, bottom panel).

From this analysis it has been also possible to describe the evolution of both the column density N_H and the total flux of the source as function of the 35 day phase. For an increase of the column density, a decrease of the flux is observed (see Figure 8.9). An observer observes less X-ray flux when more cold material is present between it and the source.

A different picture has to be drawn to describe the variation of the iron line intensity. For X-ray pulsars, the energy of the iron line is detected around 6.4 keV (Nagase 1989) and it is explained as fluorescent emission from ionized iron in a relatively cool environment (Ohashi et al. 1984). The measurement of the iron line plays a key role when investigating the circumstellar matter in

close binary systems. Studies of Vela X-1 and GX 301-2 showed that the iron line intensity and the continuum intensity are correlated. The iron line is in fact produced through the fluorescence of continuum X-ray absorbed by cool matter surrounding the central source (Nagase 1989). This picture seems to be consistent with the results of this thesis. In particular, the iron line intensity follows the 3.5 – 60 keV flux as a function of the 35 day phase, while the width of the iron line remains constant (see Figure 8.5). In addition, the correlation between the continuum intensity and the iron line intensity is confirmed. This is shown in Figure 8.6 where it is also possible to distinguish two different branches: one for 35 day phases below 0.15 and and the other one for 35 day phases above 0.15.

Unfortunately, a physical/geometrical model which takes into account all of these information is still unclear. Surely, it has been noticed that the 35 day phase 0.15 is the signature of a change in the geometry of the system. Around this 35 day phase the maximum in X-ray flux is observed. It may mark the transition between the outer edge of the accretion disk providing minimum absorption and the inner edge of the disk (probably starting with the hot corona) starting to get into the line of sight. Despite this, the results presented in Chapter 8 for both the iron line emission and the complicated evolution of the N_H as a function of the 35 day phase suggest the presence of different zones around the neutron star responsible for the observed X-ray spectrum. A good example of this geometry can be summarized by the analysis of Jimenez-Garate et al. (2002) shown in Figure 10.1. In this sketch, the atmosphere surrounding the system is defined as a thin skin on the disk which emits X-ray recombination emission. In this model, the corona and the disk atmosphere might be responsible for the narrow-line emission. In the magnetosphere, a highly ionized and Compton-thick structure is formed by the plasma which comes from the inner disk. This site is responsible for Compton scattering, X-ray absorption and recombination emission (see Jimenez-Garate et al. 2002 for details).

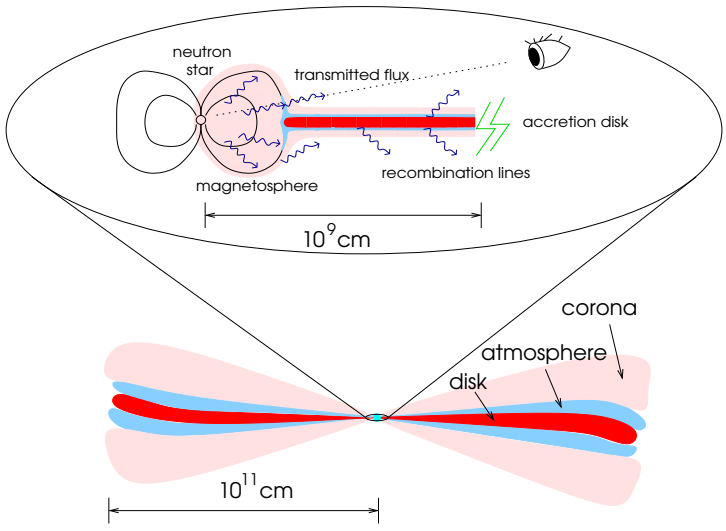

Figure 10.1: Hypothetical sketch of an accreting X-ray pulsar and the surrounding environment by Jimenez-Garate et al. (2002).

10.5 Pulse phase resolved spectroscopy

The pulse phase resolved spectroscopy of the source permitted to study the evolution of the spectral parameters as a function of the pulse phase.

As was already described, the cyclotron line energy profiles follow, to first approximation, the shape of the pulse profiles: the centroid of the cyclotron line energy is higher at the maximum of the pulse peak and decreases at the rest of the pulsation. However, the mean shape can be considered constant as a function of the 35 day phase. This has been demonstrated performing the pulse phase resolved spectroscopy for four different time intervals in order to have a good coverage of the entire Main-On of cycle 323. Thanks to the fine resolution of this analysis which improved dramatically the quantitative information about the variation of the cyclotron line profile, it is clear that there is no modulation of this absorption feature with the 35 day phase (see Figures 9.9 and 9.10). If there was free precession, an observer would look at the source at different places on the surface of the neutron star. This means that the observer should see a variation of the cyclotron line profile with 35 day phase. This is not the case: despite the fact that the profiles itself show some fluctuation, the shape of the profile with the 35 day phase is constant within statistical uncertainties.

An interesting result of the pulse phase resolved spectroscopy is the variation of the iron line intensity as a function of pulse phase. As shown in Figure 9.13, there is a minimum in correspondence of the peak of the X-ray profile as was also found in previous analyses by Zane et al. (2004), Leahy (2001) and Oosterbroek et al. (1997). This provides some constraints on the geometry of the accretion column. This may favour a geometry of a hollow cone (see Figure 2.8).

Acknowledgements

At the end of this PhD-adventure, I really would like to thank all the persons who have orbited around it.

My first acknowledgements are to Prof. Staubert and Prof. Santangelo. I am very grateful to Prof. Staubert for the patience, the shared experience and the constructive advices he gave to me during these three years. They represent a treasure which will be very important for my future, not only in astrophysics. Many thanks also to Andrea for giving me the possibility to start my PhD in his group and for being willing to know me and listen to me also in his daily busy life.

Ein sehr großes Dankeschön geht an all die Leute vom IAAT. Ich habe euch alle immer wie eine große Familie betrachtet, und ihr habt nie etwas getan, was meine Meinung ändern könnte. Besonderer Dank gilt den young colleagues für die (vielen) Kaffepausen, für das Teilnehmen an meinen Contests und PhDinners und, noch wichtiger, für den Versuch, alle meine "stupid questions" zu beantworten! Stif, Gabi (W.), Hermy, Benni und Beppe (in absolut zufälliger Reihenfolge), ihr wurdet während dieser drei Jahre zu wahren Freunden, und ich werde euch nicht vergessen. Vielen, vielen Dank! Thanks to Paddy for checking the English and Danke an Chris dafür, dass er zu meinem interessanten/langweiligen Vortrag gekommen ist. "Spasibo" also to Dima and Victor. Dima, for helping me several times and for having always an "open door" for me. Victor, for trying to convert me (unsuccessfully) to Python and for the discussions about the similarities between Russia and Italy. Many thanks also to those persons who left the institute before I could finish my PhD, but they have been important references for me: Gabi (C.), Michi, Jens, Francesco and Daniela. I did not forget you!

Outside of the Institute, many thanks to my friends Simon and Eleonora, my favorite flatmate Ale and my salsa-partner Linda! Thanks for being always so nice with me! Ein besonderer Dank geht an Damir für seine ständige Unterstützung.

Ovviamente devo ringraziare la mia famiglia, per avermi sempre sostenuto, moralmente ed economicamente, in questo nuovo percorso, tanto simile a quello intrapreso nei miei studi in Italia, quanto diverso nell'approccio e la realizzazione. Grazie a mamma e papà, a Chiara e Alberto, alla mia zietta e al mio nonno.

Grazie agli amici di sempre, che ancora oggi mi sostengono anche se da 500 km di distanza. Non sarebbe stato lo stesso senza saper di tornare in Italia e poter incontrare i miei amici di atletica. Stesso discorso per Roby, Erika e Cecia, per aver sempre cercato di incontrami anche nei weekend "toccata e fuga" in quel di Milano. Grazie all'Ale, da poco ritrovata. Grazie a Daniela e Beatrice per esserci sempre state. Vi voglio bene.

Lascio per ultimi due ringraziamenti particolari. Il primo va al Lorentz. Che dire... dopo aver condiviso l'ufficio allo IASF, ci siamo ritrovati colleghi anche allo IAAT. Le cose per cui dovrei ringraziarti sarebbero troppe, quindi mi limito a dirti Grazie. Veramente.

Infine, ancora una volta, mi "tocca" ringraziare proprio te Vale. Per tutto, dalla semplice condivisione degli alti (pochi) e bassi (tanti) del dottorato, all'amicizia che ci lega senza la quale non sarei arrivato e diventato quel che sono ora.

Curriculum vitae

17.01.1983	Born in Milan
1989 - 1994	Elementary School
	Istituto "Sant' Angela Merici", Milan, Italy
1994 - 1997	Middle School
	Scuola media statale "Donatello", Milan, Italy
1997 - 2002	High School
	Liceo Scientifico Statale "E. Vitttorini", Milan, Italy
2002 - 2005	Bachelor in *Physics*
	Università degli Studi di Milano Bicocca, Milan, Italy
2005 - 2008	Master in *Astrophysics and Space Physics*
	Università degli Studi di Milano Bicocca, Milan, Italy
2009 -	Scientific employee at Eberhard-Karls-Universität Tübingen
	Institut für Astronomie und Astrophysik (IAAT), Tübingen, Germany
	Preparation of the thesis entitled:
	"Ananlysis of X-Ray Observations of the Binary Her X-1"
	Advisor: Prof. i.R. Dr. R. Staubert

Apart from the professors of the Università degli Studi di Milano Bicocca, my academic teacher of the University of Tübingen has been Prof. Dr. A. Santangelo.

Bibliography

Anderson, C. M., Corliss, J., Scherb, F., & Potter, A. E. 1999, in AAS/Division for Planetary Sciences Meeting Abstracts, Vol. 31, AAS/Division for Planetary Sciences Meeting Abstracts #31, #58.06

Bai, T. 1980, ApJ, 239, 328

Basko, M. M. & Sunyaev, R. A. 1976, MNRAS, 175, 395

Basko, M. M. 1978, ApJ, 223, 268

Becker, R. H., Boldt, E. A., Holt, S. S., et al. 1976, in Bulletin of the American Astronomical Society, Vol. 8, Bulletin of the American Astronomical Society, 512

Becker, R. H., Boldt, E. A., Holt, S. S., et al. 1977, ApJ, 214, 879

Becker, P. A. & Wolff, M. T. 2007, ApJ, 654, 435

Blum, S. & Kraus, U. 2000, ApJ, 529, 968

Bochkarev, N. G. 1989, Soviet Astronomy, 33, 638

Bondi, H. & Hoyle, F. 1944, MNRAS, 104, 273

Bondi, H. 1952, MNRAS, 112, 195

Boroson, B., O'Brien, K., Horne, K., et al. 2000, ApJ, 545, 399

Boroson, B., Kallman, T., & Vrtilek, S. D. 2001, ApJ, 562, 925

Boyd, P., Still, M., & Corbet, R. 2004, The Astronomer's Telegram, 307, 1

Boynton, P. E., Canterna, R., Crosa, L., Deeter, J., & Gerend, D. 1973, ApJ, 186, 617

Bradt, H. V., McClintock, J. E., & Levine, A. M. 1985, The X-ray Timing Explorer, ed. Perola, G. C. & Salvati, M., 247

Brecher, K. 1972, Nature, 239, 325

Bulik, T., Meszaros, P., Woo, J. W., Hagase, F., & Makishima, K. 1992, ApJ, 395, 564

Burnard, D. J., Arons, J., & Klein, R. I. 1991, ApJ, 367, 575

Caballero, I., Santangelo, A., Kretschmar, P., et al. 2008, A&A, 480, L17

Cheng, F. H., Vrtilek, S. D., & Raymond, J. C. 1995, ApJ, 452, 825

Choi, C. S., Nagase, F., Makino, F., et al. 1994, ApJ, 437, 449

Choi, C. S., Seon, K. I., Dotani, T., & Nagase, F. 1997, ApJL, 476, L81

Clark, G. W., Woo, J. W., Nagase, F., Makishima, K., & Sakao, T. 1990, ApJ, 353, 274

Coburn, W., Heindl, W. A., Wilms, J., et al. 2000, ApJ, 543, 351

Coburn, W., Heindl, W. A., Gruber, D. E., et al. 2001, ApJ, 552, 738

Coburn, W., Heindl, W. A., Rothschild, R. E., et al. 2002, ApJ, 580, 394

Crosa, L. & Boynton, P. E. 1980, ApJ, 235, 999

Cusumano, G., di Salvo, T., Burderi, L., et al. 1998, A&A, 338, L79

Dal Fiume, D., Orlandini, M., Cusumano, G., et al. 1998, A&A, 329, L41

Davidson, K. & Ostriker, J. P. 1973, ApJ, 179, 585

DeCesar, M. E., Boyd, P. T., Markwardt, C. B., et al. 2009, in Bulletin of the American Astronomical Society, Vol. 41, American Astronomical Society Meeting Abstracts #213, #432.02

Deeter, J., Crosa, L., Gerend, D., & Boynton, P. E. 1976, ApJ, 206, 861

Deeter, J. E., Scott, D. M., Boynton, P. E., et al. 1998, ApJ, 502, 802

Dennerl, K. 1991, NASA STI/Recon Technical Report N, 932, 28202

Di Cocco, G., Caroli, E., Celesti, E., et al. 2003, A&A, 411, L189

Doroshenko, V., Suchy, S., Santangelo, A., et al. 2010, A&A, 515, L1

Drew, J. E. 1997, in Astronomical Society of the Pacific Conference Series, Vol. 121, IAU Colloq. 163: Accretion Phenomena and Related Outflows, ed. D. T. Wickramasinghe, G. V. Bicknell, & L. Ferrario, 465

Endo, T., Nagase, F., & Mihara, T. 2000, PASJ, 52, 223

Enoto, T., Makishima, K., Terada, Y., et al. 2008, PASJ, 60, 57

Fabian, A. C. 1973, Nature, 244, 212

Ferrigno, C., Becker, P. A., Segreto, A., Mineo, T., & Santangelo, A. 2009, A&A, 498, 825

Ferrigno, C., Falanga, M., Bozzo, E., et al. 2011, in The X-ray Universe 2011, ed. J.-U. Ness & M. Ehle, 69

Gerend, D. & Boynton, P. 1976, ApJ, 209, 562

Ghosh, P. & Lamb, F. K. 1979, ApJ, 234, 296

Giacconi, R., Gursky, H., Paolini, F. R., & Rossi, B. B. 1962, Physical Review Letters, 9, 439

Giacconi, R., Gursky, H., Kellogg, E., Schreier, E., & Tananbaum, H. 1971, ApJL, 167, L67

Giacconi, R., Gursky, H., Kellogg, E., et al. 1973, ApJ, 184, 227

Gold, T. 1968, Nature, 218, 731

Gruber, D. E., Matteson, J. L., Nolan, P. L., et al. 1980, ApJL, 240, L127

Gruber, D. E., Heindl, W. A., Rothschild, R. E., et al. 2001, ApJ, 562, 499

Harding, A. K. & Daugherty, J. K. 1991, ApJ, 374, 687

Heindl, W. A. & Smith, D. M. 1998, ApJL, 506, L35

Heindl, W. A., Coburn, W., Gruber, D. E., et al. 1999, ApJL, 521, L49

Heindl, W. A., Coburn, W., Gruber, D. E., et al. 2001, ApJL, 563, L35

Heindl, W., Coburn, W., Kreykenbohm, I., & Wilms, J. 2003, The Astronomer's Telegram, 200, 1

Hewish, A., Bell, S. J., Pilkington, J. D. H., Scott, P. F., & Collins, R. A. 1968, Nature, 217, 709

Hoffmeister, C. 1941, Mitteilungen der Sternwarte zu Sonneberg, 35, 1

Howarth, I. D. & Wilson, B. 1983, MNRAS, 202, 347

Hoyle, F. & Lyttleton, R. A. 1941, MNRAS, 101, 227

Illarionov, A. F. & Sunyaev, R. A. 1975, Soviet Astronomy Letters, 1, 73

in't Zand, J. 2011, ArXiv:1102.3345

İnam, S. C. & Baykal, A. 2005, MNRAS, 361, 1393

Jahoda, K. & PCA Team. 1996, in Bulletin of the American Astronomical Society, Vol. 28, American Astronomical Society Meeting Abstracts, 1285

Jahoda, K., Markwardt, C. B., Radeva, Y., et al. 2006, ApJS, 163, 401

Ji, L., Schulz, N., Nowak, M., Marshall, H. L., & Kallman, T. 2009, ApJ, 700, 977

Jimenez-Garate, M. A., Hailey, C. J., den Herder, J. W., Zane, S., & Ramsay, G. 2002, ApJ, 578, 391

Jimenez-Garate, M. A. & Khu, T. 2004, in Multiwavelength AGN Surveys, ed. R. Mújica & R. Maiolino, 191–192

Jones, C. & Forman, W. 1976, ApJL, 209, L131

Joss, P. C., Fechner, W. B., Forman, W., & Jones, C. 1978, ApJ, 225, 994

Kahabka, P. 1987, MPE Rep., No. 204, 139 pp., 204

Kahabka, P. 1989, in ESA Special Publication, Vol. 296, Two Topics in X-Ray Astronomy, Volume 1: X Ray Binaries. Volume 2: AGN and the X Ray Background, ed. J. Hunt & B. Battrick, 447–452

Katz, J. I. 1973, Nature, 246, 87

Kendziorra, E., Mony, B., Kretschmar, P., et al. 1992, in NASA Conference Publication, Vol. 3137, NASA Conference Publication, ed. C. R. Shrader, N. Gehrels, & B. Dennis, 217

Ketsaris, N. A., Kuster, M., Postnov, K. A., et al. 2000, ArXiv Astrophysics e-prints

Kii, T., Hayakawa, S., & Nagase, F. 1986, Astrophysics and Space Science, 118, 375

Klochkov, D. K., Shakura, N. I., Postnov, K. A., et al. 2006, Astronomy Letters, 32, 804

Klochkov, D. 2007, PhD thesis, Universität Tübingen.

Klochkov, D., Staubert, R., Postnov, K., et al. 2008, A&A, 482, 907

Klochkov, D., Staubert, R., Santangelo, A., Rothschild, R. E., & Ferrigno, C. 2011, A&A, 532, A126

Koyama, K., Hoshi, R., & Nagase, F. 1987, PASJ, 39, 801

Kretschmar, P., Araya-Gochez, R. A., Kreykenbohm, I., et al. 2001, in ESA Special Publication, Vol. 459, Exploring the Gamma-Ray Universe, ed. A. Gimenez, V. Reglero, & C. Winkler, 207–210

Kreykenbohm, I., Coburn, W., Wilms, J., et al. 2002, A&A, 395, 129

Kreykenbohm, I., Wilms, J., Coburn, W., et al. 2004, A&A, 427, 975

Kreykenbohm, I., Mowlavi, N., Produit, N., et al. 2005, A&A, 433, L45

Kukarkin, B. V., Kholopov, P. N., Pskovskij, Y. P., et al. 1971, General catalogue of variable stars. Volume_III., ed. Kukarkin, B. V., Kholopov, P. N., Pskovskij, Y. P., Efremov, Y. N., Kukarkina, N. P., Kurochkin, N. E., Medvedeva, G. I., Perova, N. B., Fedorovich, V. P., & Frolov, M. S.

Kunz, M. 1996, PhD thesis, Universität Tübingen.

Kunz, M., Kendziorra, E., Kretschmar, P., et al. 1996, Astronomy & Astrophysics Supplement Series, 120, C233

Kurochkin, N. E. 1972, Peremennye Zvezdy, 18, 425

Kuster, M. 2003, PhD thesis, Universität Tübingen.

Kuster, M., Wilms, J., Staubert, R., et al. 2005, A&A, 443, 753

La Barbera, A., Segreto, A., Santangelo, A., Kreykenbohm, I., & Orlandini, M. 2005, A&A, 438, 617

Lamb, F. K., Pethick, C. J., & Pines, D. 1973, ApJ, 184, 271

Lamb, F. K., Pines, D., & Shaham, J. 1975, in Bulletin of the American Astronomical Society, Vol. 7, Bulletin of the American Astronomical Society, 537

Lamers, H. J. G. L. M., van den Heuvel, E. P. J., & Petterson, J. A. 1976, A&A, 49, 327

Leahy, D. A. 1991, MNRAS, 251, 203

Leahy, D. A., Yoshida, A., & Matsuoka, M. 1994, ApJ, 434, 341

Leahy, D. A., Marshall, H., & Scott, D. M. 2000, ApJ, 542, 446

Leahy, D. A. 2001, in International Cosmic Ray Conference, Vol. 6, International Cosmic Ray Conference, 2536

Leahy, D. A. 2002, MNRAS, 334, 847

Lewin, W. H. G., van Paradijs, J., & Taam, R. E. 1993, Space Science Reviews, 62, 223

Link, B. & Epstein, R. I. 2001, ApJ, 556, 392

Lipunov, V. M. 1987, The astrophysics of neutron stars, ed. Lipunov, V. M.

Longair, M. S. 2010, High Energy Astrophysics, ed. Longair, M. S.

Lund, N., Budtz-Jørgensen, C., Westergaard, N. J., et al. 2003, A&A, 411, L231

Lutovinov, A. A., Grebenev, S. A., Pavlinsky, M. N., & Sunyaev, R. A. 2000, Astronomy Letters, 26, 691

Maisack, M., Grove, J. E., Kendziorra, E., et al. 1997, A&A, 325, 212

Makishima, K., Mihara, T., Ishida, M., et al. 1990, ApJL, 365, L59

Makishima, K., Mihara, T., Nagase, F., & Tanaka, Y. 1999, ApJ, 525, 978

Mas-Hesse, J. M., Giménez, A., Culhane, J. L., et al. 2003, A&A, 411, L261

Mavromatakis, F. 1993, A&A, 273, 147

McCray, R. A., Shull, J. M., Boynton, P. E., et al. 1982, ApJ, 262, 301

Meszaros, P. 1984, Space Science Reviews, 38, 325

Middleditch, J. & Nelson, J. 1976, ApJ, 208, 567

Middleditch, J. 1983, ApJ, 275, 278

Mihara, T., Ohashi, T., Makishima, K., et al. 1991, PASJ, 43, 501

Mihara, T., Soong, Y., & ASCA Team. 1994, in New Horizon of X-Ray Astronomy. First Results from ASCA, ed. F. Makino & T. Ohashi, 419

Mihara, T., Makishima, K., & Nagase, F. 1995, in Bulletin of the American Astronomical Society, Vol. 27, American Astronomical Society Meeting Abstracts, #104.03

Mihara, T., Makishima, K., & Nagase, F. 1998, Advances in Space Research, 22, 987

Mitsuda, K., Inoue, H., Koyama, K., et al. 1984, PASJ, 36, 741

Mowlavi, N., Kreykenbohm, I., Shaw, S. E., et al. 2006, A&A, 451, 187

Nagase, F. 1989, PASJ, 41, 1

Nagel, W. 1980, ApJ, 236, 904

Naik, S. & Paul, B. 2003, A&A, 401, 265

Nakajima, M., Mihara, T., Makishima, K., & Niko, H. 2006, ApJ, 646, 1125

Nelson, R., Salpeter, E., & Wassermann, I. 1993, ApJ, 418, 874

Oegelman, H. & Trümper, J. 1988, EXOSAT observations of Hercules X-1, ed. Pallavicini, R. & White, N. E., 169

Ohashi, T., Inoue, H., Kawai, N., et al. 1984, PASJ, 36, 719

Oosterbroek, T., Parmar, A. N., Martin, D. D. E., & Lammers, U. 1997, A&A, 327, 215

Oosterbroek, T., Parmar, A. N., Dal Fiume, D., et al. 2000, A&A, 353, 575

Orlandini, M., Fiume, D. D., Frontera, F., et al. 1998, ApJL, 500, L163

Panchenko, I. E. & Postnov, K. A. 1994, A&A, 286, 497

Parmar, A. N., Sanford, P. W., & Fabian, A. C. 1980, MNRAS, 192, 311

Parmar, A. N., Oosterbroek, T., dal Fiume, D., et al. 1999, A&A, 350, L5

Petterson, J. A. 1975, ApJL, 201, L61

Petterson, J. A. 1977, ApJ, 218, 783

Pines, D., Lamb, F. K., & Pethick, C. J. 1973, in Annals of the New York Academy of Sciences, Vol. 224, Sixth Texas Symposium on Relativistic Astrophysics, ed. D. J. Hegyi, 237

Pravdo, S. H., Becker, R. H., Boldt, E. A., et al. 1977a, ApJL, 215, L61

Pravdo, S. H., Boldt, E. A., Holt, S. S., & Serlemitsos, P. J. 1977b, ApJL, 216, L23

Pravdo, S. H., Bussard, R. W., Becker, R. H., et al. 1978, ApJ, 225, 988

Pravdo, S. H., Bussard, R. W., & White, N. E. 1979, MNRAS, 188, 5P

Priedhorsky, W. C. & Holt, S. S. 1987, Space Science Reviews, 45, 291

Pringle, J. E. & Rees, M. J. 1972, A&A, 21, 1

Prokhorov, M. E., Shakura, N. I., & Postnov, K. A. 1990, in ESA Special Publication, Vol. 311, ESA Special Publication, ed. T. D. Guyenne & J. J. Hunt, 235–237

Raguzova, N. V. & Lipunov, V. M. 1998, A&A, 340, 85

Ramsay, G., Zane, S., Jimenez-Garate, M. A., den Herder, J.-W., & Hailey, C. J. 2002, MNRAS, 337, 1185

Rappaport, S. & Joss, P. C. 1977, Nature, 266, 683

Reynolds, A. P., Quaintrell, H., Still, M. D., et al. 1997, MNRAS, 288, 43

Rothschild, R. E., Gruber, D. E., Knight, F. K., et al. 1981, ApJ, 250, 723

Rothschild, R. E., Blanco, P. R., Gruber, D. E., et al. 1998, ApJ, 496, 538

Rothschild, R. E., Markowitz, A., Rivers, E., et al. 2011, ApJ, 733, 23

Rybicki, G. B. & Lightman, A. P. 1979, Radiative processes in astrophysics, ed. Rybicki, G. B. & Lightman, A. P.

Santangelo, A., del Sordo, S., Segreto, A., et al. 1998, A&A, 340, L55

Santangelo, A., Segreto, A., Giarrusso, S., et al. 1999, ApJL, 523, L85

Schandl, S. & Meyer, F. 1994, A&A, 289, 149

Scott, D. M. 1993, PhD thesis, Washington Univ., Seattle, WA.

Scott, D. M., Wilson, R. B., Finger, M. H., & Leahy, D. A. 1997, in American Institute of Physics Conference Series, Vol. 410, Proceedings of the Fourth Compton Symposium, ed. C. D. Dermer, M. S. Strickman, & J. D. Kurfess, 748–752

Scott, D. M. & Leahy, D. A. 1999, ApJ, 510, 974

Scott, D. M., Leahy, D. A., & Wilson, R. B. 2000, ApJ, 539, 392

Shakura, N. I., Postnov, K. A., & Prokhorov, M. E. 1991, Soviet Astronomy Letters, 17, 339

Shakura, N. I., Postnov, K. A., & Prokhorov, M. E. 1998, A&A, 331, L37

Shakura, N. I., Prokhorov, M. E., Postnov, K. A., & Ketsaris, N. A. 1999, A&A, 348, 917

Shapiro, S. L. & Teukolsky, S. A. 1986, Black Holes, White Dwarfs and Neutron Stars: The Physics of Compact Objects, ed. Shapiro, S. L. & Teukolsky, S. A.

Sheffer, E. K., Kopaeva, I. F., Averintsev, M. B., et al. 1992, Soviet Astronomy, 69, 82

Shrader, C. R., Sutaria, F. K., Singh, K. P., & Macomb, D. J. 1999, ApJ, 512, 920

Shulman, S., Friedman, H., Fritz, G., Yentis, D. J., & Henry, R. C. 1975, ApJL, 199, L101

Slettebak, A. & Snow, T. P. 1988, Journal of the Royal Astronomical Society of Canada, 82, 217

Soong, Y., Gruber, D. E., Peterson, L. E., & Rothschild, R. E. 1990a, ApJ, 348, 641

Soong, Y., Gruber, D. E., Peterson, L. E., & Rothschild, R. E. 1990b, ApJ, 348, 634

Staubert, R., Bezler, M., & Kendziorra, E. 1983, A&A, 117, 215

Staubert, R., Schandl, S., Klochkov, D., et al. 2006, in American Institute of Physics Conference Series, Vol. 840, The Transient Milky Way: A Perspective for MIRAX, ed. F. D'Amico, J. Braga, & R. E. Rothschild, 65–70

Staubert, R., Shakura, N. I., Postnov, K., et al. 2007, A&A, 465, L25

Staubert, R. 2008, in: The Universe in X-Rays, ed. Trümper, J. E. & Hasinger, G.

Staubert, R., Klochkov, D., Postnov, K., et al. 2009a, A&A, 494, 1025

Staubert, R., Klochkov, D., & Wilms, J. 2009b, A&A, 500, 883

Staubert, R., Klochkov, D., Postnov, K., et al. 2010a, X-ray Astronomy 2009, Bologna; Present Status, Multi-Wavelength Approach and Future Perspectives, 1248, 209

Staubert, R., Klochkov, D., Vasco, D., & Wilms, J. 2010b, in Proceedings of the 8th INTEGRAL Workshop "The Restless Gamma-ray Universe" (INTEGRAL 2010). September 27-30 2010. Dublin Castle, Dublin, Ireland, id. 48

Staubert, R., Klochkov, D., Vasco, D., & Wilms, J. 2010c, in Proceedings of the 8th INTEGRAL Workshop "The Restless Gamma-ray Universe" (INTEGRAL 2010). September 27-30 2010. Dublin Castle, Dublin, Ireland, id. 141

Stella, L., White, N. E., & Rosner, R. 1986, ApJ, 308, 669

Still, M., O'Brien, K., Horne, K., et al. 2001a, ApJ, 554, 352

Still, M., O'Brien, K., Horne, K., et al. 2001b, ApJ, 553, 776

Swank, J. H., Becker, R. H., Boldt, E. A., et al. 1976, ApJL, 209, L57

Tananbaum, H., Gursky, H., Kellogg, E. M., et al. 1972, ApJL, 174, L143

Tauris, T. M. & van den Heuvel, E. P. J. 2006, Formation and evolution of compact stellar X-ray sources, ed. Lewin, W. H. G. & van der Klis, M., 623–665

Titarchuk, L. 1994, ApJ, 434, 570

Trümper, J., Pietsch, W., Reppin, C., et al. 1978, ApJL, 219, L105

Trümper, J., Kahabka, P., Oegelman, H., Pietsch, W., & Voges, W. 1986, ApJL, 300, L63

Tsygankov, S. S., Lutovinov, A. A., Churazov, E. M., & Sunyaev, R. A. 2006, MNRAS, 371, 19

Tsygankov, S. S., Krivonos, R. A., & Lutovinov, A. A., 2012, MNRAS, 421, 2407

Ubertini, P., Lebrun, F., Di Cocco, G., et al. 2003, A&A, 411, L131

Vasco, D., Klochkov, D., & Staubert, R. 2011, A&A, 532, A99

Vedrenne, G., Roques, J.-P., Schönfelder, V., et al. 2003, A&A, 411, L63

Verbunt, F., Pooley, D., & Bassa, C. 2008, in IAU Symposium, Vol. 246, IAU Symposium, ed. E. Vesperini, M. Giersz, & A. Sills, 301–310

Voges, W., Pietsch, W., Reppin, C., et al. 1982, ApJ, 263, 803

Voges, W., Kahabka, P., Oegelman, H., Pietsch, W., & Truemper, J. 1985, Space Science Reviews, 40, 339

Vrtilek, S. D. & Halpern, J. P. 1985, ApJ, 296, 606

Vrtilek, S. D., Mihara, T., Primini, F. A., et al. 1994, ApJL, 436, L9

Wang, Y.-M. & Welter, G. L. 1981, A&A, 102, 97

Wang, Y.-M. 1987, A&A, 183, 257

Wheaton, W. A., Doty, J. P., Primini, F. A., et al. 1979, Nature, 282, 240

White, N. E., Swank, J. H., & Holt, S. S. 1983, ApJ, 270, 711

Wilms, J., Burki, G., Bourban, G., et al. 2003, in Bulletin of the American Astronomical Society, Vol. 35, AAS/High Energy Astrophysics Division #7, 863

Wilms, J., Schönherr, G., Schmid, J., Dauser, T., & Kreykenbohm, I. 2009, in American Institute of Physics Conference Series, Vol. 1126, American Institute of Physics Conference Series, ed. J. Rodriguez & P. Ferrando, 295–300

Winkler, C., Courvoisier, T. J.-L., Di Cocco, G., et al. 2003, A&A, 411, L1

Xu, C., Vrtilek, S. D., Boroson, B., & McCray, R. 1995, in Bulletin of the American Astronomical Society, Vol. 27, American Astronomical Society Meeting Abstracts #186, 826

Yamamoto, T., Sugizaki, M., Mihara, T., et al. 2011, PASJ, 63, 751

Zane, S. & Ramsay, G. 2001, in Two Years of Science with Chandra

Zane, S., Ramsay, G., Jimenez-Garate, M. A., Willem den Herder, J., & Hailey, C. J. 2004, MNRAS, 350, 506